



**HAL**  
open science

# MRI and Fluorescence Image-Guided Drug Delivery by pH-Sensitive Polymer Nanocarriers

Marie Devreux

► **To cite this version:**

Marie Devreux. MRI and Fluorescence Image-Guided Drug Delivery by pH-Sensitive Polymer Nanocarriers. Polymers. Université de Bordeaux; Université de Mons, 2023. English. NNT: 2023BORD0162 . tel-04192899

**HAL Id: tel-04192899**

**<https://theses.hal.science/tel-04192899v1>**

Submitted on 31 Aug 2023

**HAL** is a multi-disciplinary open access archive for the deposit and dissemination of scientific research documents, whether they are published or not. The documents may come from teaching and research institutions in France or abroad, or from public or private research centers.

L'archive ouverte pluridisciplinaire **HAL**, est destinée au dépôt et à la diffusion de documents scientifiques de niveau recherche, publiés ou non, émanant des établissements d'enseignement et de recherche français ou étrangers, des laboratoires publics ou privés.

# Marie Devreux

Dissertation présentée en vue de l'obtention du grade académique de

*Doctorat en Sciences de l'Université de Mons*

*Doctorat en Sciences chimiques spécialité polymères de l'Université de Bordeaux*

---

## MRI and Fluorescence Image-Guided Drug Delivery by pH-Sensitive Polymer Nanocarriers

---

Directrice de thèse : **Prof. Sophie Laurent**

Directeur de thèse : **Dr. Olivier Sandre**

Soutenue le 23 juin 2023

*Membres du jury:*

<b>M. Jean-Michel Siaugue</b>	<b>Maître de conférences, Sorbonne université, France</b>	<b>Rapporteur</b>
<b>Mme. Françoise Chuburu</b>	<b>Professeur des Universités, Université de Reims, France</b>	<b>Rapporteuse</b>
<b>Mme. Angela Mutschler</b>	<b>Maître de conférences, Université de Bordeaux, France</b>	<b>Examinatrice</b>
<b>M. Pascal Gerbaux</b>	<b>Professeur des Universités, Université de Mons, Belgique</b>	<b>Examinateur</b>
<b>M. Robert Muller</b>	<b>Professeur Émérite, CMMI, Belgique</b>	<b>Examinateur</b>
<b>Mme. Céline Henoumont</b>	<b>Assistante professeur, Université de Mons, Belgique</b>	<b>Examinatrice</b>

Année académique 2022-2023



# Acknowledgements

---

Je tiens tout d'abord à remercier les membres du jury, Pascal Gerbaux, Céline Henoumont, Françoise Chuburu, Jean-Michel Siaugue, Robert Muller et Angela Mutschler, tout d'abord pour avoir accepté de faire partie de mon jury et d'avoir porté un intérêt à mon travail.

J'aimerais ensuite remercier mes directeurs de thèse. Sophie merci de m'avoir donné ma chance, d'avoir cru en moi, et d'avoir essayé de trouver des solutions pour me garder. Merci d'avoir été à l'écoute durant ma thèse car oui, les soucis ont été nombreux. J'espère que mon entrain et mes « Sophiiiiie » lourds de sous-entendu te manqueront quand même (un petit peu). Tu m'as aussi permis de faire l'UDEM qui, pour moi, fut une expérience vraiment sympa ! La solution finale que tu as trouvée pour me permettre de réaliser cette thèse m'a amené à rencontrer Olivier Sandre mon second encadrant. Votre regard sur mon travail m'a permis d'étendre grandement mes connaissances sur des sujets qui n'étaient encore pour moi que de la théorie vue en cours. Vous m'avez permis aussi d'avoir un regard différent sur mes recherches. Vos nombreux conseils (même en chimie organique) m'ont toujours beaucoup apporté. Pour tout ceci, je vous remercie tous les deux.

Merci Céline pour tes nombreuses corrections (où tu as certainement dû te tirer les cheveux souvent !) et pour ton aide sur toute la partie relaxométrie. Dimitri, merci pour tes nombreux conseils en chimie organique.

Par la suite, j'aimerais aussi dire un merci à M. Muller qui m'a inculqué la remise en question totale et de ne pas tenir pour acquis ce qu'on pouvait me dire. C'est une leçon que je n'oublierai pas.

J'aimerais remercier pour l'aspect biologique de cette thèse les personnes suivantes : Lionel Larbanoix, Sébastien Boutry, Coralie Genevois et Franck Couillaud. Merci pour votre regard critique sur mes recherches, les manipulations et votre partage de point de vue qui m'ont permis d'avoir un regard différent sur ces aspects-là.

Ensuite, je remercie M. Coulembier et Sébastien Moins pour leur grande aide et leurs nombreux conseils en polymère.

LCPO team 3, merci pour votre accueil et votre bienveillance (surtout à mes débuts un peu chaotique). Cette cotutelle m'a permis de découvrir un autre environnement de thèse avec de

super belles rencontres. Elle m'a permis aussi de repousser mes peurs, de sortir de ma zone de confort. Tout d'abord, mes chères copines, Élise et Anouk, les filles merci. Merci pour toutes ces belles après-midi, journées, passées ensemble. Anouk, pâtissière en herbe, même si clairement quand baptiste va en cours on préfère car on a droit à du chocolat, (et pas que je suis amoureuse de ma baleine rose), Élise, les ragots toujours à la pointe de l'actualité, ta joie au quotidien qui redonne le sourire même si tu râles. Vous serez toujours les bienvenues en Belgique, je vous accueille dès que vous voulez (prochain RDV le 18 mai 2024) ! Ensuite Diana, (je sais que tu sais lire le Français) merci d'être toi, tu es une fille qui apporte énormément de gaieté au quotidien. Merci à Chloé qui a partagé durant 1 mois mon sujet sur une machine pas si friendly ! A toutes ces rencontres : Leslie, Paul, Pierre, Mathieu, Éloïse, Mostafa, Elizabeth, Angela, Christophe, Florian, Manon, Hannah, Martin, Mégi, Nadia, Pedro, Amelie, ... .

SCGOB, merci de m'avoir accompagnée durant ces 4 ans et demi me donnant beaucoup de bon souvenir pour m'accompagner dans ce nouveau futur et de collègues qui en sont devenu des amis. Tout d'abord merci à Elodie et Johary de m'avoir accompagné durant quelques mois sur mon sujet. Malgré votre capacité à faire des bêtises, je vous aime bien quand même ! J'aimerais ensuite faire quelques spéciales cassdedi. A bob le bricoleur, mais aussi papa du labo (évidemment t'es le plus vieux donc bon) Vincent, mon compatriote de galère qui m'a abandonné Pierre, ma copine de papote (et de pâtisserie désormais) Isalyne, à mes comparses biologistes qui m'ont tellement aidée et pris du temps pour le faire Thomas et Valentin, Sarah la personne la plus serviable toujours là dans les moindres moments bons comme mauvais, Thomas pour tes nombreux conseils au quotidien, Amandine, Mélanie, Aurélie, Levy, Loris, Léa, Maléotane, Marion, Gamze, Séverine, Sophie, Camille, Sanae... .

J'aimerais remercier mes amis qui m'ont accompagné durant ces 4 longues années. Magalie, ma meilleure amie, et Thibault vous êtes des co-capitaines en or, merci de m'avoir écouté râler, pleurer, rigoler pendant des heures (alors qu'au fond vous n'avez pas du toujours comprendre grand-chose à tout sorry). Camille et Jules, sans oublier baby Arthur, j'espère vous avoir encore de nombreuses années à mes côtés sinon qui titillerait ma susceptibilité ? Sans oublier les jeux de mots... NUL. A ces amis qui en deviennent de la famille, Charlotte et Kephren, taty est prête les filles ! Perrine, toutes ces rencontres devant l'ascenseur à discuter à en perdre le temps. On oublie bien sûr pas : Carolane, Florent, Anthony, les Clems, Martin, Amandine, Logan, Maxime, Lorentz... . De si belles rencontres durant ces années d'études.

Merci à mes tatas tapas d'amour, ce genre de personnes qui nous permette de sortir de notre quotidien, Valentine, Brioux, Lou, Gauthier, Ludivine, Clément, Juliette, Maurine, Maxime, Cassandra, Valentin.

A l'une des personnes les plus importante de ma vie, Maman, Martine, sans qui, à l'heure où j'écris ces quelques lignes qui n'exprimeront jamais assez bien ce que je ressens, je ne serai pas ici. Aucun mot, aucune expression n'est assez forte pour t'exprimer à quel point je te suis reconnaissante pour tout ce que tu as fait et fait toujours pour moi. Tu nous as tenu de toutes tes forces moi et ma sœur, Emilie, que je redécouvre chaque jour et que je suis extrêmement reconnaissante d'avoir. Je serai toujours là pour toi petite sœur. Merci à ma grand-mère, Nicole, de t'être occupée de nous comme tu l'as fait avec bon-papa, Michel, parti beaucoup trop tôt et à qui j'aurai tellement aimé montrer ce que je suis devenue. J'espère que de là-haut tu es fier de moi. Merci à mon père, Thierry. Merci aussi à ma belle-famille.

Last but not least, Nicolas. Avant de te dire merci, j'aimerais te dire désolé d'être une fille aussi ennuyante mais après quasiment 10 ans de relation, un mariage approchant je pense que tu commences à le savoir. Je dois te dire merci pour énormément de choses, de m'avoir épaulé durant nos études, de me supporter et m'aimer comme je suis, d'avoir passé des soirées à lire ma thèse pour m'aider à corriger (put in evidence toi-même tu sais), de continuer à être là dans les bon comme les mauvais moment (car oui je pense qu'on a déjà eu un peu de tout à affronter). Pour tous ces moments et ces moments à venir, je t'aimais, je t'aime et je t'aimerai.

Une dernière fois merci à tous pour avoir fait de ces 4 ans (presque 5) une expérience comme elle l'a été.



## Summary

---

Cancer remains a major cause of death in the world. A lot of efforts are thus made to diagnose it at an earlier stage and to treat it more efficiently. Indeed, the actually used treatments are invasive or lead to multi drug resistance by using several times chemotherapy techniques for example. Therefore, there is for several reasons a growing interest in nanomedicine, and more particularly on polymeric nanoobjects, to improve current treatments. They are indeed tunable, that is to say that they can be synthesized as a function of the aimed application, they are able to encapsulate dyes and/or drugs in the vesicles or at their surface, they can be stimuli sensitive to perform drug delivery, and so on. Moreover, theranostic which combines drug delivery and imaging has a growing interest thanks to imaging contrast agents encapsulated in the nanoobjects, allowing to follow them *in vivo* and to diagnose the evolution state of cancers. The most used imaging technique in hospital is magnetic resonance imaging (MRI). Nevertheless, this technique has a lack in sensitivity that can be palliated by using contrast agents or bimodal systems. The most used contrast agents in clinic are based on gadolinium complexes. However, studies have proved that these contrast agents led to nephrogenic systemic fibrosis more particularly to patients with kidneys diseases as well as an accumulation in the brain after repeated injections.

Herein, we have developed polymeric nanoobjects, micelles and vesicles (also called polymersomes) which are made of a pH-sensitive polyester shell to obtain a controlled release of the encapsulated drug in the acidic tumoral environment. The polymer carrier is composed of an amphiphilic copolymer PEO-*b*-P(CL-*co*-LA) with a statistical hydrophobic block obtained by ring opening polymerization (ROP) of  $\epsilon$ -caprolactone and *L*-lactide (LLA). During the self-assemblies, these nanoobjects will encapsulate doxorubicin, a well-know anti-cancer drug as well as dyes, ZW800-1 a near infrared fluorophore derivated from indocyanine green, which is already Food and Drug Administration (FDA) approved as contrastophore in fluorescence imaging (FLI). These nanosystems were characterized by different techniques able to evidence their structure and they were evaluated *in vitro* and *in vivo*.

In a second time, to palliate to the issues induced by gadolinium complexes used in MRI, we have developed manganese complexes based on pyclen derivatives. The developed macrocycles were fully characterized and their efficiency in MRI were evaluated by different NMR techniques. Finally, their biodistribution, efficiency and impact in the organism were

determined by *in vivo* tests. The manganese complexes showed an efficiency close to that of gadolinium complexes. To improve it, it was envisaged to graft them on the surface of the nanoobjects which will modify the rotational correlation time of the complexes, and hence their efficacy. To perform this, a click chemistry between the macrocycles and the nanovesicles was planned, so that the Mn-complexes and the polymers have to be functionalized with the right chemical groups. Different strategies of synthesis were investigated to obtain the desired compounds.

# Résumé de la thèse

---

Le cancer reste une cause majeure de décès dans le monde. Beaucoup d'efforts sont dès lors réalisés afin de pouvoir le diagnostiquer à un stade précoce et le traiter plus efficacement. En effet, les traitements actuellement utilisés sont invasifs ou conduisent à une résistance aux médicaments en utilisant par exemple de nombreuses fois la chimiothérapie. C'est pourquoi il y a un intérêt croissant pour la nanomédecine et plus particulièrement pour les nano-objets polymériques afin d'améliorer les traitements actuels. Les raisons en sont qu'ils sont versatiles, c'est-à-dire qu'ils peuvent être synthétisés en fonction de l'application visée, qu'ils peuvent être greffés ou encapsuler des fluorophores et/ou des médicaments, qu'ils peuvent être sensibles à différents stimuli pour effectuer le relargage du médicament, etc. De plus, mettre en place une plateforme théranostique, combinant l'administration de médicaments et l'imagerie, est un avantage. En effet, les contrastophores encapsulés ou greffés permettent de suivre *in vivo* les nanoobjets ainsi que l'état d'évolution du cancer. La technique d'imagerie la plus utilisée à l'hôpital est l'imagerie par résonance magnétique (IRM). Néanmoins, cette technique a un manque de sensibilité qui peut être palliée en utilisant un agent de contraste ou un système bimodal. Les agents de contrastes les plus utilisés en milieu hospitalier sont basés sur des complexes de gadolinium. Cependant, des études ont prouvé que ces agents de contraste conduisent à une fibrose systémique néphrogénique plus particulièrement chez les patients souffrant de maladies rénales et à une accumulation dans le cerveau après des injections répétées.

Nous avons développé des nano-objets polymériques, des micelles et des vésicules (également appelées polymersomes) qui sont constitués d'une coque de polyester sensible au pH afin d'obtenir une libération contrôlée des médicaments encapsulés dans l'environnement tumoral acide. Le copolymère est composé d'une structure amphiphile PEO-*b*-P(CL-*co*-LA) avec une séquence hydrophobe statistique obtenue par polymérisation par ouverture de cycle (ROP) de l' $\epsilon$ -caprolactone et du *L*-lactide (*L*-LA). Ces nano-objets sont capables lors de l'autoassemblage d'encapsuler la doxorubicine comme médicament pour le traitement du cancer ainsi qu'un contrastophore, le ZW800-1 qui est un fluorophore absorbant dans le proche infrarouge dérivé du vert d'indocyanine, un contrastophore déjà approuvé par la FDA en tant que fluorophore pour l'imagerie optique par fluorescence. Ces nanosystèmes ont été caractérisés par différentes techniques capables de mettre en évidence leur structure et ils ont été évalués *in vitro* et *in vivo*.

Dans un second temps, pour pallier les problèmes induits par l'utilisation des complexes de gadolinium en IRM, nous avons développé des dérivés de pycène complexés avec des ions manganèse. Les macrocycles développés ont été entièrement caractérisés et leur efficacité en IRM a été évalué par différentes techniques de RMN. Enfin, leur biodistribution, leur efficacité et leur impact sur l'organisme ont été déterminés par des tests *in vivo*. L'efficacité des complexes de manganèse est proche de celle des complexes de gadolinium. Pour l'améliorer, il est possible de les greffer en surface des nano-objets susmentionnés afin de modifier leur temps de corrélation rotationnel, et donc leur efficacité. Pour ce faire, une stratégie par chimie click est envisagée, impliquant la fonctionnalisation des complexes de Mn et des polymères par les groupements chimiques adéquats. Différentes stratégies de synthèse ont été étudiées pour obtenir les composés désirés.

## Résumé étendu en français

---

Le cancer reste aujourd'hui une cause majeure de décès dans le monde. Beaucoup d'efforts dans le monde de la recherche sont dès lors réalisés afin de parvenir à le diagnostiquer à un stade précoce et à le traiter le plus efficacement possible. En effet, les traitements actuellement utilisés sont soit invasifs, soit conduisent à une résistance aux médicaments en utilisant, par exemple, de nombreuses injections de chimiothérapie. C'est pourquoi il y a un intérêt croissant pour la nanomédecine et plus particulièrement pour les nano-objets polymères, une catégorie d'objets particulièrement prometteurs pour l'amélioration des traitements actuels. Les raisons en sont qu'ils sont versatiles, c'est-à-dire qu'ils peuvent être facilement modifiés afin de correspondre à l'application visée de par la voie de synthèse choisie, que des molécules d'intérêt peuvent être greffées sur leur surface en fonction des bouts de chaînes utilisés, qu'ils peuvent encapsuler des contrastophores et/ou des médicaments, qu'ils peuvent être sensibles à différents stimuli pour effectuer le relargage du médicament, etc. De plus, il est possible avec ce type d'objets de mettre en place une plateforme théranostique, combinant l'administration de médicaments et le suivi par imagerie, ce qui est un avantage. En effet, les contrastophores encapsulés ou greffés permettent de suivre *in vivo* les nano-objets ainsi que, idéalement, l'évolution des tumeurs.

La technique d'imagerie la plus utilisée est l'imagerie par résonance magnétique (IRM). Néanmoins, cette technique a un manque de sensibilité qui peut être pallié par l'utilisation d'un agent de contraste ou d'un système bimodal. Les agents de contraste les plus utilisés en milieu hospitalier sont des complexes de gadolinium. Cependant, des études ont prouvé que ces agents de contraste conduisent à des fibroses systémiques néphrogéniques plus particulièrement chez les patients souffrant de maladies rénales et à une possible accumulation dans le cerveau après des injections répétées. Une alternative à ce problème serait la mise en place de complexes de manganèse qui est un ion naturellement présent dans le corps et ingéré quotidiennement. Suivant cette optique, 4 agents complexants, à base de dérivés de cyclène, ont été synthétisés et la structure moléculaire des composés intermédiaires menant aux complexes a été totalement caractérisée. (Figure II.2) Ces complexants sont obtenus sur base d'une « partie basse » dérivée de diéthylène triamine fonctionnalisée où nous venons greffer une « partie haute » obtenue grâce à la fonctionnalisation de 3-hydroxypyridine qui, après plusieurs étapes de déprotection

et/ou de fonctionnalisation, permet d'obtenir le macrocycle capable de complexer les ions manganèse.

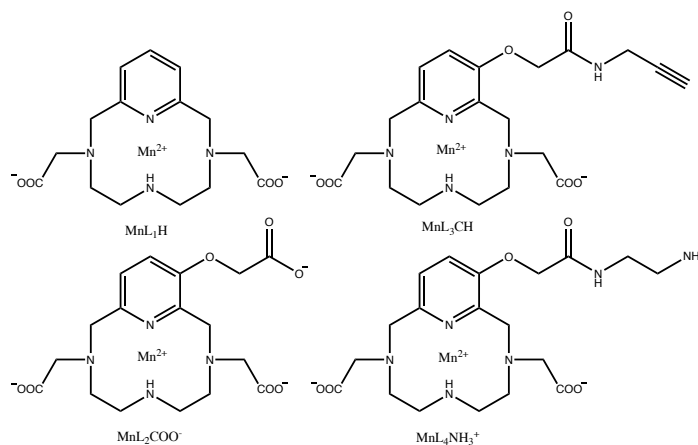


Figure II.2. Structures des 4 complexes de manganèse synthétisés et étudiés dans le cadre de ce travail  $MnL_1H$  :  $MnPy(COO^-)_2-H$ ;  $MnL_2COO^-$  :  $MnPy(COO^-)_2-OCH_2COO^-$ ;  $MnL_3CH$ :  $MnPy(COO^-)_2-OCH_2CONHCH_2CCH$  et  $MnL_4NH_3^+$  :  $MnPy(COO^-)_2-OCH_2CONH(CH_2)_2NH_3^+$ .

Les complexes de manganèse correspondants ont été entièrement caractérisés par des méthodes avancées de relaxométrie afin d'évaluer les paramètres régissant leurs propriétés et leur efficacité en tant qu'agents de contraste paramagnétiques en IRM. Cette caractérisation est importante afin d'évaluer si les complexes ont une efficacité proche de celle des complexes commerciaux de gadolinium, et pourraient potentiellement les concurrencer sur le marché, s'ils passent une évaluation plus approfondie de leur bio-sécurité. Les analyses de relaxométrie ont mis en évidence la présence d'une molécule d'eau dans leur première sphère de coordination avec un échange rapide de la molécule d'eau avec celles présentes dans son environnement et un temps de corrélation rotationnel typique de petites molécules paramagnétiques. Bien que ces composés à base de manganèse se soient révélés légèrement moins efficaces que les composés à base de gadolinium commercialisés, ce qui est attribué à un moment magnétique plus faible du métal, le potentiel de ces composés chélatants à base de pyclène reste élevé. En effet, lorsque la relaxivité des complexes est comparée avec celle d'un complexe de gadolinium commercial extraite sur la base d'images IRM d'échantillons « fantômes », (Figure II.12) les complexes de manganèse fonctionnalisés sur la pyridine présentent une relaxivité  $r_1$  proche de celle du complexe de gadolinium macrocyclique le plus courant, Gd-DOTA.

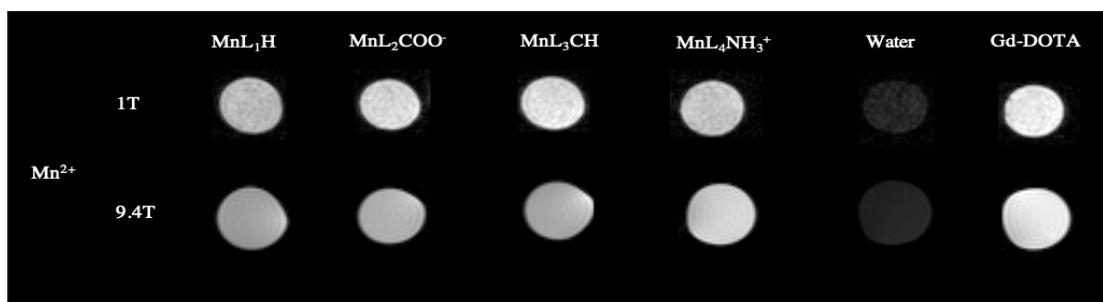


Figure II.12. Images fantômes enregistrées à approximativement 37°C et deux champs magnétiques (1 T et 9.4 T) pour chaque complexe de manganèse synthétisé à 0,5 mM comparé au Gd-DOTA à la même concentration et à l'eau pure. La séquence RARE pour 1 T et FISP pour 9.4 T ont été utilisées pour l'enregistrement.

La relaxivité de nos complexes pourrait néanmoins être améliorée de différentes manières. Tout d'abord, il serait possible de jouer sur le temps de corrélation rotationnel du complexe en le bloquant dans une nanostructure, qu'elle soit organique (par exemple, des micelles ou des vésicules) ou inorganique (par exemple, des nanoparticules de silice), tout en gardant une taille hydrodynamique suffisamment faible pour permettre une furtivité et une clairance rapide lors de l'injection en circulation systémique (ce qui est un prérequis pour les agents de contraste utilisés en clinique). De plus, les fonctions chimiques supplémentaires sur la structure pyridinique permettront la conjugaison à des vecteurs biologiquement pertinents tels que des peptides ou des anticorps afin de cibler des pathologies spécifiques.

Par la suite, une évaluation de la biodistribution *in vivo* de deux des 4 composés synthétisés,  $MnL_1H$  et  $MnL_2COO^-$ , a été réalisée afin de mettre en évidence la capacité de ces derniers à éclaircir les zones de clairances permettant ainsi leur mise en évidence. Les images *in vivo* montrent des résultats intéressants, indiquant un mécanisme de clairance majoritairement rénal. Néanmoins, les autres voies d'élimination, comme le foie, émettent aussi un signal et doivent donc être étudiées car elles suggèrent une possible déstabilisation des complexes. Les mécanismes d'absorption et d'excrétion cellulaires (ions  $Mn^{2+}$  libres ou  $Mn^{2+}$  complexés), ainsi que la possibilité de décomplexation (*in vivo*) doivent être démontrés par d'autres études biologiques. Cette décomplexation pourrait se produire par compétition avec les ions zinc et cuivre également présents dans l'organisme si l'on compare les constantes de stabilité (pour  $MnL_1H$ ) et les tests de transmétallation en présence d'ions zinc réalisés.<sup>1</sup> Pour mettre en évidence ce problème, il pourrait être intéressant d'utiliser des ions manganèse radiomarqués qui devraient permettre de suivre uniquement les ions manganèse exogènes et de pouvoir les suivre *in vivo*. Cependant, il pourrait également être intéressant d'évaluer si la présence d'un bras fonctionnalisé sur la pyridine a un impact sur le système aussi bien sur la constante

cinétique que sur la stabilité thermodynamique. D'autre part, il serait intéressant aussi de mettre en évidence la viscosité des fluides rénaux pour vérifier si le contraste est apporté uniquement par l'effet des agents de contraste ou par une modification de la viscosité induite par la présence des agents de contraste.

Sur la base des résultats, une nouvelle amélioration de l'inertie cinétique des complexes  $Mn^{2+}$  pourrait être obtenue à l'avenir en remplaçant les deux groupes complexants de l'acétate par des groupes non ionisables tels que les amides; dans ce cas, la charge positive sur les complexes cationiques  $Mn^{2+}$  résultants pourrait protéger contre la dissociation assistée par l'acide, bien que le greffage de macromolécules neutres puisse être nécessaire dans ce cas pour assurer la furtivité contre l'adsorption des protéines plasmatiques sanguines. Il sera néanmoins important de vérifier que la présence de ces fonctions amides n'augmente pas trop le temps de séjour dans la sphère interne de la molécule d'eau coordinée, ce qui conférerait une relaxivité longitudinale du proton plus faible. En conclusion, ces résultats préliminaires montrent des propriétés très encourageantes des dérivés pycènes pour les propriétés de contraste IRM, bien que des études supplémentaires soient nécessaires pour démontrer qu'ils peuvent remplacer les complexes de gadolinium dans le diagnostic clinique de maladies (cancers, accidents vasculaires cérébraux...).

Ces complexes  $Mn^{2+}$  restent donc un moyen alternatif d'éviter les problèmes des complexes  $Gd^{3+}$ , bien que des améliorations doivent encore être apportées pour finalement réaliser un essai clinique sur les humains.

Par la suite, nous avons développé des nano-objets polymères, des micelles et des vésicules (également appelées polymersomes) qui sont constitués d'une coque de polyester sensible au pH afin d'obtenir une libération contrôlée des médicaments encapsulés dans l'environnement tumoral acide. Le copolymère utilisé est composé d'une structure amphiphile PEO-*b*-P(CL-*co*-LA) avec une séquence hydrophobe statistique obtenue par polymérisation par ouverture de cycle (ROP) de l' $\epsilon$ -caprolactone (CL) et du *L*-lactide (*L*-LA). Ces copolymères ont été entièrement caractérisés puis utilisés pour former des nanostructures par deux méthodes d'autoassemblage. De plus, ces nano-objets sont capables lors de l'autoassemblage d'encapsuler la doxorubicine comme médicament pour le traitement du cancer ainsi qu'un contrastophore, le ZW800-1 qui est un fluorophore absorbant dans le proche infrarouge et dérivé du vert d'indocyanine, un contrastophore déjà approuvé par la FDA en tant que fluorophore pour l'imagerie optique par fluorescence.

La nanopréciipitation a mis en évidence la formation de micelles (plus précisément un mélange de micelles sphériques et cylindriques), tandis que la méthode de réhydratation des couches minces a donné des polymersomes. Ces deux types de nanostructures ont été caractérisées par différentes techniques telles que la DLS (Dynamic Light Scattering), le SAXS (Small Angle X-rays Scattering), la MALS (Multi-Angle Light Scattering), l'AF4 (Assymetric Flow Field-Flow Fraction) et enfin la cryo-TEM (Cryo-Transmission Electron Microscopy) pour obtenir des images confirmant les analyses précédentes. (Figure III.20 ; Figure III.21)

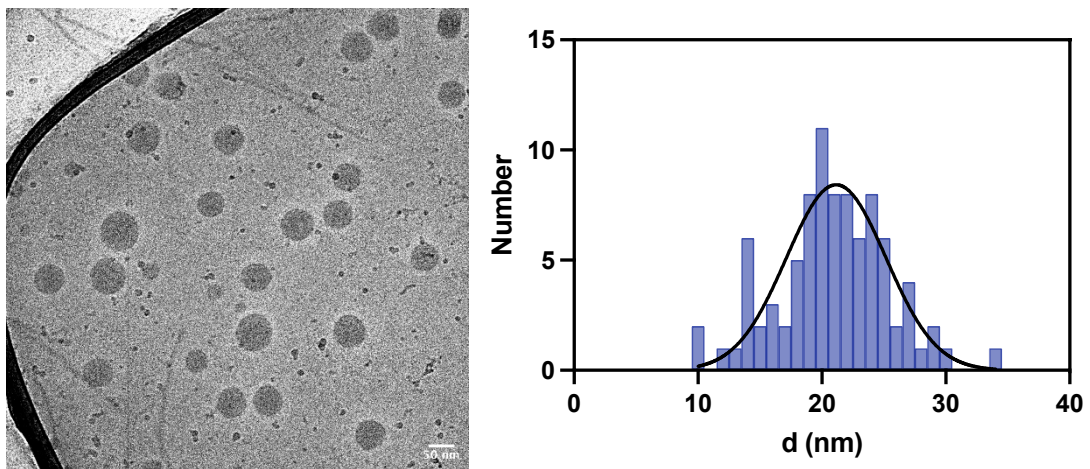


Figure III.20. Image de cryo-microscopie électronique des nanostructures composées de  $\text{PEO}_{45}\text{-}b\text{-P}(\text{CL}_{49}\text{-}co\text{-LA}_8)$  obtenues par nanopréciipitation permettant de mettre en évidence la formation de micelles cylindriques et sphériques, et l'histogramme correspondant obtenu sur la base de la mesure de 100 micelles ajusté avec une loi gaussienne.

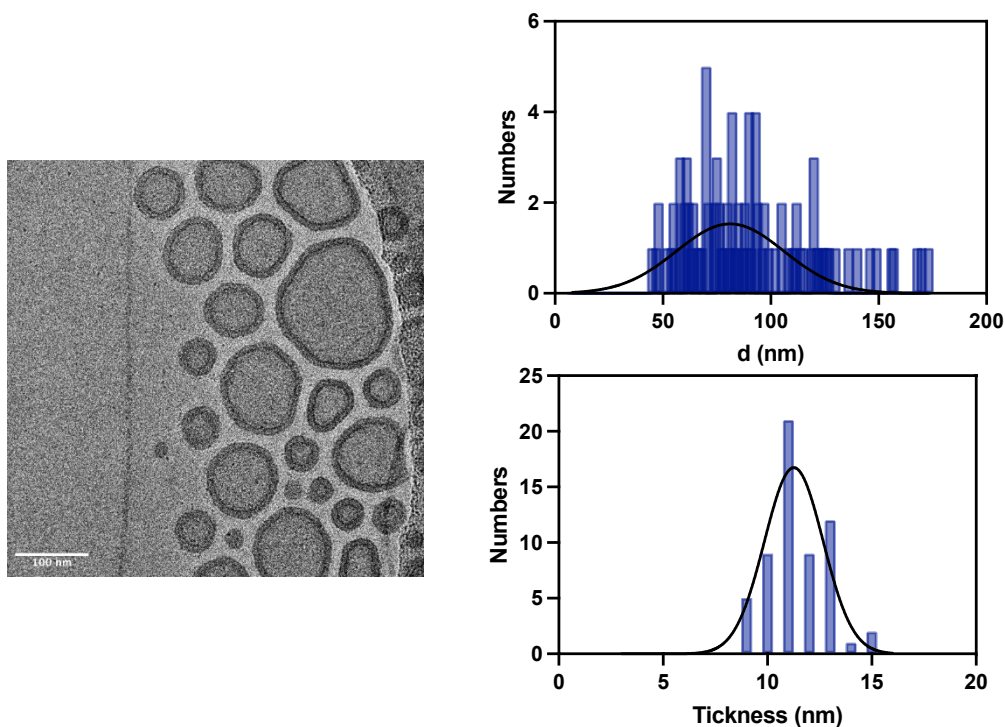


Figure III.21. Image de cryo-microscopie électronique des nanostructures composées de PEO<sub>45</sub>-*b*-P(CL<sub>35</sub>-*co*-LA<sub>5</sub>) obtenues par la méthode de réhydratation de couches minces, et les histogrammes correspondants obtenus sur la base de la mesure de 101 vésicules en haut à droite et de 59 bicouches en bas à gauche tous deux ajustés avec une loi gaussienne.

Le point suivant était donc l'encapsulation de contrastophores et/ou de médicaments dans ces nanostructures micellaires ou vésiculaires afin d'obtenir, d'un côté, la capacité de les suivre *in vitro* et *in vivo* grâce au ZW800-1, et de l'autre côté, la chimiothérapie, en l'occurrence en ajoutant la doxorubicine. Les polymersomes ont montré une plus grande capacité à encapsuler les contrastophores hydrophiles, le ZW800-1, la rhodamine B, et la doxorubicine, bien que de nouvelles analyses doivent être effectuées avec l'appareil de dissolution en flux continu afin de mettre en évidence la loi mathématique suivie pour le relargage contrôlé. En effet, cette expérience permettrait de mettre en évidence la capacité des copolymères à répondre à un stimulus de pH et à délivrer le médicament plus efficacement à l'endroit de la tumeur.

La toxicité des polymères a également été évaluée, sur plusieurs lignées cellulaires et les résultats ont mis en évidence que lorsque les cellules sont capables d'internaliser et répondent à la norme ISO 10993-5, une toxicité apparaissait à partir de 0,8 mg/mL. Enfin, les nanostructures ont été évaluées *in vivo*. Les micelles semblent avoir absorbé en surface les contrastophores et la doxorubicine au lieu de les avoir encapsulés, conduisant à une élimination directe de ceux-ci par désorption. Même au niveau de la tumeur aucun signal significatif n'a été mis en évidence. D'autre part, les polymersomes ont quant à eux montré la capacité de

s'accumuler et de rester dans le temps au niveau de la tumeur, au moins pendant 1 semaine. (Figure III.27) Il est tout de même à noter que lors des tests de biodistribution, en l'absence de tumeur, une accumulation au niveau de la rate a été observée. Ces résultats préliminaires sont encourageants pour finalement démontrer une efficacité pour traiter la tumeur en utilisant l'effet EPR avec ces systèmes. Il pourrait être intéressant d'encapsuler la doxorubicine dans de tels nano-objets, et de vérifier s'ils peuvent ralentir ou arrêter la croissance d'une tumeur voire même de l'éliminer.

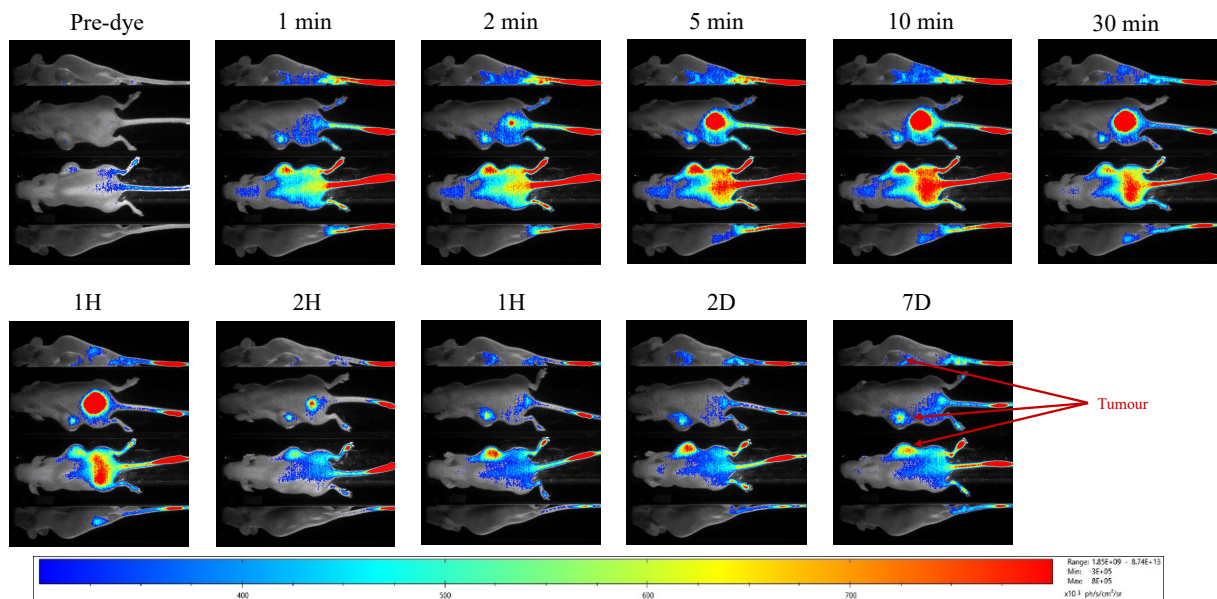


Figure III.27. Suivis FLI de la biodistribution des polymersomes à une concentration de  $10 \mu\text{M}$  en ZW800-1 sur une souris ayant développé spontanément au cours du temps une tumeur.

Ces nanostructures pourraient également être utilisées en imagerie photoacoustique grâce à la capacité du ZW800-1 de relarguer de la chaleur sous l'effet de l'excitation par des photons. En effet, cette technique d'imagerie est émergente en raison de sa capacité à obtenir un signal plus profond dans le corps car dans ce cas il s'agit d'une onde acoustique qui est détectée et non des photons comme pour l'imagerie optique par fluorescence, qui sont fortement absorbés ou dispersés par les tissus à des profondeurs supérieures à quelques mm. Notre système peut donc déjà être considéré comme une sonde d'imagerie multimodale, bien qu'il ne contienne pas pour l'instant d'effet contrasté en imagerie par résonance magnétique.

Les polymères fabriqués en PEO-*b*-P(CL-*co*-LA) ont montré leur intérêt pour l'administration de médicaments et leur accumulation possible dans la zone tumorale. Néanmoins, ils ont encore besoin de quelques améliorations. Avant tout, la synthèse doit être mieux contrôlée. Une solution consisterait à utiliser des alcoxydes d'aluminium comme le

Ti(OiPr)<sub>3</sub> qui représentent une alternative intéressante comme catalyseur et amorceur de la ROP des lactides et des lactones.<sup>2</sup> Ces derniers ont récemment été utilisés à très faible teneur (jusqu'à 0,1%) pour préparer des copolymères P(LA-co-CL) statistiques avec une fraction importante d'unités lactidyles.<sup>3-5</sup> De plus, le corps est exposé quotidiennement à l'aluminium avec des quantités d'environ 30 mg par jour.<sup>6</sup> Ainsi, les quantités catalytiques d'aluminium utilisées dans la synthèse ne devraient apporter aucune toxicité à l'organisme. Néanmoins, des étapes de lavage étendues des copolymères seront nécessaires, mais cette voie reste une option intéressante pour la suite des travaux. Après cela, il pourrait être intéressant d'augmenter le nombre d'unités lactidyles pour assurer une capacité de libération de médicament élevée, tout en permettant l'obtention de polymères ayant une faible toxicité des nanostructures résultantes. En effet, pour rappel, les unités LA ont la capacité d'être dégradées plus rapidement que les unités CL, ainsi que d'augmenter le taux de dégradation dans le microenvironnement tumoral car le pH pourrait diminuer avec la production d'acide lactique. Cependant l'augmentation du caractère semi-cristallin de la PCL par l'introduction d'une fraction de *L*-lactide pourrait aussi engendrer des problèmes de formation des polymersomes, malgré l'usage de la méthode de réhydratation de film (effectuée à 50°C, au-dessus de la température de fusion du copolymère). Il pourrait donc être intéressant de déterminer les bonnes proportions de fraction LA qui permettent la formation de polymersomes tout en augmentant la vitesse d'administration du médicament et finalement ne présentent pas de toxicité *in vitro* et *in vivo*. La vérification de toutes ces exigences permettra d'obtenir un nanosystème optimal ayant les bonnes propriétés pour le relargage contrôlé de médicaments. Il est également nécessaire de déterminer les lois régissant le relargage de médicaments sur base de ces systèmes pour prouver si l'ajout de fractions LA a un impact sur la vitesse de relargage comme prévu. Après cela, des expériences *in vivo* sur des souris porteuses de tumeurs doivent être effectuées pour prouver la capacité des polymèresomes à s'accumuler dans la tumeur par effet EPR, ainsi que la libération du médicament et sa capacité à diminuer la taille de la tumeur. Enfin, l'avantage de la bimodalité de la nanostructure doit être évalué par, d'une part, la réalisation d'une imagerie photoacoustique qui pourrait également se combiner avec l'IRM, et d'autre part, le greffage de complexes de Mn<sup>2+</sup> à la surface.

Comme discuté lors de la première partie de ce travail, une voie d'amélioration de la relaxivité serait de greffer les complexes de manganèse en surface des nano-objets susmentionnés afin de modifier leur temps de corrélation rotationnel, et donc leur efficacité.

Pour ce faire, une stratégie par chimie click est envisagée, impliquant la fonctionnalisation des complexes de  $Mn^{2+}$  et des copolymères par les groupements chimiques adéquats. La stratégie choisie pour la chimie click est une réaction sans catalyse au cuivre afin d'éviter la possible toxicité que pourraient apporter les ions cuivre au système et éviter une décomplexation des ions manganèses avec le macrocycle. Pour ce faire, des motifs dibenzocyclooctyne (DBCO) et azoture peuvent être utilisés, grâce à la tension de cycle favorisant la réaction de cycloaddition sans catalyse. Différentes stratégies de synthèse ont été étudiées pour obtenir les composés désirés. Cependant, plusieurs difficultés ont été rencontrées pour obtenir les complexes  $Mn^{2+}$  portant un groupe fonctionnel nécessaire à la cycloaddition alcyne-azoture promue par tension de cycle (SPAAC), soit les fonctions DBCO, soit les fonctions azotures. La principale difficulté rencontrée provenait de la déprotection en milieu acide et différentes stratégies ont été développées pour résoudre ce problème. La solution optimale semble être le greffage de 3-azido-1-propanamine sur  $L_2COO^-$  conduisant à l'obtention du complexe après déprotection -tBu et complexation avec des ions manganèse. Néanmoins, certaines améliorations ou d'autres techniques de caractérisation doivent être effectuées pour mettre en évidence la présence d'une fonction azoture sur les complexes.

Une fois le macrocycle obtenu, le copolymère fonctionnalisé DBCO-PEO-*b*-P(CL-*co*-LA) a été synthétisé à l'aide d'un polymère fonctionnalisé commercial DBCO-PEO avec une pureté insatisfaisante conduisant à une dispersion bimodale dans les analyses de chromatographie d'exclusion stérique. Cette synthèse devrait donc également nécessiter quelques améliorations et optimisations. Deux solutions pourraient être tentées : soit acheter le polymère à un autre fournisseur comme JenKem™, USA, soit essayer de purifier le polymère actuel. Par la suite il sera important de déterminer les proportions en DBCO-PEO-*b*-P(CL-*co*-LA) et de PEO-*b*-P(CL-*co*-LA) permettant de fonctionnaliser les polymersomes de façon optimale. Il pourrait être intéressant de déterminer le nombre de DBCO à la surface pour ajouter exactement le bon nombre de complexes  $N_3-Mn^{2+}$  dans le milieu. Cette quantité dépendra probablement de la proportion entre les polymères fonctionnalisés et non-fonctionnalisés utilisés pour former les polymersomes mais aussi de leur capacité à se trouver en surface. Enfin, une étude relaxométrique complète des polymersomes greffés devrait permettre d'évaluer l'impact du greffage des complexes sur leur temps de corrélation rotationnel et donc sur l'efficacité des nanoobjets en tant qu'agents de contraste IRM.

De plus, dans les travaux futurs, ce type de polymères fonctionnalisés DBCO pourrait également permettre de greffer des peptides ou d'autres molécules de ciblage spécifiques,

conduisant à la formation d'une nano-plateforme thérapeutique ciblée polyvalente, multimodale (fluorescence, imagerie photo-acoustique et IRM) et multi-responsive (libération de médicament en réponse à une variation de pH ou de température locale, près de la tumeur). Enfin une évolution peut-être souhaitable serait de remplacer le PEG par un autre type de bloc hydrophile, afin d'éviter tout risque d'activation du complément.

## List of abbreviations

---

AF4	Asymmetric flow field-flow fractionation
BLI	Bioluminescence imaging
BUN	Blood urea nitrogen
CAs	Contrast agents
CMC	Critical micellar concentration
Cryo-TEM	Cryo-tomography electron microscopy
$\mathcal{D}$	Dispersity
DBCO	Dibenzocyclooctyne
DIPEA	Diisopropylethylamine
DLC	Drug loading content
DLS	Dynamic light scattering
DMF	Dimethylformamide
$dn/dc$	Refraction index increment
DP	Degree of polymerization
DSC	Differential scanning calorimetry
EE	Encapsulation efficiency
EPR	Enhanced permeability and retention
FDA	Food and drug administration
$f_{\text{hydrophilic}}$	Hydrophilic fraction
FISP	Fast imaging with steady – state precession
FLI	Fluorescence imaging
FT-IR	Fourier transformation infrared
Gd-DOTA (Dotarem <sup>®</sup> )	Gadoteric acid
GOT	Glutamic oxacetic transaminase
GPT	Glutamic pyruvic transaminase
HBTU	<i>N,N,N',N'</i> -Tetramethyl- <i>O</i> -(1 <i>H</i> -benzotriazol-1-yl)uronium hexafluorophosphate
LDH	Lactate deshydrogenase
LiOH	Lithium hydroxide
MALS	Multi angle light scattering
$M_n$	Number-average molar mass
Mn-DPDP (Teslascan <sup>®</sup> )	Manganese dipyridoxyl diphosphate
MRI	Magnetic resonance imaging
MS	Mass spectrometry

MTT	3-(4,5-dimethylthiazol-2-yl)-2,5-diphenyltetrazolium bromide
$M_w$	Weight-average molar mass
NIR	Near-infrared region
NMR	Nuclear magnetic resonance
NMRD	Nuclear magnetic resonance dispersion
NPs	Nanoparticles
NSF	Nephrogenic systemic fibrosis
OI	Optical Imaging
PBS	Phosphate buffer solution
PCL	Poly( $\epsilon$ -caprolactone)
PCTA	3,6,9,15-Tetraazabicyclo[9.3.1]pentadecan-1(15),11,13-triene-3,6,9-triacetic acid
PEG	Poly(ethylene glycol)
PEO	Poly(ethylene oxide)
PLA	polylactide
PLLA	Poly( <i>L</i> -lactide)
$q$ (manganese complexes)	Number of coordinated water molecule
$q$ (nanostructures)	Scattering vectors
$r_1$	Longitudinal relaxivity
RARE	Rapid acquisition with relaxation enhancement
RF	Radiofrequency
$R_g$	Radius of gyration
$R_h$	Hydrodynamic radius
ROP	Ring opening polymerization
ROS	Reactive oxygen species
SAXS	Small angle x-rays scattering
SEC	Size exclusion chromatography
SLS	Static light scattering
SPAAC	Strain-promoted azide-alkyne cycloaddition
SPIONs	Superparamagnetic iron oxide nanoparticles
$T_1$	Longitudinal relaxation time
$T_2$	Transversal relaxation time
TEA	Triethylamine
TFA	Trifluoroacetic acid
TGA	Thermogravimetric analysis
THF	Tetrahydrofuran

$\tau_M$

Water residence time in the inner sphere

$\tau_R$

Rotational correlation time

# List of figures

---

Figure I.1. Reaction ways of anionic ROP on lactone. <sup>47</sup>	5
Figure I.2. Images developed by Lee and Feijen showing the different conformations taken by amphiphilic copolymers to form vesicles. <sup>48</sup>	6
Figure I.3. Predicted structure as a function of the packing parameter. <sup>50</sup> Reprinted with permission from Bleul et al. Techniques To Control Polymersome Size. <i>Macromolecules</i> <b>2015</b> , 48 (20), 7396–7409. Copyright © 2015 American Chemical Society.	7
Figure I.4. Transmission electron microscopy (TEM) of different nanostructures composed of polystyrene-block-poly(acrylic acid) (PS- <i>b</i> -PAA) with different polymerization degrees of each chain. <sup>51</sup>	8
Figure I.5. Phase diagram as a function of water content for (a) PS <sub>310</sub> - <i>b</i> -PAA <sub>52</sub> with, in colored area, the coexistence between two nanostructures (b) poly(butylene oxide)-block-poly(ethylene oxide) (PBO- <i>b</i> -PEO) according to the molecular weight identifying the domain of existence of each nanostructure. <sup>51</sup>	9
Figure I.6. Vesicles shape as a function of water/dioxane content for the copolymer; PS <sub>310</sub> - <i>b</i> -PAA <sub>52</sub> , and the reversible mechanism. <sup>52</sup>	10
Figure I.7. Cryo-TEM of PEO-PLA vesicles during their transformation into micelles and rods induced by a modification of pH. <sup>55</sup>	11
Figure I.8. Synthesis of self-assembled polymersomes based on PEG-P(TMC-DTC) and cNGQ-PEG-P(TMC-DTC), loaded with doxorubicin. Endocytosis is induced by in vivo targeting followed by reduction of S-S bonds by GSH, leading to release of doxorubicin. <sup>56</sup> Reprinted with permission from Xie et al. Polymeric Hybrid Nanomicelles for Cancer Theranostics: An Efficient and Precise Anticancer Strategy for the Codelivery of Doxorubicin/MiR-34a and Magnetic Resonance Imaging. <i>ACS Appl. Mater. Interfaces</i> <b>2019</b> , 11 (47), 43865–43878. Copyright © 2019 American Chemical Society.	12
Figure I.9. Formation of polymersomes developed by Saravanakumar et al. followed by their uptake in cancer cells and their mechanism of action under laser irradiation. <sup>60</sup>	14
Figure I.10. Proportion of the different mathematical models used to describe drug delivery system release profiles. <sup>64</sup>	16
Figure I.11. Typical fitting obtained according to the used mathematical models. <sup>66</sup>	17
Figure I.12. Graphical representation of burst and lag-time effects derived from Siepmann et al. <sup>67</sup>	18
Figure I.13. Cumulative release assays for MPEG- <i>b</i> -PCL and FA-PEGMA- <i>b</i> -PCL (A) and their relative results with Peppas' mathematical model (B). <sup>68</sup>	19
Figure I.14. Biodistribution of (a) drug, (b) nanocarriers by EPR effect, (c) nanocarriers with a targeting moiety. <sup>9</sup>	20
Figure I.15. Representation of the system developed by Dariva et al. based on PEG-BHETE-PLA encapsulating Ce6 and doxorubicin for which ROS species induced by NIR irradiation can break BHETE links. <sup>74</sup>	22
Figure I.16. Two mechanisms leading to the formation of polymersomes. <sup>50</sup> Reprinted with permission from Bleul et al. Techniques To Control Polymersome Size. <i>Macromolecules</i> <b>2015</b> , 48 (20), 7396–7409. Copyright © 2015 American Chemical Society.	23
Figure I.17. Schematic way to obtain vesicles by nanoprecipitation in the presence of a non-solvent. <sup>79</sup>	25
Figure I.18. Formation of polymersomes following the thin film rehydration method. <sup>36</sup>	25

Figure I.19. Cryo-TEM of self-assembly nanostructure using different techniques: nanoprecipitation (a) PEG-2k-b-PCL <sub>4.3k</sub> (b) PEG <sub>2k</sub> -b-PCL <sub>8.5k</sub> and thin film (c) PEG-2k-b-PCL <sub>4.3k</sub> (d) PEG <sub>2k</sub> -b-PCL <sub>8.5k</sub> . <sup>81</sup>	26
Figure I.20. (a) structure of the PGMA-b-PHPMA and phase diagram of PGMA-b-PHPMA leading to the formation of sphere (S), worms (W) or (vesicles) (b) as a function of the DP of both chains or (c) PHPMA DP as a function of the polymer concentration in solution. <sup>82</sup> Reprinted with permission from Blanazs et al. Predictive Phase Diagrams for RAFT Aqueous Dispersion Polymerization: Effect of Block Copolymer Composition, Molecular Weight, and Copolymer Concentration. <i>Macromolecules</i> <b>2012</b> , 45 (12), 5099–5107. Copyright 2012 American Chemical Society.	27
Figure I.21. Co-axial flow microfluidic device leading to the formation of vesicles through double-emulsion formation. <sup>45</sup>	28
Figure I.22. Representative diagram for the system characterization. NMR: nucleic magnetic resonance; MS: mass spectrometry; SEC: size exclusion chromatography; MALS: multi-angle light scattering; TGA: thermogravimetric analysis; DSC: differential scanning calorimetry; DLS: dynamic light scattering; SAXS: small angle x-rays scattering; SANS: small angle neutron scattering; TEM/Cryo-TEM: transmission electron microscopy; AFM: Atomic force microscopy; AF4: asymmetric flow field flow fractionation; DLC: drug loading content; EE: encapsulation efficiency. Inspired from Behl et al.. <sup>66</sup>	31
Figure I.23. Orientation of spins up and down after the application of a static magnetic field ( $B_0$ ).	32
Figure I.24. Spins that are in precession movement around the z and -z axes show unbalance of their population respectively up and down, resulting in a net magnetization called macroscopic magnetization, $M_0$ . A 90° RF pulse applied on the x axis ( $B_1$ along the x axis) tilts the magnetization towards the y axis. The return to equilibrium of the population of spins then occurs according to longitudinal and transverse relaxation, characterized by $T_1$ and $T_2$ relaxation times, respectively.	33
Figure I.25. Excitation of a slice in the static magnetic field $B_0$ induced by a RF pulse applied simultaneously with a $G_z$ magnetic field gradient. Inspired from Roth et al.. <sup>89</sup>	34
Figure I.26. Phase encoding of the spins by $G_y$ magnetic field gradient along y axis and frequency encoding by $G_x$ magnetic field gradient along x axis. Inspired from Roth et al.. <sup>89</sup>	34
Figure I.27. Gadolinium complexes described as $T_1$ contrast agents.	36
Figure I.28. Synthetic way for Gd-HM-Doc/34a followed by the passive targeting of tumoral cells and the action of the different components after the degradation of vesicles by the endosomes. <sup>100</sup>	37
Figure I.29. Simplified Jablonski diagram.	39
Figure I.30. Schematic representation of the PLGA-PEG-Mal polymersomes and their functionalization leading to in vivo pH stimuli following by PAI and PTT. <sup>105</sup>	40
Figure I.31. Schematic representation of the synthesized polymer followed by their self-assembly with encapsulation of doxorubicin leading to their disruption in acidic medium. <sup>110</sup>	42
Figure I.32. Grafted copolymer self-assembling into micelles showing multiple-therapeutic effects and in vivo tumor regression through combination of NIR irradiation (PDT, PTT), OI and PAI as imaging techniques. <sup>112</sup>	43
Figure II.1. Structures of the ligands or complexes discussed in this work: (A) MnDPDP <sup>134</sup> , (B) PCMA and PCMP <sup>146</sup> , (C) PCTA, PC3AM <sup>H</sup> , PC3AM <sup>Gly</sup> , and PC3AM <sup>Pip</sup> , <sup>149</sup> and (D) PC2A, PC2A-EA, and PCTA <sup>150</sup>	55

Figure II.2. Structure of the four Mn-complexes synthesized and studied in this work MnL<sub>1</sub>H: MnPy(COO<sup>-</sup>)<sub>2</sub>-H; MnL<sub>2</sub>COO<sup>-</sup>: MnPy(COO<sup>-</sup>)<sub>2</sub>-OCH<sub>2</sub>COO<sup>-</sup>; MnL<sub>3</sub>CH: MnPy(COO<sup>-</sup>)<sub>2</sub>-OCH<sub>2</sub>CONHCH<sub>2</sub>CCH and MnL<sub>4</sub>NH<sub>3</sub><sup>+</sup>: MnPy(COO<sup>-</sup>)<sub>2</sub>-OCH<sub>2</sub>CONH(CH<sub>2</sub>)<sub>2</sub>NH<sub>3</sub><sup>+</sup>. 56

Figure II.3. Cyclic voltammogram of MnL<sub>2</sub>COO<sup>-</sup> (5 M NaCl, scan rate 50 mV/s) 62

Figure II.6. Influence of  $\tau_M$  on NMRD profiles for small Gd-complexes at constant values of  $\tau_{SO}$  (100 ps),  $\tau_v$  (20 ps) and  $\tau_R$  (100 ps), showing a decrease in  $r_1$  relaxivity correlated with an increase of  $\tau_M$ . (~ 100 ns). 65

Figure II.4. P, paramagnetic center;  $\tau_{S1,2}$ , longitudinal and transversal electron relaxation times; r, shortest approach distance; q, number of coordinated water molecule;  $\tau_M$ , residence time of the water molecule in the inner sphere;  $\tau_R$ , rotational correlation time. 65

Figure II.5. <sup>1</sup>H NMRD profiles showing the increase of the relaxivity in the clinical window as a function of the increase of the rotational correlation time  $\tau_R$  (A) Short  $\tau_R$  (0.1 ns for MS-325) (B) middle  $\tau_R$  (~1 ns for EP-1084) (C) long  $\tau_R$  (10 ns for MS-325 in HSA solution).<sup>159</sup> 65

Figure II.7. Measurements of the <sup>17</sup>O water transverse relaxivity versus the inverse of temperature, at 11.75 T, in the presence of the different Mn-complexes at 2.06 mM (MnL<sub>1</sub>H, triangles), 2.58 mM (MnL<sub>2</sub>COO<sup>-</sup>, stars), 2.05 mM (MnL<sub>3</sub>CH, circles) and 1.21 mM (MnL<sub>4</sub>NH<sub>3</sub><sup>+</sup>, squares) concentration in order to determine the number of inner sphere water molecules (q) from Equation II.6 in reference 160 as a function of the maximum value  $r_{2max}^0$ . 67

Figure II.8. NMRD profiles at 25°C in order to determine the number of inner sphere water molecules (q) from Equation II.7 in reference 161 as a function of the plateau value ( $r_{1p}$ ) at low frequency and the formula weight (FW) for the four complexes: MnL<sub>1</sub>H (triangles), MnL<sub>2</sub>COO<sup>-</sup> (stars), MnL<sub>3</sub>CH (circles) and MnL<sub>4</sub>NH<sub>3</sub><sup>+</sup> (squares). 68

Figure II.9. Measurements of the <sup>17</sup>O water transverse relaxation rate as a function of the inverse of temperature, at 11.75 T, on solutions of each complex at 2.06 mM (MnL<sub>1</sub>H, triangles), 2.58 mM (MnL<sub>2</sub>COO<sup>-</sup>, stars), 2.05 mM (MnL<sub>3</sub>CH, circles) and 1.21 mM (MnL<sub>4</sub>NH<sub>3</sub><sup>+</sup>, squares). The continuous lines represent fits by the theoretical model developed in reference 162, with the parameters displayed in Table II.2. 69

Figure II.10. <sup>1</sup>H NMRD profiles at 37°C for Mn<sup>2+</sup>-complexes, showing the longitudinal relaxivity at varying proton Larmor frequencies (aka varying magnetic field). The straight lines show the theoretical fitting based on the theory of Bloembergen and Solomon.<sup>156-158</sup> 70

Figure II.11. Evolution of the normalized paramagnetic longitudinal relaxation rate in order to evaluate the transmetalation kinetics between manganese and zinc ions for the four Mn<sup>2+</sup>-complexes: MnL<sub>1</sub>H (triangles), MnL<sub>2</sub>COO<sup>-</sup> (stars), MnL<sub>3</sub>CH (circles) and MnL<sub>4</sub>NH<sub>3</sub><sup>+</sup> (squares). Experiments were performed during 5 days in phosphate buffer at 20 MHz and 37°C. The concentration of Mn-complexes and of competing Zn(II) salt used is 2.5 mM, which is much higher than its normal physiological level (~10  $\mu$ M).<sup>164</sup> 73

Figure II.12. Phantom images recorded at approximately 37°C under two different magnetic fields (1 T and 9.4 T) of each Mn<sup>2+</sup>-complex at a concentration of 0.5 mM compared with a commercial Gd-complex, Gd-DOTA, at the same concentration, and with pure water. RARE sequence for 1 T and FISP for 9.4 T. 74

Figure II.13. <sup>1</sup>H NMRD profiles at 37°C for Mn<sup>2+</sup>-complexes, showing the longitudinal relaxivity at varying proton Larmor frequency (aka varying magnetic field). The straight lines show the theoretical fitting based on the theory of Bloembergen and Solomon.<sup>156-158</sup> 75

Figure II.14. Biodistribution MRI images of MnL <sub>1</sub> H at clinical magnetic field (1T) and preclinical magnetic field (9.4T) over time	77
Figure II.15. Biodistribution MRI images of MnL <sub>2</sub> COO <sup>-</sup> at clinical magnetic field (1T) and preclinical magnetic field (9.4T) over time	78
Figure II.16. Analyses of different factors present in plasma (GPT, GOT, BUN and LDH) able to evidence inflammatory reactions or failures in organs (* n = 2 due to insufficient volume in plasma or aberrant values, otherwise n = 3)	81
Figure III.1. Representation of bilayer undergoing hydrolysis of polyester function leading in few hours to poration that delivered the encapsulated species, and in few days to the disintegration of the bilayer. <sup>180</sup>	105
Figure III.2. <sup>1</sup> H NMR (500MHz; CDCl <sub>3</sub> ) spectrum of PEO <sub>126</sub> -b-PCL <sub>142</sub> .	109
Figure III.3. <sup>1</sup> H NMR (500MHz; CDCl <sub>3</sub> ) spectrum of PEO <sub>124</sub> -b-PCL <sub>190</sub> .	110
Figure III.4. SEC of the two copolymers PEO <sub>n</sub> -b-PCL <sub>m</sub> .	111
Figure III.5. Cryo-TEM of PEO <sub>136</sub> -b-PCL <sub>208</sub> nanostructures resulting from nanoprecipitation technique.	113
Figure III.6. <sup>1</sup> H NMR (500 MHz; CDCl <sub>3</sub> ) of PEO <sub>50</sub> -b-P(CL <sub>40</sub> -co-LA <sub>6</sub> ).	116
Figure III.7. Comparison of SEC analyses before and after water washing.	117
Figure III.8. SEC analyses of THF (yellow), lactic acid (green) and PEO-b-P(CL-co-LA) (dark blue).	117
Figure III.9. DSC curve of PEO <sub>45</sub> -b-P(CL <sub>35</sub> -co-LA <sub>5</sub> ), second heat, 10°C/min. The inflection point around -50°C is ascribed to the glass transition (T <sub>g</sub> ) of the polyester. block.	119
Figure III.10. DLS analyses of PEO <sub>45</sub> -b-P(CL <sub>49</sub> -co-LA <sub>8</sub> ) nanoprecipitation, Z <sub>ave</sub> diameter = 85.7 nm; PDI = 0.23; in PBS; not loaded.	121
Figure III.11. DLS analyses of objects self-assembled by the thin film rehydration method; PEO <sub>45</sub> -b-P(CL <sub>35</sub> -LA <sub>5</sub> ), Z <sub>aver</sub> diameter = 103.2 nm; PDI = 0.16; in PBS; not loaded.	122
Figure III.12. Plot of the main decay rate of the autocorrelation function of scattered light intensity determined by the 2 <sup>nd</sup> order Cumulant method and fitting as a function of the square of the scattering vector: (A) Linear regression (B) linear regression with the constrain of zero intercept with the vertical axis (C) second order polynomial fit, which takes into account the effect of size polydispersity. (Sample PEO <sub>45</sub> -b-P(CL <sub>35</sub> -co-LA <sub>5</sub> ), prepared by the thin film hydration method, not loaded with drug and/or dye)	123
Figure III.13. Guinier plot for sample PEO <sub>45</sub> -b-P(CL <sub>35</sub> -co-LA <sub>5</sub> ), prepared by the thin film hydration method, not loaded with drug and/or dye.	125
Figure III.14. On the upper Figure, the chromatogram of elution was represented with the corresponding measurement at 3 different times (a) and (b) Fit of MALS signal giving R <sub>g</sub> according to Berry's law Eq. 3.16 and Burchard-Stockmayer plot below (c) Fit of MALS signal according to the rod theoretical shape factor and rods plot below for sample PEO <sub>45</sub> -b-P(CL <sub>58</sub> -co-LA <sub>8</sub> ), prepared by nanoprecipitation (where points represent ρ and straight line represent the elution curve).	128
Figure III.15. On the upper Figure, the chromatogram of elution was represented with the corresponding measurement at 3 different times (a), (b) and (c) Fit of MALS signal giving R <sub>g</sub> according to Debye's law Eq. III.15 and Burchard-Stockmayer plot (where points represent ρ and straight line represent the elution curve) of the shape parameter ρ along the fractogram below for sample PEO <sub>45</sub> -b-P(CL <sub>35</sub> -co-LA <sub>5</sub> ), self-assembled by the thin film rehydration method.	129

Figure III.16. Information that can be extracted from X-rays scattering for the form factor inspired from Anton-Paar documentation on SAXS. 130

Figure III.17. SAXS curves of (L)P(CL<sub>58</sub>-co-LA<sub>8</sub>)-b-PEO<sub>45</sub> samples, loaded (L) and unloaded obtained by nanoprecipitation technique as micelles structures, after subtraction of the intensity measured on a capillary filled with pure PBS buffer. The curves were fitted with the theoretical P(q) form factor of polydisperse filled spheres. In order to compare to the DLS results, the Z-average radii defined by  $RZ\text{-ave3} = R6R3$  were calculated using the Log-normal size distributions shown as insets, yielding:  $RZ\text{-ave} = 35$  and  $36.5$  nm, respectively for unloaded P(CL-co-LA) and loaded P(CL-co-LA) samples. The weight concentrations of the suspensions were measured by thermogravimetric analysis (TGA), respectively  $4.8$ , and  $4.7$  g·L<sup>-1</sup>. 132

Figure III.18. SAXS curve of PEO<sub>45</sub>-b-P(CL<sub>35</sub>-co-LA<sub>5</sub>) formulated by thin film rehydration method, after subtraction of the intensity measured on a capillary filled with pure PBS buffer. Dry extract concentration measured by TGA:  $4.9$  g·L<sup>-1</sup>, after subtraction of the weight of PBS salt. The solid line corresponds to the calculated P(q) for a hollow shell of core radius  $32.3$  nm (taking into account a polydispersity index of  $0.35$ ) and a membrane thickness of  $12.6$  nm (PDI= $0.15$ ). The  $R_g$  value is  $49$  nm as calculated by Guinier plot but as explained above, it is the upper limit that can be measured in this configuration (the curve does not exhibit a Guinier plateau towards low-q values). 133

Figure III.19. Cryo-TEM of PEO<sub>45</sub>-b-P(CL<sub>49</sub>-co-LA<sub>8</sub>) obtained by nanoprecipitation showing the presence of micelles and rods, and the corresponding histogram based on measurement of 100 micelles fitted by a gaussian function. 134

Figure III.20. Cryo-TEM of PEO<sub>45</sub>-b-P(CL<sub>35</sub>-co-LA<sub>5</sub>) obtained by thin film rehydration and on the upper right, their histogram corresponding to a measurement of 101 vesicles fitted by a gaussian function. On the bottom right, a histogram obtained on the measurement of the thickness of the membrane measured on 59 membranes fitted by a gaussian function. 134

Figure III.21 . Stability of polymersomes obtained by thin film in PBS over time by measuring their size and their PDI for 77 days (one measurement every 7 days). The  $Z_{\text{average}}$  on 3 measurements were plotted as a function of time as the PDI. 135

Figure III.22. Drug (left, doxorubicin) or dye (right, ZW800-1) release assay from polymersomes using Sotax™ USP-4 flow-through dissolution system in two different conditions of pH, at 37°C. 139

Figure III.23. Cellular viability of MNK45 cell incubated on different conditions (error bar correspond to replicated experiments, n = 3). 142

Figure III.24. confocal analyses on MKN45 with two different micelles concentrations encapsulating doxorubicin: 1) rhodamine B with  $\lambda_{\text{ex}} = 561$  nm (red channel); 2) Doxorubicin and lysotracker green excitation  $\lambda_{\text{ex}} = 496$  nm (green channel); 3) DAPI  $\lambda_{\text{ex}} = 405$  nm (blue channel 3); 4) white light channel; 5) merge of the fourth channels. 143

Figure III.25. Impact on the cells viability for a growing concentration in polymersomes revealed by MTT assays without loading of doxorubicin on HT29 cells (left) and on MCF7 cells (right). 144

Figure III.26. Impact on the cells viability for a growing concentration in polymersomes revealed by MTT assays using encapsulated doxorubicin compared with free doxorubicin in same amount than it encapsulated on HT29 (left) and on MCF7 (right). 145

Figure III.27. Confocal analyses on MCF7 and HT29 at different polymersome concentrations which encapsulated doxorubicin: 1) LysoTracker $\lambda_{ex}$ = 640 nm (deep-red channel); 2) doxorubicin $\lambda_{ex}$ = 488 nm (green channel); 3) Hoechst $\lambda_{ex}$ = 405 nm (blue channel) ; 4) merge of the three channels.	147
Figure III.28. Confocal microscope analyses on MCF7 and HT29 at different polymersome concentrations which encapsulated rhodamine B and ZW800-1: 1) LysoTracker deep red $\lambda_{ex}$ = 670 nm (red channel); 2) rhodamine B $\lambda_{ex}$ = 488 nm (green channel); 3) Hoechst $\lambda_{ex}$ = 405 nm (blue channel); 4) merge of the three channels.	148
Figure III.29. Bioluminescence image to control the implanted tumor in the right posterior leg.	149
Figure III.30. Distribution of micelles over time at two different polymer concentrations (2 mg/kg and 7 mg/kg in polymers) tracked by FLI.	150
Figure III.31. Ex vivo FLI of control and injected mice organs with two different polymer concentrations (2 mg/kg and 7 mg/kg in polymers) performed 1 day post-injection.	150
Figure III.32. FLI monitoring of the biodistribution of polymersomes at a concentration of 10 $\mu$ M in ZW800-1 over time (the scale of artificial colors was readjusted between 7 and 13 days).	152
Figure III.33. Ex vivo FLI observations of organs after different times of sacrifice.	153
Figure III.34. Analyses of different factors present in plasma (GPT, GOT, BUN and LDH) able to put in evidence inflammatory reactions or failures in organs (* : n= 2 and ** : n=1 due to insufficient volume in plasma or aberrant values).	154
Figure III.35. FLI monitoring of the biodistribution of polymersomes at a concentration of 10 $\mu$ M in ZW800-1 on a mouse developing a spontaneous tumor over time.	155
Figure III.36. Ex vivo FLI of organs and tumor of the mouse presenting a spontaneous tumor (left) FLI of tumor and organs; (right) tumor slices showing the region of accumulation of the polymersomes.	156
Figure III.37. (left) negative control with saline solution and (right) polymersomes at a concentration of 10 $\mu$ M in ZW800-1.	158
Figure IV.1. Resulting compounds evidenced by Shi et al. and their proportion according to the acidic conditions used. <sup>236</sup>	186
Figure IV.2. FT-IR spectra of compound <b>12</b> (in blue) and compound <b>14</b> (in black) showing the disappearance of the N <sub>3</sub> characteristic vibration peak at 2100 cm <sup>-1</sup> wave number.	190
Figure IV.3. SEC traces in THF of DBCO-PEO and DBCO-PEO-b-P(CL-co-LA).	191
Figure IV.4. <sup>1</sup> H NMR (500 MHz; CDCl <sub>3</sub> ) spectrum of DBCO-PEO bought to Biochempeg (USA).	192
Figure IV.5. <sup>1</sup> H NMR (500 MHz; CDCl <sub>3</sub> ) spectrum of DBCO-PEO-b-P(CL-co-LA).	192

## List of schemes

- Scheme II.1. Synthesis of the lower part of the pyclen chelates from a triamine derivative: (a) NaOH, Nos-Cl, diethylether, THF, r.t. overnight (b) Cbz-Cl, DIPEA, THF, r.t. 1h30 (c) BrCH<sub>2</sub>CO<sub>2</sub>tBu, K<sub>2</sub>CO<sub>3</sub>, CH<sub>3</sub>CN, reflux 3-5 h (c<sub>ii</sub>) PhSH, K<sub>2</sub>CO<sub>3</sub>, 60°C 2-4 h. 57
- Scheme II.2. Synthesis of the pyclen derivatives: (d) Na<sub>2</sub>CO<sub>3</sub>, CH<sub>3</sub>CN, reflux. 58
- Scheme II.3. Synthesis of two Mn-complexes: (e) Pd/C, EtOH or MeOH, H<sub>2</sub> atm, r.t. overnight (f) NaOH, EtOH, r.t. 7h (g) and (h) CF<sub>3</sub>CO<sub>2</sub>H, CH<sub>2</sub>Cl<sub>2</sub>, r.t. overnight (i) MnCl<sub>2</sub>·4H<sub>2</sub>O, H<sub>2</sub>O, pH 5-6, 40°C, Ar atm, overnight. 11a is compound (MnL<sub>1</sub>H), 11b is compound (MnL<sub>2</sub>COO<sup>-</sup>). 59
- Scheme II.4. Synthesis of MnL<sub>3</sub>CH: (j) HBTU, NH<sub>2</sub>CH<sub>2</sub>CCH, DIPEA, CH<sub>2</sub>Cl<sub>2</sub>, r.t. 4h30 (k) TFA, CH<sub>2</sub>Cl<sub>2</sub>, r.t. 1 day (l) MnCl<sub>2</sub>·4H<sub>2</sub>O, H<sub>2</sub>O, pH = 5-6, 40°C overnight. The final product is compound (MnL<sub>3</sub>CH). 60
- Scheme II.5. Synthesis of MnL<sub>4</sub>NH<sub>3</sub><sup>+</sup>: (m) NH<sub>2</sub>CH<sub>2</sub>CH<sub>2</sub>NH<sub>2</sub>, r.t. (n) HCl<sub>anh</sub>, Et<sub>2</sub>O or HBr<sub>anh</sub>, AcOH, 70°C then r.t. (o) MnCl<sub>2</sub>·4H<sub>2</sub>O, H<sub>2</sub>O, pH 5-6, r.t.. The final product is compound (MnL<sub>4</sub>NH<sub>3</sub><sup>+</sup>). 61
- Scheme III.1. ROP reaction for PEO-b-P(CL-co-LA). 115
- Scheme III.2. Synthetic scheme of ZW800-1, adapted from reference 211, with some modifications in our work (a) 3-methyl-2-butanone AcOH, Ar atm, 180°C overnight (b) KOH, 2-propanol, 40°C, few hours (c) (3-bromopropyl)trimethylammonium bromide, toluene, atm Ar 120°C, overnight (d) Vielsmeier-Haack : i) DMF, POCl<sub>3</sub>, 0°C ; ii) cyclohexanone/DCM, reflux (100°C), 2 h iii) Aniline/EtOH, 0°C to r.t. (e) AcONa, EtOH atm Ar, reflux, 6 h (f) NaOH/MeOH, 2 h (g) H<sub>2</sub>O/DMSO, atm Ar, 70°C, 6 h. 136
- Scheme IV.1. First strategy for the synthesis of DBCO-Mn-complexes. Expected reactions: (a) HBTU, DIPEA, CH<sub>2</sub>Cl<sub>2</sub> at r.t. (b) TFA/CH<sub>2</sub>Cl<sub>2</sub> at r.t. (c) MnCl<sub>2</sub>·4H<sub>2</sub>O, H<sub>2</sub>O, pH = 5-6, 40°C, Ar atm, overnight. 184
- Scheme IV.2. Synthesis of compound **3**, (a) HBTU, DIPEA, CH<sub>2</sub>Cl<sub>2</sub>, few h at r.t.. 185
- Scheme IV.3. Proposed mechanism by Shi et al. for the amino-DBCO rearrangement in the presence of TFA.<sup>236</sup> 186
- Scheme IV.4. Second strategy for the synthesis of DBCO-Mn-complexes. Expected reactions: (b) TFA/CH<sub>2</sub>Cl<sub>2</sub> at r.t. (c) MnCl<sub>2</sub>·4H<sub>2</sub>O, H<sub>2</sub>O, pH = 5-6, 40°C, Ar atm, overnight (d) EDC·HCl, pH = 6, THF/H<sub>2</sub>O, r.t.. 187
- Scheme IV.5. First strategy for the synthesis of N<sub>3</sub>-Mn-complexes. Expected reactions: (e) TEA, DPPA, CH<sub>2</sub>Cl<sub>2</sub> at r.t. (b) TFA/CH<sub>2</sub>Cl<sub>2</sub> at r.t. (c) MnCl<sub>2</sub>·4H<sub>2</sub>O, H<sub>2</sub>O, pH = 5-6, 40°C, Ar atm, overnight. 188
- Scheme IV.6. Curtius rearrangement and hydrolysis of isocyanate function that can be observed on azide functions. 189
- Scheme IV.7. Second strategy for the synthesis of N<sub>3</sub>-Mn-complexes. Expected reactions: (a) HBTU, DIPEA, CH<sub>2</sub>Cl<sub>2</sub> at r.t. (b) TFA/CH<sub>2</sub>Cl<sub>2</sub> at r.t. (c) MnCl<sub>2</sub>·4H<sub>2</sub>O, H<sub>2</sub>O, pH = 5-6, 40°C, Ar atm, overnight which was validated. 190

## List of tables

---

Table I.1. Comparative table of the different imaging techniques discussed above.	44
Table II.1. Evaluation of the number of coordinated water molecules in the inner sphere for all complexes (q) by the two different relaxometric techniques described in the text.	68
Table II.2. Determination of the residence time at 37°C and 11.75 T of the coordinated water molecule ( $\tau_M$ ), as well as the other parameters characterizing this exchange : $A/\hbar$ , the hyperfine coupling constant between the oxygen nucleus of the bound water molecule and the $Mn^{2+}$ ion; $\tau_v$ , the correlation time modulating the electronic relaxation of $Mn^{2+}$ ; $E_v$ , the activation energy related to $\tau_v$ ; B, related to the mean-square value of the zero-field splitting energy, $\Delta$ , through $B = 2.4\Delta^2$ ; $\Delta H^\ddagger$ and $\Delta S^\ddagger$ the enthalpy and entropy of activation, respectively, of the water exchange process. The number of coordinated water molecules was set to $q = 1$ .	69
Table II.3. Results of the theoretical fitting of $^1H$ NMRD profiles at 37°C with Bloembergen and Solomon's theory using the MINUIT minimization software. Parameters, such as the distance of closest approach ( $d_{NMR}$ ) and the water diffusion coefficient (D) governing the outer sphere mechanism, or the distance between the coordinated proton of the water molecule and the manganese ion (r) related to the inner sphere mechanism, can be set constant during the fitting procedure thanks to their prior determinations. <sup>156-158</sup> The values of q and $\tau_M$ used were also predetermined thanks to their separate evaluation described above, thereby allowing to evaluate the rotational correlation time ( $\tau_R$ ), the electronic relaxation time to ground level at zero magnetic field ( $\tau_{SO}$ ) and the correlation time that modulates electronic orbital relaxation ( $\tau_V$ ).	71
Table II.4. Values of longitudinal relaxivity calculated from the water proton relaxation time $T_1$ measured at approximately 37°C under a field of 9.4T (400 MHz).	75
Table III.1. Structure of PEO-b-PCL copolymers from literature and used in this work (either commercial or synthesized). * from SEC $\perp$ from NMR. The degrees of polymerizations (DP) of each block were calculated using the monomer molar masses, respectively 114 $g \cdot mol^{-1}$ for CL and 44 $g \cdot mol^{-1}$ for EO.	108
Table III.2. Structure of PEO-b-P(CL-co-LA) copolymers used in this work for the different analyses where the index represents the DP of the different moieties calculated from $^1H$ NMR.	120
Table III.3. Ratio of the $\rho$ parameter ( $R_g/R_h$ ) according to the different regression methods for $R_h$ determination. $R_g$ was obtained by a Guinier plot of the static light scattering data (Figure III.13).	125
Table III.4. Extraction of the $R_g$ and $R_h$ values from the different fittings of Figure III.14.	128
Table III.5. Extraction of the $R_g$ and $R_h$ values from the different fitting of Figure III.15.	129
Table III.6. Comparison of DLC and EE* between micelles/rods and polymersomes.	138
Table IV.1. Measurements of osmolarity, ESI-MS and colorimetric tests with orange xylene on all fractions	197



# Contents

---

***Acknowledgements***

***Summary***

***Résumé de la thèse***

***Résumé étendu en français***

***List of abbreviations***

***List of figures***

***List of schemes***

***List of tables***

<b>Chapter I</b>	<b>2</b>
Chapter I: state of the art	2
I.1 Introduction	2
I.2 Nanomedicines	4
I.2.1 Synthesis of amphiphilic polymers	5
I.2.2 Theory of self-assembly with diblock copolymers	7
I.2.3 Drug delivery	10
I.3 Nanocarriers	21
I.3.1 Micelles	21
I.3.2 Polymersomes	22
I.3.3 Characterization techniques	28
I.4 Theranostic nanocarriers in cancer treatments	31
I.4.1 Magnetic resonance imaging (MRI)	32
I.4.2 Photoacoustic imaging (PAI)	38
I.4.3 X-rays Computed Tomography (X-rays CT)	40
I.4.4 Fluorescence imaging (FLI)	41
I.4.5 Comparison of the different bioimaging modalities	43
<b>Aim</b>	<b>48</b>
<b>Chapter II</b>	<b>52</b>
Chapter II: Mn <sup>2+</sup> complexes with pyclen-based derivatives: synthesis, relaxometry characterizations and <i>in vivo</i> evaluation as MRI contrast agents.	52
II.1 Introduction	52

II.2 Results and discussion	56
II.2.1 Synthesis of the pyclen-based Mn <sup>2+</sup> complexes	56
II.2.2 Oxidation state	61
II.2.3 Relaxometric characterization	62
II.2.4 <i>In vivo</i> experiments	75
II.3 Conclusions and perspectives	82
II.4 Annexes	84
II.5. Materials and methods	89
<b>Chapter III</b>	<b>104</b>
Chapter III: Synthesis and characterization of pH-sensitive polymeric nanocarriers self-assembly and their <i>in vitro</i> and <i>in vivo</i> evaluation.	104
III.1 Introduction	104
III.2. Results and discussion	107
III.2.1. Synthesis and characterization of diblock copolymers, PEO- <i>b</i> -PCL	107
III.2.2. PEO- <i>b</i> -PCL self-assembly	111
III.2.3. Synthesis and characterization of diblock copolymers, PEO- <i>b</i> -P(CL- <i>co</i> -LA)	114
III.2.4. PEO- <i>b</i> -P(CL- <i>co</i> -LA) self-assembly	120
III.2.5. Encapsulation of active substances and dyes in PEO- <i>b</i> -P(CL- <i>co</i> -LA) self-assembly	135
III.2.6 <i>In vitro</i> tests on PEO- <i>b</i> -P(CL- <i>co</i> -LA) self-assembly	140
III.2.7. <i>In vivo</i> tests on PEO- <i>b</i> -P(CL- <i>co</i> -LA) self-assembly	149
III.3. Conclusion and perspectives	157
III.4 Annexes	159
III.4. Materials and methods	166
<b>Chapter IV</b>	<b>180</b>
Chapter IV: Grafting of manganese complexes onto polymeric nanocarriers	180
IV.1 Introduction	180
IV.2 Results and discussion	184
IV.2.1 Click chemistry on N <sub>3</sub> -PEO- <i>b</i> -P(CL- <i>co</i> -LA)	184
IV.2.2 Click chemistry on DBCO-PEO- <i>b</i> -P(CL- <i>co</i> -LA)	187
IV.2.3 Synthesis of the copolymer with DBCO end-group	191
IV.2 Conclusion and perspectives	193
IV.3 Materials and methods	194
<b>Chapter V</b>	<b>200</b>
Chapter V: Conclusions and outlooks	200
<b>References</b>	<b>207</b>
<b>List of publications and communications</b>	<b>237</b>

# **Chapter I**

State of the art

# Chapter I

---

## Chapter I: state of the art

### I.1 Introduction

Cancers are the second cause of death in the world according to the world health organization (WHO) statistics in 2020, and are therefore a growing societal issue. Efforts are recurrently made to improve the different ways of treatment.<sup>7</sup>

For localized tumors, surgery is the leading technique as it allows to remove all or a large part of cancer cells and it is a local treatment. Nevertheless, the surgical intervention is invasive, and, unfortunately, all cancer cells cannot usually be removed, so that chemotherapy or radiotherapy must be used to complete the treatment, to prevent relapses and to treat proximal, and to some extent, distal metastases. Actually the different treatments approved by the Food and Drug Administration (FDA) are not specific, are usually composed of small organic molecules, some of them being hydrophobic, which leads to fast clearance and/or toxic accumulation, and can modify the integrity of healthy cells, with for example hair loss or bone marrow issues.<sup>8-11</sup> Moreover, multiple injections of chemotherapy can lead to multi-drug resistance that reduces the capacity of treatments to have an impact on cancer cells.<sup>12</sup> These different drawbacks show the necessity to find new alternatives allowing better diagnosis and/or treatment. Among all the possibilities, the nanotechnologies represent an elegant manner to develop new treatments in the medical field due to their tunability. That is why there is a growing interest in nanotechnology in the research world, both in academia and in pharmaceutical industry. Indeed, the nanostructures can be tailored for both diagnosis and treatment and designed to increase the bioavailability of the active principals. Moreover, a lot of efforts are made to properly characterize them to obtain a final nanostructure dedicated to the intended application.<sup>13</sup> Two families of nanoparticles (NPs) are developed: (i) inorganic and (ii) organic. Among the inorganic nanoparticles developed, magnetic nanoparticles like superparamagnetic iron oxide nanoparticles (SPIONs) are widely used for hyperthermia treatment. For example, using such particles leads to a local heating in the zone of accumulation

induced by the applied magnetic field, allowing to kill the cancer cells.<sup>14–16</sup> SPIONs can also be designed for diagnosis using magnetic resonance imaging, leading to a theranostic platform. Metallic nanoparticles, such as gold nanoparticles, are also used due to their biocompatibility, stability, etc. They can be synthesized in different shapes, which is useful for drug delivery and they have optical properties that can be used for imaging.<sup>17–20</sup> Quantum dots are another type of interesting particles because of their ability to be imaged by fluorescence. Nevertheless, they have a relative cytotoxicity and need to be coated to improve their uptake and their solubility, limiting their use.<sup>21–24</sup> On the other hand, organic nanoparticles can also be designed. Among the different structures used to form nanoparticles, dendrimers are branched polymers with a spherical shape. They can be functionalized on the surface and used as drug carriers.<sup>25,26</sup> Liposomes and polymeric vesicles are other interesting drug carriers due to their ability to be easily tuned. Indeed, their surface can be modified with different functionalities of interest, such as a targeting molecule. Their surface and shape can also be modified to obtain different mechanical characteristics to enhance for instance the drug delivery efficacy. Moreover, they can easily be used for specific drug delivery: they will improve the cellular uptake and the cytotoxicity of the encapsulated drug will be reduced for healthy cells whereas the drug can be specifically delivered at the site of interest using different stimuli.<sup>11,27–29</sup> Among all those studied systems<sup>10,11,29–33</sup>, vesicles such as liposomes have attracted attention since they can encapsulate a lot of both hydrophilic and hydrophobic compounds, and exhibit long blood circulation if they are functionalized.<sup>34,35</sup> Nevertheless, liposomes, despite having a higher rate of encapsulation than micelles, keep a high permeability and low stability that cannot be easily mitigated due to their low chemical versatility. That is why polymeric vesicles, called polymersomes, have been proposed as they represent an elegant alternative due to their high chemical versatility induced by the synthesis of the polymeric components.<sup>36</sup>

Polymer nanoparticles seem to be a good option for specific drug delivery, using responsiveness to different parameters such as pH, temperature or external fields (magnetic, light...). Indeed, some polymers have already shown their biocompatibility like poly(ethylene oxide) (PEO), and biodegradability and biocompatibility like poly( $\epsilon$ -caprolactone) (PCL), poly(lactide) PLA, poly(lactic-*co*-glycolic acid) (PLGA), .... Various polymeric nanoparticles are already used for different therapeutic areas and drug delivery.<sup>29,25,37–39</sup>

## **I.2 Nanomedicines**

Nanomedicine comprises nanomaterials (defined as nano due to their size between 1-100 nm) that are used in the framework of treatments in medicine. These types of treatment are emergent for cancer therapy due to their capacity to palliate some issues as the side effects induced by current treatments, low specificity, rapid clearance, etc. Indeed, nanocarriers allow to increase the blood residence time, they can encapsulate toxic or poorly soluble molecules to decrease their side effects, they can be easily modified to have, for example, a targeting molecule, and so on. Moreover, according to the used molecule or purpose, the drug release can be induced by an internal or external stimulus. The high panel of actions brought by nanomedicines is actually an important developing research area.<sup>40</sup>

In the 1960s, the first generation of controlled release systems has been developed. Nanoparticles such as liposomes or micelles, encapsulating the treatment, reach the zone of interest by passive accumulation due to the abnormalities of blood vessels present in tumor sites. A second generation has been developed in 1980s where nanoparticles were given long term release. In 2000s, an increase of their drug delivery capacity was obtained with still a passive targeting principle. Indeed, functionalization of the nanoparticles with, for instance, poly(ethylene oxide) (PEO) moieties allows to increase the circulation time and to decrease the uptake by the reticuloendothelial system (RES). In 2010s, researches focused on the third generation of nanoparticles including the active targeting by the addition of a marker.<sup>41-44</sup>

These nanocarriers are composed of an amphiphilic structure, that is to say a molecule having two different behaviors: hydrophobic and hydrophilic. Lipids are natural amphiphilic moieties while synthetic counterparts can be designed by synthesizing copolymers. The system, in aqueous medium, tends to reduce the contact surface of the hydrophobic part with water. This leads to self-assemblies governed by the hydrophilic-hydrophobic interaction balance, leading to thermodynamically stable particles, also influenced by their kinetics of formation.

### I.2.1 Synthesis of amphiphilic polymers

In the following section, living polymerization reactions will be described. Indeed, these synthesis methods are preferentially used for several reasons: they lead to chains that grow simultaneously, giving low molar mass dispersity index,  $\mathcal{D}$ , and allowing a sequential synthesis by a polymerization on the chain termination of the first block. This type of reactions allows thus a better control of the synthesis.<sup>45,46</sup> Among this family of polymerizations, we can cite: (i) ring opening polymerization (ROP), (ii) reversible addition-fragmentation chain transfer polymerization (RAFT), and (iii) atom transfer reversible polymerization (ATRP).

*Ring opening polymerization* (ROP) takes place with cyclic monomers that contain cleavable bonds. This technique allows to add heteroatoms in the backbone. For example, for the synthesis of polycaprolactone chains from lactone, anionic ROP will be the usual way with a nucleophilic attack of the initiator on the tight cycle, followed by a propagation induced by the formed hydroxylate or carboxylate, depending on the way. Due to the stability of the intermediate species, the carboxylate way is often preferred. ( $\beta$  on Figure I.1)<sup>47</sup> The ROP mechanism can be anionic, cationic, organic or radical, depending on the initiator and/or the catalyst.

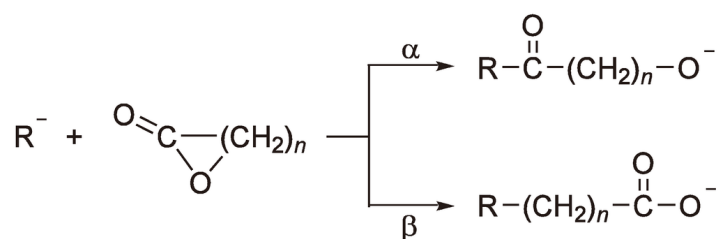


Figure I.1. Reaction ways of anionic ROP on lactone.<sup>47</sup>

*Reversible addition-fragmentation chain transfer polymerization* (RAFT) is a radical reaction that typically uses thiocarbonylthio molecules as chain transfer agent. It leads to chains with a narrow distribution and can be used with a large panel of solvents and chemical functions. This technique is principally used in Polymerization-Induced Self-Assembly (PISA) that will be described in the following section. It is characterized by the use of a large number of vinyl monomers with polar side groups, like (meth)acrylates, acrylonitrile, acrylamide, ... and the use

of a molecule called RAFT agent. The RAFT agent is composed of an activating group, able to stabilize the intermediate radical and its activity, and a good leaving group to initiate the propagation of the polymerization. RAFT agents will impact the reactivity of the polymerization and have to be chosen as a function of the desired final polymers.<sup>45,46</sup>

*Atom transfer radical polymerization* (ATRP) is a radical process of polymerization that uses a transition metal as catalyst, like copper  $\text{Cu}^+$ . It allows to obtain complex polymers with high molecular weight, and low molar mass dispersity. Basically, ATRP is based on a halogen species present on the initiator that is transmissible to the growing chain. The monomer is also able to stabilize the propagation of the chain that is catalyzed by the transition metal complex. The system uses a redox reaction between the catalyst and the halogen atom on the chain.<sup>46</sup>

These reactions allow to form different amphiphilic polymers leading to different types of bilayers during the self-assembly into vesicles, which can therefore be more complex than simple micelles. (Figure I.2) In general, two types of copolymers are designed: diblock (AB) or triblock (ABC or ABA or BAB) copolymers where A and C are hydrophilic chains and B hydrophobic chains.<sup>48</sup>

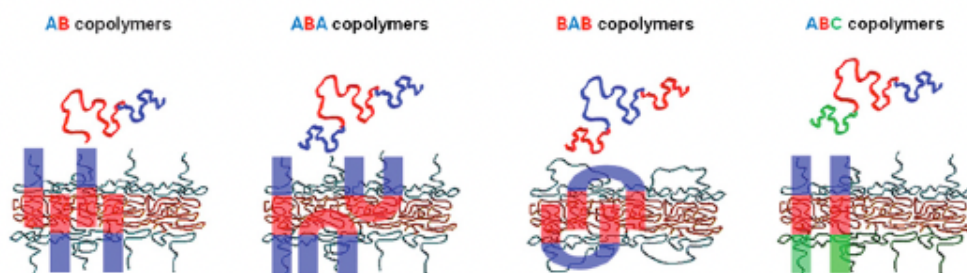


Figure I.2. Images developed by Lee and Feijen showing the different conformations taken by amphiphilic copolymers to form vesicles.<sup>48</sup>

In the framework of this thesis, we will focus on the AB diblock type copolymers. Indeed, studies have shown that diblock copolymers lead to self-assembled vesicles allowing more drug loading (that will be detailed below) and having a higher thermodynamic stability than those obtained from triblock copolymers concerning micelles.<sup>49</sup>

## I.2.2 Theory of self-assembly with diblock copolymers

In general, self-assembly of diblock copolymers depends on the ratio between the hydrophilic and hydrophobic parts. The prediction of the resulting nanoparticle structure will depend on the packing parameter ( $P_c$ ) that can be defined by the following equation:

$$P_c = \frac{v}{a_0 l_c} \quad (\text{Equation I.1})$$

$v$ , volume of the hydrophobic chain;  $a_0$ , area occupied by the hydrophilic group and  $l_c$ , length of the diblock.

According to the ratio obtained for  $P_c$ , the type of nanostructures can be predicted, as shown in Figure I.3. A  $P_c$  lower than 0.3 leads to spherical micelles due to the conical shape, between 0.3 and 0.5 rod-like micelles are obtained, that are similar to elongated cylinders, and finally polymeric vesicles also called polymersomes are obtained with a  $P_c$  value ranging between 0.5 and 1.<sup>50</sup> Indeed, the system tends to a structure which minimizes the total interfacial energy.<sup>51</sup>

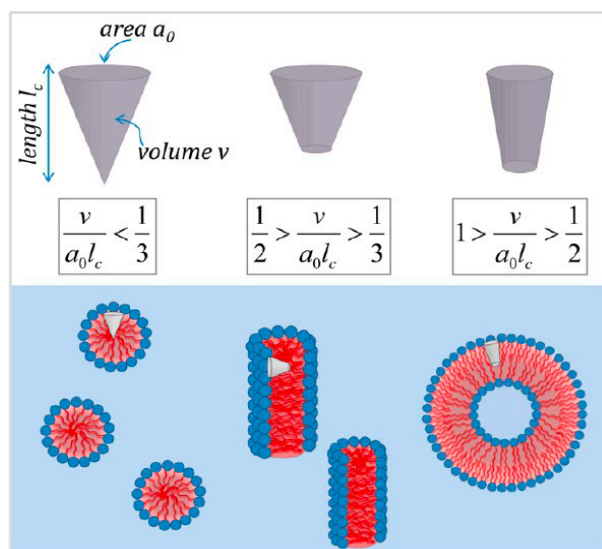


Figure I.3. Predicted structure as a function of the packing parameter.<sup>50</sup> Reprinted with permission from Bleul *et al.* Techniques To Control Polymersome Size. *Macromolecules* **2015**, 48 (20), 7396–7409. Copyright © 2015 American Chemical Society.

While the packing parameter gives a rough idea of the structure, the reality is quite different with various intermediate structures that can be identified in solution as demonstrated by Mai

and Eisenberg.<sup>51</sup> Indeed, structures such as micelles, lamellae, rods, large compound micelles and vesicles have been observed in suspension. Usually, the first identified structures are micelles, which are often used as drug delivery systems. However, they can only encapsulate hydrophobic drugs as they only have a hydrophobic core. Other structures that can be observed quite similar to the micelles but with anisotropic, elongated morphology, are the rods or worm-like micelles. Finally, the most interesting structures that can also be identified consist of a bilayer membrane formed by the diblock copolymers enclosing an aqueous compartment, which are called vesicles. In such structures, hydrophilic tails point out to the solution but also to the core of the vesicles. Due to this particular morphology, vesicles exhibit both hydrophilic and hydrophobic pockets allowing the encapsulation of either hydrophilic or hydrophobic drugs. Indeed, hydrophilic drugs can be encapsulated in the hydrophilic core while hydrophobic drugs can be encapsulated in the hydrophobic bilayer, simultaneously. (Figure I.4)

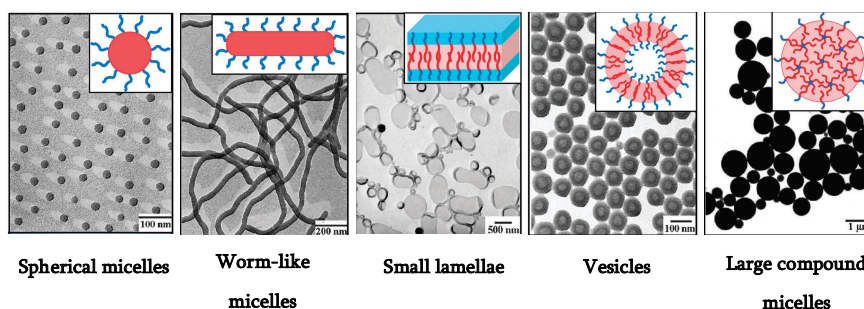


Figure I.4. Transmission electron microscopy (TEM) of different nanostructures composed of polystyrene-block-poly(acrylic acid) (PS-*b*-PAA) with different polymerization degrees of each chain.<sup>51</sup>

While the relative sizes of the hydrophobic and hydrophilic blocks are important parameters to determine the resulting nanostructures, the copolymer concentration, water content and nature of common solvent will also impact their formation. First, the *copolymer concentration* impacts the morphology of the aggregates, that can change with the concentration. When the core size of micelles increases, it leads to a stretching of the chains. Regarding the *water content*, it also determines the final structure of the self-assemblies. Indeed, the first added drops of water lead to the formation of micelles until the critical water content concentration is reached, where the shape of the aggregates can be modified and lead to other layouts. The size of the aggregates grows during the increase of water volume to reduce the interfacial energy until a reorganization of the system at nanometric scale occurs. *Common solvent* can also lead to modifications in structuration. Indeed, the solubility parameters of both moieties of the copolymer have to be

similar to have a hydrophobic region perfectly soluble in the solvent. If this parameter differs, the place occupied by the hydrophobic chain will decrease. This will modify repulsion forces. (Figure I.5)<sup>51</sup>

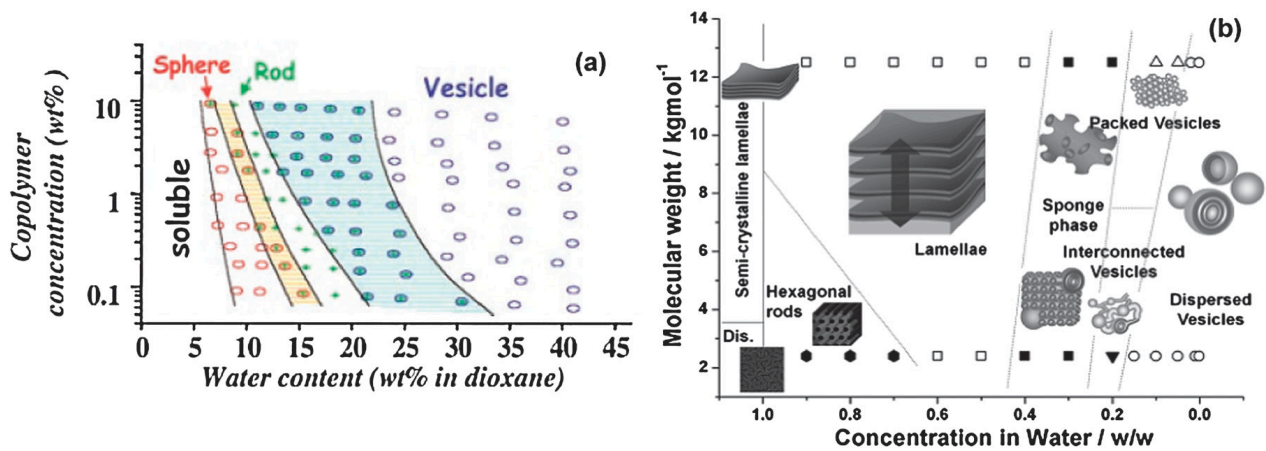


Figure I.5. Phase diagram as a function of water content for (a) PS<sub>310</sub>-*b*-PAA<sub>52</sub> with, in colored area, the coexistence between two nanostructures (b) poly(butylene oxide)-*block*-poly(ethylene oxide) (PBO-*b*-PEO) according to the molecular weight identifying the domain of existence of each nanostructure.<sup>51</sup>

For instance, Choucair and Eisenberg evidenced the nanostructures of polystyrene-*b*-poly(acrylic acid) formed in dioxane by varying the water/dioxane ratio. When the critical water concentration is reached, the nanoobjects start to form with a water/dioxane ratio between 8-15 % (w/w) for this polymer. After the formation of spheres, addition of water leads first to short rods, and then to long rods at 14% of water. The switch between one to another structure leads to the coexistence of different structures during the addition of water. Finally, bigger and bigger vesicles were obtained due to the supplementary addition of water. They also evidenced the thermodynamical stability of these structures by measuring their size over a long period of time. In a second time, they performed the inverse transformation by adding dioxane in their solution to evidence the reversibility of these systems. This led to a reduction of the water content and hence a modification of the nanostructures with a switch in the inverse order going from big vesicles to spheres. (Figure I.6)<sup>52</sup>

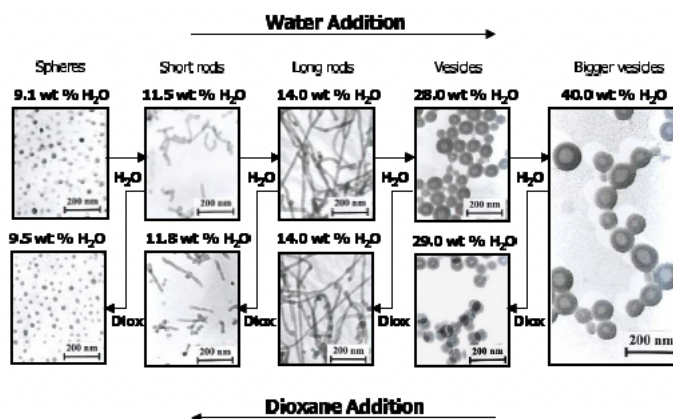


Figure I.6. Vesicles shape as a function of water/dioxane content for the copolymer; PS<sub>310</sub>-*b*-PAA<sub>52</sub>, and the reversible mechanism.<sup>52</sup>

### I.2.3 Drug delivery

As discussed above, specific drug delivery to cancer cells is beneficial for the treatment of this disease. Nevertheless, apart from burst release that may occur in the first minutes after injection, it is necessary to activate the release by using an endogenous or exogenous stimulus. Endogenous stimuli are produced by a local modification of the environment such as the pH, whereas external stimuli are induced by the manipulator. The nanoobjects will reach their objective by two principal ways: a passive targeting based on the enhanced permeability and retention effect (EPR) of the tumoral tissue, or an active targeting of cancer cells induced by a specific functionalization. Once the nanoobjects have reached their objective, the release of drug and/or dyes can be characterized by different mathematical theories to evidence the kinetic behavior of the nanoplatform, *i.e.* the release profile of drug percentage release *vs.* time.

#### I.2.3.1 Stimuli-sensitive drug delivery

Endogenous phenomena<sup>53,54</sup>

*pH responsive polymers* having an acid-cleavable function, such as poly(lactic acid) (PLA) or polycaprolactone (PCL), are able to undergo acid hydrolysis of their ester functions leading to the degradation of the hydrophobic chain. This phenomenon is possible because the pH decreases from 7.4 in normal condition, to ~6.5 in tumoral environment. Moreover, after

internalization in cells, the vesicles can be trapped by the endosomes, and end up in lysosomes which also possess an acid pH of 5.0-5.5 and 4.0-4.5, respectively. The degradation of the hydrophobic chains occurring in vesicle membranes leads to a shape transition into micelles. This transition can be explained by an increase in the hydrophilic fraction,  $f_{\text{hydrophilic}}$ , causing a modification of the molecular structure, from cylindrical to conical. The micelles are afterwards decomposed or destabilized. Ahmed *et al.* evidenced the destruction of polymersomes made of PEO-*b*-PLA. Figure I.7 evidences the modification over time of the obtained vesicles using Cryo-TEM. First, there is formation of pores rapidly followed by the destruction of the nanostructure leading to the formation of micelles and rods.<sup>55</sup>

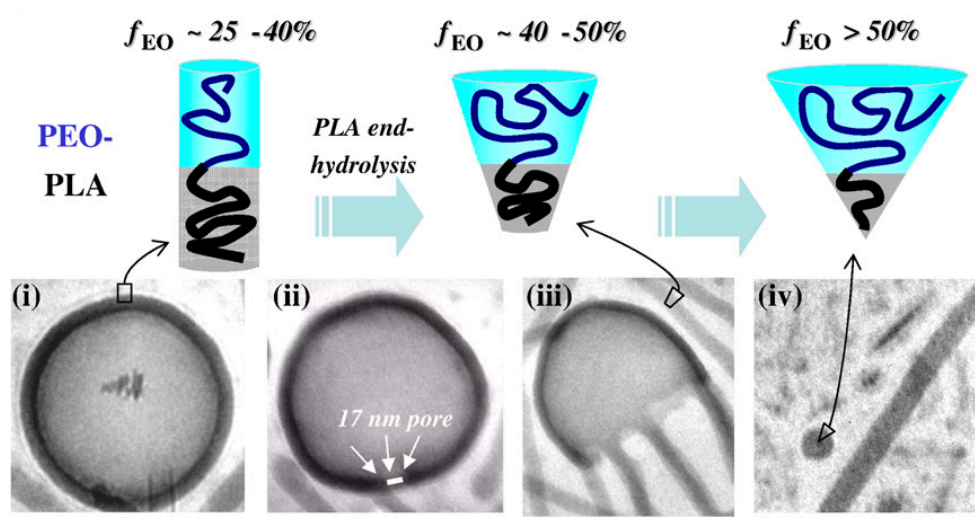


Figure I.7. Cryo-TEM of PEO-PLA vesicles during their transformation into micelles and rods induced by a modification of pH.<sup>55</sup>

*Redox potential* inside and outside cells are different as well as in certain tumor tissues. The most endogenous reducing agent is the glutathione enzyme (GSH) that is present at a concentration of 2-20  $\mu\text{M}$  out of the cells and up to 10 mM inside cells. In this type of reactions, disulfide bonds are the principal breakable links in reductive condition. This phenomenon leads to a disassembly of the nanocarriers. These disulfide bonds are obtained during the synthesis of copolymers and can take place for example between hydrophobic and hydrophilic chains. To illustrate this phenomenon, Zou *et al.* developed polymersomes loaded with doxorubicin based on cyclic peptide (cNGQ) grafted to poly(ethylene glycol)-*b*-poly(trimethylene carbonate-*co*-dithiolane trimethylene carbonate) (PEG-*b*-P(TMC-DTC)). DTC moieties possess the disulfide bond able to be reduced by the GSH. The polymersomes resulting of a self-assembly between PEG-*b*-P(TMC-DTC) and cNGQ-PEG-*b*-P(TMC-DTC) (8:2, w/w) show specific targeting of

lung orthotopic cancer models, and exhibit low toxicity, high selectivity with high accumulation and a fast drug release. They evidenced that in reductive conditions, a release of doxorubicin upper than 80% occurred within 24 h instead of 16% within 24 h in non-reductive conditions. They also evidenced the stability of the nanoparticles in normal physiological conditions.<sup>53,54,56</sup>

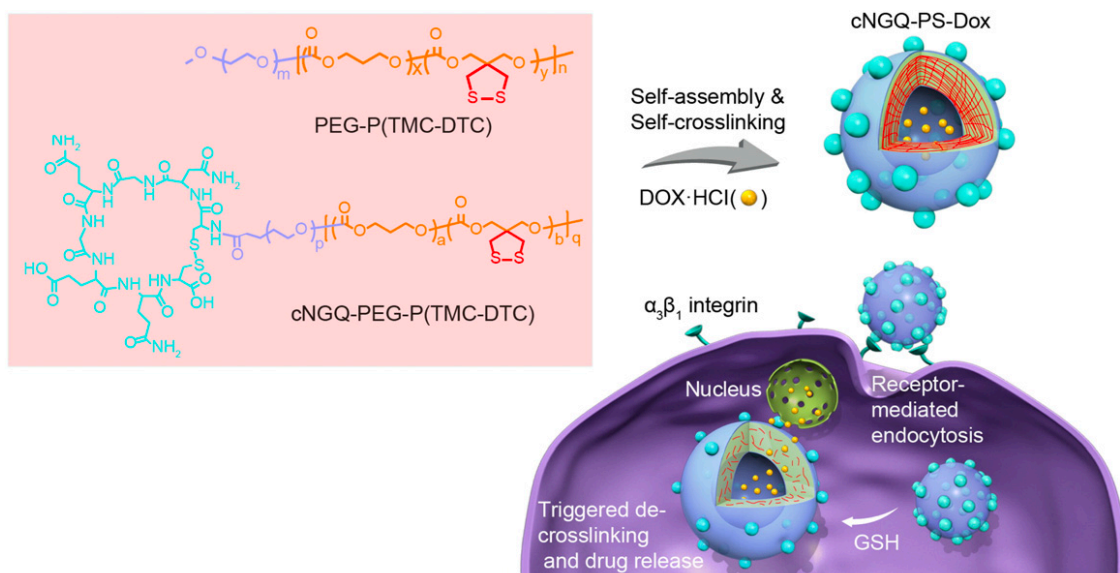


Figure I.8. Synthesis of self-assembled polymersomes based on PEG-P(TMC-DTC) and cNGQ-PEG-P(TMC-DTC), loaded with doxorubicin. Endocytosis is induced by *in vivo* targeting followed by reduction of S-S bonds by GSH, leading to release of doxorubicin.<sup>56</sup> Reprinted with permission from Xie *et al.* Polymeric Hybrid Nanomicelles for Cancer Theranostics: An Efficient and Precise Anticancer Strategy for the Codelivery of Doxorubicin/MiR-34a and Magnetic Resonance Imaging. *ACS Appl. Mater. Interfaces* **2019**, 11 (47), 43865–43878. Copyright © 2019 American Chemical Society.

*Enzymes* are involved in a lot of biological processes with a high specificity and catalytic properties. Copolymers that are able to be selectively recognized by enzymes are developed. Copolymers are then degraded by enzymes or their reversible interaction with the enzymes leads to a switch between assembly and disassembly of the nanocarriers. Interestingly, tumoral systems possess specific enzymes, allowing the development of drug carriers having specific interactions only with those enzymes. For instance, micelles made with cholesterol-PLGVVRK-PEG, where PLGVVRK is a responsive peptide linker to matrix metalloproteinase – 2 (MMP-2) overexpressed in tumor cells were developed by Barve *et al.*. These micelles bearing a target moiety and encapsulating the drug cabazitaxel were able to specifically deliver the drug at the tumor site.<sup>53,54,57</sup>

*Temperature* can be modified by an endogenous phenomenon or an exogenous stimulus. Indeed, a modification of the temperature can occur following an inflammation, a tumor or an infection. An external stimulus can also be applied to increase temperature in area of interest which is called hyperthermia. In the case of drug delivery, the most used polymer is the poly(N-isopropylacrylamide) (PNIPAM) because its lower critical solution temperature (LCST) is around 32°C (This temperature can be tuned by modifying the structure). Indeed, below the LCST, the polymer is soluble in water while above the LCST, the polymer becomes insoluble. This assembly/disassembly structure allows drug release as a function of temperature.<sup>53,54</sup>

Exogenous phenomena<sup>53,54</sup>

*Magnetic field responsive* nanocarriers are usually obtained by encapsulation of superparamagnetic iron oxide nanoparticles (SPIONs) in polymeric vesicles. This versatile system allows a precise diagnosis by magnetic resonance imaging (MRI) and treatment of the pathology thanks to magnetic hyperthermia (MH). With an alternating magnetic field (AMF), it is possible to increase the temperature in the accumulation site of the SPIONs due to the thermal losses associated with the reorientation of their magnetic moments. This local heating can increase the permeability of the nanocarrier and induce increased drug release. Moreover, the increased temperature can also act also as a treatment by killing cancer cells. Based on all possibilities brought by using this type of system, Khlaledian *et al.* developed PLA-PEG-FA (FA = folic acid) as targeted polymersomes loaded with SPIONs and doxorubicin to perform hyperthermia and chemotherapy conjointly. This bimodal system is able to release around 90% of encapsulated doxorubicin and to increase the temperature to 44.2°C, with a higher number of apoptotic cells compared to the results obtained with free doxorubicin.<sup>53,54,58</sup>

*Ultrasound* application (at a higher intensity of the acoustic wave than in echography) leads to two types of effect: a localized increase of the temperature or a cavitation in the nanostructure inducing the drug release. Moreover, ultrasound favors the cellular uptake by inducing an increase of the membrane permeability. Indeed, ultrasound leads to the formation of bubbles in the membranes, which explains the cavitation and increase of permeability.<sup>53,54</sup>

Light as visible, ultraviolet or near infrared can induce the disruption of specific bonds present in the copolymer. Usually, the near infrared range of wavelength is preferred to avoid tissue absorption and allow deeper penetration. Azobenzene, spirobenzopyran or nitrobenzyl groups are known to be cleavable under light exposure, allowing drug delivery. Light can also induce photothermal effect, produced by the presence of compound responding to light. Such thermosensitive polymersomes could thus allow drug delivery. It is also possible to induce release by photo-oxidation which is allowed in this case by the presence of compounds responding to light and able to promote radicals.<sup>53,54,59</sup> Using light allows to couple different strategies of treatment as demonstrated by Saravanakumar *et al.* Indeed, they developed polymersomes composed of poly(ethylene oxide)-poly( $\beta$ -aminoacrylate)-poly(ethylene oxide) triblock where the  $\beta$ -aminoacrylate units can be cleaved by reactive oxygen species (ROS). The polymersomes were co-loaded with doxorubicin for chemotherapy, and with IR-780, which will generate ROS under laser irradiation, able to perform photodynamic therapy (PDT) and photothermal therapy (PTT), and to cleave  $\beta$ -aminoacrylate destructing the polymersomes and releasing the drug. These photo-chemotherapy loaded polymersomes exhibited an excellent antitumor effect both *in vitro* and *in vivo*. (Figure I.9)<sup>60</sup>

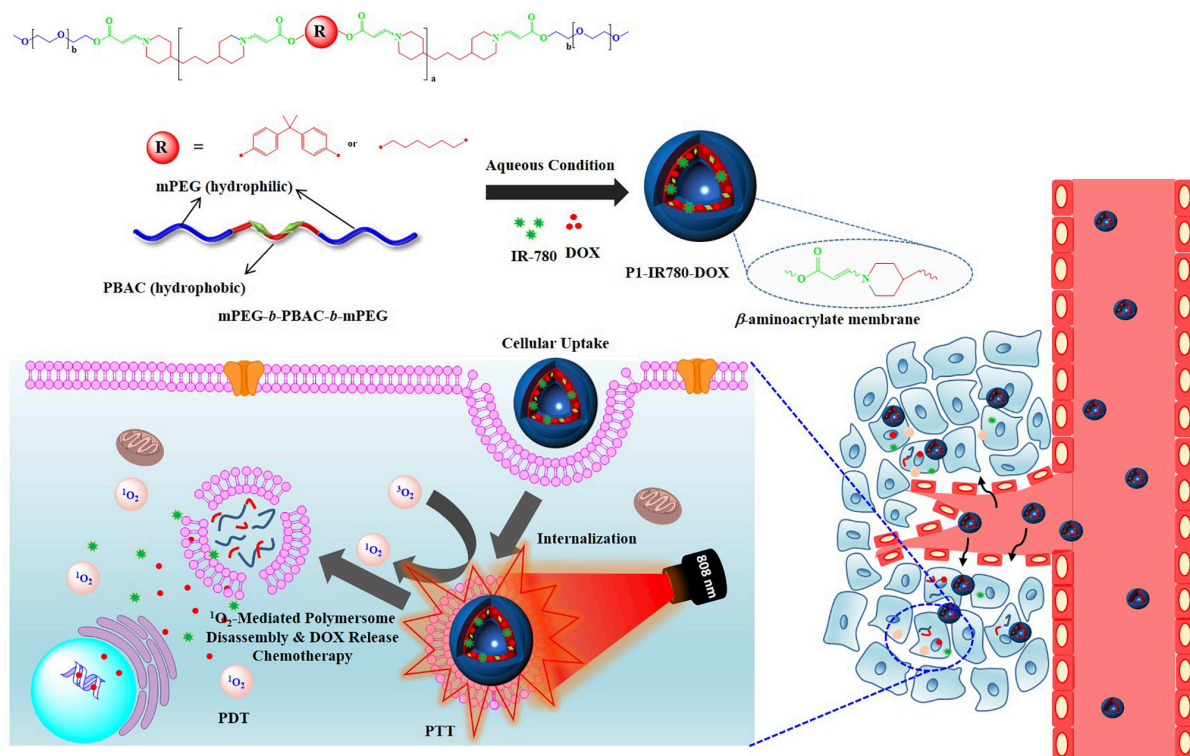


Figure I.9. Formation of polymersomes developed by Saravanakumar *et al.* followed by their uptake in cancer cells and their mechanism of action under laser irradiation.<sup>60</sup>

Of course, all these stimuli can be combined in multimodal systems having 2 or more types of response.

### *1.2.3.2 Permeability of the membrane*

Another important parameter in drug delivery is the permeability of the membrane. Indeed, this parameter impacts the capacity of the drug to pass through the membrane. A high permeability of the system can lead to an undesired premature drug release. This parameter depends on the membrane thickness, on the glass transition temperature of the copolymer, determining the mobility of the chains, and on the proportion of hydrophilic/hydrophobic chains.<sup>61</sup> The crystallinity of the copolymer also impacts the release. An amorphous copolymer leads to a higher permeability than a semi-crystalline structure due to the higher flexibility of the amorphous chains. This was observed for vesicles based on PCL, which possess a melting temperature around 50°C.<sup>62</sup> The drug used (in term of size, charge, solubility and partition coefficient between apolar and polar phases) also has an impact on the predetermination of the drug capacity to pass through the hydrophobic or hydrophilic domains of the membrane.<sup>61,63</sup>

### *1.2.3.3 Drug delivery laws*

Due to the several drug delivery nanocarrier types, many mathematical models were developed to fit with the studied systems. (Figure I.10) Those models allow to fit the obtained data in term of drug delivery and to predict the behavior of the nanocarriers. It allows to exhibit the needed drug concentration to maintain in bloodstream, to control the release rate and the time needed to release the dose, *i.e.* all the parameters of pharmacokinetics (blood half-life, area-under-the curve, ...). This release occurs according to different phenomena as diffusion, erosion, absorption and degradation.<sup>64,65</sup> In the following section, Fick's model based on a simple diffusion and the two most used models respectively of Peppas and Higuchi will be discussed.

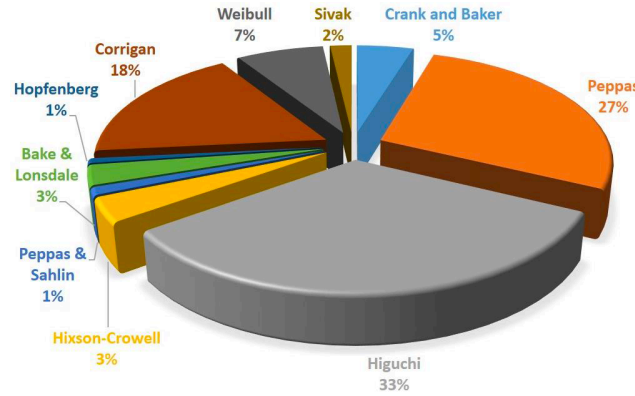


Figure I.10. Proportion of the different mathematical models used to describe drug delivery system release profiles.<sup>64</sup>

Fick's model is based on the linear diffusion of the drug over time, giving first order kinetics:<sup>64</sup>

$$\frac{dM(t)}{dt} = \frac{A D K (M_0 - M(t))}{L V} \quad (\text{Equation I.2})$$

Where  $M(t)$ , is the quantity of drug released at time  $t$ ;  $M_0$ , the initial drug mass;  $V$ , the total deposition volume of the drug;  $A$ , the total surface area of nanocarrier;  $L$ , the thickness of the membrane;  $D$ , the diffusion coefficient of the drug.

The integration of this first order kinetics equation gives an exponential law (*i.e.* logarithm of release decreases linearly with time), which is not obtained in all cases. Therefore, other mathematical models were proposed. The Higuchi's model was developed for planar structures and can be adapted for spheres. It is based on a drug release law increasing linearly with the square root of time:<sup>64</sup>

$$\frac{M(t)}{M_\infty} = K_H \sqrt{t} \quad (\text{Equation I.3})$$

Where  $M(t)/M_\infty$ , the drug release fraction per unit surface area;  $K_H$ , the Higushi's constant depending on diffusion, tortuosity, concentration and porosity coefficients of the releasing matrix;  $t$ , the time.

Nevertheless, this model is limited. Indeed, the concentration in drug has to be larger than the solubility of the drug in the medium and the diffusion has to be unidirectional and constant.<sup>64</sup> Initially introduced for hydrogels, Peppas's model is based on a power law of exponent  $n$  describing the release, which is not obligatory a square root ( $n \neq 1/2$ ):<sup>64</sup>

$$\frac{M(t)}{M_\infty} = K t^n \quad (\text{Equation I.4})$$

Where  $M(t)$ , is the drug released at time  $t$ ;  $M_{\infty}$ , the final amount of drug released;  $K$ , a constant depending on the nanocarrier shape and geometry (cylinder, parallelepiped slab...);  $t$ , the time and  $n$ , an exponent depending on the release mechanism (obtained experimentally by the slope in a log-log representation).

Figure I.11 exhibits typical *in vitro* release profiles obtained for nanocarriers corresponding to one of the three mathematical models discussed above.<sup>66</sup>

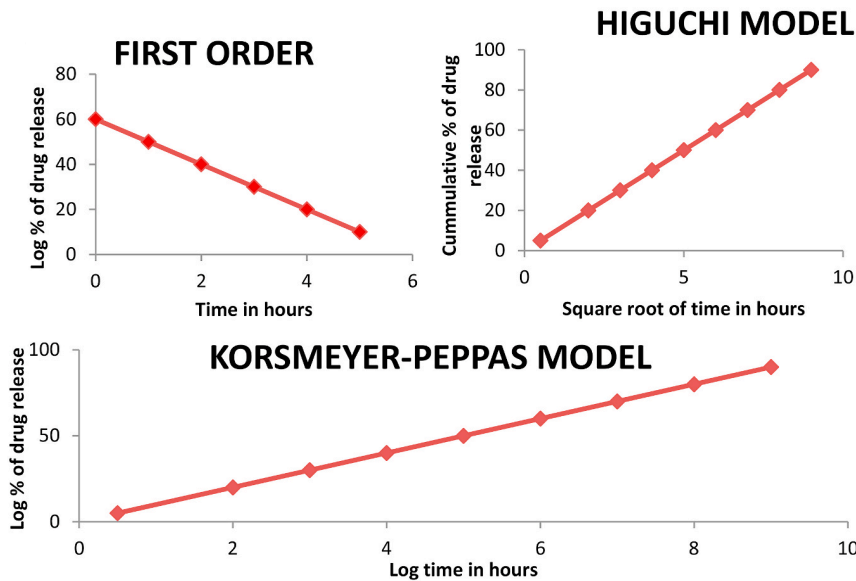


Figure I.11. Typical fitting obtained according to the used mathematical models.<sup>66</sup>

It is also important to keep in mind that a phenomenon called “burst release” can occur during the first minutes of release tests. This phenomenon can take place when the membrane is saturated in drug, leading to a high and rapid release. It happens also when the drug has a certain affinity for the membrane of the nanocarrier. It thus depends on the membrane thickness and the mobility of the drug in the layer. The opposite phenomenon is the “lag-time” that is induced by a totally drug-free layer. Drug will therefore need more time to pass through the layer and induce the UV-vis or chromatographic signal increase of the detection system. (Figure I.12)<sup>67</sup>

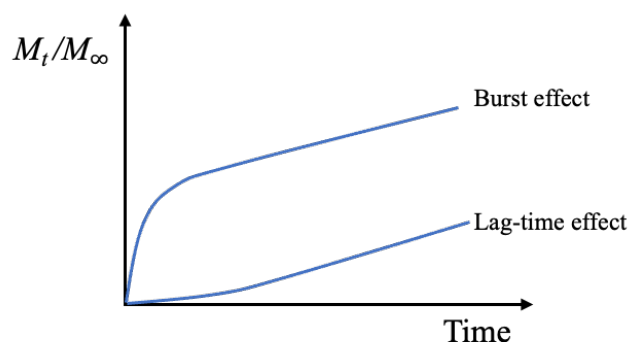


Figure I.12. Graphical representation of burst and lag-time effects derived from Siepmann *et al.*<sup>67</sup>

Those delivery mathematical laws can be applied to polymeric nanoparticles. To exemplify the type of results obtained after cumulative release assays, Brandt *et al.* developed micelles composed of PEG-*b*-PCL encapsulating methotrexate to evidence if the folic acid (FA) grafted onto the surface could influence its release. The cumulative release was performed in PBS 0.01M at 37°C to compare the release in presence or not of FA. The results were then plotted in a logarithmic scale and fitted with Peppas' model. FA-PEGMA-*b*-PCL exhibits a maximum release of 55% after 30 h while MPEG-*b*-PCL exhibits a maximum release of 42% after 80 h. This evidences that the release behavior is modified by the presence of FA. The release exponent ( $n$ ) and the kinetic factor ( $K$ ) extracted from the fitting of FA-PEGMA-*b*-PCL and MPEG-*b*-PCL give 0.57/0.243 and 0.75/0.0150 ( $n/K$ ) respectively. The obtained  $n$  value for FA-PEGMA-*b*-PCL and MPEG-*b*-PCL allows to affirm that the behavior is non-Fickian in the fitting region ( $n > 1/2$ ). This non-Fickian behavior evidences that the delivery is not due to the diffusion of the methotrexate but rather to a relaxation and/or degradation of PCL chains.<sup>68</sup>

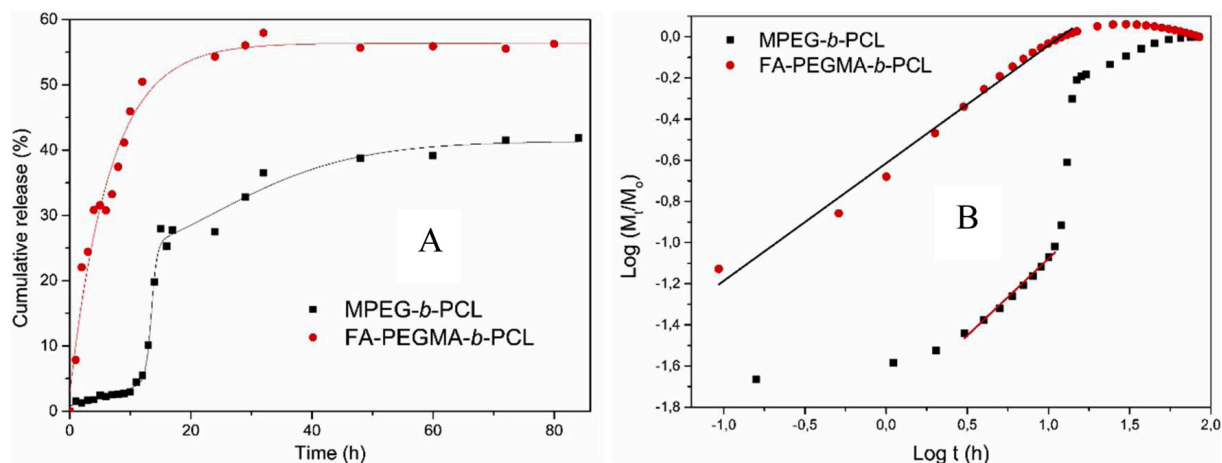


Figure I.13. Cumulative release assays for MPEG-*b*-PCL and FA-PEGMA-*b*-PCL (A) and their relative results with Peppas' mathematical model (B).<sup>68</sup>

In the previous sections, the different phenomena involved for drug delivery *in vivo* have been described and it is now necessary to understand how to guide the nanocarriers to the target, allowing specific drug delivery to the area of interest. The following section will therefore be dedicated to the description of the different possibilities for passive and active targeting.

#### 1.2.3.4 Passive and active targeting

*Passive targeting* takes place thanks to enhanced permeability and retention (EPR) effect. This effect is based on the abnormalities that appear in the tumor microenvironment. Indeed, tumors exhibit poor lymphatic drainage and vessels with a higher permeability than healthy vessels. These two points allow an accumulation of the nanostructures in the tumor site. Nevertheless, nanoparticles used in passive targeting have to stay in the bloodstream enough time to allow accumulation before opsonization, first step of their elimination by the RES.<sup>8,9,40</sup>

*Active targeting* is made possible thanks to the covalent grafting of a peptide, antibody fragment, sugar... or other type of moiety. This ligand will have a high affinity for a receptor present in the area of interest or at the surface of cancer cells allowing nanoparticles recognition and uptake. Moreover, the addition of a targeting ligand increases the specificity for tumor cells and thus further decreases the risk to reach healthy cells. (Figure I.14)<sup>8,9,40</sup>

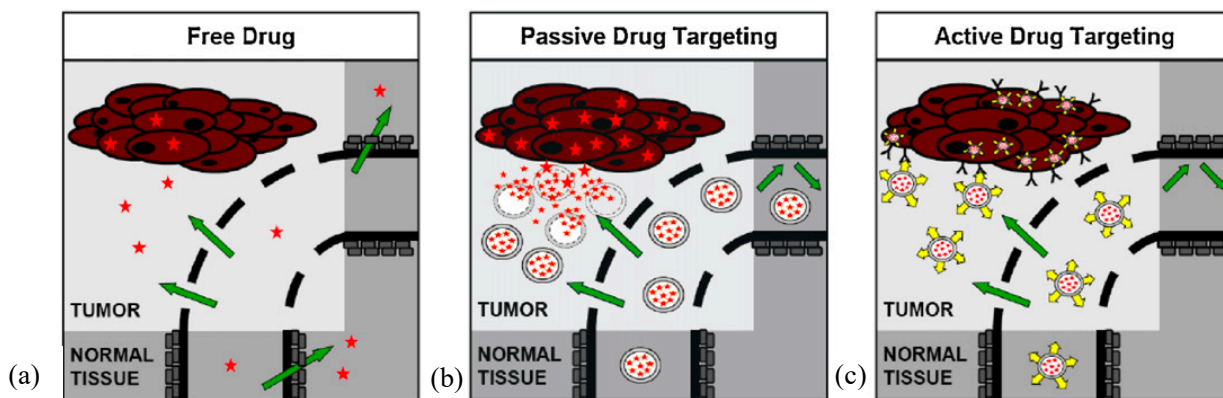


Figure I.14. Biodistribution of (a) drug, (b) nanocarriers by EPR effect, (c) nanocarriers with a targeting moiety.<sup>9</sup>

Nevertheless, each targeting method possess its advantages and disadvantages. Indeed, passive targeting isn't possible for all type of tumors because the microenvironment is different. The passivity of nanostructure can lead to accumulation in liver and spleen during the elimination way.<sup>40</sup> Moreover, high quantities of drug/nanocarrier have to be used to ensure a sufficient accumulation. On the other hand, active targeting needs modification of the copolymer to covalently bind a ligand. Those ligands, as peptides for example, can be expensive and are not valid for all tumors.

In the following section, we will focus on pH sensitive structures and more particularly on polyester moieties. Indeed, the development of polymeric nanocarriers is widespread around the world and, taking into account the versatile tunability of polymers, it leads each year to a very high number of publications. For example, if we search on SciFinder-n articles with the following keywords: “polymeric”, “nanostructures” and “cancer”, Sci-Finder exhibits 10k publications only during the year 2021.<sup>69</sup> Regarding this information, in the framework of this thesis, we will principally focus on polyester-based nanostructures.

It is important to note that polyester moieties as PLA and PCL have shown their biocompatibility. Indeed, PLA forms lactic acid over time during the degradation process, which is finally extracted from the body, as CO<sub>2</sub> or glucose and glycogen. PCL is eliminated by two principal ways: it is generating hydroxycaproic acid which is eliminated by the kidneys, and CO<sub>2</sub> which is exhaled.<sup>70,38</sup> The chemistry of the surface will also impact the way of elimination.<sup>71,38</sup> If non-degraded polymeric vesicles are reaching the blood stream, the NPs can use different ways of elimination in terms of surface, size and charge principally. The principal

way of elimination is the liver by the Kupffer cells and the macrophages, which are part of the reticuloendothelial system (RES).<sup>48</sup>

### I.3 Nanocarriers

#### I.3.1 Micelles

Micelles play a role of scavenger for hydrophobic drugs in the core of their nanostructure. Their formulations can differ in size and shape leading to formation of micelles from 10 to 100 nm. The circulation time in the bloodstream is due to the type of corona, that's to say the hydrophilic part of the diblock. In general, PEG moieties are used for hydrophilic corona. Thanks to their size and circulation time, these structures are good candidates for anti-cancer drug delivery. Micelles are formed in solution, when the critical micellar concentration (CMC) is reached in solution. For polymeric micelles, the CMC is usually low ( $10^{-6}$  to  $10^{-7}$  M) leading to stable nanostructures which keep this assembly *in vivo*.<sup>49,72,73</sup> This type of structure was the first used in 1984 to perform drug delivery with an anti-cancer drug.<sup>49</sup>

Based on PEG-1,2-bis(2-hydroxyethylthio) ethylene-PLA (PEG-BHETE-PLA), Dariva *et al.* determined a CMC of  $2.63 \times 10^{-2}$  g/L which increases to  $5.57 \times 10^{-2}$  g/L in the presence of Nile red. The particularity of those nanostructures is the presence of BHETE links that are breakable with ROS species induced by irradiation of encapsulated Chlorine e6 (Ce6). The authors demonstrate a release of the co-encapsulated doxorubicin under light irradiation depending on the  $M_n$  of PLA chains: PLA<sub>1k</sub> exhibited the same release profile than control (control was performed without light irradiation) whereas of PLA<sub>5k</sub> evidenced a significant difference in the release profile. (Figure I.15)<sup>74</sup>

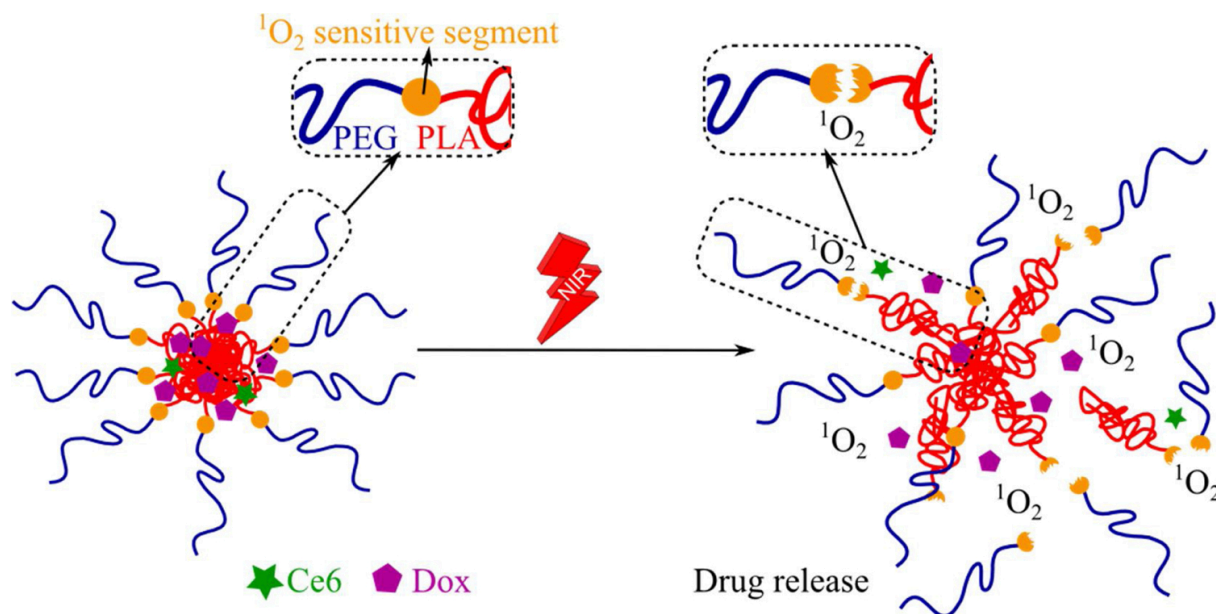


Figure I.15. Representation of the system developed by Dariva *et al.* based on PEG-BHETE-PLA encapsulating Ce6 and doxorubicin for which ROS species induced by NIR irradiation can break BHETE links.<sup>74</sup>

As discussed previously, the chemical modification of polymers leading to the formation of micelles by self-assembly allows an active targeting. For instance, Hu *et al.* developed micelles, based on MPEG-PCL, containing a curcumin treatment to treat colorectal cancers. They modified the copolymer by grafting folate which has a high affinity for FA receptors present on tumor cell surface. Their resulting micelles have a size of  $30.5 \pm 0.65$  nm with a PDI of 0.17. The resulting curcumin concentration in plasma evidences the interest of its encapsulation in micelles since its concentration became higher over time than that of free curcumin. Results also evidenced an increased therapeutic effect compared to free curcumin, with a decrease in tumor proliferation.<sup>75</sup>

Nevertheless, due to their size, micelles are not able to encapsulate high amounts of drug and lead to a fast release that can occur before reaching the target.<sup>72</sup>

### I.3.2 Polymersomes

To palliate to micelles issues, polymeric vesicles (*i.e.* polymersomes) were developed. Their synthetic way allows to tune a lot of parameters as the type of stimuli responsiveness, the thickness of the membrane, the permeability, the size, etc. This gives access to a very wide applications panel. Moreover, these structures have proved their stability and a long blood circulation time by the introduction of specific polymers, such as PEG moiety. These structures

have the capacity to encapsulate a lot of hydrophobic drugs in their hydrophobic bilayer and hydrophilic drugs in their hydrophilic core highlighting their high versatility.

The formation of polymersomes takes place according to two supposed mechanisms. Both mechanisms start with the formation of micelles induced by the presence of amphiphilic moieties in solution. The first mechanism represents an expansion of micelles, leading first to the formation of a growing bilayer, and finally to the formation of vesicles induced by the surface tension. The second mechanism leads to vesicles by the fusion of growing micelles induced by the recombination of the domains with the same affinity for the medium. The preferred mechanism will depend on the polymer and solvent properties. (Figure I.16)<sup>50</sup>

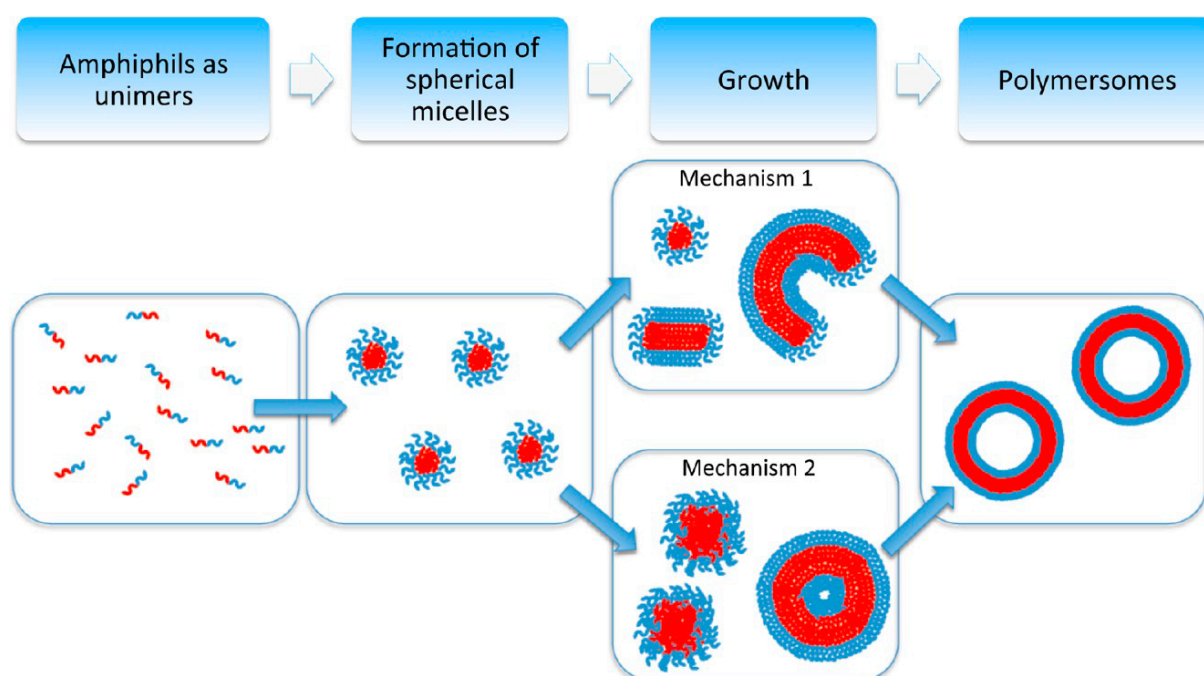


Figure I.16. Two mechanisms leading to the formation of polymersomes.<sup>50</sup> Reprinted with permission from Bleul *et al.* Techniques To Control Polymersome Size. *Macromolecules* **2015**, 48 (20), 7396–7409. Copyright © 2015 American Chemical Society.

Different methods can be used to form polymersomes that will be described in the following section. There are basically two types of techniques: solvent-free and solvent-assisted methods.

*Nanoprecipitation* is a technique introduced 25 years ago in pharmaceutical sciences, that can be easily scaled up.<sup>76</sup> It consists in solubilization under stirring of the copolymer in an organic solvent that is miscible to the aqueous media. This method is similar to a solvent switch

since the organic solvent, the initial major constituent of the solution, will become the minor constituent after addition of the aqueous medium. If a drug needs to be encapsulated, it is placed in the organic phase or in the aqueous medium, depending on its polarity. The organic phase can then be eliminated with different techniques as natural evaporation, dialysis, or evaporation under reduced pressure. A lot of parameters will modify the size of the polymersomes or the drug encapsulation rate such as the ratio between the two solvents, the polymer concentration, the stirring rate, the drug concentration, the flow rate, etc.<sup>41,77</sup> Adams *et al.* determined the degree of polymerization (DP) needed for PEO and PCL to lead to the formation of vesicles : using different DP values of both chains, they showed that  $f_{\text{hydrophilic}}$  needs to be in the 15-23% range. To form the nanostructures, they added water at different rates in a solution of 10 mg/mL in copolymer solubilized in THF. Formation of vesicles takes place by the same steps than those evidenced by Choucair and Eisenberg (PS-*b*-PAA).<sup>78</sup> When the addition of water is started, the micelle formation first comes from a supersaturation of the chains in the non-solvent domain during its addition. This thermodynamical instability is then compensated by the solute molecule association called nucleation. Nucleation takes place until the system passes below the critical supersaturation concentration. The step of nucleation is then followed by the addition on nuclei of other molecules leading to the growth of the nuclei. This step is called condensation. This phenomenon takes place until the concentration in solute becomes below the equilibrium saturation concentration. Finally, coagulation occurs between different nuclei that aggregate to form the nanostructures. (Figure I.17)<sup>79</sup> This mechanism is not only putative, as more and more studies are published on the deciphering of the polymersome formation steps, in particular using environmental electron microscopy technique.<sup>80</sup>

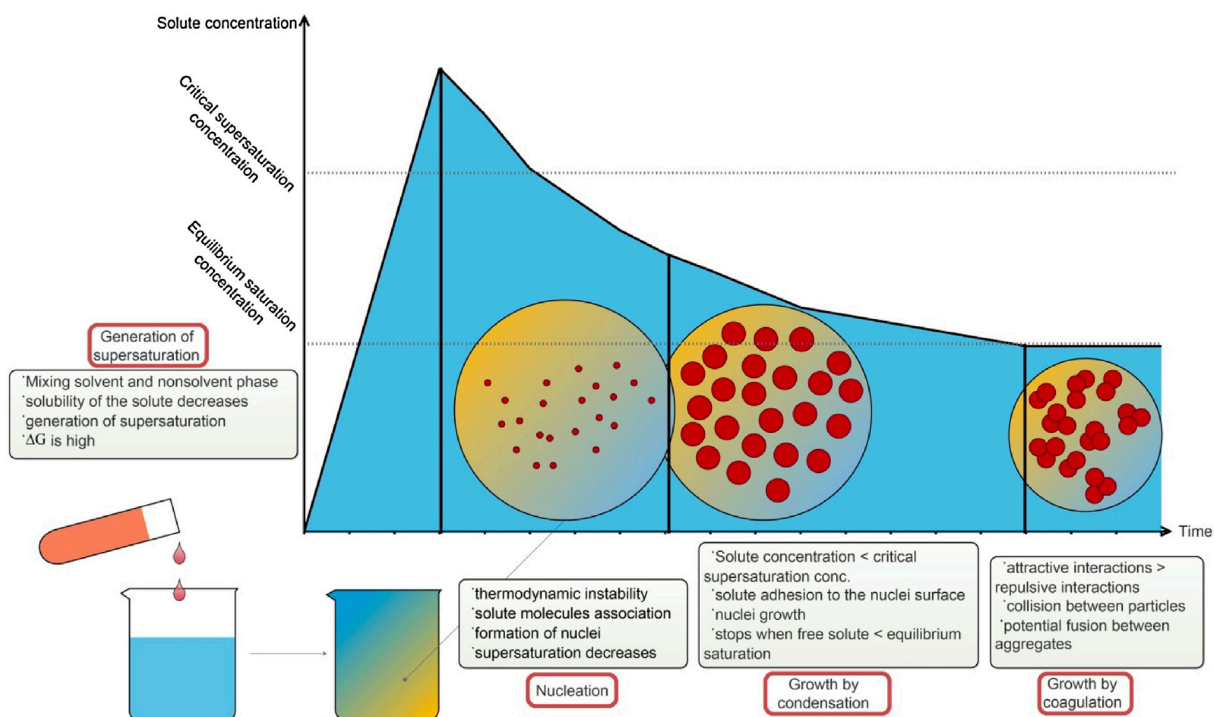


Figure I.17. Schematic way to obtain vesicles by nanoprecipitation in the presence of a non-solvent.<sup>79</sup>

*Thin film rehydration* technique basically starts by the formation of a film on a round bottom flask walls after the solubilization of the copolymer in a volatile organic solvent which is eliminated under reduced pressure. This film is then rehydrated by an aqueous medium.<sup>45,77</sup>

Rehydration under stirring induces swelling of the film followed by the budding of nanostructures. Nevertheless, this technique leads to the formation of “onion-like” (*i.e.* multi-lamellar) structures exhibiting a broad distribution of sizes. It can be used for the formation of either such multilayered vesicles or of small unilamellar vesicles (SUV), after sonication.<sup>36</sup>

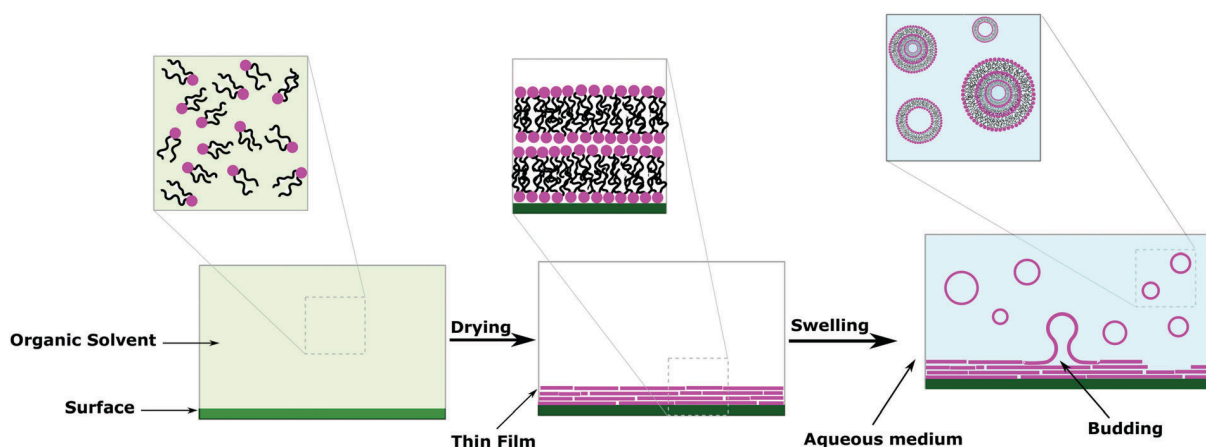


Figure I.18. Formation of polymersomes following the thin film rehydration method.<sup>36</sup>

Sui *et al.* evidenced the differences in the obtained nanostructures using the same copolymer with the two different preparation methods, nanoprecipitation and thin film rehydration. They evidenced that, with the thin film, polymersomes could only be obtained with a hydrophilic fraction of the copolymer of 19%. A higher  $f_{\text{hydrophilic}}$  of 32% leads to micelles.<sup>81</sup>

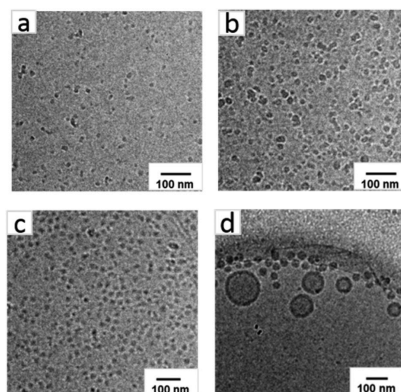


Figure I.19. Cryo-TEM of self-assembly nanostructure using different techniques: nanoprecipitation (a) PEG-2k-*b*-PCL<sub>4.3k</sub> (b) PEG<sub>2k</sub>-*b*-PCL<sub>8.5k</sub> and thin film (c) PEG-2k-*b*-PCL<sub>4.3k</sub> (d) PEG<sub>2k</sub>-*b*-PCL<sub>8.5k</sub>.<sup>81</sup>

*Polymerization induced self-assembly* (PISA) is based on a direct polymerization of the soluble chain in the solvent followed by the copolymerization of the insoluble chain, leading to a simultaneous formation of nanostructures. In most cases, RAFT polymerization is used to form the copolymer. The DP will increase until reaching the CMC leading to the formation of the nanostructures. Their morphology will depend on DP of both chains. For instance, with poly(glycerol monomethacrylate)-block-poly(2-hydroxypropyl methacrylate) (PGMA-*b*-PHPMA) where PGMA is the soluble chain in aqueous media, Blanazs *et al.* evidenced the DP of both chains needed to reach the desired nanostructure (Figure I.20 (b)) and the fact that polymer concentration in solution also impact the nanostructuration. (Figure I.20 (c)) Moreover, contrarily to the other techniques, this method can be performed at high polymer concentration, which can impact the structure of the nanoplateforms. (Figure I.20)<sup>45,46,82,83</sup>

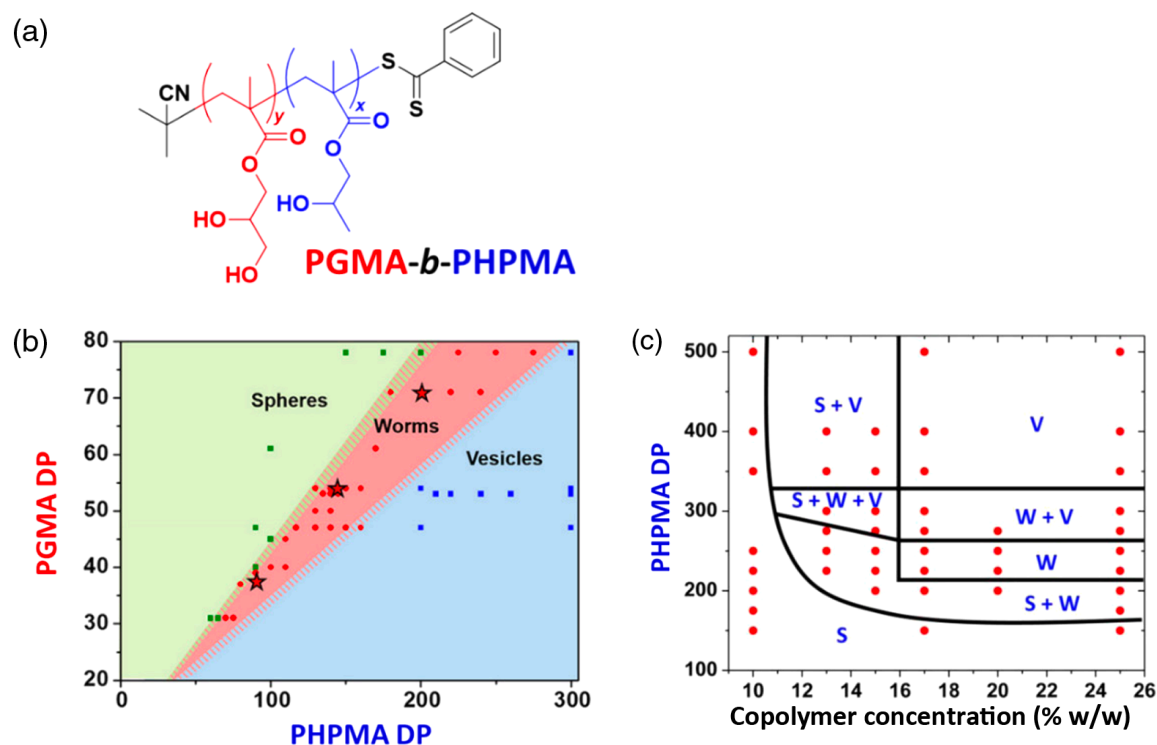


Figure I.20. (a) structure of the PGMA-*b*-PHPMA and phase diagram of PGMA-*b*-PHPMA leading to the formation of sphere (S), worms (W) or (vesicles) (b) as a function of the DP of both chains or (c) PHPMA DP as a function of the polymer concentration in solution.<sup>82</sup> Reprinted with permission from Blanz *et al.* Predictive Phase Diagrams for RAFT Aqueous Dispersion Polymerization: Effect of Block Copolymer Composition, Molecular Weight, and Copolymer Concentration. *Macromolecules* **2012**, 45 (12), 5099–5107. Copyright 2012 American Chemical Society.

*Microfluidic* devices are based on 2 pumps controlling either the flow rate (syringe-pump) or the pressure (air pump, pressurizing a vial) that delivers on the one side the organic phase solubilizing the copolymer and on the other side the aqueous medium. (Figure I.21) The principle consists in controlling exactly (in a reproducible manner) the mixing time necessary to reach homogeneous mixture of the two solutions, determined by the total flow rate and by the dimensions of the channel. Another type of chip enables formation of a double emulsion: The first emulsion produced by the first injection is reinjected in a second tube with a second water channel leading to the formation of the double emulsion. This method allows to encapsulate hydrophobic, hydrophilic or both types of drugs.<sup>45,77,84</sup> This technique takes place in chips which are different as a function of the desired application, for example to produce either micelles or vesicles in a continuous flow. As explained and demonstrated by Lebleu *et al.* microfluidics is a powerful technique to control the size of both types of nanostructures with a low size dispersity. They used poly(ethylene glycol)-*b*-poly(trimethylene carbonate) (PEG-*b*-PTMC) where they varied the length of the PTMC chains to tune the membrane thickness. Their controlled nanoprecipitation by microfluidic device evidenced that the resulting structures are

depending on the hydrophilic fraction, the best yield in vesicles being found with  $f \approx 17\%$ . In this device, the size is controlled by modifying different parameters such as total flow rate, ratio of water to solvent flow rates, and copolymer concentration, and they found the best parameters to obtain monodisperse samples with a size of  $d_h \approx 100$  nm (hydrodynamic diameter).<sup>85</sup>

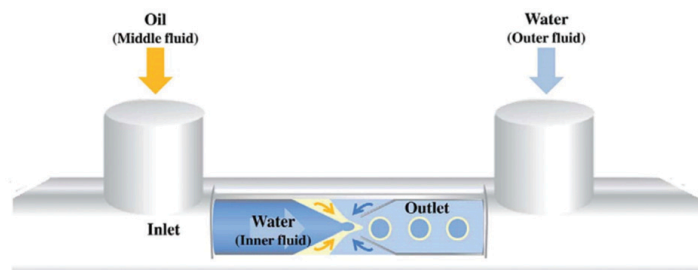


Figure I.21. Co-axial flow microfluidic device leading to the formation of vesicles through double-emulsion formation.<sup>45</sup>

Other alternative techniques as direct hydration, electroformation and emulsion can also be used. Briefly, direct hydration consists in a direct addition of the aqueous medium on the copolymer. Electroformation is also a free organic solvent method where the polymer is deposited on an electrode followed by the application of an alternating voltage in the aqueous medium leading to the formation of vesicles. Finally, emulsion is governed by the addition of drops of non-miscible organic solution of the copolymer (in *e.g.* in toluene or mineral oil) into an aqueous medium until a water-in-oil-in-water emulsion is obtained, before adding it on top of another aqueous phase, with the appropriate amphiphilic copolymer (usually PBut-*b*-PEO). The crossing of the interface by the W/O leads to the formation of a double emulsion W/O/W, which eventually forms vesicles when the solvent is eliminated by evaporation or another mean, although this final step can sometimes be tricky.<sup>45,77,86</sup>

### I.3.3 Characterization techniques

First, the constituting copolymer needs to be characterized by well-known molecular techniques such as NMR and mass spectroscopies, size exclusion chromatography (SEC) with either polystyrene calibration or with absolute determination of the molar mass, using multi-angle light scattering (MALS) detection (please note that for the MALS analysis, even simple copolymers need to determine beforehand the refractive index increment  $dn/dc$ , as it differs from the one of each block). To evidence the crystallinity rate and melting temperature of the

copolymer that could impact their self-assembly and the diffusion of drug as discussed above, thermal characterizations can be performed such as thermogravimetry analysis (TGA) and differential scanning calorimetry (DSC).

Then the resulting nanoobjects can first be characterized by light scattering techniques. The basic lab tool used to determine the size of self-assembled nanoobjects in suspension is dynamic light scattering (DLS), giving access to the diffusion coefficient allowing to extract the hydrodynamic radius ( $R_h$ ) based on Stokes-Einstein equation. Combined to the static light scattering (SLS) that gives access to the gyration radius ( $R_g$ ), the shape ratio  $R_g/R_h$  can be extracted, giving indications on the nanostructure morphology (spheres, cylinders, vesicles...). Nevertheless, this technique necessitates a monodisperse sample to have access to the correct ratio. Indeed, a ratio of 1 highlights formation of vesicles whereas micelles have a ratio of 0.775. The second more common technique is based on X-rays interaction with the dispersed matter. Small angle X-rays scattering (SAXS) will give access to the size of the nanostructure and the thickness of the membrane of the polymersomes. More precisely, a highly collimated (*i.e.* parallel) and monochromatic X-rays beam is shined through the sample, and the scattering pattern (*i.e.* the deviated flux of photons) is collected by a CCD camera, located at long distance (usually around ~2-3 m) of the sample, therefore at a small angle compared to the direct beam. The intensity in the “Fourier space” can be angularly averaged and plotted versus the scattering vector,  $q$  (in  $\text{\AA}^{-1}$  units). Each point of the curve of scattering intensity  $I(q)$  corresponds to a probed length scale  $d \sim \pi/q$ , typically in the range from 1 to 500  $\text{\AA}$ . The information on the spatial features of the particles (*e.g.* the shell thickness) can be extracted based on different models which calculate the “form factor”  $P(q)$  of simple geometric shapes (spheres, rods, shells...). Small angle neutron scattering (SANS), which allows to evidence the conformation of chains and the membrane thickness is based on the same principle than SAXS. The main difference is that in this case a neutron beam is used instead of X-rays, resulting in a different contrast: in SAXS, it is determined by the number of electrons in the atoms constituting the scattering molecules, whereas in SANS it results from the composition of nuclei (carbon, hydrogen, deuterium, oxygen...), in both cases by comparison with the solvent. Therefore in SANS one can use different mixtures of  $\text{H}_2\text{O}$  and  $\text{D}_2\text{O}$  to adjust the contrast on either the hydrophilic or the hydrophobic block, whereas SAXS “sees” the globality of the copolymer chains. Another tool particularly relevant to study polydisperse samples is asymmetric flow field flow fractionation (AF4) combined to MALS detector. This chromatographic technique does not use any stationary phase, as it is based on natural separation of different populations of particles

moving in a laminar flow of eluant having a parabolic flow, crossed by a perpendicular flow. The detection by MALS at the end of the flow cell gives access to  $R_g$  and  $R_h$  of the fractions, which have been separated according to their hydrodynamic size, hence they are monodisperse. Further, microscopy techniques can also be used as transmission electron microscopy (TEM). This technique is based on the transmission of electrons coming from an electron beam through the matter, therefore it is limited to very thin samples (less than 100 nm). In practice, the suspension is deposited onto a thin carbon layer (around 10 nm thick) covering square holes of a copper grid. However, this technique requires in general the staining of the specimen to increase the contrast of the organic polymer due to the need of heavy elements to interact with electrons. Moreover, an electron microscope needs high vacuum conditions incompatible with solvent, which usually leads to the deformation of nanoobjects and other drying artifacts. To palliate to these issues, cryo-TEM is based on the same technique but in aqueous medium where a thin layer of the sample (also ~100 nm) on the grid is vitrified to avoid the presence of ice crystals. Another microscopy technique is atomic force microscopy (AFM), which is basically based on an atom-sized tip that either stays at constant height above the sample (contact mode) or hits the sample periodically (tapping mode). Measuring a laser deflection of the cantilever while scanning the tip over the sample leads to surface cartography and can also give access to the rigidity (Young's modulus) of the nanoobjects (from the analysis of the phase signal).

Finally, drug delivery systems (DDS) are characterized by the drug loading content (DLC) that represents the mass of drug divided by the total mass of the system (drug + carrier) and the drug encapsulation efficiency (DEE) that represents the fraction mass of drug retained relatively to the mass engaged at the beginning of the formulation step. After that, the law followed by the system to release drug and/or dyes can be determined by cumulative release assays in a continuous flow under different conditions as temperature, pH, and so on, whereby drug/dyes release can be followed for example by UV-Vis or HPLC (for non-absorbing drugs).

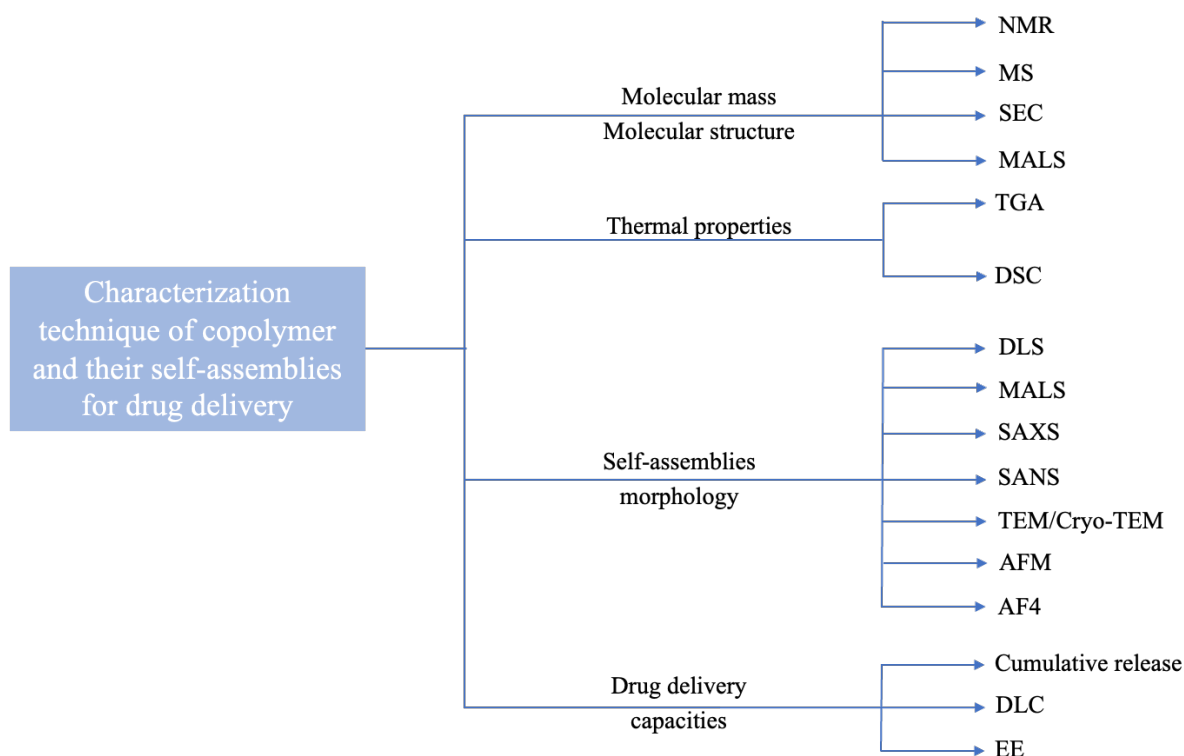


Figure I.22. Representative diagram for the system characterization. NMR: nucleic magnetic resonance; MS: mass spectrometry; SEC: size exclusion chromatography; MALS: multi-angle light scattering; TGA: thermogravimetric analysis; DSC: differential scanning calorimetry; DLS: dynamic light scattering; SAXS: small angle x-rays scattering; SANS: small angle neutron scattering; TEM/Cryo-TEM: transmission electron microscopy; AFM: Atomic force microscopy; AF4: asymmetric flow field flow fractionation; DLC: drug loading content; EE: encapsulation efficiency. Inspired from Behl *et al.*<sup>66</sup>

## I.4 Theranostic nanocarriers in cancer treatments

An emerging tool arising in the nanoparticles field is the theranostic nanocarrier system. This allows to merge diagnosis and treatment in the same object. Indeed, the tunability of nanocarriers makes them good candidates to be functionalized for both drug delivery and imaging. Theranostic allows to perform guided drug delivery, to evidence the drug delivery induced by internal stimuli, to evaluate the efficiency on tumor treatment, the clearance of the nanostructures, or the morphological and biochemical structure of the targeted tissues.<sup>87,88</sup>

The next section describes the different imaging techniques that can be used for theranostic, illustrated with different examples.

## I.4.1 Magnetic resonance imaging (MRI)

Magnetic resonance imaging (MRI) is a powerful non-invasive bio-imaging technique daily used in the medical field due to its high spatial resolution. MRI is essentially based on water protons nuclear magnetic resonance, due to its high abundance in the body, but also in other components of tissues (fats, proteins...). Nuclei can be associated to a microscopic magnet, and can be described and quantified by the magnetic dipolar moment ( $\vec{\mu}$ ):

$$\vec{\mu} = \hbar \gamma \vec{I} \quad (\text{Equation 1.5})$$

$\hbar$ , Plank constant;  $\gamma$ , gyromagnetic factor of the nucleus;  $\vec{I}$ , nuclear spin

Once an external magnetic field,  $B_0$ , is applied, all magnetic dipolar moments get a precession motion (*i.e.* a rotation around its axis) at the so-called Larmor frequency ( $\omega_0$ ) defined as:

$$\nu_0 = \frac{\gamma}{2\pi} B_0 \quad (\text{Equation 1.6})$$

(*i.e.* at angular frequency:  $\omega_0 = \gamma B_0$  (rad/s), where  $\omega_0 = 2\pi \nu_0$ )

with  $B_0$ , magnetic field strength.

This results from the interaction of  $B_0$  with the nuclear magnetic moment,  $\vec{\mu}$ , which causes the splitting in two energy levels of the proton spin states. The lower energy level corresponds to spins parallel to the magnetic field (spins up), whereas the higher energy level corresponds to spins anti-parallel to the magnetic field (spins down). (Figure I.23)

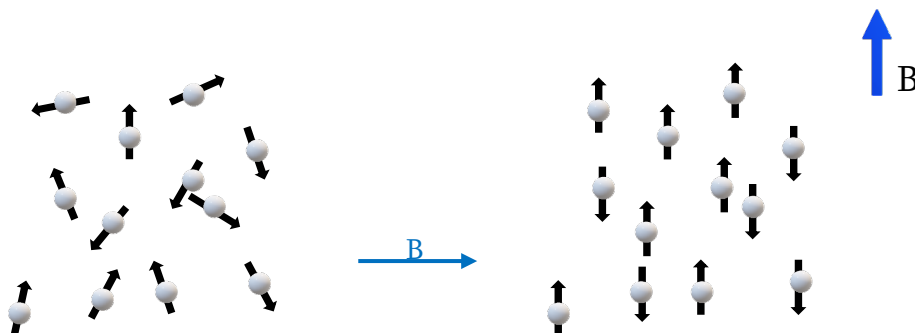


Figure I.23. Orientation of spins up and down after the application of a static magnetic field ( $B_0$ ).

This slight unbalance between spin populations up and down results in a net magnetization called macroscopic magnetization ( $\vec{M}_0$ ), having the same orientation than  $B_0$  (that will be set along the  $Z$  axis). An NMR experience consists in tilting  $M_0$  away from the  $Z$  axis due to the application of a perpendicular oscillating electromagnetic field ( $B_1$ ) (radiofrequency pulse), inducing precession around the perpendicular axis at the angular velocity  $\omega_1 = \gamma B_1$ . After having switched off  $B_1$ , the return to equilibrium occurs according to two mechanisms: longitudinal relaxation (characteristic time  $T_1$ ) and transversal relaxation (characteristic time  $T_2$ ).  $T_1$ , also called spin-lattice relaxation time, reflects the equilibrium return of the longitudinal magnetization  $M_Z$ , and corresponds to the time needed for  $M_Z$  to reach  $1 - e^{-1} \sim 2/3$  of its equilibrium value after a  $90^\circ$  RF pulse.  $T_2$ , also called, spin-spin relaxation, represents the loss of coherence in the  $XY$  plan. It describes the time needed for  $M_{XY}$  to lose  $e^{-1} \sim 2/3$  of its initial value. (Figure I.24)

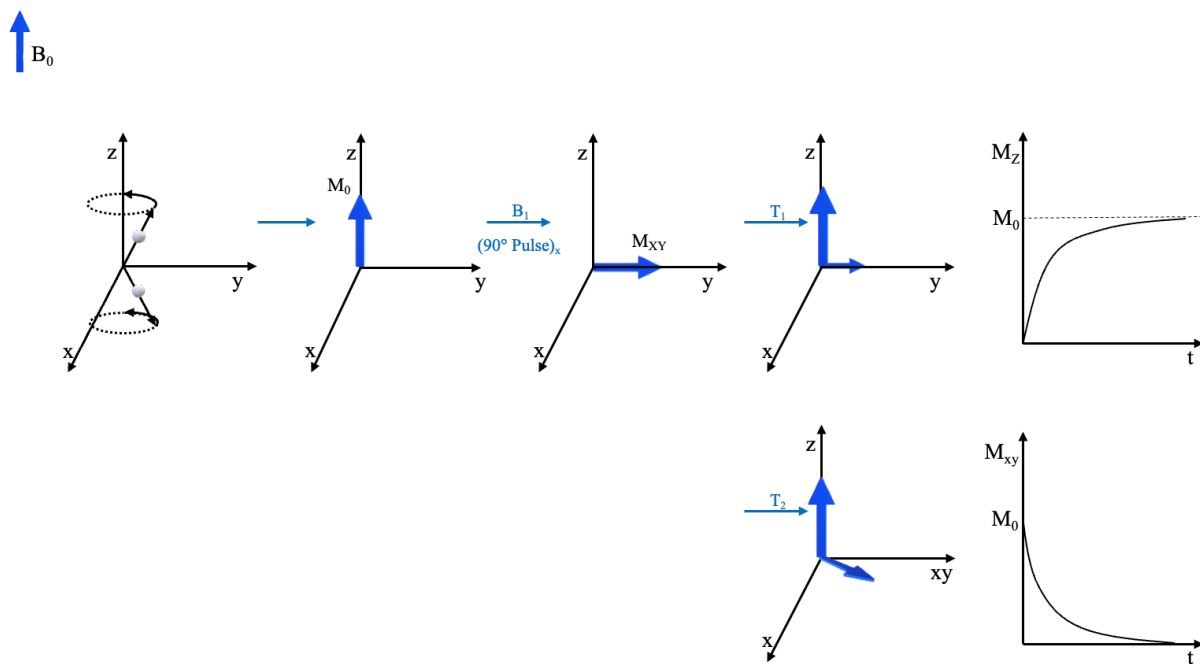


Figure I.24. Spins that are in precession movement around the  $z$  and  $-z$  axes show unbalance of their population respectively up and down, resulting in a net magnetization called macroscopic magnetization,  $M_0$ . A  $90^\circ$  RF pulse applied on the  $x$  axis ( $B_1$  along the  $x$  axis) tilts the magnetization towards the  $y$  axis. The return to equilibrium of the population of spins then occurs according to longitudinal and transverse relaxation, characterized by  $T_1$  and  $T_2$  relaxation times, respectively.

To obtain MR images, the first step is to select the slice of interest according to sagittal, axial or coronal slices depending on the  $x$ ,  $z$  or  $y$  axis, respectively. The slice is selected by applying a linear magnetic field gradient simultaneously to a selective RF pulse to excite the

spins. (Figure I.25). The spatial encoding of the spins in the selected slice is performed by using two different gradients. The  $x$  gradient, as frequency encoding, is applied simultaneously to the registering of the signal, allowing to encode the spins position along the  $x$  axis directly in the free induction decay (FID) signal. The  $y$  gradient, as phase encoding, is applied after the RF pulse and allows to encode the position of the spins along the  $y$  axes as a phase shift of the magnetization vectors. (Figure I.26) This encoding then allows to reconstruct the images.<sup>89</sup>

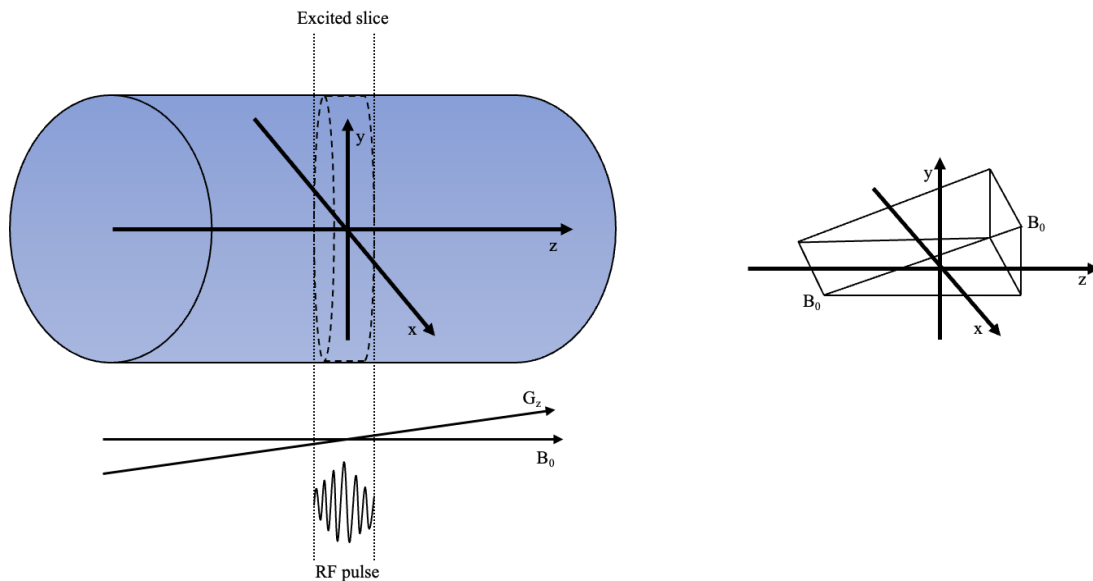


Figure I.25. Excitation of a slice in the static magnetic field  $B_0$  induced by a RF pulse applied simultaneously with a  $G_z$  magnetic field gradient. Inspired from Roth *et al.*<sup>89</sup>

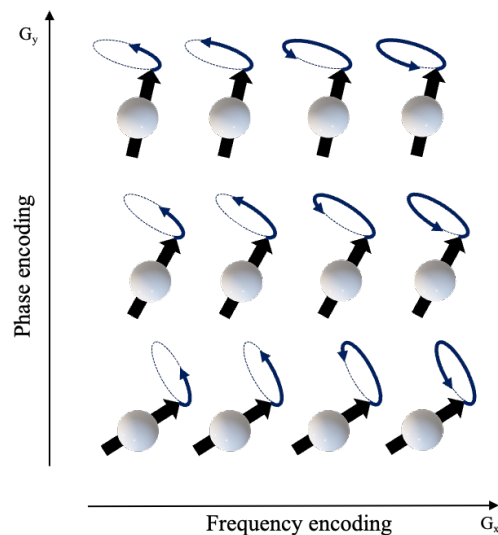


Figure I.26. Phase encoding of the spins by  $G_y$  magnetic field gradient along  $y$  axis and frequency encoding by  $G_x$  magnetic field gradient along  $x$  axis. Inspired from Roth *et al.*<sup>89</sup>

However, due to the low sensitivity of MRI, the natural contrast is not always sufficient, so that contrast agents (CAs) must be used. Those contrast agents will decrease the water proton relaxation times and can be divided in two categories: paramagnetic or  $T_1$  or “positive CAs” and superparamagnetic or  $T_2$  or “negative CAs”. The  $T_2$  agents, mainly based on superparamagnetic iron oxide nanoparticles (SPIONs), preferentially decrease the  $T_2$  relaxation time of the water protons, inducing a darkening of the area of accumulation on the images. For this reason, they are nowadays not used anymore by radiologists but are still the object of many research studies around the world. The development of very small iron oxides nanoparticles (VSIONs) is promising as they could be used as  $T_1$  agents.  $T_1$  CAs decrease the  $T_1$  relaxation time of the neighboring water protons, enlightening the area of accumulation on the images.

In this framework, we will focus on  $T_1$  contrast agents rather than  $T_2$  agents. The first contrast agent used and approved in MRI is based on a gadolinium complex. Indeed, gadolinium ions  $Gd^{3+}$  were chosen thanks to their paramagnetic state ( $S=7/2$  spin), and hence their high capacity to modify the water proton relaxation times. The first gadolinium complex developed and commercialized was the Gd-DTPA (Magnevist<sup>®</sup>) followed few years after by the first Gd-complex based on a macrocycle, gadoteridol (ProHance<sup>®</sup>). Nevertheless, at the end of the 20<sup>th</sup> century, Cowper *et al.* published and evidenced the first reporting information of the relation between the multiple injections of gadolinium-based contrast agents (GBCAs) and nephrogenic systemic fibrosis (NSF) in patients suffering from chronic kidney disease.<sup>90–92</sup> To respond to that issue coming from the first GBCAs, the last developed and the most used  $T_1$  contrast agent in clinic is Gd-DOTA (Dotarem<sup>®</sup>), that is based on macrocyclic 1,4,7,10-Tetraazacyclododecane-1,4,7,10-tetraacetate gadolinium complex (Gd-DOTA).<sup>93</sup> Researches are continually in development to increase the efficacy of GBCAs in order to avoid to increase the Gd-complexes injected doses. Therefore, the last developed Gd-complex is based on the PCTA structure and is called Gadopiclenol (Elucirem<sup>®</sup>) which was approved by the FDA in 2021. This structure allows the presence of 2 water molecules in the inner sphere which will increase the relaxivity.<sup>94–96</sup> (The theoretical explanation will be given in **Chapter II**) Nevertheless, it is important to keep in mind that recent studies have evidenced the presence in brain of gadolinium species with an higher rate of accumulation in the case of linear complexes instead of macrocyclic ones, even in patients with no kidney disease.<sup>94,97,98</sup> In view of the Gd-complexes issues, the researchers are continually developing alternatives with an equal or higher efficiency. (Figure I.27)

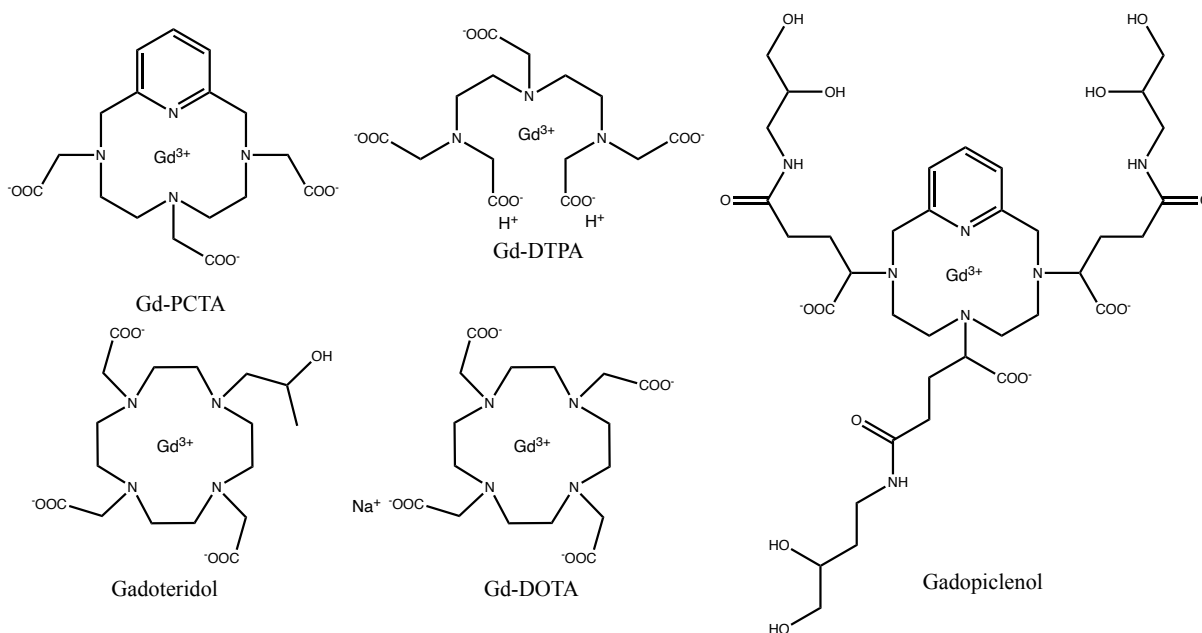


Figure I.27. Gadolinium complexes described as  $T_1$  contrast agents.<sup>90-96</sup>

Moreover, both  $T_1$  and  $T_2$  agents were incorporated in polymeric vesicles to obtain theranostic nanovectors. As examples, Babaei *et al.*<sup>99</sup> have synthesized, by double emulsion, polymersomes constituted of polycaprolactone-poly(glyceryl methacrylate) synthesized by ROP, and containing Doxorubicin and a manganese complex made of 1,10-phenantroline ( $\text{Mn}(\text{Phen})_2\text{Cl}_2$ ), as  $T_1$  MRI contrast agent in order to treat colon adenocarcinoma.  $\text{Mn}(\text{Phen})_2\text{Cl}_2$  is loaded in the membrane due to its hydrophobicity whereas doxorubicin is present in the aqueous core of the vesicles. In order to increase the doxorubicin release of 40 % during the first 24 hours on the tumor site, estimated at pH 5.4, they grafted an aptamer, AS1411, capable to bind the nucleoli receptor overexpressed on certain tumoral cells. Based on the same stimulus, Xie *et al.* developed micelles constituted of Gd-DTPA-PEG-*b*-PCL and poly(ethylene imine)-polycaprolactone (PEI-*b*-PCL). In their case, treatment is brought by two molecules: doxorubicin as chemotherapy and microRNA-34a as tumor suppressor in breast cancer. Micelles in this case can deliver hydrophobic treatments induced by the acidic pH of endosomes. Their area of accumulation was enhanced on MR images thank to the presence of Gd-DTPA. Results evidence better rate of penetration and better efficacy towards cancer cells for hybrid micelles as compared to free doxorubicin and increased expression of miRNA-34a. (Figure I.28)<sup>100</sup>

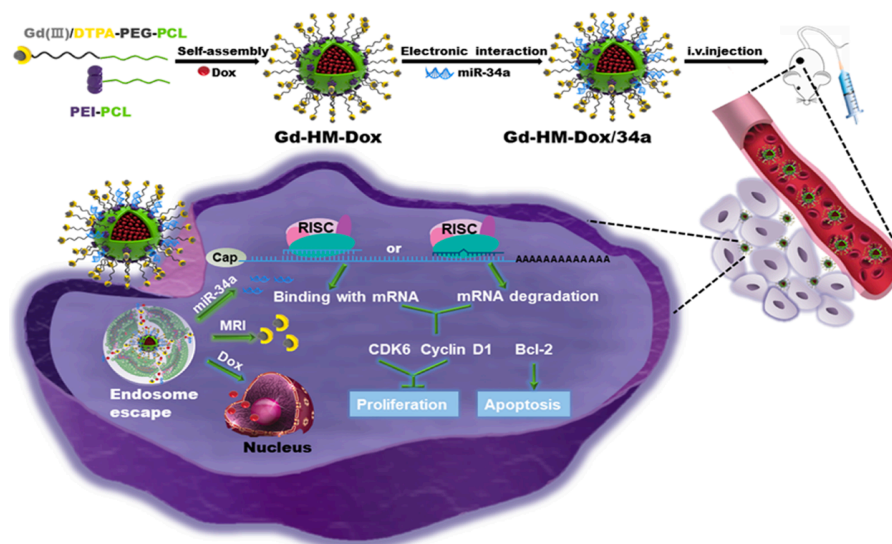


Figure I.28. Synthetic way for Gd-HM-Dox/34a followed by the passive targeting of tumoral cells and the action of the different components after the degradation of vesicles by the endosomes.<sup>100</sup>

Lui *et al.*<sup>101</sup> have investigated the use of ultrasmall superparamagnetic iron oxide particles (USPIONs) as  $T_1$  agents, encapsulated in polymer vesicles composed of cleavable poly(ethylene glycol)-poly(propylene sulfide-SS-poly(ethylene glycol), PEG-PPS-SS-PEG. The  $T_1$  and  $T_2$  effects of the USPIONs were decreased due to the confinement in the nanoparticles which limits the exchange of the water molecules with the environment. During the degradation of the vesicles, the water could again diffuse in the vicinity of the particles, leading to an increased  $T_1$  effect and thus an enlightenment of the area of accumulation. The degradation was induced by glutathione (GSH) activity cleaving the S-S bonds and thus the PEG chains, which was proven by a negative control in the presence of *L*-buthionine sulphoximine (BSO), an inhibitor of the gamma-glutamylcystein synthesis leading to a decrease of GSH expression.

An increased  $T_2$  effect was also investigated by Liu *et al.*<sup>102</sup> by the incorporation of SPIONs in polymersomes made of folic acid-poly(*L*-glutamic acid)-*b*-poly( $\epsilon$ -caprolactone) (FA-PGA-*b*-PCL). The SPIONs were generated *in situ* in the hydrophilic PGA corona of the polymersomes. Briefly, the polymersomes were obtained in the presence of H<sub>2</sub>O/DMF followed by addition of a NaOH solution leading to the coprecipitation reaction of the Fe<sup>2+</sup>/Fe<sup>3+</sup> ions in interaction with the PGA corona. The  $r_2$  obtained is 611.6 mM<sup>-1</sup>s<sup>-1</sup> at 60 MHz and 37°C leading to a decrease of the iron concentration to inject. This extremely high  $r_2$  value can be explained by two parameters: the increase of the diameter of the SPIONs, their clustered state, and the decrease of the water diffusion coefficient in the vicinity of the particles. The authors also

showed the importance of the presence of the FA to target the tumors. Indeed, the presence of FA led to an increase of the efficiency of drug delivery at the target due to the binding with FA receptors on the surface of the tumors. Doxorubicin was loaded by a passive technique in the polymersomes, which showed a higher drug efficacy than that of free doxorubicin.

To palliate to the lack in sensitivity of MRI, another alternative is to couple MRI with a more sensitive technique such as optical fluorescence. In this way, *Zavvar et al.* used PEG-*b*-PCL polymeric vesicles incorporating quantum dots, constituted of copper-indium-zinc, doped with gadolinium. The theranostic platform is obtained by the encapsulation of doxorubicin, in the hydrophilic part, the doped QDs with a size of 3 nm being in the hydrophobic part. This step does not impact the fluorescence of the QDs and can be followed by the covalent grafting of an aptamer on the surface in order to target tumors. The aptamer increases the accumulation of polymersomes in the tumor, leading to a decrease of tumor growth.<sup>103</sup>

#### I.4.2 Photoacoustic imaging (PAI)

Photoacoustic imaging is a more recent technique, characterized by high spatial resolution and deep penetration in tissues. It uses a laser beam sending photons that are absorbed by different moieties. The energy of photons is absorbed, and electrons pass to a vibrational excited state. The loss of energy of these electrons can occur according to different ways. The PAI uses the mechanism of non-radiative relaxations such as heat. The increase of temperature in the environment of excited molecule propagates and leads to a transient swelling of tissues. This modification induces acoustic waves that are detected with sensors. (Figure I.29)

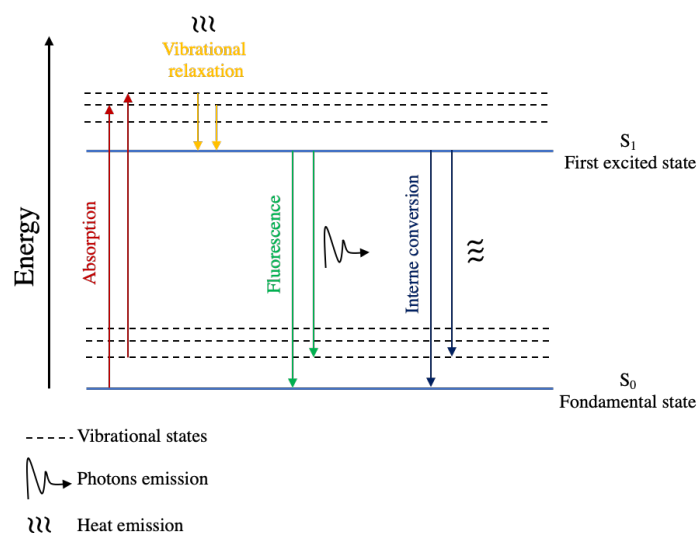


Figure I.29. Simplified Jablonski diagram.

The wavelength used in this type of experiment allows to selectively excite exogenous molecules or endogenous species and detect their signal. Based on this technique, a natural contrast can thus be obtained by endogenous species like hemoglobin, water, lipids, etc. In order to perform molecular imaging, a contrastophore such as small dyes or nanoparticles, with an absorption in the near-infrared (NIR), is used to avoid noise arising from endogenous species.<sup>104</sup>

Li *et al.* developed Mal-PEG-PLGA nanoparticles, loaded with croconaine dye (Croc<sub>815</sub> and Croc<sub>770</sub>) with or without targeting abilities, obtained by emulsion-solvent evaporation. Those dyes are pH sensitive with a NIR absorbance modified when the pH is varied. Moreover, they show high photothermal conversion efficiency, making them promising candidates for photothermal therapy (PTT), leading to a theranostic platform. The dye release is monitored by the pH and the intensity of the laser irradiation. A combination of these two parameters leads to an optimal release of the dye due to the degradation of PLGA in acidic medium on one side, and the increase of the energy from the dye on the other side. Results show better efficiency for PPC<sub>815</sub> (targeting NPs) than CPC<sub>770</sub> (non-targeting NPs) with the capability for PPC<sub>815</sub> to inhibit the growth of the tumor.<sup>105</sup> Using laser irradiation also leads to double treatment using conjointly chemo-photothermal therapies. (Figure I.30) Based on this principle, Yang *et al.* developed micelles made of poly(ethylene oxide)-*block*-poly(acrylamine-*co*-acrylonitrile-*co*-vinyl imidazole) (mPEG-PAAV). PAI was brought by IR780 molecule showing good efficiency for photothermal therapy and combined chemotherapy was performed using doxorubicin.<sup>106</sup>

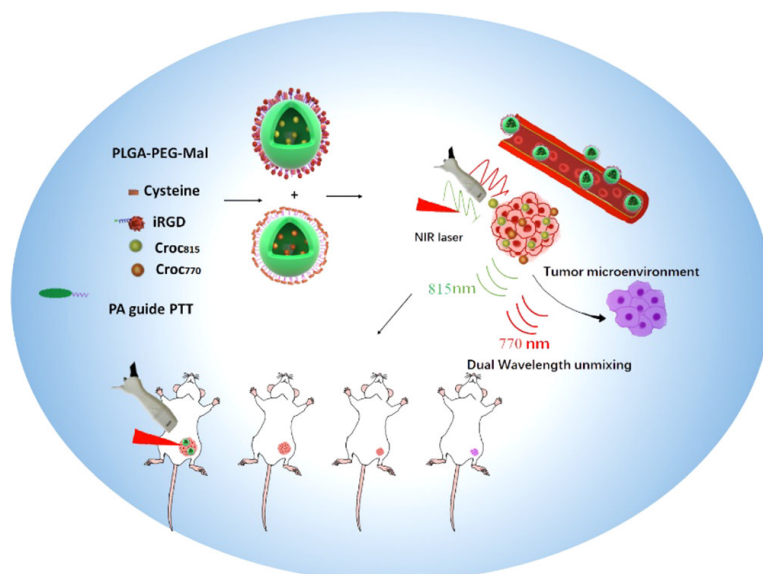


Figure I.30. Schematic representation of the PLGA-PEG-Mal polymersomes and their functionalization leading to *in vivo* pH stimuli following by PAI and PTT.<sup>105</sup>

### I.4.3 X-rays Computed Tomography (X-rays CT)

Basically, X-rays, that are electromagnetic waves, are delivered to patient. The beam interacts differently as a function of the matter. Resulting attenuated X-rays are detected in several directions, leading to the formation of images. The X-rays are more or less attenuated as a function of the nature of tissues. Indeed, the mineralized bone tissues attenuate much more the X-rays than soft tissues like muscles, which leads to an anatomical image contrast. The computed tomography takes place principally for the formation of 3D images. It allows to reconstruct 3D images using several projected 2D images.<sup>107</sup> Despite its high spatial resolution, it suffers from a lack of sensitivity in soft tissues like tumors that can be palliated using contrast agents, usually based on iodinated compounds (*e.g.* Lipiodol, by Guerbet S.A.). Nevertheless, high doses are needed that cannot be provided by small organic molecules due to their fast elimination. The nanoparticles seem to be an alternative to increase the quantities of iodine species. On that aim, Zou *et al.* developed cRGD-XIPS polymersomes loaded with doxorubicin and iodine which were obtained by co-self-assembling cRGD-PEG-p(DTC-IC) and PEG-p(DTC-IC) (poly(ethylene glycol)-*b*-poly(dithiolane trimethylene carbonate-*co*-ionidated trimethylene carbonate), where cRGD is a cyclic peptide targeting melanoma. These polymers led to spontaneous disulfide-crosslinking avoiding a natural release of doxorubicin. The authors designed, as negative control, polymersomes composed of PEG-PIC and cRGD-PEG-PIC

(cRGD-IPS) which were not able to form disulfide crosslinking. These nanostructures showed after 12 h a leakage of approximately 40% of the doxorubicin, whereas the crosslinked structure was destabilized only in intracellular conditions, leading to a release of 80% of doxorubicin in 24 h. These results show an increase of iodine-based CT image contrasting and enhanced treatment efficacy with the presence of the targeting cRGD.<sup>108</sup>

As explained for MRI, the CT can also be coupled with a molecular imaging technique like single-photon or positron emission tomography (SPECT/PET) to increase the sensibility of the CT X-rays. Based on the work by Zou *et al.*, PEG-PIC was prepared with some of the iodine radiolabeled with <sup>125</sup>I for dual imaging (SPECT-CT) or <sup>131</sup>I for radiotherapy (RT) *via* an isotopic exchange. The exchange of isotope impacted neither the biological properties nor the stability of the structure. <sup>131</sup>I showed acute RT toxicity for breast cancer cells with simultaneous SPECT-CT contrast provided by <sup>125</sup>I.<sup>109</sup>

#### I.4.4 Fluorescence imaging (FLI)

Fluorescence imaging (FLI) is principally used for preclinical studies (on small animals) with the aim to develop innovative therapies in the clinical sphere. FLI uses the same phenomenon than PAI, but in this case the photon energy absorbed by the contrastophore is released through a light emission called fluorescence that can be detected by ultrasensitive cameras. (Figure I.29)

Cyanine dyes are widely used in this type of studies owing to their low cytotoxicity and high molar extinction coefficient. Moreover, cyanines can be tuned to be covalently grafted on nanostructures. Yang *et al.* used cyanines as initiator for ATRP followed by two different reactions to obtain finally the poly(DMDEA-*co*-GMA)-*g*-PEG leading to polymeric NPs of 131 nm diameter in DLS by self-assembly in aqueous medium. The presence of cyanine as end-group of the polymeric backbone allows diagnosis by FLI, but also treatment by photothermal therapy (PTT). Results evidenced temperature raise of medium increasing as a function of the nanostructure concentration. They examined if the NIR light irradiation does not impact the dye. Results showed good photothermal stability with only 19.5% loss of the absorbance after 6 min of irradiation. In comparison, free dye has a decrease of 71.2 % after the same time of irradiation. Moreover, the polycationic block is pH-responsive, enabling drug release on the tumor site. Doxorubicin has been encapsulated as a model drug and showed approximately 50

% release after 6 h and two acidic treatments, at pH 6.5 and 5.4. As a control, cumulative assays show negligible release of doxorubicin in PBS. Finally, the nanostructures at up to 1 mg/mL concentration were evaluated *in vitro* and showed cell viability higher than 80%. (Figure I.31)<sup>110</sup>

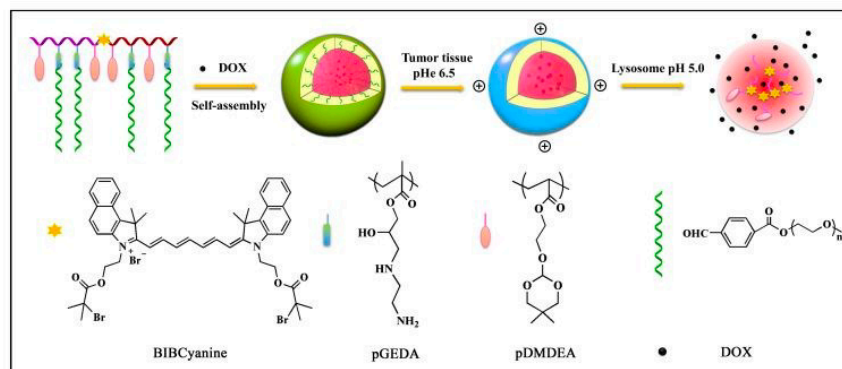


Figure I.31. Schematic representation of the synthesized polymer followed by their self-assembly with encapsulation of doxorubicin leading to their disruption in acidic medium.<sup>110</sup>

Another pH-sensitive triblock, where the cyanine is encapsulated or grafted onto the polymer, was developed by Yang *et al.* The polymersomes were made of poly(*N*-vinylpyrrolidone)-*block*-poly(dimethylsiloxane)-*block*-poly(*N*-vinylpyrrolidone) (PVPON-PDMS-PVPON) and were obtained by nanoprecipitation or the thin film method. The grafting of the cyanine on the polymeric backbone generated a red shift and a broader peak compared to non-grafted cyanines, that could be due to a quench of the fluorescence resulting from their proximity. They developed these structures in order to encapsulate PARP1 siRNA, having a low stability in physiological medium, to treat breast cancer by gene therapy, and showed that the breast cancer cells proliferation decreased of 34% after 6 days.<sup>111</sup> Micelles technology also used FLI: Yang *et al.* developed a block copolymer made of PEO and an acrylate derivative grafted with bis(oxy)bis(ethane-2,1-diyl) diacrylate (IR820), ferrocene and cinnamaldehyde. This complex copolymer self-assembles to form micellar nanoparticles. IR820 was used to obtain a diagnosis by photoacoustic and optical imaging, whereas the cancer therapy is provided by the release of cinnamaldehyde that leads to the formation of hydrogen peroxide. In presence of ferrocene, H<sub>2</sub>O<sub>2</sub> then produces hydroxyl radicals OH<sup>•</sup> by Fenton-like reaction. The authors evidenced that those nanocarriers were able to lead to significant decrease of cancer cells in combination with NIR irradiation increasing temperature through PTT. This overall oxidative-photothermal-photodynamic and imaging structure led to tumor size decrease. (Figure I.32)<sup>112</sup>

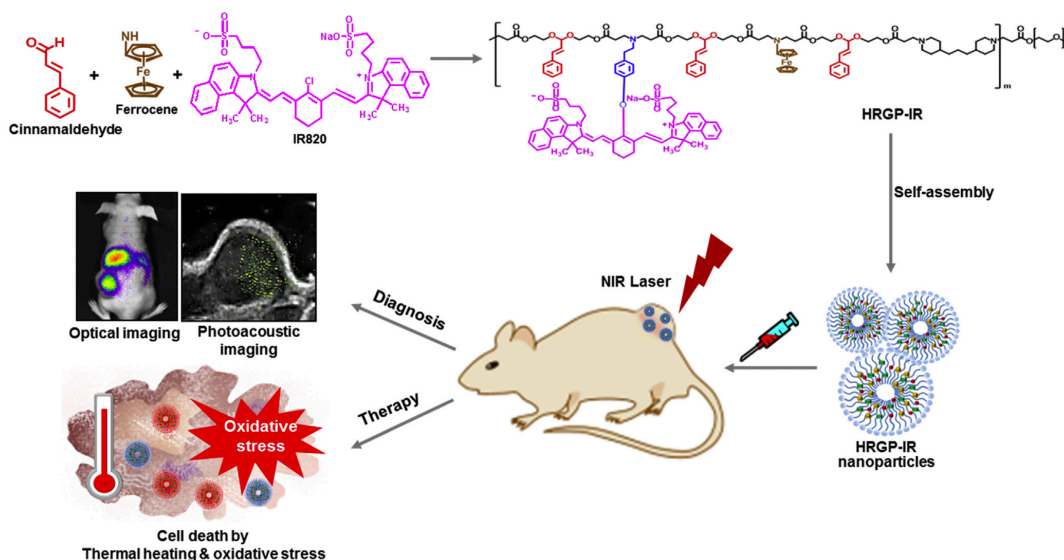


Figure I.32. Grafted copolymer self-assembling into micelles showing multiple-therapeutic effects and *in vivo* tumor regression through combination of NIR irradiation (PDT, PTT), OI and PAI as imaging techniques.<sup>112</sup>

Moreover, well-known doxorubicin, which is daily used to treat cancers, is naturally fluorescent. In this way, this drug is used in more and more applications. In the treatment of breast cancers, Moulahoum *et al.* developed pH sensitive polymersomes, made of PEO-*b*-PCL. As explained previously, doxorubicin was used for diagnosis by FLI and for therapy. The structure was specific thanks to grafting of Histatin 5, a histidine-rich peptide. Histatin was used due to its natural propensity in acidic medium to arrange its structure into alpha-helix. Results show an increase of internalization of doxorubicin in presence of Histatin 5.<sup>113</sup>

#### I.4.5 Comparison of the different bioimaging modalities

The previously described techniques (MRI, X-ray CT, PAI and FLI) are not the only ones available. The other possible bioimaging techniques will be briefly described below.

The positron emission tomography (TEP) uses radioisotopes previously formed and incorporated in organic molecules, such as <sup>18</sup>F in fluorodeoxyglucose (FDG). The used isotopes are neutron deficient and are naturally transmuted into a stable isotope by the transformation of a proton to a neutron, with an emission of positron (anti-electron e<sup>+</sup>). The emitted positrons have an energy proper to each radioisotope, and they enter in annihilation with electrons present in the medium. This leads to the production of two gamma photons emitted in two diametrically opposed directions. The exact position of the emitter can then be determined using a ring of detectors, when two of them detect the two opposed photons in coincidence, usually at a 511

keV energy. Single photon emission computed tomography (SPECT) uses radioisotopes emitting  $\gamma$ -rays which are collected on one side. Tomography allows to reconstruct images based on the collected  $\gamma$ -photons. Last but not least because of its non-invasiveness, ultrasound imaging (US) is based on ultrasound waves sent to the body, while their echoes are detected to provide an echography image. This technique depends on the different capacities of tissues, organs, vessels, and bones to reflect the US signal, combined with its ability to measure also body fluid velocities (Doppler imaging) or tissue elasticity modulus (elastography).

All these techniques have obviously different characteristics such as sensitivity, spatial resolution, and penetration depth. Those are compared in Table I.1.

Table I.1. Comparative table of the different imaging techniques discussed above.

	Detected species	Molecular sensitivity <sup>114</sup>	Spatial resolution <sup>114</sup>	Penetration depth <sup>114</sup>	Drawback
MRI	Electromagnetic signal	$\mu\text{M}$ - $\text{mM}$	10 – 100 $\mu\text{m}$	No limit	Low sensitivity
PAI	Acoustic waves	pM	50 – 500 $\mu\text{m}$	< 5cm	Pre-clinical
X-rays CT	X-rays	mM <sup>115</sup>	$\sim$ 100 $\mu\text{m}$ <sup>116</sup>	No limit	X-rays
FLI	Fluorescence	nM	2 – 10 mm	< 5cm	Low spatial resolution
PET	2 $\gamma$ -photons	pM	1 – 2 mm	No limit	Ionizing
SPECT	$\gamma$ -rays	pM	1 – 2 mm	No limit	Ionizing
US	Ultrasound	/	50 – 500 $\mu\text{m}$	< 5cm	Low penetration depth

MRI keeps a major place in medicine as bio-imaging technique, owing to its high spatial resolution enabling to image anatomical features of size down to 50-80  $\mu\text{m}$ . Nevertheless, the lack in sensitivity sometimes requires the use of contrast agents. An alternative is multimodal imaging coupling to MRI another technique of better sensitivity. The most used contrast agent in medicine are based on gadolinium complexes. However, the major dangers of Gd-based

contrast agents are the nephrogenic systemic fibrosis principally observed on patients with kidneys diseases, and their potential accumulation in the brain. There is thus a growing interest to introduce new MRI contrast agents based on safer complexes. On the other hand, it could be interesting to couple this technique with a more sensitive technique such as FLI which has, on its side, a lack in spatial resolution. FLI is the most sensible technique that does not use any ionizing radiations though it is rarely used in clinics, except for lymphography with indocyanine green (to visualize the superficial lymphatic system, *e.g.* for breast sentinel node biopsy). According to these arguments, the bimodality obtained by combining MRI and FLI, and the development of new types of contrast agents, are currently deeply investigated to obtain image guided drug delivery systems, an example of which will be provided by this PhD thesis.



# **Aim of the thesis**

## Aim

---

This thesis presents pH sensitive polymeric nanoobjects with an original structure composed of poly(ethylene oxide) as hydrophilic block and a statistical copolymer made of poly(*L*-lactic acid-*co*- $\epsilon$ -caprolactone) as hydrophobic block. This amphiphilic copolymer can self-assemble into nanostructures such as micelles or vesicles also called polymersomes, able to encapsulate several molecules. With the aim to improve the cancer diagnosis and treatment, a theranostic nanoplatform will be developed by encapsulating doxorubicin, a well-known anti-cancer drug, and ZW800-1, a near infrared fluorophore used as contrast agent in fluorescence imaging (FLI). Moreover, bimodality for the diagnosis will be brought by the grafting on the vesicles surface of magnetic resonance imaging (MRI) contrast agents. This bimodality is advantageously induced since it allows to combine the spatial resolution of MRI with the high sensitivity of optical imaging.

As discussed in the introduction, the gadolinium complexes currently used as MRI contrast agents are concerned by several issues, and so alternatives need to be found. We will describe in chapter **II** the development of complexes based on manganese ions. Indeed, these ions are naturally present in food, and they present paramagnetic properties, allowing to modify the relaxation times of protons. The macrocycle able to complex manganese ions is based on a cyclen derivative, bringing the right number of coordination links to leave a free coordination bond available for one water molecule. Moreover, the macrocycle can be functionalized thanks to its original structure, with pendants groups. Finally, the efficiency of Mn-complexes will be evaluated by different relaxometric techniques and *in vivo* on mice.

The polymers used in this thesis will be synthesized and fully characterized in chapter **III**. Their self-assembly behavior is evaluated, and the formation of micelles or polymersomes is shown depending on the protocol, their structure being characterized by different analytical techniques. Their encapsulation capacity of different molecules, such as dyes and drugs, will be also evaluated. The used anti-cancer drug is doxorubicin, an already used treatment in chemotherapy that showed its efficiency against different cancers. Nevertheless, its high toxicity brings a lot of side effects due to its impact on healthy cells. Studies evidenced that encapsulated doxorubicin prevents substantially those incoming effects. An exogenous fluorophore absorbing in the near infrared region will be also encapsulated to obtain a signal which can be reliably associated to the presence of the nanoobjects. The chosen fluorophore

will be the ZW800-1, an indocyanine green derivative, characterized by a higher stability than the parent molecule, indocyanine green which is already approved by the FDA. This dye has  $\lambda_{exc}$  and  $\lambda_{em}$  at 772 and 788 nm respectively in FBS (fetal bovine serum), which is in the therapeutic window (spectral region with the lowest absorbance of the endogenous molecules). These resulting nanoplateforms will be evaluated *in vitro* on different cellular lines and *in vivo* on mice.

Finally, a bimodal system, active both in FLI and MRI, could be obtained by grafting the Mn-complexes described in chapter II onto the nanoobjects surface. This immobilization of the Mn-complexes should moreover have the additional effect of improving their efficacy. To that aim, a strategy based on click chemistry will be envisaged to graft the Mn-complexes on the polymeric vesicles since it seems to be the best way to obtain a high selective reactivity. Chapter IV will describe the different tested strategies to functionalize the copolymer and the macrocycle with the right chemical groups. This strategy will allow to control the quantity of grafted MRI contrast agents by mixing different proportions of functionalized and unfunctionalized polymers, while encapsulating low amount of dye. Indeed, because of the difference of sensibility between MRI and FLI, the required amount of contrastophore is not the same.

This leads to the final chapter V, which will conclude this thesis and bring some perspectives on this work with critical overview of the most encouraging routes towards the final obtention of a bimodal, multifunctional and multi-stimuli-responsive (pH, temperature...) drug nanocarrier for innovative anticancer therapies.



# Chapter II

## Chapter II

---

### Chapter II: $Mn^{2+}$ complexes with pyclyen-based derivatives: synthesis, relaxometry characterizations and *in vivo* evaluation as MRI contrast agents.

The first part of this chapter was published as M. Devreux *et al.*, *Mn<sup>2+</sup> complexes with pyclyen-based derivatives as contrast agents for magnetic resonance imaging: synthesis and relaxometry characterization*, **Inorganic Chemistry** **2021**, 60(6), 3604-3619. The second part presents original results obtained on these systems and are not included in the published article, in particular the study of their *in vivo* biodistribution by MRI in mice.

#### II.1 Introduction

Gadolinium complexes are currently the main authorized contrast agents (CAs) used in clinic for medical diagnosis by Magnetic Resonance Imaging (MRI). In fact, this powerful non-invasive imaging technique often requires the use of a CA to compensate its lack of sensitivity. Different classes of CAs have been developed for MRI, among which gadolinium complexes are by far the most used in the clinical field thanks to their property to decrease the proton water longitudinal relaxation time, highlighting the areas where the CA is accumulated.<sup>117</sup> Nevertheless, since more than a decade some researches have demonstrated that the injection of gadolinium complexes to patients with kidneys failure can trigger the apparition of a disease called nephrogenic systemic fibrosis (NSF).<sup>118-121</sup> This is particularly true for linear gadolinium complexes based on acyclic ligands such as Gd-DTPA (gadopentetic acid) that are less thermodynamically and kinetically stable than those based on macrocyclic complexes such as Gd-DOTA (gadoteric acid). Therefore, some marketed Gd-based CAs (GBCAs) are no longer recommended for those patients.<sup>118,119,122</sup> In addition, more recent studies have shown accumulation in the brain of gadolinium CAs in subjects with normal renal function.<sup>123,124</sup> Further investigations were carried out on rats to compare macrocyclic (Gadoteridol<sup>®</sup>) with linear (Gadodiamide<sup>®</sup>) marketed agents and to quantify the Gd-species retained in the brain. It was concluded that Gadoteridol<sup>®</sup> was much less retained than Gadodiamide<sup>®</sup> and fully detected in the urines as its intact and soluble Gd-species, whereas Gadodiamide<sup>®</sup> was found mostly as

insoluble species.<sup>125,126</sup> This situation explains that scientists are much interested in finding a safer next generation of MRI CAs based on Gd-free alternatives, and one of these could be the use of manganese-based CAs.<sup>127–129</sup> Manganese ions are essential and naturally present in the body under the form  $\text{Mn}^{2+}$  or  $\text{Mn}^{3+}$  with 5 or 4 unpaired d-orbital electrons, respectively. The normal physiological concentration of manganese in the serum of healthy subjects is about 0.5–1.2  $\mu\text{g/dL}$  (9–22  $\mu\text{M}$ ), and part of its important biological roles in the organism is to act as a cofactor activating some enzymes or as a constituent in metalloenzymes. Manganese ions also play a role in the development of the immune and nerve system functions and in the regulation of the amount of vitamins and sugar in the blood.<sup>130,131</sup> The first use of manganese as MRI CA was an oral formulation containing liposome-encapsulated  $\text{MnCl}_2$  salt (LumenHance<sup>®</sup>) indicated for gastrointestinal examinations. However, several studies have shown that too high doses of free manganese ions could induce a neurodegenerative disorder called manganism, a disease with symptoms similar to those of the Parkinson's disease. Despite toxicity of free  $\text{Mn}^{2+}$  ions, manganese enhanced MRI (MEMRI) using  $\text{MnCl}_2$  is used for preclinical studies in mice with brain<sup>132</sup> or lung<sup>133</sup> model tumors. To avoid adverse effects, manganese complexes have been developed, and the second manganese-based CA approved by the Food and Drug Administration (FDA) in 1997 was manganese dipyridoxyl diphosphate (Mn-DPDP, Teslascan<sup>®</sup>, Figure II.1) for use as a liver specific hepatobiliary CA.<sup>134</sup> This structure is based on a linear ligand and has low thermodynamic and kinetic stabilities, with consequently a certain amount of free manganese ions released *in vivo*. The efficacy of Mn-DPDP as a MRI CA is quite low because the ligand does not allow the coordination of any water molecule in the inner sphere of the metal coordination. Its efficiency comes therefore from the part of the released manganese ions, with a relaxivity of  $2.8 \text{ s}^{-1}\cdot\text{mM}^{-1}$  at 20 MHz and  $40^\circ\text{C}$  in an aqueous solution; as a point of comparison, the relaxivity of Gd-DOTA, a well-known commercialized macrocyclic CA, is  $3.5 \text{ s}^{-1}\cdot\text{mM}^{-1}$  at 20 MHz and  $3.1 \text{ s}^{-1}\cdot\text{mM}^{-1}$  at 60 MHz and  $37^\circ\text{C}$ .<sup>135,136</sup> As a result and for safety concerns (potential toxicity of released free  $\text{Mn}^{2+}$ ), Mn-DPDP is no longer commercialized for clinical use, so that there is still a need for Gd-free alternatives, with a higher thermodynamic stability and kinetic inertness in order to avoid the release of free manganese ions *in vivo*, and with a higher efficacy to be competitive with GBCAs.<sup>120,121,127,136</sup> As a possibility, researchers examined Mn-porphyrins, where the manganese cation is at the center of a heme ring. They found very high longitudinal and transverse relaxivities, of 9.33 and  $12.0 \text{ s}^{-1}\cdot\text{mM}^{-1}$  respectively at 3T ( $20^\circ\text{C}$ ), thereby enabling MRI detection *in vivo* of Mn-labelled cells.<sup>137,138</sup> Porphyrins exhibit multiple advantages such as being able to stabilize manganese in its higher oxidation states Mn(III) or even Mn(V). However, their synthesis is

delicate in the perspective of scale-up production for an envisioned clinical use. Moreover, such compounds are highly light-sensitive, and are therefore intensively studied in a context of therapeutic agents for photodynamic therapy. Slightly larger ring-shaped ligands called texaphyrins complexing  $\text{Mn}^{2+}$  were recently proposed as bimodal CAs (MRI and photoacoustic imaging).<sup>139</sup> Another bimodal system for MRI and positron emission tomography (PET) based on a pycnen ligand complexing  $\text{Mn}^{2+}$  or  $^{52}\text{Mn}^{2+}$  was also studied by Csupász *et al.*<sup>140</sup> On the other hand, Mn-based nanoparticles (NPs) were also tested : purely inorganic ones, like antiferromagnetic MnO or paramagnetic Mn-doped ferrocyanide NPs (Prussian blue), or organic ones made with DSPE-MPEG encapsulating doxorubicin complexed with  $\text{Mn}^{2+}$ .<sup>141,142</sup>

In view of this effort to develop macrocyclic ligands with a high affinity for Mn(II) and a high efficiency as MRI CAs,<sup>143</sup> this chapter explores the potential of four Mn(II) complexes based on the pycnen core (3,6,9,15-tetraazabicyclo[9.3.1]pentadeca-1(15),11,13-triene) and carrying an additional site for the conjugation to a molecule of interest, for instance a chemotoxic drug or a polymeric vector. Pycnen is an interesting 12-membered macrocyclic structure incorporating a *N*-pyridyl donor that rigidifies and pre-organizes the ligand coordinating groups (in particular rendering the 4 nitrogen atoms coplanar), an attribute which could improve the kinetic inertness of the resulting complex. Pycnen ligands have been reported recently for the coordination of luminescent lanthanide cations to develop optical probes for near-infrared imaging.<sup>144</sup> The pyridine subunit also provides an enhanced degree of lipophilicity that could promote mixed renal and hepatobiliary clearances, another interesting attribute in the context of patients with reduced kidney function. The choice of pycnen-based chelating agents was also guided by their availability as “tailor-made” synthetic chelators prepared according to a versatile and potentially up-scalable strategy, which consists in assembling two synthons previously “dressed” with all the final required functionalities: the donor groups to satisfy the electronic demand of the paramagnetic ion, and an additional function to allow its conjugation to a molecule of interest.<sup>145–149</sup> Since Mn(II) has typically a coordination number of 6 or 7, ligands for Mn(II) cannot exceed hexadenticity to allow the presence of at least one water co-ligand in its inner sphere which is a crucial parameter to ensure interesting relaxometric properties for MRI applications. Consequently, it was necessary to cleverly functionalize the pycnen derivative in order to limit it to 6 coordination bonds with  $\text{Mn}^{2+}$  while providing a sufficiently high degree of coordination to preserve a satisfying thermodynamic stability of the complex.

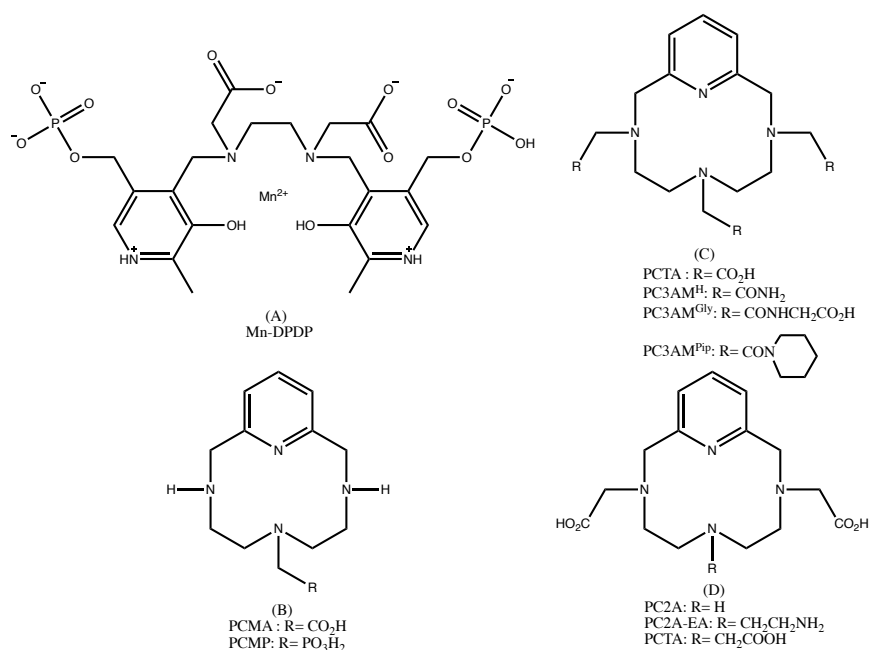


Figure II.1. Structures of the ligands or complexes discussed in this work: (A) MnDPDP<sup>134</sup>, (B) PCMA and PCMP<sup>146</sup>, (C) PCTA, PC3AM<sup>H</sup>, PC3AM<sup>Gly</sup>, and PC3AM<sup>Pip</sup>,<sup>149</sup> and (D) PC2A, PC2A-EA, and PCTA<sup>150</sup>

The pyclen ([12]PyN4) macrocyclic core is now recognized to form efficient chelators for the Mn<sup>2+</sup> cation complexation, and some studies can be found on the interest of such pyridine-containing (PC) ligands (Figure II.1). Drahos *et al.* have studied the influence of the nature of the coordinating group on one arm of the macrocycle on the thermodynamic stability, the kinetic inertness, the redox potential, and the <sup>1</sup>H and <sup>17</sup>O relaxation. They found that the mono-functionalized pyclens PCMA and PCMP with an acetate or a methyl phosphonate pendant arm give ternary hexacoordinate Mn<sup>2+</sup> complexes accommodate with one water co-ligand (Figure II.1), both of them being rather stable.<sup>147</sup> With a similar purpose, Garda *et al.* studied the influence on the proton relaxometry, the thermodynamic stability and the kinetic inertness of the presence of a primary, a secondary or a tertiary amide instead of the carboxylate functions of the PCTA which is a well-know pyclen derivative.<sup>150</sup> However, the corresponding Mn(II)-complexes show quite low relaxivities, less than 2 s<sup>-1</sup>·mM<sup>-1</sup> at 37°C and 20 MHz. In a more recent study, Botar *et al.* have developed a pH-responsive CA, [Mn(PC2A-EA)] stable and inert, with a maximum relaxivity at slightly acidic pH of 3.5 s<sup>-1</sup>·mM<sup>-1</sup> at 20 MHz and 37°C.<sup>151</sup> Botar *et al.* also developed di-(2-picolyl)amine (DPA) grafted on PC2A to obtain a manganese complex responsive to Zn<sup>2+</sup> ions. The addition of DPA, in their case, was used to image glucose that stimulate zinc secretion. All these results show that much efforts are still to be done to increase the efficacy of Mn-complexes as MRI contrast agents.<sup>152</sup>

## II.2 Results and discussion

In this work, it was decided to study a series of four  $N_4O_2$  hexadentate pyclen chelators including three structures carrying an additional function grafted onto the pyridine ring to allow conjugation to a molecule of interest (Figure II.2). The “naked” complex  $MnL_1H$ , where  $-H$  designates the absence of any substituent in the ortho position of the pyridine ring, will be used as a reference to evaluate the impact of this additional subunit on the relaxometric properties of the corresponding Mn-complexes. Our previous work showed indeed that the functionalization of the carboxylate moiety into an amide bond on the pyridine arm of Gd-PCTA leads to a loss of one water molecule in the inner sphere, giving  $q = 1$  instead of  $q = 2$ .<sup>149</sup> The syntheses are reported herein, together with the full relaxometric characterization of the corresponding Mn-complexes in order to have a complete understanding of their efficiency as MRI CAs (Figure II.2).

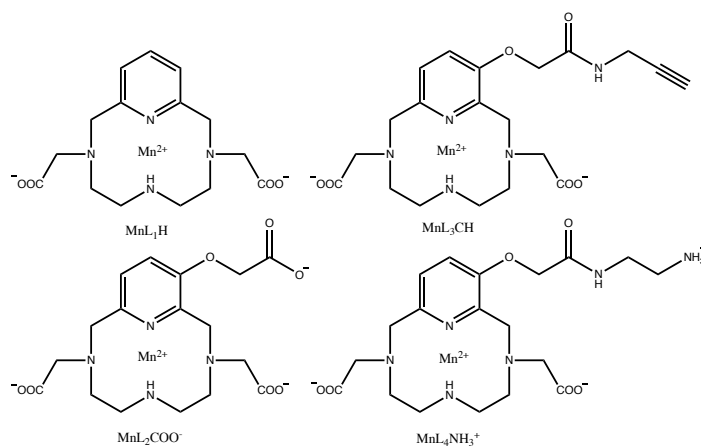
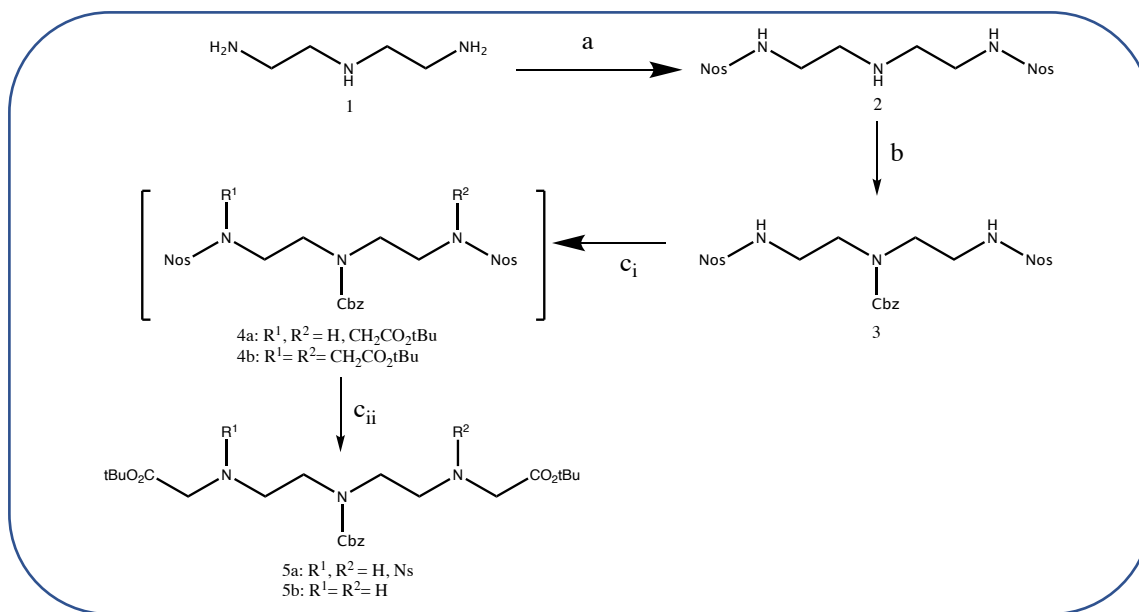


Figure II.2. Structure of the four Mn-complexes synthesized and studied in this work  
 $MnL_1H$ :  $MnPy(COO^-)_2-H$ ;  $MnL_2COO^-$ :  $MnPy(COO^-)_2-OCH_2COO^-$ ;  $MnL_3CH$ :  
 $MnPy(COO^-)_2-OCH_2CONHCH_2CCH$  and  $MnL_4NH_3^+$ :  $MnPy(COO^-)_2-$   
 $OCH_2CONH(CH_2)_2NH_3^+$ .

### II.2.1 Synthesis of the pyclen-based $Mn^{2+}$ complexes

The synthetic route to triamine **5b** is similar to what we described previously for the analogous compound bearing three acetate arms (Scheme II.1).<sup>149</sup> The selectively  $N,N'$ -protected diethylenetriamine derivative **2** was reacted in tetrahydrofuran (THF) with a slight excess of both benzyl chloroformate and diisopropylethylamine (DIPEA) to afford the fully protected compound **3** in 94% yield. The next two steps, grafting of the acetate arms onto the

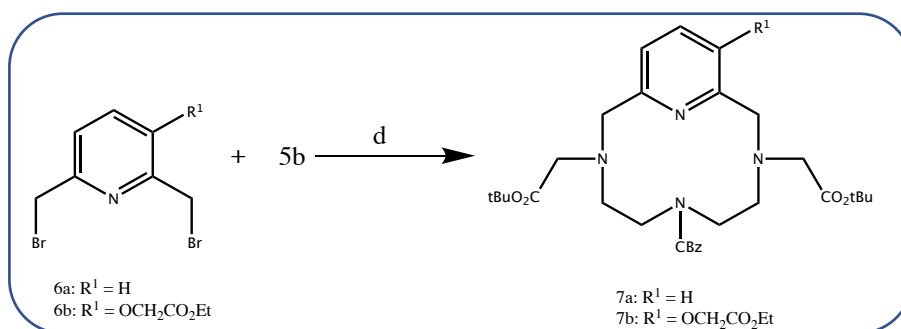
secondary sulfonamides followed by cleavage of the *o*-nitrobenzenesulfonyl (Nosyl) protecting groups, were carried out in one-pot in warmed acetonitrile. For each of the two steps, the total consumption of both the starting materials and the monofunctionalized intermediate (*i.e.* **3** and **4a** for the first step; **4b** and **5a** for the second one) was carefully monitored (TLC and/or mass spectrometry) and led to synthon **5b** with a yield of 85%.



Scheme II.1. Synthesis of the lower part of the pycnel chelates from a triamine derivative: (a) NaOH, Nos-Cl, diethylether, THF, r.t. overnight (b) Cbz-Cl, DIPEA, THF, r.t. 1h30 (c<sub>i</sub>)BrCH<sub>2</sub>CO<sub>2</sub>tBu, K<sub>2</sub>CO<sub>3</sub>, CH<sub>3</sub>CN, reflux 3-5 h (c<sub>ii</sub>)PhSH, K<sub>2</sub>CO<sub>3</sub>, 60°C 2-4 h.

The synthetic routes for the obtention of the **6a** and **6b** compounds were evaluated in the framework of my master's thesis by PhD F. Dioury and have been published in *EurJIC*, **2019**, 29, 3354–3365 “Bimodal Probe for Magnetic Resonance Imaging and Photoacoustic Imaging Based on a PCTA-Derived Gadolinium(III) Complex and ZW800–1”. (Scheme AII.1)

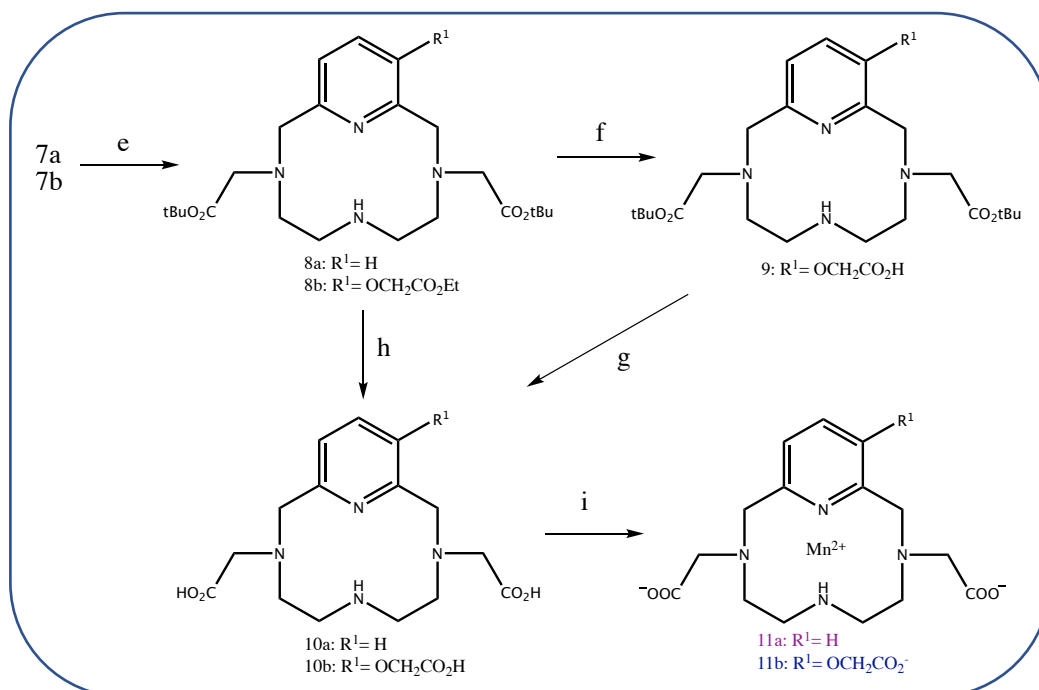
As previously described for PCTA derivatives, the pycnel macro-ring formation was achieved by reacting the triamine **5b** with a small excess of 2,6-dibromomethylpyridine **6a-b** under heterogeneous conditions in refluxing acetonitrile at moderate dilution (0.01M) with sodium carbonate as scavenger (Scheme II.2).<sup>149</sup> In such conditions, the corresponding macrocycles **7a-b** were isolated in 39 and 64% yields respectively.



Scheme II.2. Synthesis of the pyclen derivatives: (d) Na<sub>2</sub>CO<sub>3</sub>, CH<sub>3</sub>CN, reflux.

Successive step-by-step deprotections were then necessary in order to allow the selective grafting of different molecules of interest on the additional pendant group attached on the pyridine moiety of the macrocycle (Scheme II.3 ; Scheme II.4 ; Scheme II.5).

The carboxybenzyl group of compounds **7a-b** was smoothly removed by a pallado-catalyzed hydrogenolysis under an atmospheric pressure of H<sub>2</sub> at room temperature and afforded compounds **8a-b** (Scheme II.3). The reaction can be performed in MeOH and EtOH but the use of MeOH for **8b** can lead to transesterification. However, obtaining a mixture (if partial) of both methyl and ethyl esters does not impact the next saponification step. The controlled removal of the ethyl ester group of compound **8b** was then achieved by mild saponification with NaOH and provided the corresponding carboxylate **9** in 67% yield. The *tert*-butyl ester functions of the prochelators **8a** and **9** were removed by treatment with trifluoroacetic acid and led to the pyclen-based chelating agents **10a-b** that were finally complexed to Mn(II) ions by reaction with an equimolar amount of manganese dichloride tetrahydrate at controlled pH (*ca.* 5-6) to give the Mn<sup>2+</sup> complexes **11a-b**.



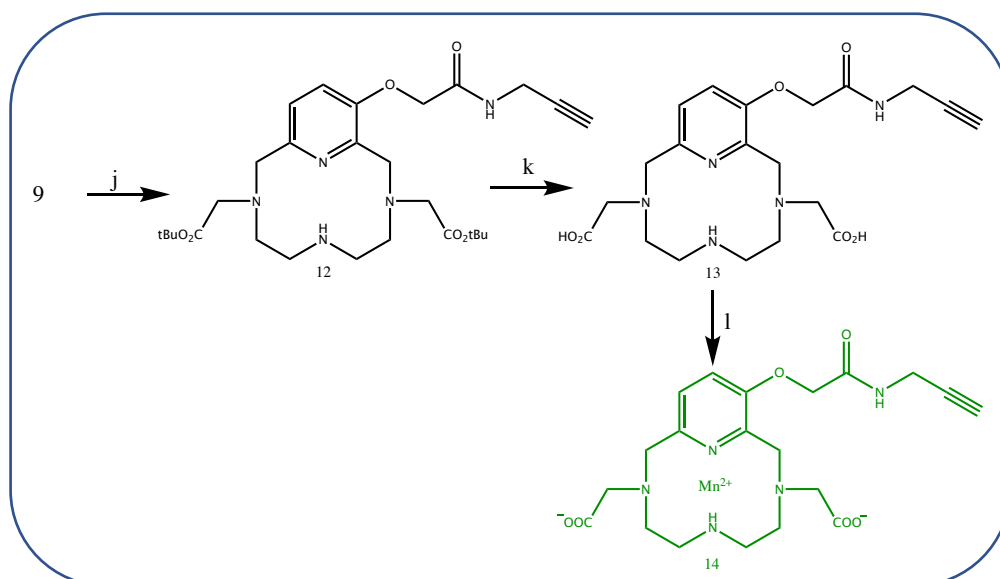
Scheme II.3. Synthesis of two Mn-complexes: (e) Pd/C, EtOH or MeOH, H<sub>2</sub> atm, r.t. overnight (f) NaOH, EtOH, r.t. 7h (g) and (h) CF<sub>3</sub>CO<sub>2</sub>H, CH<sub>2</sub>Cl<sub>2</sub>, r.t. overnight (i) MnCl<sub>2</sub>·4H<sub>2</sub>O, H<sub>2</sub>O, pH 5-6, 40°C, Ar atm, overnight. 11a is compound (MnL<sub>1</sub>H), 11b is compound (MnL<sub>2</sub>COO<sup>-</sup>).

Compound **9** has an additional carboxylic acid function on the pyridine subunit to allow subsequent conjugation to an amine function of different molecules of interest (Scheme II.3). As previously shown for a bifunctional Gd-PCTA complex,<sup>149</sup> the resulting amide bond can act as an additional donor group so that the overall denticity of the chelator is increased, and the coordination of a water molecule as co-ligand in the inner sphere of the paramagnetic center is compromised, with a negative impact on the relaxivity of the chelate. Consequently, it was decided to study the impact of this additional amide bond on the relaxivity of the Mn<sup>2+</sup> complexes.

Both compounds **14** and **17** were designed with a dual purpose: to study the influence of an additional pendant amide bond on relaxometry, and to vary the function to allow subsequent conjugation for forthcoming studies with different chemical reactions: by click chemistry with Huisgen's 1,3-cycloaddition on the alkyne end-group, or by coupling the primary amine with carboxylic acid groups (Scheme II.4 ; Scheme II.5).

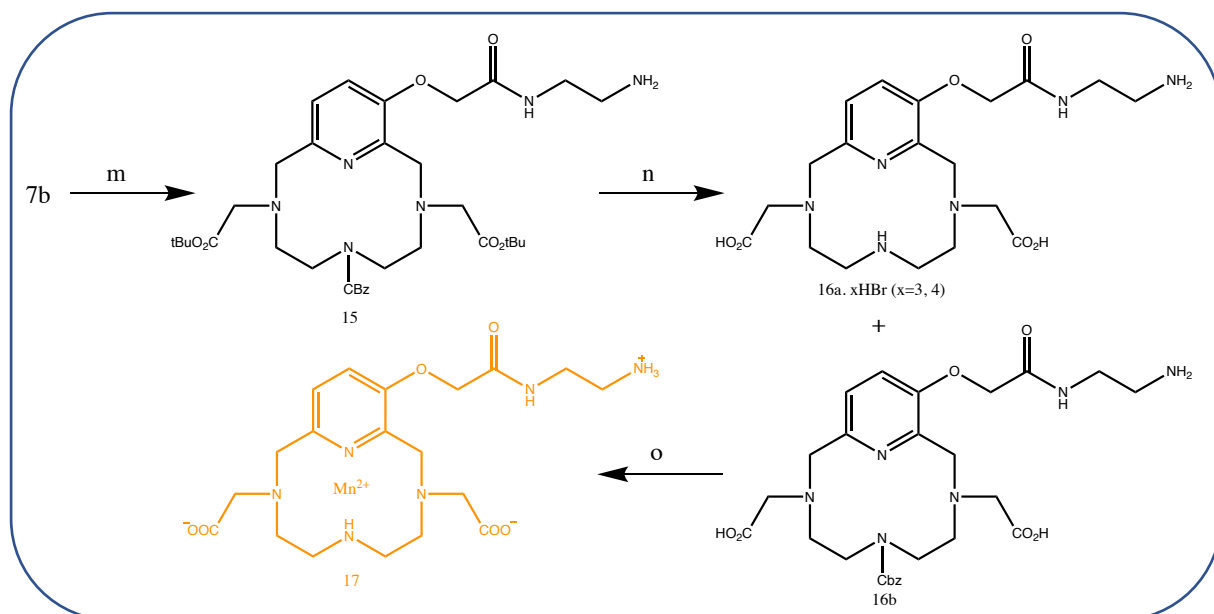
On the one hand, propargylamine was grafted to compound **9** using the uronium-based activating agent HBTU (*O*-(benzotriazol-1-yl)-*N,N,N',N'*-tetramethyluronium hexafluorophosphate) and afforded the carbamoyl derivative **12** (over 90 % yield) whose *tert*-butyl ester functions were then removed upon treatment with trifluoroacetic acid. The resulting

pyclen-based chelating agent **13** as a trifluoroacetic salt was finally complexed to Mn(II) as previously done for **10a-b** (Scheme II.4).



Scheme II.4. Synthesis of MnL<sub>3</sub>CH: (j) HBTU, NH<sub>2</sub>CH<sub>2</sub>CCH, DIPEA, CH<sub>2</sub>Cl<sub>2</sub>, r.t. 4h30 (k) TFA, CH<sub>2</sub>Cl<sub>2</sub>, r.t. 1 day (l) MnCl<sub>2</sub>·4H<sub>2</sub>O, H<sub>2</sub>O, pH = 5-6, 40°C overnight. The final product is compound (MnL<sub>3</sub>CH).

On the other hand, the ethyl ester derivative **7b** was submitted to aminolysis in ethylenediamine at room temperature for 1 hour and led to the expected amido derivative **15** in 58% yield. Compound **15** was then submitted to acidolyses with hydrogen bromide in warmed acetic acid to cleave both the *tert*-butyl ester and the carbamate functions and led to the expected ligand **16a** in 72% yield. It is noteworthy that upon treatment with hydrogen chloride in diethyl ether solution at room temperature, even repeatedly, only partial cleavage of the benzyloxycarbamate function was observed and gave a mixture of the desired compound **16a** and of the intermediate **16b** (as hydrochloride forms). Complexation with Mn<sup>2+</sup> ions finally proceeded very easily, in few minutes at room temperature (Scheme II.5).



Scheme II.5. Synthesis of MnL<sub>4</sub>NH<sub>3</sub><sup>+</sup>: (m) NH<sub>2</sub>CH<sub>2</sub>CH<sub>2</sub>NH<sub>2</sub>, r.t. (n) HCl<sub>anh</sub>, Et<sub>2</sub>O or HBr<sub>anh</sub>, AcOH, 70°C then r.t. (o) MnCl<sub>2</sub>·4H<sub>2</sub>O, H<sub>2</sub>O, pH 5-6, r.t.. The final product is compound (MnL<sub>4</sub>NH<sub>3</sub><sup>+</sup>).

In order to ensure the presence of the oxidation state 2+, the complexation reactions were performed under argon atmosphere and in the presence of sodium dithionite Na<sub>2</sub>S<sub>2</sub>O<sub>4</sub> (approximately 1.3 eq), a reducing agent reported in literature to control the oxidation state of Mn-porphyrins.<sup>153</sup>

## II.2.2 Oxidation state

The presence of Mn<sup>3+</sup>, obtained by the spontaneous oxidation of Mn<sup>2+</sup> in the presence of oxygen, would reduce the relaxometric capacity of the complexes.<sup>147</sup> To evidence the oxidation state of manganese ions, cyclic voltammetry measurements were performed. Mn<sup>2+</sup> and Mn<sup>3+</sup> having different coordination numbers, consequently the geometry of their corresponding complexes is not the same. With 7 coordination links, Mn<sup>2+</sup> favors trigonal prism geometry whereas Mn<sup>3+</sup>, which exhibits 6 coordination links, is characterized by a favorable octahedral structure. Cyclic voltammogram of MnL<sub>2</sub>COO<sup>-</sup> (ligand 2) shows an oxidation potential E<sub>ox</sub> = +470 mV and no reducing potential E<sub>red</sub>, evidencing an irreversible effect. This irreversible Mn(II)/Mn(III) redox process is commonly encountered for Mn-complexes and is due to the lack of ligand-field to stabilize the high spin d<sup>5</sup> configuration of Mn(II). This leads to a consequent contribution of the inner sphere to electron transfer.<sup>1</sup> This electrochemical

experiment allowed thus to demonstrate the main presence of the 2+ oxidation state in the  $\text{MnL}_2\text{COO}^-$  studied. (Figure II.3)

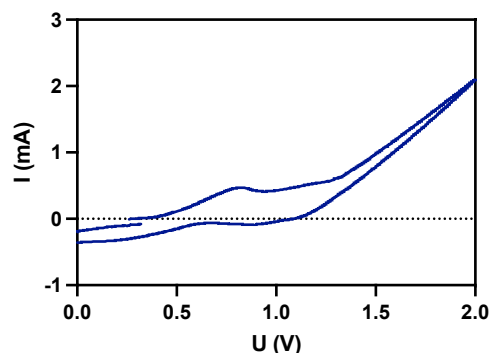


Figure II.3. Cyclic voltammogram of  $\text{MnL}_2\text{COO}^-$  (5 M NaCl, scan rate 50 mV/s)

As those measurements are compound consuming, it was assumed that the complexation under Ar atmosphere allowed to obtain Mn (II)-complexes with all the ligands.

### II.2.3 Relaxometric characterization

Paramagnetic complexes such as gadolinium and manganese complexes will mainly decrease the water protons longitudinal relaxation time  $T_1$ . Longitudinal relaxation time needed  $T_1$  is defined as the time needed for the longitudinal magnetization  $M_Z$  vector to reach  $1 - e^{-1} \sim 2/3$  of its equilibrium value  $M_0$  after a  $90^\circ$  pulse.  $T_1$  is measured by the inversion-recovery

sequence which consists in an impulsion of  $180^\circ$ , followed by a delay  $\tau$ , a second impulsion at  $90^\circ$ , and finally the recording of the free induction decay (FID). The longitudinal relaxivity, which is the slope of the decay rate  $R_1$  (inverse of  $T_1$ ) versus metal molar concentration gives access to the efficiency of the complexes. (Equation II.1)

$$r_1 = \frac{\left(\frac{1}{T_1}\right) - R_1^d(\text{water})}{[\text{Mn}_{\text{complex}}^{2+}]} \text{ s}^{-1} \cdot \text{mM}^{-1} \quad (\text{Equation II.1})$$

where  $R_1^d$  represents the diamagnetic contribution to the decay rate of pure water.

In other words, the relaxivity represents the capacity of one millimole per liter of the contrast agent to decrease the relaxation time of the water molecules present in its vicinity. The higher is the relaxivity, the more efficient is the contrast agent to modify the contrast of MR images.

In the case of  $T_1$  agents like Mn-complexes, a high relaxivity will be translated on images by an enlightenment of the area of accumulation, thanks to appropriate radiofrequency spin-echo sequences with very short echo times which operate a “ $T_1$ -weighting” of the MR images.<sup>154</sup>

Relaxivity depends on three mechanisms: (i) the inner sphere, which corresponds to the first coordination sphere of the metal containing one or several coordinated water molecule(s) (ii) the outer sphere corresponding to its bulk water diffusing in the close vicinity of the complex, and (iii) the second sphere coming from water molecules slightly bound to the complex through hydrogen-bonds for example. Since the outer sphere mechanism mainly depends on the diffusion of water, it cannot be easily tuned to increase the relaxivity as only a temperature change could significantly modify the diffusion, which is impossible *in vivo* where the temperature is fixed at 37°C. Alternatively, the hydrodynamic diameter of the CA could also be changed to tune the  $T_1$  contrast as introduced by Hannecart *et al.* with ultrasmall iron oxide nanoparticles coated by a thermosensitive polymer brush, but again it requires a change of temperature, which can be obtained *in vivo* only by local hyperthermia with special excitation by a laser or ultrasounds.<sup>155</sup> Concerning the inner sphere mechanism, it is of quantum mechanic origin and is governed by both scalar and dipolar interactions between the nuclear spins of water molecules and the orbital spins of the f or d-layer electrons of the magnetic center. The scalar interaction is negligible for all the Gd-complexes and for most of the Mn-complexes,<sup>121</sup> so that only the dipolar contribution will determine the inner sphere mechanism. It is given by Equation II.2 where  $q$  is the number of coordinated water molecule(s),  $\tau_M$  is the residence time of these coordinated water molecules and  $T_{1m}$  is the longitudinal relaxation time of the coordinated water molecule, defined by Equation II.3 according to the paramagnetic relaxation theory of Solomon-Bloembergen-Morgan.<sup>156–158</sup>

$$r_1^{is} = \frac{q/[H_2O]}{T_{1m} + \tau_M} \quad (\text{Equation II.2})$$

$$\frac{1}{T_{1m}} = \frac{2}{15} \left( \frac{\mu_0}{4\pi} \right) \frac{\gamma_H^2 g_c^2 \mu_B^2 S(S+1)}{r_{MH}^6} \left[ \frac{7 \tau_{c2}}{1 + \omega_S^2 \tau_{c2}^2} + \frac{3 \tau_{c1}}{1 + \omega_H^2 \tau_{c1}^2} \right] \quad (\text{Equation II.3})$$

$$\text{where} \quad \frac{1}{\tau_{c1,2}} = \frac{1}{\tau_R} + \frac{1}{\tau_M} + \frac{1}{\tau_{s1,2}} \quad (\text{Equation II.4})$$

$\mu_0$ , vacuum permeability;  $r_{MH}$ , distance between the metal ion and the water hydrogen of the coordinated water molecule;  $\gamma_H$ , proton magnetogyric ratio;  $g_e$ , electronic gyromagnetic factor;  $\mu_B$ , Bohr magneton;  $\omega_{S,H}$  Larmor frequency of electron or proton;  $\tau_{c1,2}$ , correlation time for magnetic fluctuation;  $\tau_R$ , rotational correlation time and  $\tau_M$ , water residence time in the inner coordination sphere

Among all these parameters, three were proven to have a huge influence on the relaxivity at the magnetic fields used in clinic (the clinical window), the number of coordinated water molecules ( $q$ ), the rotational correlation time ( $\tau_R$ ) and the water residence time in the inner sphere ( $\tau_M$ ). (Figure II.4) In order to increase  $q$ , it is necessary to modify the ligand structure to decrease the number of donor sites and hence its denticity. Such modifications can thus lead to a destabilization of the complex, characterized by a lower stability constant. On the other hand,  $\tau_R$  can be modified by grafting the small complexes on a bigger structure. Indeed, the larger the molecule, the longer will be its rotational correlation time, with a beneficial effect on the interaction between the nuclear and electronic spins, and thus on the relaxivity in the clinical window. (Figure II.5) Concerning  $\tau_M$ , the chemical nature of the donor groups of the ligand will have a huge influence. It has notably been shown that amide donor groups will lead to longer water residence time in the inner sphere as compared to carboxylate groups, which has a detrimental effect on the relaxivity of the complex (as shown on Figure II.6).<sup>117,159</sup>

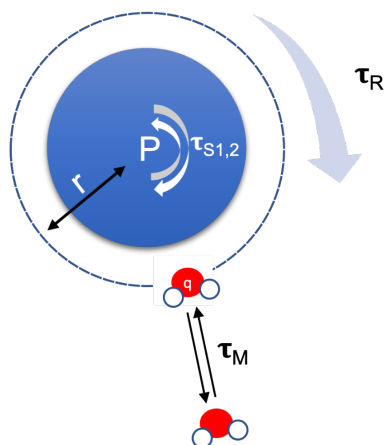


Figure II.4. P, paramagnetic center;  $\tau_{S1,2}$ , longitudinal and transversal electron relaxation times;  $r$ , shortest approach distance;  $q$ , number of coordinated water molecule;  $\tau_M$ , residence time of the water molecule in the inner sphere;  $\tau_R$ , rotational correlation time.

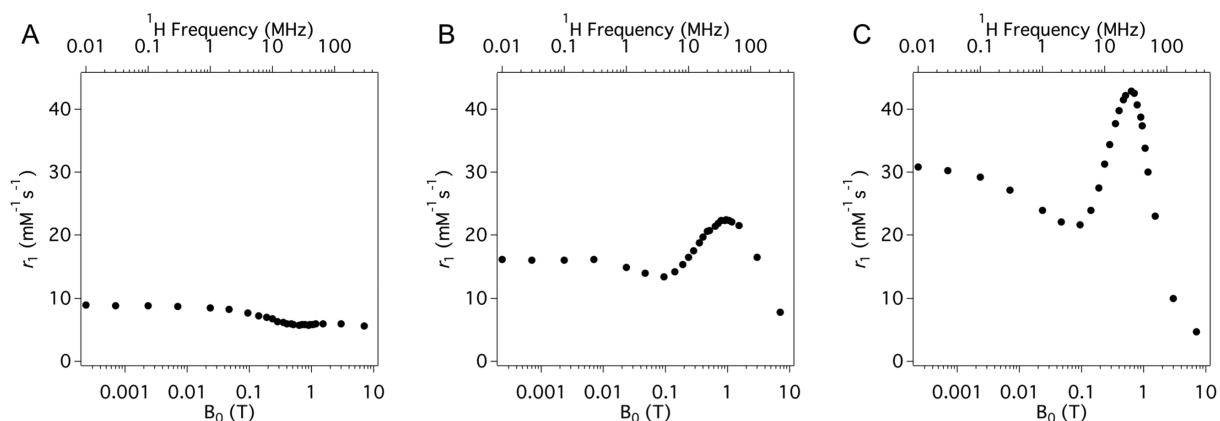


Figure II.5.  $^1\text{H}$  NMRD profiles showing the increase of the relaxivity in the clinical window as a function of the increase of the rotational correlation time  $\tau_R$  (A) Short  $\tau_R$  (0.1 ns for MS-325) (B) middle  $\tau_R$  ( $\sim 1$  ns for EP-1084) (C) long  $\tau_R$  (10 ns for MS-325 in HSA solution).<sup>117</sup>

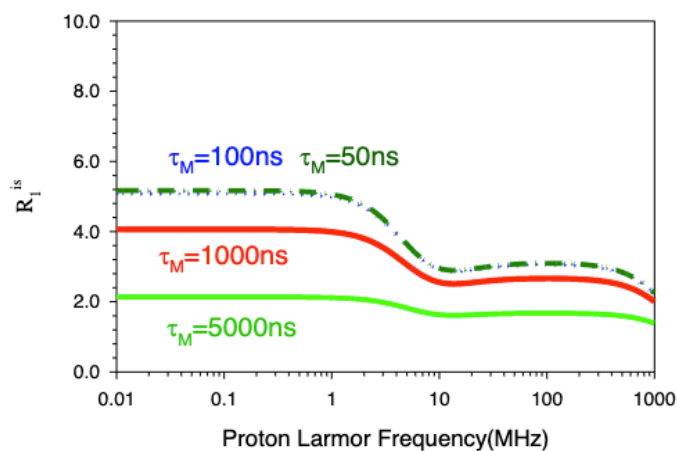


Figure II.6. Influence of  $\tau_M$  on NMRD profiles for small Gd-complexes at constant values of  $\tau_{SO}$  (100 ps),  $\tau_v$  (20 ps) and  $\tau_R$  (100 ps), showing a decrease in  $r_1$  relaxivity correlated with an increase of  $\tau_M$ . ( $\sim 100$  ns).

In the following sections, all of those three parameters will be evaluated according to different methods.

### II.2.3.1 Determination of the number of coordinated water molecules

The determination of the number of water molecules in the inner coordination sphere ( $q$ ) is very important to estimate the efficacy of the complexes as MRI contrast agents, as the longitudinal proton relaxivity  $r_1$  is directly related to this number. Two different techniques were used to determine this  $q$  parameter for the Mn(II) complexes, developed by E. Gale *et al.*,<sup>160</sup> and by J. Peters and C. Geraldes, respectively.<sup>161</sup> The first technique is based on <sup>17</sup>O NMR spectroscopy where the water transverse relaxivity  $r_2$  is measured as a function of temperature. In a similar way as  $r_1$ ,  $r_2$  is defined according to the linear variation with metal concentration of the transversal relaxation rate  $R_2=1/T_2$ , and is equal to:

$$r_2 = \frac{\left(\frac{1}{T_2}\right) - R_2^d(\text{water})}{[\text{Mn}_{\text{complex}}^{2+}]} \text{ s}^{-1} \cdot \text{mM}^{-1} \quad (\text{Equation II.5})$$

where  $T_2$  is the transverse relaxation time, and  $R_2^d$  represents the diamagnetic contribution of pure water.

The method is based on the maximum <sup>17</sup>O transverse relaxivity,  $r_{2\text{max}}^0$ , measured in this case at low temperature. (Figure II.7) This equation is obtained by different approximations, as explained by E. Gale *et al.*, and the  $r_{2\text{max}}^0$  measured at 11.75 T leads to the results shown in Table II.1. The number  $q$  is approximately the same for all complexes and close to one.<sup>160</sup>

$$q \cong \frac{r_{2\text{max}}^0}{510} \quad (\text{Equation II.6})$$

To confirm these results, a second technique was used, based on the measurement of NMRD profiles (*i.e.* the water proton longitudinal relaxivity  $r_1$  as a function of magnetic field or proton resonance frequency) at 25°C, developed by J. Peters and C. Geraldes.<sup>161</sup> (Figure II.8) This is based on another equation related to the proton longitudinal relaxivity at low field,  $r_{1p}$  (taken on the plateau of the NMRD profile) and the formula weight (FW) of the complex.

$$q = \frac{r_{1p}}{9.16 \{1 - e^{(-2.97 \times FW \times 10^{-3})}\}} \quad (\text{Equation II.7})$$

The results (Table II.1) confirm the presence of one coordinated water molecule in the inner sphere for the four synthesized complexes. The slight difference between the results coming from the two techniques can be explained by the fact that both methods rely on different approximations. The presence of one coordinated water molecule is an interesting result since it shows that the presence of the arm on the pyridine moiety, with or without amide bond, does not change the number of coordinated water molecules, meaning that this appended functionality does not participate to the coordination bonds with the manganese ion. It will thus allow further grafting of molecules of interest (see Chapter IV of this thesis).

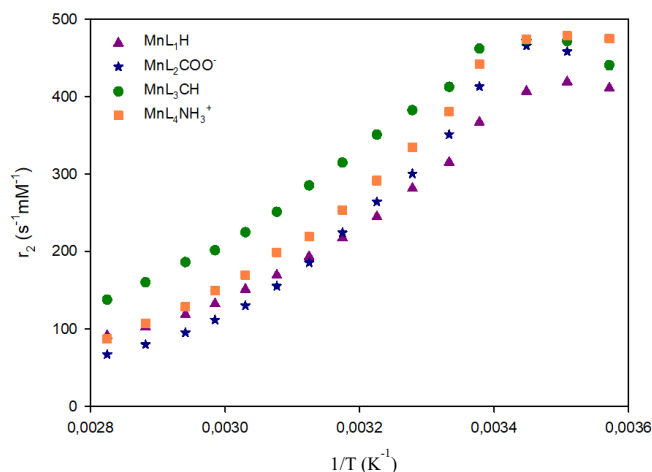


Figure II.7. Measurements of the <sup>17</sup>O water transverse relaxivity *versus* the inverse of temperature, at 11.75 T, in the presence of the different Mn-complexes at 2.06 mM (MnL<sub>1</sub>H, triangles), 2.58 mM (MnL<sub>2</sub>COO<sup>-</sup>, stars), 2.05 mM (MnL<sub>3</sub>CH, circles) and 1.21 mM (MnL<sub>4</sub>NH<sub>3</sub><sup>+</sup>, squares) concentration in order to determine the number of inner sphere water molecules ( $q$ ) from Equation II.6 in reference 160 as a function of the maximum value  $r_{2max}^0$ .

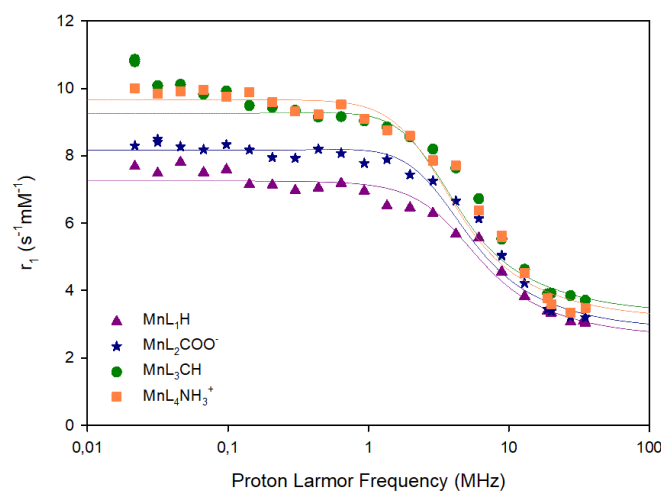


Figure II.8. NMRD profiles at 25°C in order to determine the number of inner sphere water molecules ( $q$ ) from Equation II.7 in reference 161 as a function of the plateau value ( $r_{1p}$ ) at low frequency and the formula weight (FW) for the four complexes:  $\text{MnL}_1\text{H}$  (triangles),  $\text{MnL}_2\text{COO}^-$  (stars),  $\text{MnL}_3\text{CH}$  (circles) and  $\text{MnL}_4\text{NH}_3^+$  (squares).

Table II.1. Evaluation of the number of coordinated water molecules in the inner sphere for all complexes ( $q$ ) by the two different relaxometric techniques described in the text.

	$r_{2\text{max}}^0$ ( $\text{s}^{-1} \cdot \text{mM}^{-1}$ ) (67.8 MHz)	$q$ (Eq. 2.6)	$r_{1p}$ ( $\text{s}^{-1} \cdot \text{mM}^{-1}$ ) (25°C and 0.02 MHz)	$q$ (Eq. 2.7)
$\text{MnL}_1\text{H}$	419.2	$0.82 \pm 0.2$	7.7	$1.25 \pm 0.4$
$\text{MnL}_2\text{COO}^-$	458.4	$0.90 \pm 0.2$	8.3	$1.30 \pm 0.4$
$\text{MnL}_3\text{CH}$	473.4	$0.93 \pm 0.2$	9.4	$1.35 \pm 0.4$
$\text{MnL}_4\text{NH}_3^+$	478.6	$0.94 \pm 0.2$	10.0	$1.42 \pm 0.4$

### II.2.3.2 Determination of the exchange rate of the coordinated water molecule

The technique which allows to determine the lifetime of the coordinated water molecule was developed by T. Swift and R. Connick.<sup>162</sup> It is based on the measurement of the  $^{17}\text{O}$  transverse relaxation rate as a function of the inverse of temperature, as for the determination of  $q$  for the Mn(II) complexes. (Figure II.9). The results (Table II.2) show that the coordinated water molecule is in a fast exchange regime for the four studied complexes since residence times  $\tau_M$  of the order of 6 ns are obtained.

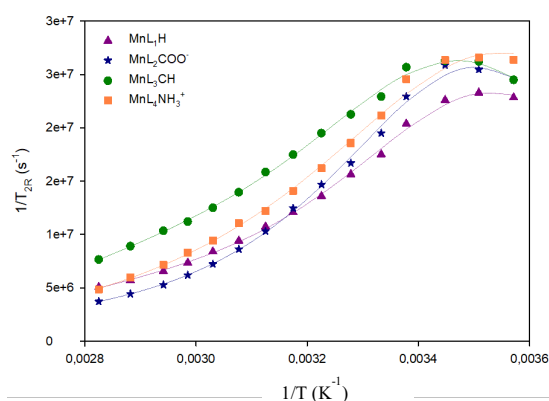


Figure II.9. Measurements of the  $^{17}\text{O}$  water transverse relaxation rate as a function of the inverse of temperature, at 11.75 T, on solutions of each complex at 2.06 mM ( $\text{MnL}_1\text{H}$ , triangles), 2.58 mM ( $\text{MnL}_2\text{COO}^-$ , stars), 2.05 mM ( $\text{MnL}_3\text{CH}$ , circles) and 1.21 mM ( $\text{MnL}_4\text{NH}_3^+$ , squares). The continuous lines represent fits by the theoretical model developed in reference 162, with the parameters displayed in Table II.2.

Table II.2. Determination of the residence time at 37°C and 11.75 T of the coordinated water molecule ( $\tau_M$ ), as well as the other parameters characterizing this exchange :  $A/\hbar$ , the hyperfine coupling constant between the oxygen nucleus of the bound water molecule and the  $\text{Mn}^{2+}$  ion;  $\tau_v$ , the correlation time modulating the electronic relaxation of  $\text{Mn}^{2+}$ ;  $E_v$ , the activation energy related to  $\tau_v$ ;  $B$ , related to the mean-square value of the zero-field splitting energy,  $\Delta$ , through  $B = 2.4\Delta^2$ ;  $\Delta H^\ddagger$  and  $\Delta S^\ddagger$  the enthalpy and entropy of activation, respectively, of the water exchange process. The number of coordinated water molecules was set to  $q = 1$ .

	$\tau_M(\text{ns})$	$\Delta H^\ddagger$ ( $\text{kJ}\cdot\text{mol}^{-1}$ )	$\Delta S^\ddagger$ ( $\text{J}\cdot\text{mol}^{-1}\cdot\text{K}^{-1}$ )	$A/\hbar$ ( $10^6 \text{ rad}\cdot\text{s}^{-1}$ )	$B$ ( $10^{20} \text{ s}^{-2}$ )	$\tau_V^{298\text{K}}$ (ps)	$E_v$ ( $\text{kJ}\cdot\text{mol}^{-1}$ )
$\text{MnL}_1\text{H}$	$6.5 \pm 0.4$	$29.7 \pm 0.1$	$7.4 \pm 0.2$	$-39.9 \pm 2.5$	$3.3 \pm 0.1$	$1.4 \pm 0.1$	$33.2 \pm 3.1$
$\text{MnL}_2\text{COO}^-$	$6.1 \pm 0.7$	$32.4 \pm 0.2$	$16.7 \pm 0.3$	$-39.9 \pm 0.8$	$5.2 \pm 0.6$	$3.2 \pm 0.5$	$36.3 \pm 4.6$
$\text{MnL}_3\text{CH}$	$8.4 \pm 0.9$	$26.3 \pm 0.2$	$-5.7 \pm 0.3$	$-37.8 \pm 1.15$	$1.2 \pm 0.1$	$1.2 \pm 0.4$	$36.9 \pm 7.5$
$\text{MnL}_4\text{NH}_3^+$	$6.35 \pm 0.7$	$25.1 \pm 0.1$	$-7.4 \pm 0.8$	$-32.2 \pm 0.7$	$0.2 \pm 0.3$	$1.6 \pm 2$	$39.9 \pm 38.1$

### II.2.3.3 Relaxometric measurements and NMRD profiles to assess the efficiency as MRI CAs

As a reminder, the relaxivity is defined as the increase of the water proton relaxation rate induced by one mmol per liter of paramagnetic complexes. Longitudinal ( $r_1$ ) relaxivities were measured at 37°C and respectively 0.47 T (20 MHz) and 1.41 T (60 MHz) (Table II.3).

They are lower than that of the commercially available gadolinium complexes (the data for Gd-DOTA are, for comparison,  $3.5 \text{ s}^{-1}\cdot\text{mM}^{-1}$  at 20 MHz and  $3.1 \text{ s}^{-1}\cdot\text{mM}^{-1}$  at 60 MHz and  $37^\circ\text{C}$ ), as expected, partly due to the intrinsic lower number of unpaired electrons for manganese (5) compared to that for gadolinium (7). The relaxivities could however be increased by grafting the complexes on macromolecular entities that would reduce the tumbling rate of the complex, which enhances the interaction time between the nuclear magnetic moments of the water protons and the orbital one of the paramagnetic complex during an echo time of the NMR radiofrequency field pulse sequence, and therefore the spin relaxation mechanism.<sup>136</sup> This was envisioned as an outlook of the current chapter and will be the topic of Chapter IV.

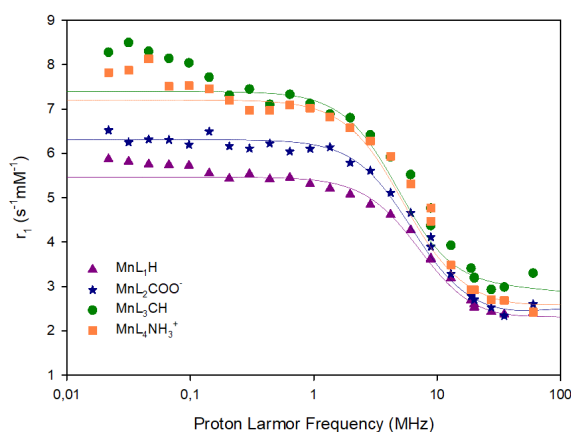


Figure II.10.  $^1\text{H}$  NMRD profiles at  $37^\circ\text{C}$  for  $\text{Mn}^{2+}$ -complexes, showing the longitudinal relaxivity at varying proton Larmor frequencies (aka varying magnetic field). The straight lines show the theoretical fitting based on the theory of Bloembergen and Solomon.<sup>156-158</sup>

NMRD profiles were acquired for the four cyclen-based manganese complexes in order to evaluate the efficacy of each complex depending on the magnetic field or frequency used. The fitting of these profiles according to the theory of Solomon and Bloembergen allows extracting important parameters to understand this efficacy such as the rotational correlation time ( $\tau_R$ ) or “tumbling time”, the electronic relaxation time at zero field ( $\tau_{S0} = \tau_{S1} = \tau_{S2}$  at  $H = 0$ ) and the correlation time that modulates electronic relaxation ( $\tau_V$ ).<sup>156-158</sup> Among the four studied complexes,  $\text{MnL}_1\text{H}$  has a  $r_1$  NMR dispersion profile below the other curves, especially at low field. This difference can be explained by the electronic properties of the complex which are slightly less favorable than for the other ones:  $\tau_{S0}$  is indeed lower compared to the values of the three other complexes. This is again encouraging for the future studies where we plan to graft other molecules thanks to the arm present on the pyridine moiety. (Figure II.10) It is also important to note that NMRD profiles do not exhibit scalar dispersion, which is

observed for the octahedral-aquated Mn(II) ions. For Mn-complexes, the scalar distribution is rarely observed and takes place for longer  $\tau_m$  and for slower electronic relaxation than those obtained in this work.<sup>121</sup>

Table II.3. Results of the theoretical fitting of <sup>1</sup>H NMRD profiles at 37°C with Bloembergen and Solomon's theory using the MINUIT minimization software. Parameters, such as the distance of closest approach ( $d_{\text{NMR}}$ ) and the water diffusion coefficient ( $D$ ) governing the outer sphere mechanism, or the distance between the coordinated proton of the water molecule and the manganese ion ( $r$ ) related to the inner sphere mechanism, can be set constant during the fitting procedure thanks to their prior determinations.<sup>156-158</sup> The values of  $q$  and  $\tau_M$  used were also predetermined thanks to their separate evaluation described above, thereby allowing to evaluate the rotational correlation time ( $\tau_R$ ), the electronic relaxation time to ground level at zero magnetic field ( $\tau_{SO}$ ) and the correlation time that modulates electronic orbital relaxation ( $\tau_V$ ).

	MnL <sub>1</sub> H	MnL <sub>2</sub> COO <sup>-</sup>	MnL <sub>3</sub> CH	MnL <sub>4</sub> NH <sub>3</sub> <sup>+</sup>
$d_{\text{NMR}}$ (nm) [a]	0.36	0.36	0.36	0.36
$D$ (m <sup>2</sup> ·s <sup>-1</sup> ) [a]	3.3×10 <sup>-9</sup>	3.3×10 <sup>-9</sup>	3.3×10 <sup>-9</sup>	3.3×10 <sup>-9</sup>
$r$ (nm) [a]	0.28	0.28	0.28	0.28
$\tau_R$ (ps) [b]	48.7 ± 3.8	57 ± 5.2	65.6 ± 0.85	59 ± 0.6
$\tau_M$ (ns) [a]	6.5	6.1	8.4	6.35
$\tau_{SO}$ (ps) [b]	119 ± 19.2	155 ± 29.5	224 ± 31.6	272 ± 6760.0
$\tau_V$ (ps) [b]	5.7 ± 1.2	3.4 ± 0.7	8.7 ± 8.0	3.1 ± 61.6
$q$ [a]	1	1	1	1
$r_1$ at 20MHz (s <sup>-1</sup> ·mmol <sup>-1</sup> ·L)	2.6	2.7	3.2	2.9
$r_1$ at 60MHz (s <sup>-1</sup> ·mmol <sup>-1</sup> ·L)	2.4	2.6	3.3	2.4

[a] Parameters pre-set at constant values during the fitting procedure [b] Parameters obtained by the fitting of NMRD profiles with Bloembergen and Solomon's model.

#### II.2.3.4 Transmetalation evaluation

It is now well-established that the kinetic inertness of a complex is a more important parameter than its intrinsic thermodynamic stability for *in vivo* applications. In order to define the stability of the manganese complexes against the most important endogenous divalent metal cations present in body fluids (Zn<sup>2+</sup>, Cu<sup>2+</sup>, Ca<sup>2+</sup>, Mg<sup>2+</sup>), a transmetalation study was performed in the presence of Zn(II) as exchanging metal cation. The choice of Zn<sup>2+</sup> ions as challenger to

assess the *in vivo* transmetalation behavior of the Mn(II) complexes was governed by the following considerations:<sup>163,164</sup> i) three of the four competitive endogenous cations are diamagnetic and therefore do not respond to NMR (except Cu<sup>2+</sup> ions which are paramagnetic) ; ii) Zn<sup>2+</sup> is the second most abundant transition metal in the human body (33 ppm) after Fe<sup>3+</sup> (60 ppm); iii) for a given exogenous ligand, complexes of Zn<sup>2+</sup> as well as Cu<sup>2+</sup> have generally higher stability than the corresponding Mn<sup>2+</sup> complex as ascribed to LFSE effect (ligand field stabilization energy), whereas alkaline earth ions Ca<sup>2+</sup> and Mg<sup>2+</sup>, although present at higher concentrations in blood plasma than Zn<sup>2+</sup>, form generally less stable complexes with the exogenous ligands generally studied for Mn<sup>2+</sup> due to their absence of d electronic orbitals; iv) the concentration of Zn<sup>2+</sup> in blood is higher compared to that of Cu<sup>2+</sup> (5 to 100 times higher).<sup>165</sup> As previously described by our team,<sup>164,166</sup> the transmetalation rate was assessed by measuring the progress of the proton relaxivity at 37°C and 20 MHz. The method consists in using a solution of the Mn-complexes at a concentration of 2.5 mM in phosphate buffer in the presence of an equimolar amount of zinc chloride. The proton longitudinal relaxation time ( $T_1$ ) is then measured in order to determine the paramagnetic relaxivity  $R_{1P}$  as a function of time. Indeed, when the exchange between Mn<sup>2+</sup> and Zn<sup>2+</sup> takes place, a precipitate of manganese phosphate (either Mn<sub>3</sub>(PO<sub>4</sub>)<sub>2</sub> or MnPO<sub>4</sub>) is formed. This process leads to an increase of  $T_1$  and thus a decrease of  $R_{1P}$  compared to its initial value  $R_{1P}(t=0)$ , as ascribed to the decrease of paramagnetic ion concentration in solution.

The results are similar for all the studied Mn complexes and show, during the first day, a small fast yet transient increase of the ratio  $R_{1P}/R_{1P}(t=0)$ , which could be due to the presence of transient polynuclear species coordinated to both Mn<sup>2+</sup> and Zn<sup>2+</sup>. This step is followed by a decrease of about 50% of the relaxation rate due to the formation of the insoluble solid as explained previously. This decrease is however quite slow ( $t_{1/2}$  half-life of approximately 1350 min) and we can notice that at the first measurement of the second day, the relaxation rate reached 80% of the initial value. (Figure II.11)

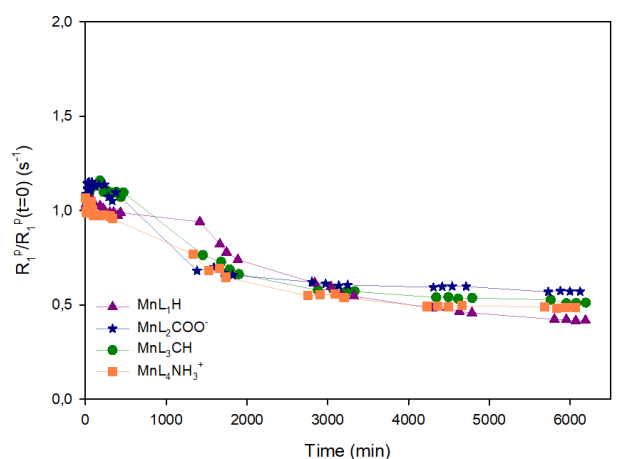


Figure II.11. Evolution of the normalized paramagnetic longitudinal relaxation rate in order to evaluate the transmetalation kinetics between manganese and zinc ions for the four  $\text{Mn}^{2+}$ -complexes:  $\text{MnL}_1\text{H}$  (triangles),  $\text{MnL}_2\text{COO}^-$  (stars),  $\text{MnL}_3\text{CH}$  (circles) and  $\text{MnL}_4\text{NH}_3^+$  (squares). Experiments were performed during 5 days in phosphate buffer at 20 MHz and 37°C. The concentration of Mn-complexes and of competing Zn(II) salt used is 2.5 mM, which is much higher than its normal physiological level ( $\sim 10 \mu\text{M}$ ).<sup>164</sup>

As a conclusion, even though this study highlights a lack of kinetic stability towards the transmetalation with zinc ions after a long time, we can be confident for the use of those complexes *in vivo* given their expected fast clearance from the organism. Further *in vitro* toxicity and *in vivo* pharmacokinetic studies are however necessary to definitively demonstrate the biosafety of these paramagnetic MRI CAs, and a first study will be presented in the next sections.

### II.2.3.5 Phantom images

To record an image, a slice was excited with a radiofrequency (RF) pulse associated with a magnetic field gradient. In the sequence, two parameters are important to define the image contrast: the time between the repetition of two sequences (TR) and the echo time between the first RF pulse and the detection of the signal (TE). Two different sequences were used in this work: (i) the RARE sequence (rapid acquisition by repeated echoes) allows to record rapid spin-echo MR imaging. It consists in one  $90^\circ$  pulse followed by a determined number of successive  $180^\circ$  pulses (called “a train”), each used to encode one line of the same image. (ii) The FISP sequence (fast imaging with steady- state precession) is a gradient echo sequence using a low angle pulse to excite the spins. It allows very short TR and TE for  $T_1$ -weighting and can also be set to record  $T_2^*$ -weighted images.

$T_1$ -weighted images allow to discriminate tissues characterized by different water proton longitudinal relaxation times  $T_1$ , by carefully defining the parameters TR and TE: TR should be small, so that the return of magnetization to its equilibrium value depends on the tissue according to its  $T_1$ , allowing to obtain a contrast between tissues based on  $T_1$ . Tissues characterized by a short  $T_1$  present a high recovery of their magnetization and hence a good signal, whereas tissues characterized by a long  $T_1$  present a low recovery of their magnetization, and hence a poor signal. TE should also be small to avoid any tissue differentiation based on  $T_2$  differences.

As a proof of concept of the use of these manganese-complexes as MR CAs, phantom MR images were recorded both at preclinical (9.4 T) and clinical magnetic fields (1 T), for each manganese complex at a concentration of 0.5 mM, and compared with Gd-DOTA at the same concentration and with pure water. (Figure II.12)

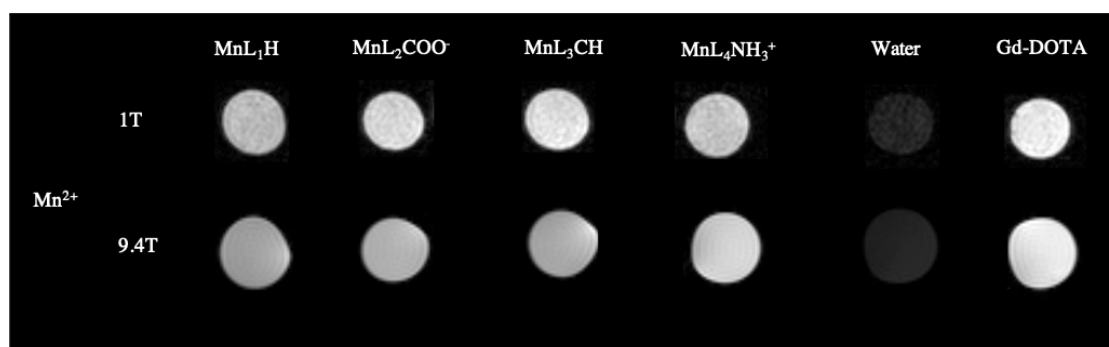


Figure II.12. Phantom images recorded at approximately 37°C under two different magnetic fields (1 T and 9.4 T) of each  $Mn^{2+}$ -complex at a concentration of 0.5 mM compared with a commercial Gd-complex, Gd-DOTA, at the same concentration, and with pure water. RARE sequence for 1 T and FISP for 9.4 T.

As expected, the  $T_1$ -weighted images are highlighted for the four Mn-complexes compared to pure water, but their contrast is less enhanced than with Gd-DOTA. Among the Mn-complexes, we can also notice a smaller highlighting effect for  $MnL_1H$ , which can be related to its smaller relaxivity because of the absence of the arm on the pyridine structure (Figure II.1; Table II.4).

Table II.4. Values of longitudinal relaxivity calculated from the water proton relaxation time  $T_1$  measured at approximately 37°C under a field of 9.4T (400 MHz).

	MnL <sub>1</sub> H	MnL <sub>2</sub> COO <sup>-</sup>	MnL <sub>3</sub> CH	MnL <sub>4</sub> NH <sub>3</sub> <sup>+</sup>	Gd-DOTA
$r_1$ (s <sup>-1</sup> ·mM <sup>-1</sup> ) 9.4T, 37°C	2.8 ± 0.1	2.7 ± 0.1	3.1 ± 0.1	2.95 ± 0.1	3.2 ± 0.1

## II.2.4 *In vivo* experiments

The *in vivo* experiments being performed at 1 T and 9.4 T, the longitudinal relaxivity of the two tested complexes was measured at high field (7 T and 11.75 T) and 37°C. The NMRD profiles shown at Figure II.10 were thus completed with those new values and shown at Figure II.13.

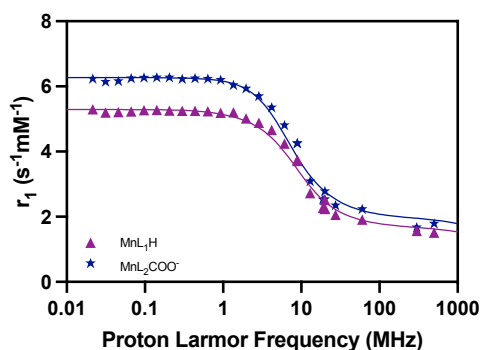


Figure II.13. <sup>1</sup>H NMRD profiles at 37°C for Mn<sup>2+</sup>-complexes, showing the longitudinal relaxivity at varying proton Larmor frequency (aka varying magnetic field). The straight lines show the theoretical fitting based on the theory of Bloembergen and Solomon.<sup>156-158</sup>

After injection of a 100 μmol Mn/kg dose, results both at 1 T and 9.4 T evidence a signal enhancement higher than 100% for both complexes in kidney pelvis with higher enhancement for MnL<sub>2</sub>COO<sup>-</sup>. This observation is in accordance with the NMRD profiles recorded. An enhancement of roughly 30% (20-40%) is observed in the liver up to 2 hours post-injection, suggesting that manganese ions are distributed in this tissue. (Figure AII.1 ; Figure AII.2) A signal enhancement above 100% that was observed in the gallbladder of some mice somehow confirmed hepatocyte uptake of manganese and its biliary excretion. (Figure AII.3 ; Figure AII.4)

Figure II.14 evidences the biodistribution of MnL<sub>1</sub>H with a clear enlightenment in the kidneys compared to pre-injection, which is more evidenced on images acquired at 9.4 T. Figure II.15 evidences the biodistribution of the second complex, MnL<sub>2</sub>COO<sup>-</sup>, and leads to the same observation. When comparing signal enhancements allowed by both ligands, the enlightenment

of kidneys for the second complexes appears higher, which corroborates the relaxivity measured at an equivalent magnetic field.

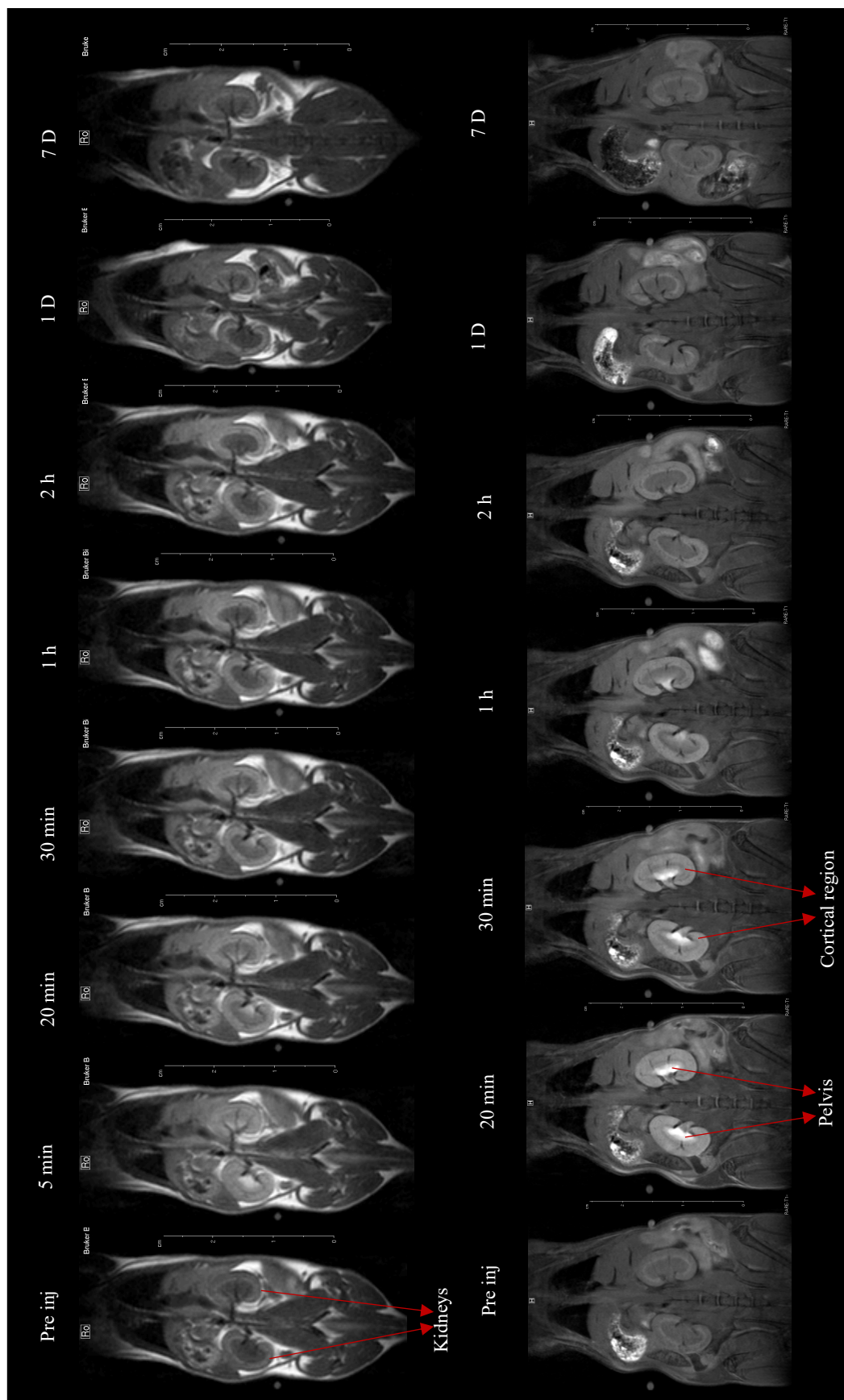


Figure II.14. Biodistribution MRI images of MnL<sub>1</sub>H at clinical magnetic field (1T) and preclinical magnetic field (9.4T) over time

1 T

9.4 T

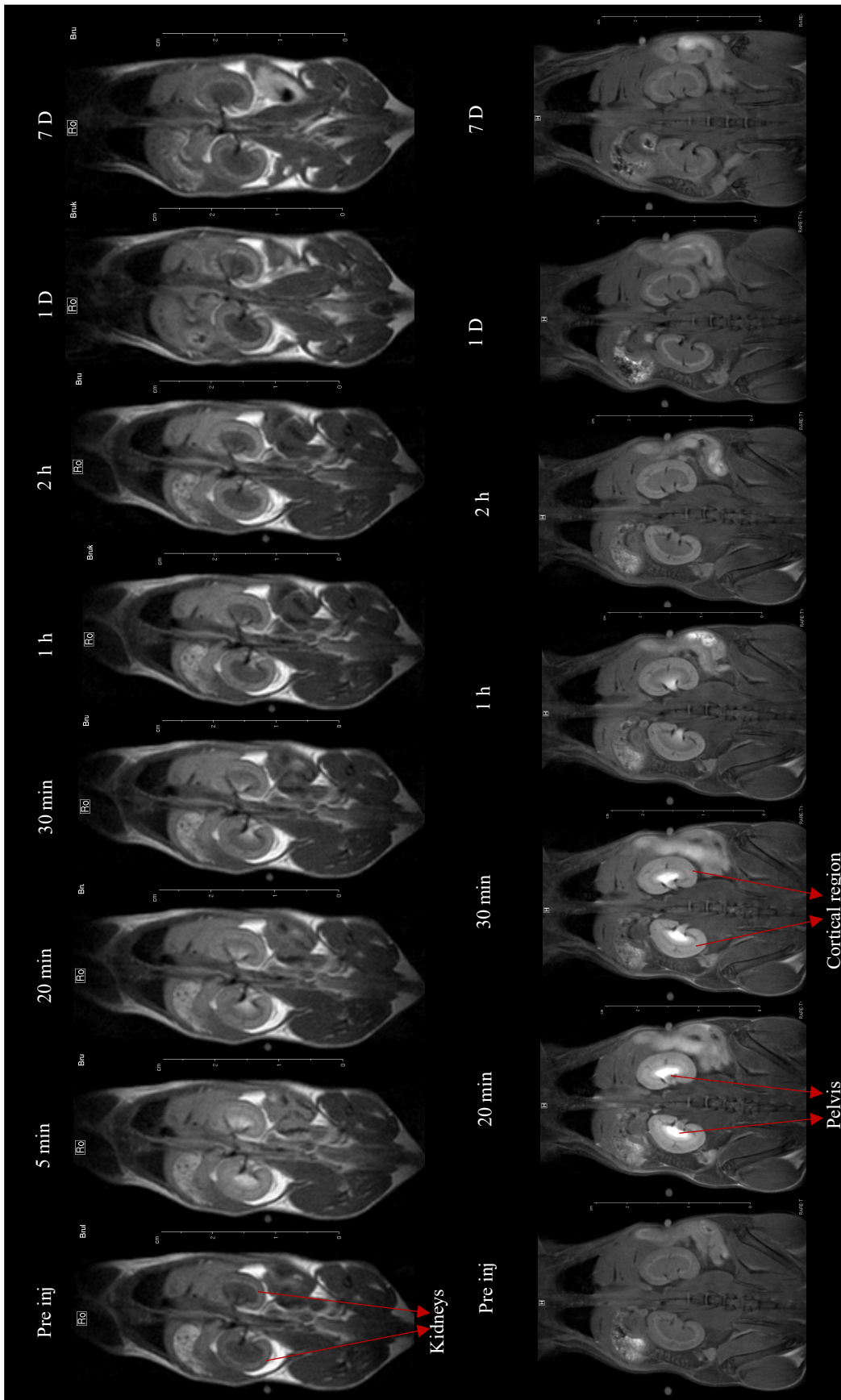


Figure II.15. Biodistribution MRI images of  $MnL_2COO^-$  at clinical magnetic field (1T) and preclinical magnetic field (9.4T) over time

1 T

9.4 T

The contrast observed in the kidneys evidences rapid clearance of manganese complexes. Indeed, a signal increase quickly appears after injection and is visible (with different behaviors in cortical region and pelvis) within the 2 hours of observation; a weak signal remains after one day in the cortical region and no signal enhancement is detected after seven days. This suggests that the main clearance organ is kidney. Dynamic images were recorded at 9.4 T before, during and up to 16 minutes after injection. Measurements were focused on plasmatic compartment (signal enhancement in heart left ventricle). As expected, enhancement in first minutes is more pronounced for the second complex. The signal quickly decreases over time (visually as an exponential function) due to an expected large extracellular distribution and a fast renal filtration of the rather small complexes. (Figure AII.5 ; Figure AII.6) Regarding the late (D1) signal observed in the kidney cortical region, it can be induced by the modification of the water protons relaxation time due to the presence of the contrast agent, or by a modification of the viscosity of the fluids present in renal tubules. Indeed, researches have shown that contrast media, particularly iodinated molecules used in CT-scan, induce an increase of the viscosity measured in urine, also decreasing tubular flow rate. Nevertheless, the mechanism that induces this phenomenon is still not well known.<sup>167-169</sup>

A modest signal enhancement can also be evidenced in the liver up to 2 hours post-injection. It disappears at day 1 and is no longer present at day 7 but allows to suppose that liver contributes to some clearance. This observation may lead to the hypothesis that  $Mn^{2+}$ -complexes could release free  $Mn^{2+}$  ions, that would be taken up by organs such as the liver *via* channels or carriers (also as calcium “analog”).<sup>170</sup> Manganese ions (used as co-factor for several enzymes) would then undergo elimination through the hepato-biliary way. This phenomenon was indeed evidenced in different studies.<sup>171-174</sup> For instance, Mn-DPDP has a structure similar to vitamin B6, and enters the hepatocytes *via* the vitamin B6 carrier. The hepato-biliary way of elimination was observed for Mn-DPDP and could also be explained by the uptake of free  $Mn^{2+}$ , then undergoing biliary excretion *via* metal transporters.<sup>175,176</sup> Nevertheless, all of these hypotheses have to be confirmed by further studies that would investigate the *in vivo* behavior ( $Mn^{2+}$  release, (hepato)cellular uptake, elimination) of our four types of complexes.

To evidence cell damages or inflammation induced by the injection of  $Mn^{2+}$ -complexes, blood was collected from each mouse to extract the plasma and evaluate different markers allowing to highlight injuries of those tissues. The first two markers are GOT (glutamic oxacetic transaminase or aspartate aminotransferase), and GPT (glutamic pyruvic transaminase or alanine aminotransferase), which are released by cells from damaged tissues or organs.<sup>177</sup> The third marker, LDH, lactate deshydrogenase, monitors the same type of failures than GOT and

GPT which are released after cell death. Kidney failure was evaluated by BUN (blood urea nitrogen) dosage and cannot be evaluated by uric acid dosage due to a too weak concentration in plasma. Concerning the BUN dosage, kidneys show no significant modification compared to control ( $p > 0.05$ ). For the three other evaluated markers,  $p$  remained above the significant value when comparing plasma from injected animals to those from controls. Nevertheless, results show a weak increase of GOT, GPT and LDH values. This could be explained by the low number of blood samples ( $n = 3$ ). If the same tests were performed on a larger number of samples, the difference could become significant. If those markers indeed show a significant increase, it could mean that  $\text{MnL}_1\text{H}$  and  $\text{MnL}_2\text{COO}^-$  induce damages to tissues as the liver, and cell death. (Figure II.16) As suggested by MR images, renal excretion is the main clearance mechanism for the complexes, but this does not seem to negatively impact kidneys according to BUN dosage (histological studies could help in confirming that). Nevertheless, manganese ions arising from supposed decomplexation might induce toxic impact on organs such as the liver. Indeed, it may seem obvious that free manganese ions are taken up and excreted by liver cells *via* existing manganese trafficking pathways, rather than the complex itself. The dosage of markers GOT, GPT and LDH, together with observations made on images, may confirm the hypotheses of hepato-biliary manganese clearance with a possible toxic impact on the liver.

The hypothesis of *in vivo* decomplexation can be correlated with transmetallation tests explained above, where a partial decomplexation was observed. (Figure II.11)

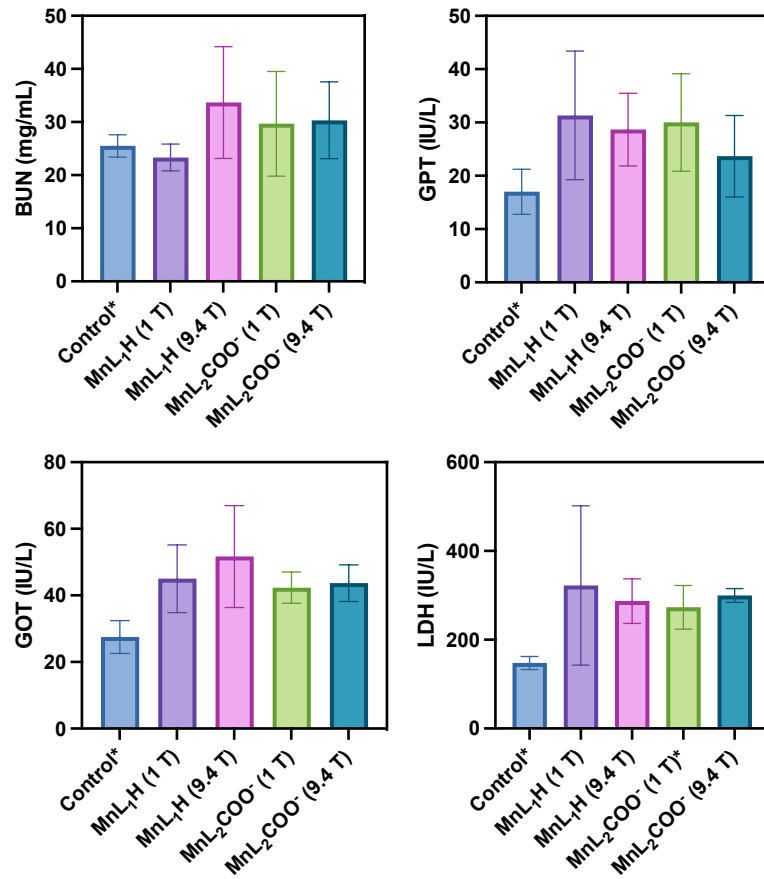


Figure II.16. Analyses of different factors present in plasma (GPT, GOT, BUN and LDH) able to evidence inflammatory reactions or failures in organs (\*  $n = 2$  due to insufficient volume in plasma or aberrant values, otherwise  $n = 3$ )

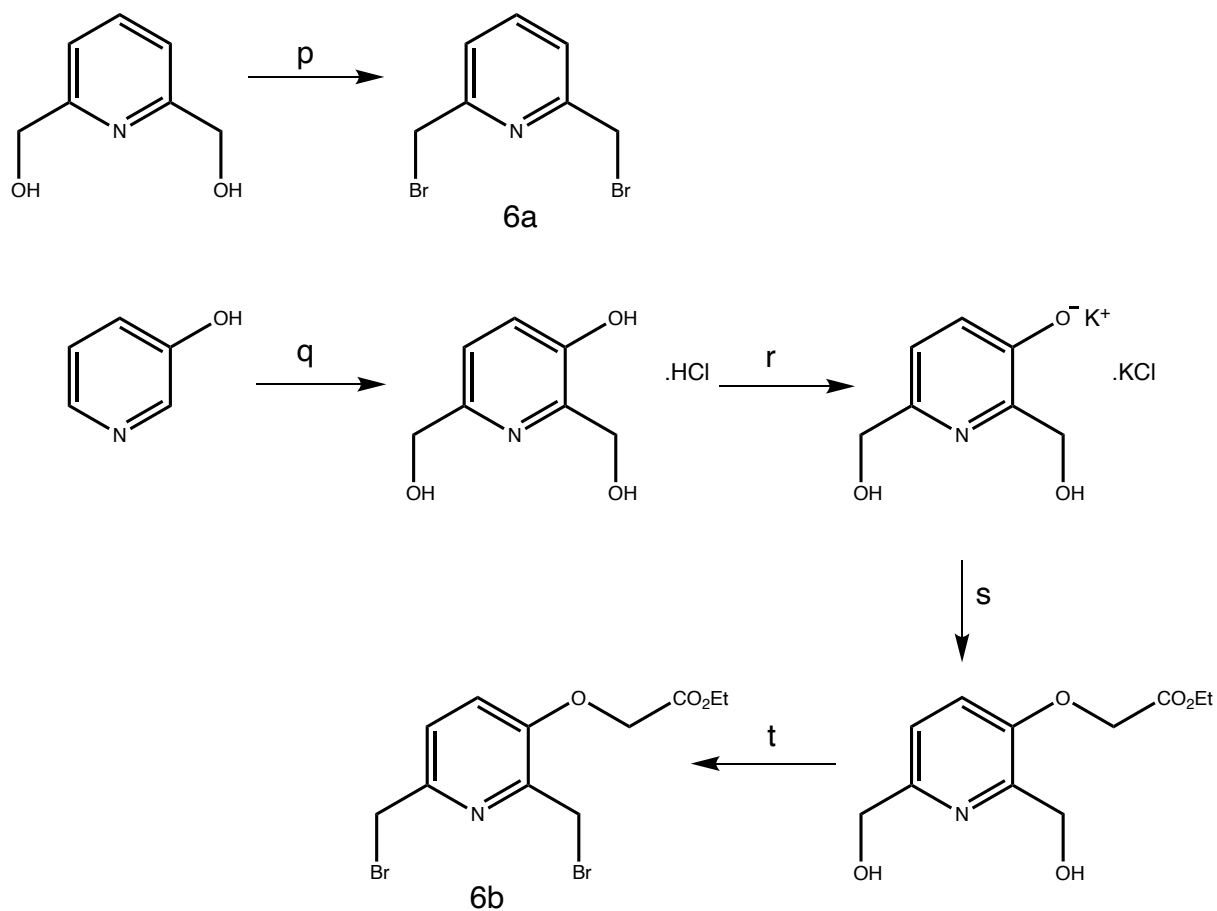
### II.3 Conclusions and perspectives

Four pycLEN-based complexing agents were synthesized and the molecular structure of intermediated compounds after each step of the synthesis was characterized. The corresponding manganese complexes were prepared and fully characterized by advanced NMR relaxometry methods to evaluate the parameters governing their properties and efficacy as paramagnetic MRI contrast agents. This characterization is important in order to evaluate if the complexes have an efficacy close to the commercial gadolinium complexes, and could potentially replace them on market, if they pass further evaluation of their biosafety.

Although these Mn-based compounds have been shown to be slightly less effective than the marketed Gd-based compounds as ascribed to lower magnetic moment of the metal, the potential of these pycLEN-based chelating compounds remains high. Their relaxivity could indeed be improved by different ways. Firstly, it will be possible to play on the rotational correlation time of the complex by blocking them in a nanostructure either organic (*e.g.* micelle or vesicle) or inorganic (*e.g.* silica nanoparticle), while keeping sufficiently small hydrodynamic size and stealthness to allow rapid clearance when injected in systemic circulation (which is a prerequisite for CAs used in clinic). Moreover, the additional chemical functions on the pyridine moiety will allow conjugation to biologically relevant vectors such as peptides or antibodies in order to target specific pathologies. On the basis of reported results, further improved kinetic inertness of the Mn<sup>2+</sup>-complexes might be obtained in future by replacing the two acetate complexing groups by non-ionizable groups such as amides; in this case, the positive charge on the resulting cationic Mn<sup>2+</sup>-complexes could be protective against acid-assisted dissociation, although grafting of neutral macromolecules might be necessary in that case to insure stealthness against adsorption of blood plasma proteins. It will nevertheless be important to verify that the presence of those amide functions does not increase too much the residence time in the inner sphere of the coordinated water molecule, which would impart longitudinal proton relaxivity. As a conclusion, these preliminary results show very encouraging properties of pycLEN derivatives for MRI contrast properties, although further study is necessary to demonstrate that they can replace gadolinium complexes in clinical diagnosis of diseases (cancers, strokes...). *In vivo* images show interesting results, indicating a major clearance mechanism that involves kidneys. Nevertheless, the other elimination ways (involving the liver) have to be investigated as they suggest that the stability of the complex has to be ensured *in vivo*. Thus, the cellular uptake and excretion mechanisms (Mn or Mn-complex), as well as the possibility of (*in vivo*) decomplexation have to be enlightened by further

biological studies. Those Mn-complexes remain thus an alternative way to avoid the issues of Gd-complexes, although improvements still must be undergone to eventually achieving a clinical assay on humans.

## II.4 Annexes



Scheme AII.1. Synthesis pathway to obtain the pyridine compounds 6a and 6b : (p) HBr (aq, 48%), H<sub>2</sub>SO<sub>4</sub> (aq, 96%), reflux 31 h<sup>138</sup>; (q) hydroxypyridine, NaOH, formaldehyde, acetic acid, DMF, 90°C over 90 min following by r.t. overnight; (r) K<sub>2</sub>CO<sub>3</sub>, EtOH, H<sub>2</sub>O, r.t., 3 h; (s) BrCH<sub>2</sub>CO<sub>2</sub>Et, DMC, 80°C, 1 h 30; (t) CBr<sub>4</sub>, PPh<sub>3</sub>, CH<sub>3</sub>CN, 0°C to r.t., overnight.

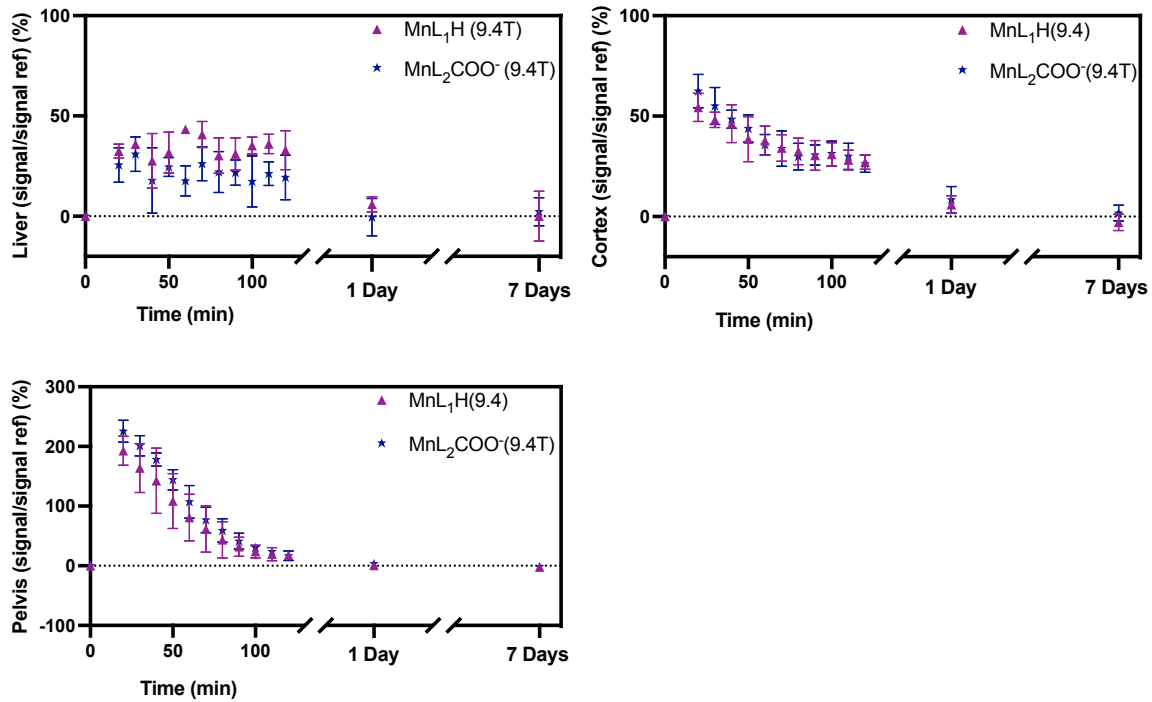


Figure AII.1. Detected signals over time on mice measured at 9.4 T on different zones of interest (liver on the upper left; cortex on the upper right, pelvis on the below left) to enhance the resulting contrast compared to a reference ( $n = 3$  for MnL<sub>1</sub>H and  $n = 4$  for MnL<sub>2</sub>COO<sup>-</sup>).

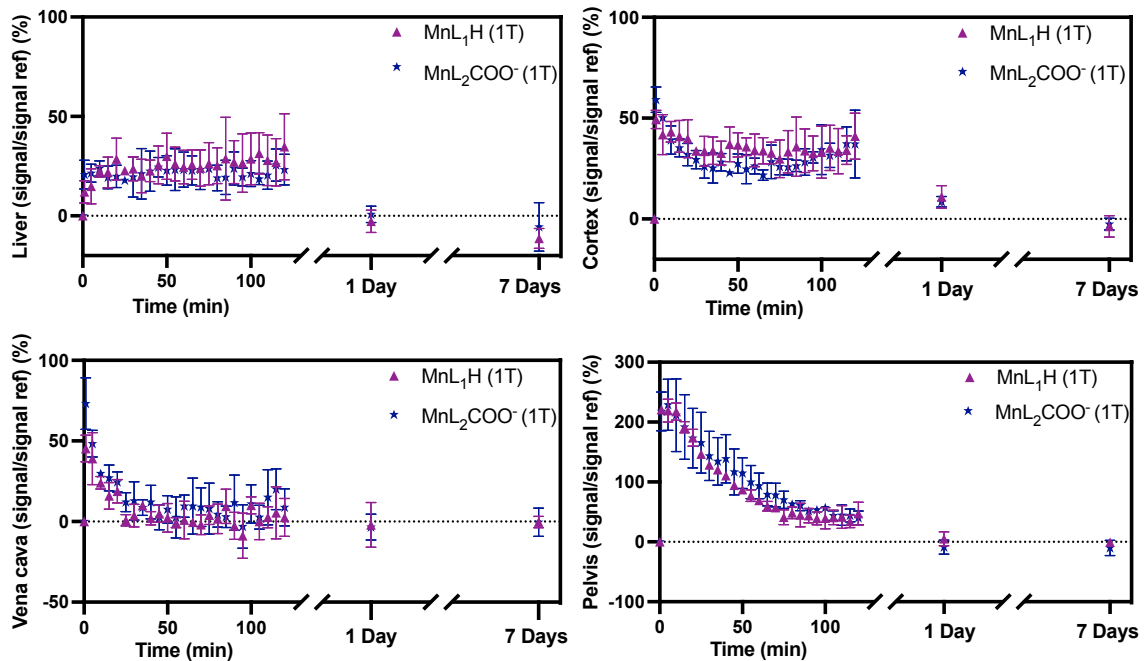


Figure AII.2. Detected signal over time on mice measured at 1 T on different zones of interest (Liver on the upper left; cortex on the upper right; vena cava on the below left and pelvis on the below right) to enhance the resulting contrast compared to a reference ( $n = 3$  for MnL<sub>1</sub>H and  $n = 3$  for MnL<sub>2</sub>COO<sup>-</sup>).

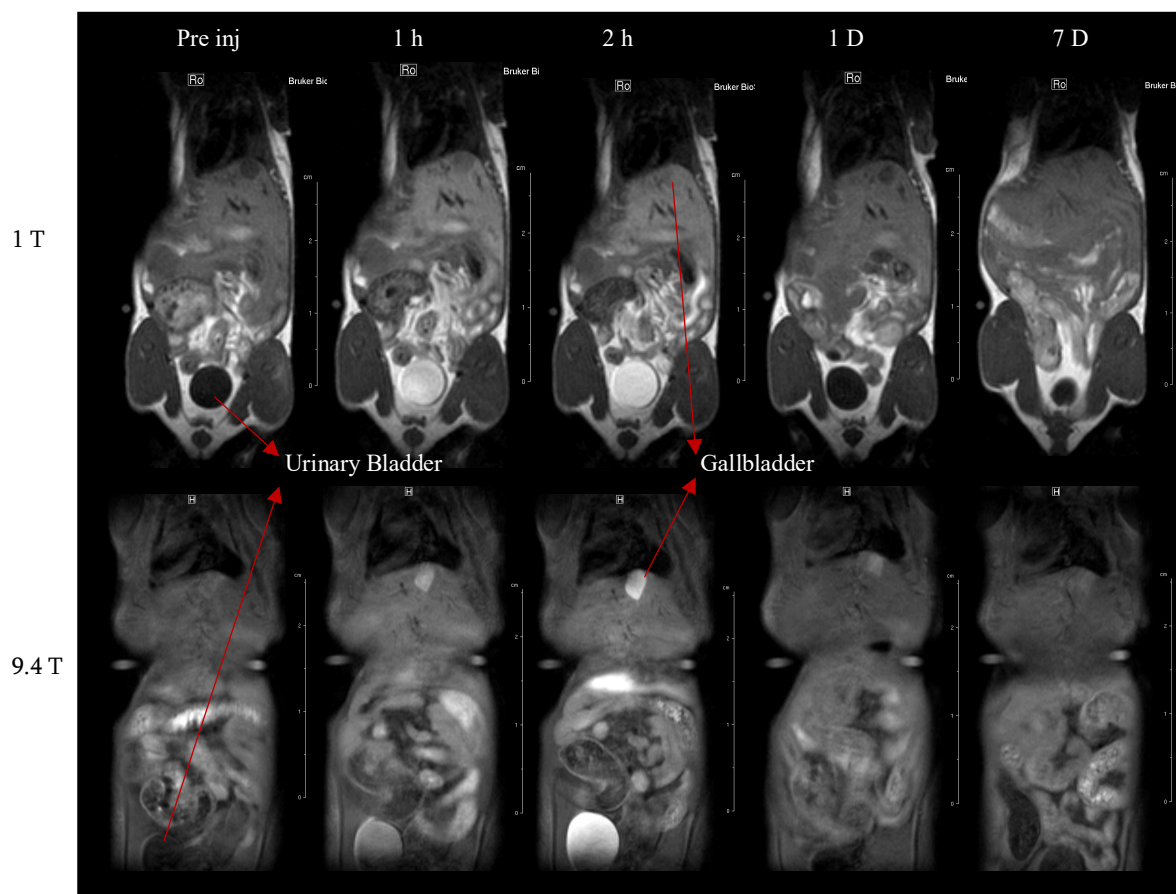


Figure AII.3. Enlightenment phenomenon of gallbladder and urinary bladder at two different magnetic fields induced by MnL<sub>1</sub>H over time.

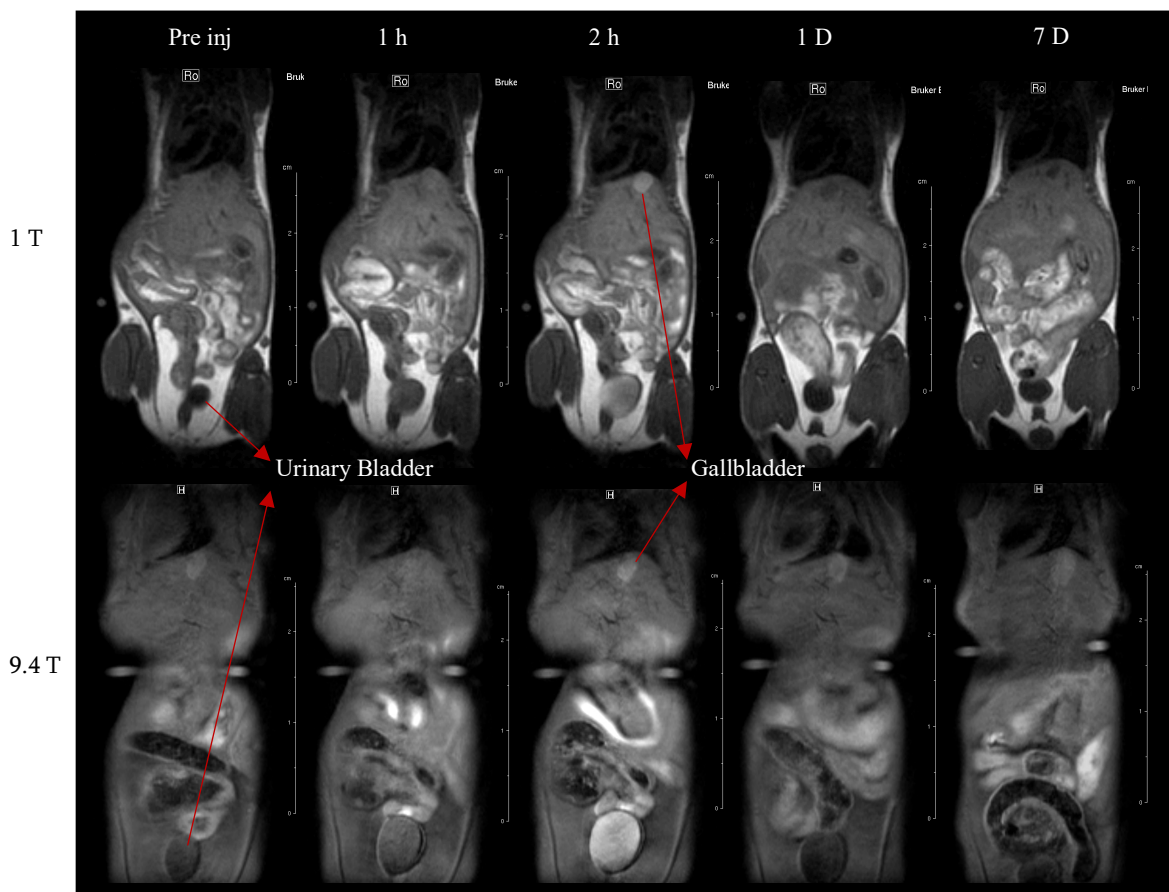


Figure AII.4. Enlightenment phenomenon of gallbladder and urinary bladder at two different magnetic fields induced by  $\text{MnL}_2\text{COO}^-$  over time.

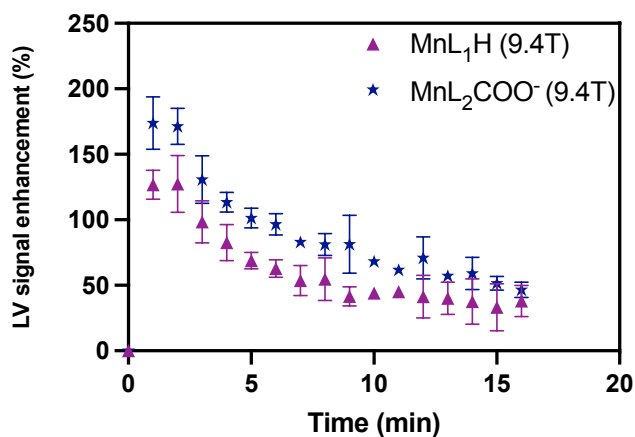


Figure AII.5. Dynamic rate of enhancement in the left ventricle (LV) of the heart for both ligands at 9.4 T, from injection to 16 minutes post-injection, showing a signal increase that is more pronounced for the second ligand in first minutes, followed by a progressive decrease of the signal ( $n = 3$  for both ligands).

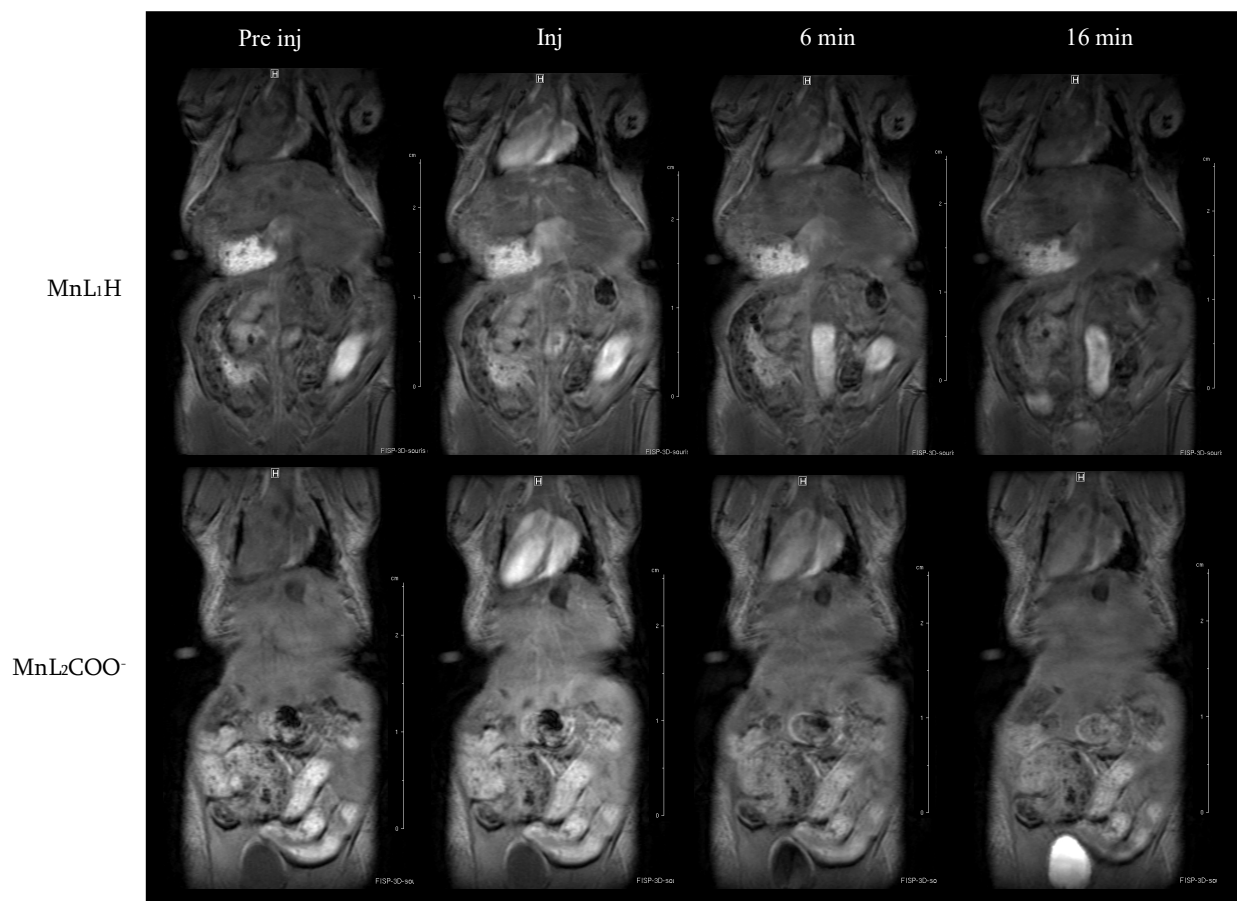


Figure AII.6. Dynamic MRI images (that consist of taking images each minute from the injection to approximately 20 min leading to the formation of a little movie allowing to follow the enlightenment) at pre-injection, during injection, 6 min and 16 min post-injection for both ligands at 9.4 T using FISP sequence.

## II.5. Materials and methods

### II.5.1 Chemical Materials

#### *II.5.1.1 Chemical and physical measurements*

The NMR spectra ( $^1\text{H}$ ,  $^{13}\text{C}$ , COSY, DEPT) were recorded at 298K and reported in ppm. (Bruker<sup>®</sup> AVANCEII-500 at 500 MHz, Bruker<sup>®</sup> AVANCE NEO at 400 MHz or Bruker<sup>®</sup> AVANCE NEO at 600 MHz, USA). The multiplicity of the peaks is defined as s (singlet), d (doublet), t (triplet) and m (multiplet). The reactions were monitored by mass spectrometry (Waters<sup>®</sup>, ZQ-2000, USA) and all the compounds were characterized by mass spectrometry (Waters<sup>®</sup> ZQ-2000, Waters<sup>®</sup> QDa, Waters<sup>®</sup> Quattro Premier or Waters<sup>®</sup> QTofUs, USA). The ESI-LRMS was performed on 3200 QTrap (AB Sciex). The pH was controlled by Mettler Toledo<sup>®</sup> fiveEasy pH/mV (Swiss). The relaxometry and NMRD profiles measurements were performed on Bruker<sup>®</sup> MiniSpec at 20 and 60 MHz at 37°C (USA) and on a fast field cycling (FFC) relaxometer between 0.02 and 40 MHz (Spinmaster, Stelar<sup>®</sup>, Italy).  $^{17}\text{O}$  NMR measurements were performed on a Bruker<sup>®</sup> AVANCEII-500 at 67.8 MHz. The MRI measurements were performed at 1T (Bruker<sup>®</sup> ICON, USA) and 9.4T (Bruker<sup>®</sup> Biospec, USA) with a Rapid Acquisition with Relaxation Enhancement sequence (RARE) (1T: TE = 12 ms, TR = 300 ms, resolution =  $258 \times 255 \mu\text{m}$ , RARE factor = 2, 8 averages, slice thickness = 1.25 mm; 9.4T: TE = 8 ms, TR = 389 ms, resolution  $172 \times 176 \mu\text{m}$ , RARE factor = 1, 4 averages, slice thickness = 1 mm, fat suppression) or with fast imaging with steady-state precession (FISP) (TE = 1.5 ms, TR = 4.4 ms, flip angle =  $15^\circ$ , 5 averages, resolution =  $125 \times 125 \times 1000 \mu\text{m}$ , 20 repetitions (4 before injection) were scanned for dynamic signal enhancement acquisitions (1 min time resolution). Image analysis was performed using ParaVision 5.1 (Bruker, USA) tools, by drawing of regions of interest in liver, kidney (pelvis and outer region (cortex possibly including OSOM (outer segment of outer medulla), gallbladder, when possible, vena cava (1T) or heart left ventricle (9.4T FISP images).

#### *II.5.1.2 Chemical material and methods*

The flash chromatography was performed on Biotage<sup>®</sup> flash chromatography using pre-packed cartridges. The collection is based on absorption at 254 and 270 nm by UV detection.

## II.5.2 Chemical Methods

## II.5.2.1 Synthesis of the lower part

2-Nitro[N(2{[(2-nitrophenyl)sulfonylamino]ethylamino})-ethyl]benzenesulfonamide *compound 2*: It is synthesized according to the protocol of Devreux *et al.*<sup>149</sup>

Benzyl N,N-bis(2-((2-nitrophenyl)sulfonylamino)ethyl)carbamate *compound 3*: DIPEA (7.7 mL, 44.2 mmol, 1.2 eq) is added to a solution of disulfonamido amine **2** (17.6 g, 37.1 mmol) in THF (100 mL), followed by benzyl chloroformate (6.3 mL, 44.1 mmol, 1.2 eq) in one portion. The reaction is stirred overnight during which insoluble matter appeared. The mixture is concentrated to dryness. The crude material is taken up in CH<sub>2</sub>Cl<sub>2</sub> (100 mL), and is washed with water (4 x 30 mL). The organic layer is dried then concentrated to dryness to afford the desired compound **2** as a brown oil (21.2 g, 34.8 mmol). Yield 94%. <sup>1</sup>H NMR (CDCl<sub>3</sub>, 400 MHz) δ (ppm): conformed to reported data of Kim *et al.*<sup>178</sup>

Di-*tert*-butyl 2,2'-((((benzyloxy)carbonyl)azanediyl)bis(ethane-2,1-diyl))bis

(azanediyl)diacetate *compound 5b*: A suspension of the previously prepared compound **3** (1.61 g, 2.65 mmol) with potassium carbonate (810 mg, 5.86 mmol, 2.2 eq) in acetonitrile (22 mL) is refluxed for 15 minutes. *tert*-Butyl bromoacetate (900 μL, 6.09 mmol, 2.3 eq) is added in one portion. The reaction is monitored by MS and/or TLC (Cyclohexane/AcOEt 1/1 v/v, UV detection). After 1.5h, total conversion of both the starting triamine **3**, and of the mono-*N*-alkylated intermediate **4a** is observed leading to the di-*N*-alkylated disulfonamide **4b**. The reaction mixture is cooled, and a second portion of potassium carbonate (1.60 g, 11.92 mmol, 4.4 eq) is added, followed by thiophenol (810 μL, 7.94 mmol, 3.0 eq) in one portion. The reaction is monitored by MS and/or TLC (Cyclohexane/AcOEt 1/1 v/v, UV detection; CH<sub>2</sub>Cl<sub>2</sub>/MeOH 97.5/2.5 v/v, UV and ninhydrin stain detection). After 2.5h, total conversion of the intermediate compounds **4b** and **5a** is obtained. The reaction mixture is allowed to cool to room temperature. Insoluble matter is filtered off through Celite<sup>®</sup>, and the organic filtrate is concentrated to dryness. The resulting canary yellow colored oil is purified by chromatography on silica gel (CH<sub>2</sub>Cl<sub>2</sub>/MeOH 10/0 to 8/2 v/v) and led to the desired product **5b** as an orange oil (1.051 g, 2.26 mmol). Yield 85%. <sup>1</sup>H NMR (CDCl<sub>3</sub>, 400 MHz) δ (ppm): 1.44 (s, 18H, -*t*Bu); 2.73-2.90 (m, 4H, -N-CH<sub>2</sub>-CH<sub>2</sub>-N-); 3.22-3.36 (m, 4H, -CH<sub>2</sub>-CO<sub>2</sub>*t*Bu); 3.44 (broad s, 4H, -N-CH<sub>2</sub>-CH<sub>2</sub>-N); 5.12 (s, 2H, -CH<sub>2</sub>-Ph); 7.26-7.38 (m, 5H, CH<sub>Ar</sub>). <sup>13</sup>C NMR (CDCl<sub>3</sub>, 100 MHz) δ (ppm): 28.1 (-*t*Bu); 47.7, 48.0, 48.2, and 48.5 (-N-CH<sub>2</sub>-CH<sub>2</sub>-N); 51.2 (-CH<sub>2</sub>-CO<sub>2</sub>*t*Bu); 67.3 (-

CH<sub>2</sub>-Ph); 81.6 (C<sub>quat</sub>tBu); 127.9, 128.0, and 128.6 (CH<sub>Ar</sub>); 136.7 (C<sub>quat</sub>Ph); 156.4 (-N-CO<sub>2</sub>Ph); 171.0 (-CO<sub>2</sub>tBu).

### II.5.2.2 Synthesis of the upper parts

2,6-Bis(bromomethyl)pyridine *compound 6a*: It is synthesized according to the protocol of Dioury *et al.*<sup>146</sup>

Ethyl ((2,6-bis(bromomethyl)pyridin-3-yl)oxy)acetate *compound 6b*: It is synthesized according to the protocol of Devreux *et al.*<sup>149</sup>

### II.5.2.3 Synthesis of MnPy(COO)<sub>2</sub>-H (Compound MnL<sub>1</sub>H)

Benzyl 3,9-bis(2-tert-butoxy-2-oxo-ethyl)-3,6,9,15-tetraazabicyclo[9.3.1] pentadeca-1(14),11(15),12-triene-6-carboxylate *compound 7a*: Solid Na<sub>2</sub>CO<sub>3</sub> (480 mg, 4.53 mmol, 4 eq) is added to a solution of diamine lower part **5b** (530 mg, 1.14 mmol) with 2,6-bis(bromomethyl)pyridine **6a** (401 mg, 1.52 mmol, 1.3 eq) in acetonitrile (115 mL). The suspension is refluxed until completion of the reaction (MS and/or TLC monitoring; 1 hour). The insoluble matter is filtered off, and the filtrate is concentrated to dryness. The crude material obtained is purified by chromatography on silica gel (CH<sub>2</sub>Cl<sub>2</sub>/MeOH, 100/0 to 98/2 v/v). to give the desired compound **7a** as a thick oil (253 mg, 0.445 mmol). Yield 39%. <sup>1</sup>H NMR (CDCl<sub>3</sub>, 400 MHz) δ (ppm): 1.43, and 1.44 (2 s<sup>#</sup>, 18H, -tBu); 2.68-2.90 (m, 4H, -N-CH<sub>2</sub>-CH<sub>2</sub>-N-); 3.16-3.27 (broad t, *J* 7-7.80 Hz, 4H, -N-CH<sub>2</sub>-CH<sub>2</sub>-N-); 3.34, and 3.41 (2 broad s<sup>#</sup>, 4H, -N-CH<sub>2</sub>-); 3.91-4.06 (m, 4H, -N-CH<sub>2</sub>-); 5.01 (s, 2H, -CH<sub>2</sub>-Ph); 7.13-7.31 (m, 7H, Ph, and -CH<sub>2</sub>-C(N)-CH=CH); 7.61 (t, *J* 7.6 Hz, 1H, -CH<sub>2</sub>-C(N)-CH=CH). <sup>#</sup>Double signal that may be due to rotamers (carbamate bond: free-rotation obstruction) <sup>13</sup>C NMR (CDCl<sub>3</sub>, 100 MHz) δ (ppm): 28.2 (-tBu); 44.9, and 45.3<sup>\$</sup> (-N-CH<sub>2</sub>-CH<sub>2</sub>-N-); 51.6, and 52.1<sup>\$</sup> (-N-CH<sub>2</sub>-CH<sub>2</sub>-N-); 59.0, and 59.2<sup>\$</sup> (-N-CH<sub>2</sub>-); 60.0, and 60.2<sup>\$</sup> (-N-CH<sub>2</sub>-); 66.8 (-CH<sub>2</sub>-Ph); 81.2 (C<sub>quat</sub>tBu); 122.9 (-CH<sub>2</sub>-C(N)-CH=CH); 127.6, 127.8, 128.4 (3 CH<sub>Ar</sub>Ph); 137.0 (C<sub>quat</sub>Ph); 137.5 (-CH<sub>2</sub>-C(N)-CH=CH); 156.1, 157.3, 157.7<sup>&</sup> (NCO<sub>2</sub>, and 2 C<sub>quat</sub>Pyr); 170.6 (CO<sub>2</sub>). <sup>\$</sup>Although the symmetrical structure, each <sup>13</sup>C appears to be diastereotopic; that may be due to rotamers from the carbamate bond (free-rotation obstruction). <sup>&</sup>Broad and small signal.

tert-Butyl 2-{9-[2-(tert-butoxy)-2-oxoethyl]-3,6,9,15-tetraazabicyclo[9.3.1] pentadeca-1(14),11(15),12-trien-3-yl}acetate *compound 8a*: Compound **7a** (240 mg, 0.42 mmol) is

solubilized in EtOH following by the addition of Pd/C (24 mg). The solution is stirred 10 days under H<sub>2</sub> at atmospheric pressure. Insoluble material is filtered through Celite<sup>®</sup> and the filtrate is concentrated at relatively high temperature to eliminate the toluene, which is the by-product, to give the desired compound **8a**. The crude product is directly engaged in the next synthesis step. <sup>1</sup>H NMR (CD<sub>3</sub>OD, 500 MHz)  $\delta$  (ppm) : 1.46 (s, 18H, -tBu); 2.64-3.01 (broad s, 4H, -N-CH<sub>2</sub>-CH<sub>2</sub>-N-); 3.31 (broad t, *J* 5.3 Hz 4H, -N-CH<sub>2</sub>-CH<sub>2</sub>-N-); 3.51 (s, 2H, N-CH<sub>2</sub>-N-); 3.99 (s, 4H, -CH<sub>2</sub>-CO<sub>2</sub>tBu); 7.01 (d, *J* 7.66 Hz, 1H, -CH=CH-CH=); 7.56 (t, *J* 7.65 Hz, 1H, -CH=CH-CH=).

2-[9-(Carboxymethyl)-3,6,9,15-tetraazabicyclo[9.3.1]pentadeca-1(14),11(15),12-trien-3-yl]acetic acid *compound 10a*: Compound **8a** (10 mg; 0.023 mmol) is solubilized in dichloromethane (1 mL) and stirred, followed by the addition of trifluoroacetic acid (1 mL). Overnight, the solution is concentrated and washed two times with diethylether (4 mL) to give the desired compound **10a** (12 mg, 0.018mmol). Yield 79.8 %. <sup>1</sup>H NMR (CD<sub>3</sub>OD, 500 MHz)  $\delta$  (ppm): 3.11 (broad t, *J* 5.21 Hz, 4H, -N-CH<sub>2</sub>-CH<sub>2</sub>-N-); 3.21 (broad t, *J* 5 Hz, 4H, -N-CH<sub>2</sub>-CH<sub>2</sub>-N-); 3.62 (s, 4H, -N-CH<sub>2</sub>-N-); 4.12 (s, 4H, -CH<sub>2</sub>-CO<sub>2</sub>tBu); 7.25 (d, *J* 7.71 Hz, 2H, CH=CH-CH=); 7.79 (t, *J* 7.7 Hz, 1H, -CH=CH-CH=).

2-(12-[[2-(2-aminoethyl)carbamoyle]methoxy]-9-(carboxymethyl)-3,6,9,15-tetraazabicyclo[9.3.1]pentadeca-1(15),11,13-trien-3-yl)acetic acid manganese *compound 11a*: A solution of MnCl<sub>2</sub>.4H<sub>2</sub>O (7 mg, 0.035 mmol) in water (0.5 mL) is added dropwise to a solution of compound **10a** (12 mg, 0.018 mmol) in water (1 mL). The pH is adjusted and maintained to 5 < pH < 6 with 0.1 M aqueous solution of NaOH. The mixture is warmed at 40°C overnight under Ar atm. The presence of free Mn<sup>2+</sup> is revealed by the colorimetric test with orange xylenol. The aqueous mixture is treated with Chelex<sup>®</sup> resin, then freeze-dried to give the desired compound **11a**. ESI-MS (C<sub>15</sub>H<sub>20</sub>MnN<sub>4</sub>O<sub>4</sub>): *m/z* 398.09 [M+Na]<sup>+</sup>.

#### II.5.2.4 Synthesis of MnPy(COO<sup>-</sup>)<sub>2</sub>-OCH<sub>2</sub>CO<sub>2</sub><sup>-</sup> (Compound MnL<sub>2</sub>COO<sup>-</sup>)

Benzyl 3,9-bis(2-tert-butoxy-2-oxo-ethyl)-12-(2-ethoxy-2-oxo-ethoxy)-3,6,9,15-tetraazabicyclo[9.3.1]pentadeca-1(14),11(15),12-triene-6-carboxylate *compound 7b*: Solid Na<sub>2</sub>CO<sub>3</sub> (466 mg, 4.40 mmol, 4 eq) is added to a solution of triamine lower part **5b** (513 mg, 1.10 mmol) with dibromomethyl compound **6b** (444 mg, 1.21 mmol, 1.1 eq) in acetonitrile

(110 mL). The suspension is refluxed until completion of the reaction (MS and/or TLC monitoring; 1 hour). The insoluble matter is filtered off, and the filtrate is concentrated to dryness. The crude material obtained is purified by chromatography on silica gel (CH<sub>2</sub>Cl<sub>2</sub>/MeOH, 100/0 to 98/2 v/v) to give the desired compound **7b** as a thick oil (471 mg, 0.702 mmol). Yield 64%. <sup>1</sup>H NMR (CDCl<sub>3</sub>, 400 MHz) δ (ppm): 1.27 (t, 3H, *J* 7.1 Hz, -Et); 1.45 (s, 9H, -tBu); 1.48 (s, 9H, -tBu); 2.68-3.01 (m, 4H, -N-CH<sub>2</sub>-CH<sub>2</sub>-N-); 3.20-3.55 (m, 8H, -N-CH<sub>2</sub>-CH<sub>2</sub>-N- (4H) and -N-CH<sub>2</sub>-); 3.95 (d, 2H, *J* 10.2 Hz, -N-CH<sub>2</sub>-); 4.19 (d, 2H, *J* 7.3 Hz, -N-CH<sub>2</sub>-); 4.24 (d, 2H, *J* 7.1 Hz, -Et); 4.66 (s, 2H, -O-CH<sub>2</sub>-CO<sub>2</sub>-Et); 5.04 (s, 2H, -CH<sub>2</sub>-Ph); 7.04 (d, *J* 8.4 Hz, 1H, -CH<sub>2</sub>-C(N)-CH=CH-C(OR) -C); 7.18 (broad dd, <sup>ξξ</sup> <sup>4</sup>*J* ≈ <sup>3</sup>*J* 8.4 Hz, 1H, -CH<sub>2</sub>-C(N)-CH=CH-C(OR) -C); 7.24-7.37 (m, 5H, -Ph). <sup>ξξ</sup>That resonance looks like a broad unsymmetrical triplet that can be attributed to a doublet of doublet with similar <sup>3</sup>*J* (8.4 Hz, vicinal coupling) and <sup>4</sup>*J* coupling constants; the unusually high long-range <sup>4</sup>*J* coupling constant (≈ 8.4 Hz) may be due to a pseudo W-conformation of the four sigma bonds between the two coupled <sup>1</sup>H. <sup>13</sup>C NMR (CDCl<sub>3</sub>, 100 MHz) δ (ppm): *Caution*: Some of the <sup>13</sup>C are doublet due to the presence of rotamers. 14.2 (CH<sub>3</sub>\_Et); 28.3 (CH<sub>3</sub>\_2 -tBu); 44.6, 45.0, 45.5, 46.1<sup>§§</sup> (2 -N-CH<sub>2</sub>-CH<sub>2</sub>-N-); 51.3, 51.8, 52.0, 52.4<sup>§§</sup> (2 -N-CH<sub>2</sub>-CH<sub>2</sub>-N-); 54.5, 54.6<sup>§</sup> (-N-CH<sub>2</sub>-); 58.7, 58.9, 59.5 (3 -N-CH<sub>2</sub>-); 61.6 (CH<sub>2</sub>\_Et); 65.8 (-O-CH<sub>2</sub>-CO<sub>2</sub>-Et); 66.8 (-CH<sub>2</sub>-Ph); 81.0, 81.2 (2 C<sub>quat</sub>tBu); 119.8, 119.9<sup>§</sup> (CH<sub>Ar</sub>Pyr); 123.8 (CH<sub>Ar</sub>Pyr); 127.6, 127.8, 128.5 (3 CH<sub>Ar</sub>Ph); 137.1 (C<sub>quat</sub>Ph); 147.6, 151.8<sup>ξ</sup>, 156.2 (NCO<sub>2</sub>, and 3 C<sub>quat</sub>Pyr); 166.4, 168.3, 170.7-170.9<sup>&</sup> (3 CO<sub>2</sub>). <sup>§</sup>Double signal for the assigned <sup>13</sup>C (rotamers); <sup>§§</sup>Double signal for each of the assigned <sup>13</sup>C; <sup>&</sup>Broad and small signal; <sup>ξ</sup>Higher signal than the adjacent one; may account for several <sup>13</sup>C.

Ethyl 2-({3,9-bis[2-(tert-butoxy)-2-oxoethyl]-3,6,9,15-tetraazabicyclo[9.3.1]pentadeca-1(15),11,13-trien-12-yl}oxy)acetate *compound 8b*: Compound **7b** (55 mg, 0.082 mmol, 1 eq) is solubilized in MeOH (20 mL) followed by the addition of Pd/C (6 mg). The solution is placed under H<sub>2</sub> at atmospheric pressure and is stirred during 24h. Insoluble material is filtered through Celite<sup>®</sup> and the filtrate is concentrated at relatively high temperature to eliminate the toluene, which is the by-product, to give the desired compound **8b**. The crude product is directly engaged in the next synthesis step. <sup>1</sup>H NMR (CD<sub>3</sub>OD, 500 MHz) δ (ppm) : 1.28 (t, *J* 7.15 Hz, 3H, -CH<sub>2</sub>-CH<sub>3</sub>); 1.46 (s, 9H, -tBu); 1.47 (s, 9H, -tBu); 3.07-3.12 (m, 4H, -N-CH<sub>2</sub>-CH<sub>2</sub>-N-); 3.16-3.21 (m, 4H, -N-CH<sub>2</sub>-CH<sub>2</sub>-N-); 3.47 (s, 2H, -N-CH<sub>2</sub>-N-); 3.52 (s, 2H, -N-CH<sub>2</sub>-N-); 3.96 (s, 2H, -N-CH<sub>2</sub>-CO-); 4.17 (s, 2H, -N-CH<sub>2</sub>-CO-); 4.23 (q, *J* 7.11 Hz, 2H, -O-CH<sub>2</sub>-CH<sub>3</sub>); 4.82 (s, 2H, -O-CH<sub>2</sub>-CO-); 7.11 (d, *J* 8.42 Hz, 1H, -O-C=CH-CH=C-); 7.27 (d, 1H, *J* 8.43 Hz, -O-C=CH-CH=C-).

2-({3,9-Bis[2-(tert-butoxy)-2-oxoethyl]-3,6,9,15-tetraazabicyclo[9.3.1]pentadeca-1(15),11,13-trien-12-yl}oxy)acetic acid *compound 9*: Compound **8b** (481 mg, 0.90 mmol, 1 eq) is solubilized in ethanol (7mL) and put under stirring. A solution of aqueous 1M NaOH is then added (1 mL, 1 mmol, 1.1 eq). The solution is stirred during few hours, then concentrated under vacuum. The crude product is purified by flash chromatography on RP18 column (MeOH/H<sub>2</sub>O from 3/7 to 10/0 v/v) to give the desired compound **9** (310 mg, 0.61 mmol). Yield 67%. <sup>1</sup>H NMR (CD<sub>3</sub>OD, 500 MHz)  $\delta$  (ppm): 1.47 (s, 9H, -*t*Bu); 1.47 (s, 9H, -*t*Bu); 2.99-3.06 (m, 4H, -N-CH<sub>2</sub>-CH<sub>2</sub>-N-); 3.11-3.16 (m, 4H, -N-CH<sub>2</sub>-CH<sub>2</sub>-N-); 3.26 (s, 2H, -N-CH<sub>2</sub>-N-); 3.53 (s, 2H, -N-CH<sub>2</sub>-N-); 3.94 (s, 2H, -N-CH<sub>2</sub>-CO-); 4.18 (s, 2H, -N-CH<sub>2</sub>-CO-); 4.46 (s, 2H, -O-CH<sub>2</sub>-CO-); 7.05 (d, 1H, *J* 8.41 Hz, -O-C=CH-CH=C); 7.11 (d, *J* 8.41 Hz, 1H, -O-C=CH-CH=C).

2-{{3,9-Bis(carboxymethyl)-3,6,9,15-tetraazabicyclo[9.3.1]pentadeca-1(15),11,13-trien-12-yl}oxy}acetic acid **10b**: The compound **9** (10 mg, 0.019 mmol) is solubilized in dichloromethane (1 mL) and put under stirring followed by the addition of trifluoroacetic acid (1 mL). The solution is stirred overnight. It is then concentrated and washed two times with diethyl ether (4 mL) to give the desired compound **10b** as TFA salt. <sup>1</sup>H NMR (CD<sub>3</sub>OD, 500 MHz)  $\delta$  (ppm): 3.08-3.14 (broad s, 4H, -N-CH<sub>2</sub>-CH<sub>2</sub>-N-); 3.18-3.26 (broad m, 4H, -N-CH<sub>2</sub>-CH<sub>2</sub>-N-); 3.62 (s, 2H, -N-CH<sub>2</sub>-N-); 3.69 (s, 2H, -N-CH<sub>2</sub>-N-); 4.06 (s, 2H, -N-CH<sub>2</sub>-CO<sub>2</sub>H); 4.27 (s, 2H, -N-CH<sub>2</sub>-CO<sub>2</sub>H); 4.82 (s, 2H, -O-CH<sub>2</sub>-CO<sub>2</sub>H); 7.19 (d, 1H, *J* 8.29 Hz, -O-C=CH-CH=C-); 7.34 (d, 1H, *J* 8.43 Hz, -O-C=CH-CH=C-).

2-(12-{{(2-aminoethyl)carbamoyl}methoxy}-9-(carboxymethyl)-3,6,9,15-tetraazabicyclo[9.3.1]pentadeca-1(15),11,13-trien-3-yl)acetic acid manganese *compound 11b*: A solution of MnCl<sub>2</sub>.4H<sub>2</sub>O (6 mg, 0.03 mmol) in water (0.5mL) is added dropwise to a solution of compound **10b** (11 mg, 0.016 mmol) in water (1 mL). The pH is adjusted and maintained to 5 < pH < 6 with 0.1 M aqueous solution of NaOH. The mixture is warmed at 40°C overnight under Ar atm. The presence of free Mn<sup>2+</sup> is revealed by the colorimetric test with orange xlenol. The aqueous mixture is treated with Chelex<sup>®</sup> resin, then freeze-dried to give the desired compound **11b**. ESI-MS (C<sub>17</sub>H<sub>22</sub>MnN<sub>4</sub>O<sub>7</sub>): *m/z* 472.10 [M+Na]<sup>+</sup>.

#### II.5.2.5 Synthesis of $MnPy(COO^-)_2-OCH_2CO_2NHCH_2CCH$ (Compound $MnL_3CH$ )

Tert-butyl 2-{9-[2-(tert-butoxy)-2-oxoethyl]-12-[[prop-2-yn-1-yl]carbamoyl]methoxy}-3,6,9,15-tetraazabicyclo[9.3.1]pentadeca-1(15),11,13-trien-3-yl}acetate *compound 12*: Compound **9** (10 mg, 0.019 mmol) and HBTU (15 mg, 0.04 mmol, 2.1 eq) are solubilized in  $CH_2Cl_2$  (2 mL) followed by the addition of propargylamine (2  $\mu$ L, 0.031 mmol, 1.6 eq) and DIPEA (8  $\mu$ L, 0.047 mmol, 2.47 eq). The solution is stirred during few hours at room temperature then the middle is washed three times with water (5 mL) to give the desired compound. The crude product is directly engaged in the next synthesis step.  $^1H$  NMR ( $CDCl_3$ , 500 MHz)  $\delta$  (ppm): 1.45 (s, 18H, *-tBu*) 2.22 (t,  $J$  2.56 Hz, 1H,  $-C\equiv CH$ ); 3.03-3.11 (m, 4H,  $-N-CH_2-CH_2-NH-$ ); 3.21-3.28 (m, 4H,  $-N-CH_2-CH_2-NH-$ ); 3.43 (s, 2H,  $-C-CH_2-N-$ ); 3.47 (s, 2H,  $-C-CH_2-N-$ ); 3.92 (s, 2H,  $-N-CH_2-CO-$ ); 4.08-4.16 (m, 4H,  $-N-CH_2-CO-$  and  $-NH-CH_2-C-$ ); 4.54 (s, 2H,  $-O-CH_2-CO-$ ); 7.02 (d,  $J$  8.39 Hz, 1H,  $-O-C=CH-CH=C-$ ); 7.07 (d,  $J$  8.39 Hz, 1H,  $-O-C=CH-CH=C-$ ).

2-[9-(Carboxymethyl)-12-[[prop-2-yn-1-yl]carbamoyl]methoxy}-3,6,9,15-tetraazabicyclo[9.3.1]pentadeca-1(15),11,13-trien-3-yl]acetic acid *compound 13*: Compound **12** (119 mg, 0.218 mmol) is solubilized in  $CH_2Cl_2$  (3 mL) and stirred followed by the addition of trifluoroacetic acid (3 mL). Overnight, the solution is concentrated and washed two times with diethyl ether to give the desired compound **13** as TFA salt.  $^1H$  NMR ( $CD_3OD$ , 500 MHz)  $\delta$  (ppm): 2.60 (t,  $J$  2.54 Hz, 1H,  $-C\equiv CH$ ); 3.10-3.16 (m, 4H,  $N-CH_2-CH_2-NH-$ ); 3.19-3.25 (m, 2H,  $N-CH_2-CH_2-NH-$ ); 3.25-3.30 (m, 2H,  $N-CH_2-CH_2-NH-$ ); 3.69 (s, 2H,  $-N-CH_2-C-$ ); 3.80 (s, 2H,  $-N-CH_2-C-$ ); 4.03 (d,  $J$  2.56 Hz, 2H,  $-NH-CH_2-C$ ); 4.15 (s, 2H,  $-N-CH_2-COOH$ ); 4.38 (s, 2H,  $-N-CH_2-COOH$ ); 4.71 (s, 2H,  $-O-CH_2-CO-$ ); 7.28 (d,  $J$  8.49 Hz, 1H,  $-O-C=CH-CH=C-$ ); 7.41 (d,  $J$  8.49 Hz, 1H,  $-O-C=CH-CH=C-$ ).

2-(12-[[2-Aminoethyl]carbamoyl]methoxy)-9-(carboxymethyl)-3,6,9,15-tetraazabicyclo[9.3.1]pentadeca-1(15),11,13-trien-3-yl]acetic acid manganese *compound 14*: A solution of  $MnCl_2 \cdot 4H_2O$  (4 mg, 0.02 mmol) in water (0.5 mL) is added dropwise to a solution of compound **13** (8 mg, 0.01 mmol) in water (1 mL). The pH is adjusted and maintained to  $5 < pH < 6$  with 0.1 M aqueous solution of NaOH. The mixture is warmed at  $40^\circ C$  overnight under Ar atm. The presence of free  $Mn^{2+}$  ions is revealed by the colorimetric test with orange xylenol. The aqueous mixture is treated with Chelex<sup>®</sup> resin, then freeze-dried to give the desired compound **14**. ESI-MS ( $C_{20}H_{25}MnN_5O_6$ ):  $m/z$  509.14  $[M+Na]^+$ .

*II.5.2.5 Synthesis of MnPy(COO-)-2-OCH<sub>2</sub>CO<sub>2</sub>NHCH<sub>2</sub>CH<sub>2</sub>NH<sub>2</sub> (Compound MnLANH<sub>3</sub><sup>+</sup>) : was synthesized by Dr Dioury F.*

Benzyl 12-[2-(2-aminoethylamino)-2-oxo-ethoxy]-3,9-bis(2-tert-butoxy-2-oxo-ethyl)-3,6,9,15-tetraazabicyclo[9.3.1]pentadeca-1(14),11(15),12-triene-6-carboxylate *compound 15*: A solution of the previously prepared ethyl ester **7b** (470 mg, 701 μmol) in ethylenediamine (2.3 mL, 34.4 μmol, 50 eq) is stirred at room temperature until completion of the reaction (MS monitoring; 1 hour). The crude medium is diluted in CH<sub>2</sub>Cl<sub>2</sub> (15 mL) and is washed with water (3 mL). The organic layer is dried then concentrated to dryness. The resulting material is purified by chromatography on silica gel (CH<sub>2</sub>Cl<sub>2</sub>/MeOH/NH<sub>3</sub> 7N in MeOH 95/2.5/2.5 to 90/5/5 v/v/v) and led to the desired product **15** as a beige solid (279 mg, 0.407 μmol). Yield 58%. <sup>1</sup>H NMR (CDCl<sub>3</sub>, 400 MHz) δ (ppm): 1.34-1.53 (m, 18H, -tBu); 1.94 (broad s, 2H, -NH<sub>2</sub>); 2.55-2.66 (m, 2H, -N-CH<sub>2</sub>-CH<sub>2</sub>-N-); 2.66-2.88 (m, 4H, -N-CH<sub>2</sub>-CH<sub>2</sub>-N(2H) and -CH<sub>2</sub>-NH<sub>2</sub>); 2.96-3.09 (m, 2H, -N-CH<sub>2</sub>-CH<sub>2</sub>-N-); 3.28-3.50 (m, 8H, -CO-NH-CH<sub>2</sub>-, -N-CH<sub>2</sub>- (4H), -N-CH<sub>2</sub>-CH<sub>2</sub>-N- (2H)); 3.89 and 3.93 (2 br s<sup>§</sup>, 2H, -N-CH<sub>2</sub>-); 4.02 and 4.05 (2 br s<sup>§</sup>, 2H, -N-CH<sub>2</sub>-); 4.56 (broad s, 2H, -O-CH<sub>2</sub>-); 5.01 (s, 2H, -CH<sub>2</sub>-Ph); 7.16 (d, *J* 8.4 Hz, 1H, -CH<sub>2</sub>-C(N)-CH=CH-C(OR)-C); 7.21-7.33 (m, 6H, -CH<sub>2</sub>-C(N)-CH=CH-C(OR)-C, and Ph); 8.15, and 8.25<sup>§</sup> (2 broad t, 1H (≈53/47), -CO-NH-). <sup>§</sup>Double signal due to two conformers (double-bond character of the amide bond: *cis* and *trans* conformations) or two rotamers (free rotation obstruction due to Cbz steric hindrance). <sup>13</sup>C NMR (CDCl<sub>3</sub>, 100 MHz) δ (ppm): *Caution*: As previously observed for the precursor **7b**, nearly all of the <sup>13</sup>C are doublet due to the presence of rotamers (double bond character of the amide bond and/or free-rotation obstruction of the carbamate bond). 28.18, 28.23 (CH<sub>3</sub>-tBu); 41.8, 42.1, 42.2, 42.3 (-CO-NH-CH<sub>2</sub>-CH<sub>2</sub>-NH<sub>2</sub>)<sup>#</sup>; 44.9, 45.4 (-N-CH<sub>2</sub>-CH<sub>2</sub>-N-)<sup>#</sup>; 50.9, 51.0, 51.6, 51.8 (2 -N-CH<sub>2</sub>-CH<sub>2</sub>-N-)<sup>#</sup>; 54.2, 54.5 (-N-CH<sub>2</sub>-)<sup>#</sup>; 58.8, 59.0, 59.1, 59.4 (-N-CH<sub>2</sub>-CH<sub>2</sub>-N-, and 3 -N-CH<sub>2</sub>-); 66.9 (-CH<sub>2</sub>-Ph); 67.2 (-O-CH<sub>2</sub>-); 81.2, 81.47, 81.52 (2 C<sub>quat</sub>tBu)<sup>§</sup>; 119.65, 119.68 (-CH<sub>2</sub>-C(N)-CH=CH-C(OR)-C)<sup>#</sup>; 124.97, 125.01 (-CH<sub>2</sub>-C(N)-CH=CH-C(OR)-C)<sup>#</sup>; 127.57, 127.65, 127.83, 127.90, 128.46 (3 CH<sub>Ar</sub>Ph)<sup>§</sup>; 136.85, 136.94 (C<sub>quat</sub>Ph)<sup>#</sup>; 145.9, 146.1, 149.2, 149.7, 151.7, 151.8, 155.9, 156.0 (-N-CO<sub>2</sub>, and 3 C<sub>quat</sub>Pyr)<sup>#</sup>; 168.21, 168.24, 170.4, 170.6, 170.7, 170.8 (2 CO<sub>2</sub>, and CONH)<sup>#</sup>. <sup>#</sup>Double signal for (each of) the assigned <sup>13</sup>C (rotamers); <sup>§</sup>Double signal for at least one of the assigned <sup>13</sup>C.

2-(12-{[(2-Aminoethyl)carbamoyl]methoxy}-9-(carboxymethyl)-3,6,9,15-tetraazabicyclo[9.3.1]pentadeca-1(15),11,13-trien-3-yl)acetic acid *compound 16a.xHBr*: A concentrated solution of the fully protected precursor **15** previously prepared (210 mg, 0.307 μmol) in CH<sub>2</sub>Cl<sub>2</sub> (0.250 mL) is diluted in acetic acid (2 mL). A solution of hydrogen

bromide in acetic acid (33% w/w, 0.500 mL) is then added and a white precipitate appeared instantly. The mixture is vigorously stirred and heated at 70°C for 7 hours and then at room temperature overnight. The dark orange supernatant is removed by suction and the solid material is washed several times with Et<sub>2</sub>O until a clear wash is obtained. The organic solvents are completely removed first under reduced pressure and then by freeze-drying after solubilization in water to give the desired compound as a brownish solid material (200 mg, 0.288 mmol on the basis of an estimated PM = 693.38 for 3HBr/4HBr hydrobromide forms in 85/15 mol/mol at pH 0.7<sup>1</sup>). Yield (crude) 94%. The crude material can be purified by chromatography on RP18 (CH<sub>3</sub>CN/H<sub>2</sub>O 9/1 v/v) after raising the pH from 0.7 to about 4.5 (NaOH<sub>aq</sub>) and leads to the desired product as a beige solid (115 mg, 0.221 mmol on the basis of an estimated PM = 516.97 for .1HBr/.0HBr/.2HBr hydrobromide forms in 73/15/12 mol/mol/mol at pH 4.5<sup>1</sup>). Yield 72%. <sup>1</sup>H NMR (D<sub>2</sub>O, pH<1) δ (ppm): 3.14 (broad t, 2H, -CH<sub>2</sub>-NH<sub>2</sub>-); 3.20-3.38 (m, 6H, -N-CH<sub>2</sub>-CH<sub>2</sub>-NH-); 3.44 (broad s, 2H, -N-CH<sub>2</sub>-CH<sub>2</sub>-N-); 3.56 (broad t, 2H, -CO-NH-CH<sub>2</sub>-); 4.00 (s, 2H, -N-CH<sub>2</sub>-); 4.06 (s, 2H, -N-CH<sub>2</sub>-); 4.47 (s, 2H, -N-CH<sub>2</sub>-); 4.65 (s, 2H, -N-CH<sub>2</sub>-); 4.80\* (2H, -O-CH<sub>2</sub>-CO-N-); 7.57 (d of AB system, J 8.4 Hz, 1H, CH<sub>Ar</sub>); 7.71 (d of AB system, J 8.4 Hz, 1H, CH<sub>Ar</sub>). \*Fully superimposed with the deuterated solvent (deduced from corr <sup>1</sup>H/<sup>13</sup>C 2D experiment). <sup>13</sup>C NMR (D<sub>2</sub>O, pH<1): 36.6 (-CO-NH-CH<sub>2</sub>-); 39.0 (-CH<sub>2</sub>-NH<sub>2</sub>-); 43.7, 43.9 (2 -N-CH<sub>2</sub>-CH<sub>2</sub>-NH-); 51.0, 52.2 (2 -N-CH<sub>2</sub>-CH<sub>2</sub>-NH-); 54.0, 56.7, 57.1, 57.4 (4 -N-CH<sub>2</sub>-); 67.3 (-O-CH<sub>2</sub>-CO-N-); 125.0 (2 CH<sub>Ar</sub>); 142.1, 144.3, 152.0 (3 C<sub>quat</sub>Pyr); 170.6, 172.2, 172.3 (2 CO<sub>2</sub>, and -CO-NH-).

2-(12-[[2-(2-aminoethyl)carbamoyl]methoxy]-9-(carboxymethyl)-3,6,9,15-tetraazabicyclo[9.3.1]pentadeca-1(15),11,13-trien-3-yl)acetic acid manganese compound **17**: A solution of the previously prepared ligand **16a.xHBr** (~0.17 mmol) in deionized H<sub>2</sub>O (3 mL) is adjusted to pH ~ 5.5 with an aqueous solution of NaOH. Manganese(II) chloride tetrahydrate (33 mg, 0.168 mmol) is added in one portion which immediately induced a decrease of pH down to 2.2. The pH is carefully adjusted again to ~ 5.7 with aqueous NaOH. The resulting mixture is stirred at room temperature for 5 minutes. A monitoring by MS indicated a total conversion to the desired manganese complex with no trace of free ligand. The pH is then raised

---

<sup>1</sup> Note: Chemicalize was used for prediction of pK<sub>a</sub>s and speciation curves (December, 2019; <https://chemicalize.com/>, developed by ChemAxon): at highly acidic pH<1, species charged +3 and +4 are predominant for compound **16a** (85%, and 15% respectively at pH 0.7); at pH 4.5 (chromatographed solution), species charged +1, neutral, and charged +2 are predominant for compound **16a** (73%, 15%, and 12% respectively).

up to  $\sim 7.5$  ( $\text{NaOH}_{\text{aq}}$ ) and stirring maintained overnight. The fine brown precipitate formed is filtered off over a  $0.2 \mu\text{m}$  membrane (PALL<sup>®</sup>, Acrodisc<sup>®</sup>). The filtrate is concentrated by freeze-drying. The solid obtained (113 mg) is purified by chromatography on RP18 ( $\text{MeOH}/\text{H}_2\text{O}$  9/1 v/v) and leads to the desired product **17** as a beige solid (108 mg,  $x \text{H}_2\text{O} \cdot y \text{HCl}$  or  $\text{NaCl}$  probable form(s)). ESI-LRMS  $m/z$ : 492.2  $[\text{M}+\text{H}]^+$ , 514.1  $[\text{M}+\text{Na}]^+$ .

#### II.5.2.6 Determination of $\text{Mn}^{2+}$ concentration for relaxometric and $^{17}\text{O}$ measurements

The detection of free manganese ions is performed with the xylenol orange test. To do so, 300  $\mu\text{L}$  of phosphate or acetate buffer, one drop of pyridine, one drop of the compound solution and one drop of xylenol orange (0.1 g per 100 mL). The color is pink or orange for phosphate or acetate buffer respectively without manganese ions and gets purple when free manganese ions are present. The solution is then treated with a Chelex<sup>®</sup> 100 resin (sodium form) to eliminate those free ions.

The  $\text{Mn}^{2+}$  concentration determination is performed either by relaxometry or ICP-AES, on samples digested with nitric acid. The first method consists in measuring the water paramagnetic longitudinal relaxation rate of the digested solution at 20 MHz. It is then compared to the paramagnetic relaxation rate of a 1 mM solution of free manganese ions ( $R_1 = 8 \text{ s}^{-1}$  at 20 MHz and  $37^\circ\text{C}$ ) in order to extract the manganese concentration.<sup>120</sup> To ensure the results, ICP-AES measurements are also performed on a Varian Liberty Series II, based on a  $\text{Mn}^{2+}$  calibration curve. The concentrations obtained respectively from ICP-AES or relaxometry methods are respectively 1.80 and 1.76 mM ( $\text{MnL}_1\text{H}$ ), 5.09 and 5.66 mM ( $\text{MnL}_2\text{COO}^-$ ), 7.85 and 8.05 mM ( $\text{MnL}_3\text{CH}$ ), and 2.47 and 2.35 mM ( $\text{MnL}_4\text{NH}_3^+$ ).

#### II.5.2.7 Relaxometry measurement

The longitudinal relaxation times ( $T_1$ ) are determined at 20 MHz and 60 MHz on Bruker<sup>®</sup> Minispec mq20 and mq60 relaxometers (USA). These measurements allow to obtain the relaxivity of the complexes according to the following equation  $r_1 = \frac{(\frac{1}{T_1}) - R_1^{\text{d}}(\text{water})}{[\text{Mn}_{\text{complex}}^{2+}]} \text{ s}^{-1} \cdot \text{mM}^{-1}$

<sup>1</sup>(3) where  $R_1^{\text{d}}(\text{water}) = 0.2826 \text{ s}^{-1}$  at  $37^\circ\text{C}$ .

The NMRD profiles were recorded at  $37^\circ\text{C}$  and  $25^\circ\text{C}$  on a Stelar<sup>®</sup> fast field cycling (FFC) relaxometer (Stelar, Mede, Italy) and the least-squares fitting of the data was performed using a home-made program (Fitting2000) and equations from the Salomon and Bloembergen (SBM) theory.

### II.5.2.8 Temperature dependent $^{17}\text{O}$ NMR measurements

The transverse  $^{17}\text{O}$  relaxation rates ( $R_2=1/T_2$ ) are measured in aqueous solutions of each manganese complex ( $\text{MnL}_1\text{H}$ ; 2.06 mM,  $\text{MnL}_2\text{COO}^-$ ; 2.58 mM,  $\text{MnL}_3\text{CH}$ : 2.05 mM and  $\text{MnL}_4\text{NH}_3^+$ : 1.21 mM) in the temperature range 7 – 81°C, on a Bruker® AvanceII-500 (USA) (11.75 T, 67.8 MHz) spectrometer. The temperature is calculated according to a previous calibration with ethylene glycol and methanol. Proton decoupling is applied during all the acquisitions. Transverse relaxation times ( $T_2$ ) are obtained by the measurement of the signal width at mid-height. For the determination of  $\tau_M$ , the data are presented as the reduced transverse relaxation rate  $R_2^R=1/T_2^R= 55.55R_2^P /([\text{Mn}_{\text{complex}}]\cdot q)$ , where  $[\text{Mn}_{\text{complex}}]$  is the molar concentration of the complex,  $q$  is the number of coordinated water molecules and  $R_2^P$  is the paramagnetic transverse relaxation rate obtained after subtraction of the diamagnetic contribution from the observed relaxation rate. The treatment of the experimental data is performed as already described and the fitting of the data is obtained with a home-made program.<sup>179</sup>

For the determination of the number of coordinated water molecules, the data are presented as the transverse relaxivity  $r_2 = R_2^P/[\text{Mn}_{\text{complex}}]$  where the concentration of the Mn-complex is expressed in millimolar ( $\text{mmol}\cdot\text{L}^{-1}$ ).

### II.5.2.9 Transmetalation

The transmetalation is performed in a phosphate buffer solution (pH 7.06) and on the Bruker® Minispec mq20 relaxometer (USA). 300  $\mu\text{L}$  of a solution of each complex at a concentration of 2.5 mM is prepared in a phosphate buffer ( $[\text{NaH}_2\text{PO}_4] = 0.026 \text{ mol/L}$  et  $[\text{Na}_2\text{HPO}_4] = 0.041 \text{ mol/L}$ ) and 3  $\mu\text{L}$  of a 250 mM  $\text{ZnCl}_2$  solution (1 eq) is added in the studied Mn-complexes solutions. Then, the longitudinal relaxation time ( $T_1$ ) is measured as a function of time to obtain the evolution of  $R_1^P$  following the equation:  $R_1^P = \left(\frac{1}{T_1}\right) - R_{1(\text{water})}^d$  (4) where  $R_{1(\text{water})}^d = 0.2826 \text{ s}^{-1}$  is the diamagnetic contribution. During 5 days, the ratio  $R_1^P/R_{1^P(t=0)}$  is determined at regular intervals to evidence the transmetalation kinetics induced by the presence of zinc cations, which could lead to a release of manganese ions and their precipitation by phosphates. This release induces the formation of a precipitate of either  $\text{Mn}_3(\text{PO}_4)_2$  or  $\text{MnPO}_4$ , which leads to a decrease of the paramagnetic relaxation rate.<sup>164</sup>

#### *II.5.2.10 Cyclic voltammetry measurements*

The cyclic voltammetry was performed on a potentiostat/galvanostat (SP-150e, Bio-Logic Science Instruments, France). Measurements were performed in a small cell (QVMF2141, ProSense<sup>®</sup>, The Netherlands). The semi-permeable membranes were at first immersed in 5 M NaOH. Complexes were dissolved in 500  $\mu$ L of 5M NaOH solution and placed in the small cell immersed in 5M NaOH solution. Three-electrodes cells with Ag/AgCl<sub>(aq)</sub> as reference electrode, Pt as working electrode and Pt wire as counter electrode were used. Measurements were recorded from -2.5 V to 2.5 V at a scan rate of 50 mV/s.

### II.5.3 Biological material and methods

#### *II.5.3.1 Mouse strains and housing conditions*

Female 6 weeks old Balb/c mice (13 for MRI and 3 for control sampling) were purchased from Charles River (Ecully, France) and kept under individually ventilated cage (IVC) housing conditions (12 h / 12 h night and day cycles,  $22 \pm 2^\circ\text{C}$ ,  $55 \pm 10\%$  relative humidity) and were given dry food and water ad libitum. All experiments were performed in accordance with EU Directive 2010/63/EU for animal experiments and were approved by the CEBEA (Comité d'Ethique et du Bien-Etre Animal) of the CMMI under approval numbers CMMI-2021-01. At the end of experiments, mice were sacrificed by cervical dislocation.

#### *II.5.3.2 In vivo images*

The MRI experiments were performed at 1T (Bruker<sup>®</sup> ICON, USA) and 9.4T (Bruker<sup>®</sup> Biospec, USA) with a Rapid Acquisition with Relaxation Enhancement sequence (RARE) (1T: TE = 12 ms, TR = 300 ms, resolution =  $258 \times 255$  microns, RARE factor = 2, 8 averages, slice thickness = 1.25 mm; 9.4T: TE = 8 ms, TR = 389 ms, resolution  $172 \times 176$  microns, RARE factor = 1, 4 averages, slice thickness = 1 mm, fat suppression) or with fast imaging with steady-state precession (FISP) (TE = 1.5 ms, TR = 4.4 ms, flip angle =  $15^\circ$ , 5 averages, resolution =  $125 \times 125 \times 1000$   $\mu\text{m}$ , 20 repeats (4 before injection) were scanned for dynamic signal enhancement acquisitions (1 min time resolution)). Image analysis was performed using ParaVision<sup>™</sup> 5.1 (Bruker, USA) tools, by drawing of regions of interest in liver, kidney (pelvis and outer region (cortex possibly including OSOM (outer segment of outer medulla), gallbladder, when possible, *vena cava* (1T) or heart left ventricle (9.4 T FISP images).

### *II.5.3.3 Mice sacrifice and plasma collection*

Retro-orbital blood collection was performed under deep isoflurane anesthesia. Mice were then sacrificed immediately by cervical dislocation. Blood samples were centrifuged for 10 min at 10,000 rpm to separate the plasma from the cellular fraction. At least 250  $\mu$ L of plasma had to be obtained for dosage of several toxicity markers using Spotchem EZ Sp-4430 (Arkay<sup>S</sup>) colorimeter. “Panel-1” and “Panel-2” strip sets were used and one relevant marker of each was considered to identify possible tissue or organ damages (with glutamate oxaloacetate transaminase (GOT), glutamate pyruvate transaminase (GPT) and lactate dehydrogenase (LDH)) and kidney (with blood urea nitrogen (BUN)) damages, as a preliminary (due to a limited amount of mice) assessment.



# Chapter III

## Chapter III

---

### **Chapter III: Synthesis and characterization of pH-sensitive polymeric nanocarriers self-assembly and their in vitro and in vivo evaluation.**

#### **III.1 Introduction**

There is a growing interest in nanomedicine in the research world due to their tunability. Indeed, the nanostructures can be used for both diagnosis and treatment, a property usually coined by the term “theranostic”. Moreover, the developed drug delivery nanosystems can also be designed to increase the bioavailability of the active drug in the organism. Furthermore, many efforts are allocated to their design and characterization to obtain a final nanostructure dedicated to the intended application.<sup>13</sup> Polymer nanoparticles, including polymer micelles and polymersomes, seem to be a good option for specific drug delivery since they can endow the system with responsiveness to different internal parameters such as pH, temperature, redox potential and so on, or by using an external field (electric, magnetic, light, X or gamma rays...). Among many compositions, some polymers have already shown their biocompatibility like poly(ethylene oxide) (PEO), as well as their biodegradability and biocompatibility like poly( $\epsilon$ -caprolactone) (PCL), poly(lactic) acid (PLA), poly(lactic-*co*-glycolic acid) (PLGA), .... Various polymeric nanoparticles are already used for different therapeutic areas and drug delivery as theranostic platforms such as those based on PEO-polyesters diblock copolymers which are currently in phase 3 clinical trials or even on the market.<sup>38,77,87</sup>

As explained in chapter I, this work focuses on a drug already used in medicine which is the doxorubicin, a chemotherapeutic agent. As a reminder, multiple injections lead to a lot of side effects and multidrug resistance, that is why using nanoparticles for its administration could be an alternative. On the market, the Doxil<sup>®</sup>, a pegylated liposome loaded with doxorubicin, is already approved by the FDA. But as discussed previously, liposomes have a high permeability and a low stability that cannot be easily mitigated due to their low chemical versatility.<sup>36</sup> Therefore, an improvement of these systems seems to be necessary.

In this work, it is proposed to induce the drug delivery of doxorubicin using pH stimulus. As a reminder, polyester moieties such as, PCL and PLA, are pH-sensitive due to the acidic catalyzed hydrolysis of the ester function. These responsive functions can induce a self-portion of the membrane encapsulating the drug in these nanostructures. (Figure III.1)<sup>180</sup>

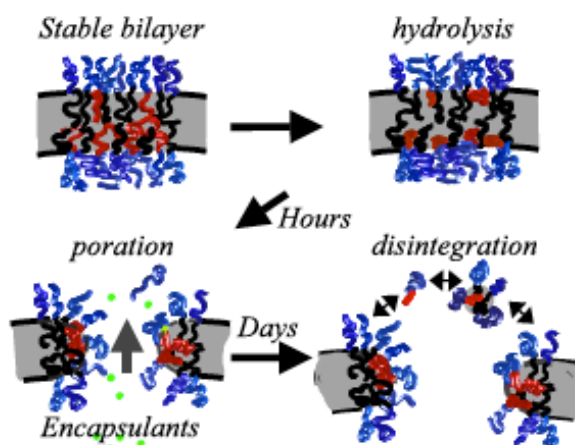


Figure III.1. Representation of bilayer undergoing hydrolysis of polyester function leading in few hours to poration that delivered the encapsulated species, and in few days to the disintegration of the bilayer.<sup>180</sup>

Different recent systems based on the polyester structure were described in chapter I, giving an overview of all possibilities brought by this type of moiety. Nevertheless, PCL possesses a slow rate of degradation through hydrolysis due to its high hydrophobicity and its crystallinity. Using it conjointly with PLA moiety should auto-catalyze the degradation of the PCL chains by the increasing presence of lactic acid.<sup>181</sup> In this way of action, two possibilities can be used: mixing of two different amphiphilic copolymers or synthesis of multiblock copolymers. Khodaverdi *et al.* developed polymersomes and micelles loaded with docetaxel, as chemotherapeutic agent, made of a blend of PEG-PCL and PEG-PLA. They used different fractions in PEG-PLA from 0 to 100 % per step of 25% to form micelles or polymersomes by single emulsion-solvent evaporation. The chains used for micelles (size: 30-50 nm) were composed of PEG<sub>5k</sub>-PCL<sub>5k</sub> and/or PEG<sub>5k</sub>-PLA<sub>5k</sub> whereas for polymersomes (size 140-180 nm), PEG<sub>5k</sub>-PCL<sub>15k</sub> and/or PEG<sub>5k</sub>-PLA<sub>15k</sub> were used. They highlighted that the lowest burst release for both structures occurs for a ratio of 75/25% but these polymersomes also exhibit the largest toxicity on cells. On the other hand, micelles and polymersomes made only with PLA based copolymers exhibit the highest burst release. Therefore, the balance ratio between both copolymers has a clear impact on the drug release. It is also important to note that the drug used in this work is hydrophobic. Finally, the zero-order and Higuchi model used to fit the release data enabled

them to highlight the involved diffusion mechanism.<sup>182</sup> On their side, Goyal *et al.* developed polymersomes based on a triblock copolymer, PEG-SS-PLA-PCL-OH, loaded with bacoside and SPIONs, and conjugated with lactoferrin. Interestingly, the disulfide bonds incorporated between the PEG and PLA moieties endow the system with redox responsiveness *via* the glutathione (GSH). They first evidenced the accumulation of their nanostructure in the brain thanks to the loaded SPIONs, which allow the observation by MRI of a  $T_2$  signal up to 48 hours. Then, they evaluated the drug release and evidenced that, at pH 6.6, a release of 63.4% occurs instead of 35.0% at pH 7.4, and it is increased to 69.5% and 72.4% respectively in the presence of GSH.<sup>181,183</sup>

A last strategy is to synthesize hydrophobic chains composed of both CL and LA. Based on it, Chu *et al.* synthesized MPEG-P(CL-*co*-LA) (MPEG<sub>2k</sub>-PCL/LA<sub>2k</sub>) giving micelles loaded with docetaxel obtained by thin film rehydration, with critical micelle concentration (CMC) as low as 0.005 mg/mL. The hydrophobic chains were synthesized in different ratios of the LA moiety, from 0 to 100 %, giving micelles with a size of *ca.* 25 nm. They evidenced several things such as faster degradation correlated with an increase of LA content, no difference in drug loading content (DLC) and encapsulation efficiency (EE) as a function of LA ratio, and an increase of docetaxel internalization in cells compared to free docetaxel.<sup>184</sup> A triblock system composed of P(CL-*co*-LA)-*b*-PEG-*b*-P(CL-*co*-LA) can also be used, as developed by Yang *et al.*, giving polymersomes obtained by the double-emulsion route, loaded with hemoglobin (Hb) as oxygen carrier. Three different triblocks were synthesized in different fractions, leading to a size of *ca.* 170 nm. The Hb loading was tuned by using different solvent ratios and compositions (this modification also impact the size of the particles), leading to EE values up to 67.5%.<sup>185</sup>

All those information, developed in chapter I and above, leave to think that micelles and polymersomes made of polyester moieties lead to interesting nanostructures able to undergo a disruption by an endogenous stimulus.

## III.2. Results and discussion

### III.2.1. Synthesis and characterization of diblock copolymers, PEO-*b*-PCL

To form polymeric vesicles, also called polymersomes, an amphiphilic polymer is needed, which is a sequenced copolymer composed of a hydrophilic and a hydrophobic segment in the chain, in different proportions. Since these nanoobjects will be used for targeted drug-delivery, it is necessary to use a stimuli-responsive polymer allowing to deliver a chemotoxic drug under particular physicochemical conditions. In the case of tumor environment, a signal that can be used is the significant decrease of pH ascribed to the specific tumor cell physiology, related to their fast growth in a usually hypoxic condition.<sup>186</sup> Well-known biocompatible polyester able to respond to such a stimulus is poly( $\epsilon$ -caprolactone) (PCL). Indeed, PCL undergoes acidic catalyzed hydrolysis of the ester function leading to the degradation of the PCL chain. The other block (*i.e.*, the hydrophilic part) of the copolymer is usually constituted of PEO chain for previously discussed reasons. For our study, at first, commercial PEO-*b*-PCL batches were purchased from Polymer Source (Canada) or Sigma Aldrich® (France). However, these commercial copolymers were of poor quality. Indeed, SEC analysis shows different distributions and <sup>1</sup>H NMR analysis evidences the presence of impurities. Therefore, it was decided to synthesize tailored copolymers instead, and to focus on a structure composed for the hydrophobic block of polycaprolactone (PCL).

Table III.1. Structure of PEO-*b*-PCL copolymers from literature and used in this work (either commercial or synthesized). \* from SEC  $\perp$  from NMR. The degrees of polymerizations (DP) of each block were calculated using the monomer molar masses, respectively 114 g·mol<sup>-1</sup> for CL and 44 g·mol<sup>-1</sup> for EO.

$M_w^*$ (g/mol)	$\bar{D}^*$	$M_n^*$ (g/mol)	DP <sub>CL</sub>	DP <sub>EO</sub>	$M_n^{\text{PCL}\perp}$ (g/mol)	$M_n^{\text{PEO}\perp}$ (g/mol)	$f_{\text{hydrophilic}}$ (%)	References
38749	1.4	26770	143	70	16016	3080	16	Commercial (Polymer Source P19769-EOCL)
25217	1.4	18012	114	114	12996	5016	28	commercial (Aldrich 570311)
48154	1.6	30096	220	114	25080	5016	17	commercial (Aldrich 799033)
29770	1.8	16370	126	142	16188	5544	25	synthesized in Mons
46918	1.7	27002	124	190	21660	5456	20	synthesized in Mons
18981	1.23	15432	118	45	13452	1980	13	Hocine <i>et al.</i> <sup>187</sup>
20606	1.08	19080	150	45	17100	1980	10	Konishcheva <i>et al.</i> <sup>188</sup>
11465	1.58	7256	53	28	6042	1214	17	Konishcheva <i>et al.</i> <sup>188</sup>
7820	1.4	5586	5	114	570	5016	90	Šachl <i>et al.</i> <sup>189</sup>
9097	1.4	6498	13	114	1482	5016	77	Šachl <i>et al.</i> <sup>189</sup>
12130	1.4	8664	32	114	3648	5016	58	Šachl <i>et al.</i> <sup>189</sup>

### III.2.1.1 Determination of the composition of the PEO-*b*-PCL by <sup>1</sup>H NMR

Two copolymers with two different polymerization degrees (DP) were synthesized by Prof O. Coulembier and S. Moins at the SMPC laboratory, UMONS, by ring opening polymerization (ROP) of  $\epsilon$ -CL by a MPEG-OH macroinitiator of  $M_n = 5000$  g·mol<sup>-1</sup> using 1,5,7-triazabicyclo 4.4.0 dec-5-ene (TBD) as organic catalyst of the reaction.

Analysis of <sup>1</sup>H NMR spectra allows to determine approximately the DP of the copolymers. (Figure III.2 ; Figure III.3) The spectrum is calibrated on the chain end of the polyethylene oxide (PEO) moiety, which is a -CH<sub>3</sub>. This peak represents 3 protons under the form of a singlet

(peak **a** at  $\delta = 3.37$  ppm), which is usually well defined. The  $DP_{EO}$  can be obtained according to the following equation:

$$DP_{EO} = (I_{3.63 \text{ ppm}})/4 \quad (\text{Equation III.1})$$

The DP of the PCL chain can be obtained with Equation III.2. Peak **f** at  $\delta = 4.05$  ppm is ascribed to 2 protons present on the poly( $\epsilon$ -caprolactone) chain.

$$DP_{CL} = (I_{4.05 \text{ ppm}})/2 \quad (\text{Equation III.2})$$

Figure III.2 allows extracting the DP of each block of the first polymer giving  $DP_{EO}$  ( $n \sim 126$ ) as  $5.5 \text{ kg.mol}^{-1}$  and  $DP_{CL}$  ( $m \sim 142$ ) as  $16.2 \text{ kg.mol}^{-1}$ , where  $n$  and  $m$  stand for formula  $PEO_n$ - $b$ - $PCL_m$ , giving  $PEO_{126}$ - $b$ - $PCL_{142}$  which represents a hydrophilic fraction  $f = 25\%$ . For the other polymer on Figure III.3, results based on the  $^1\text{H}$  NMR give  $PEO_{124}$ - $b$ - $PCL_{190}$  with an associated hydrophilic fraction  $f = 20\%$ .

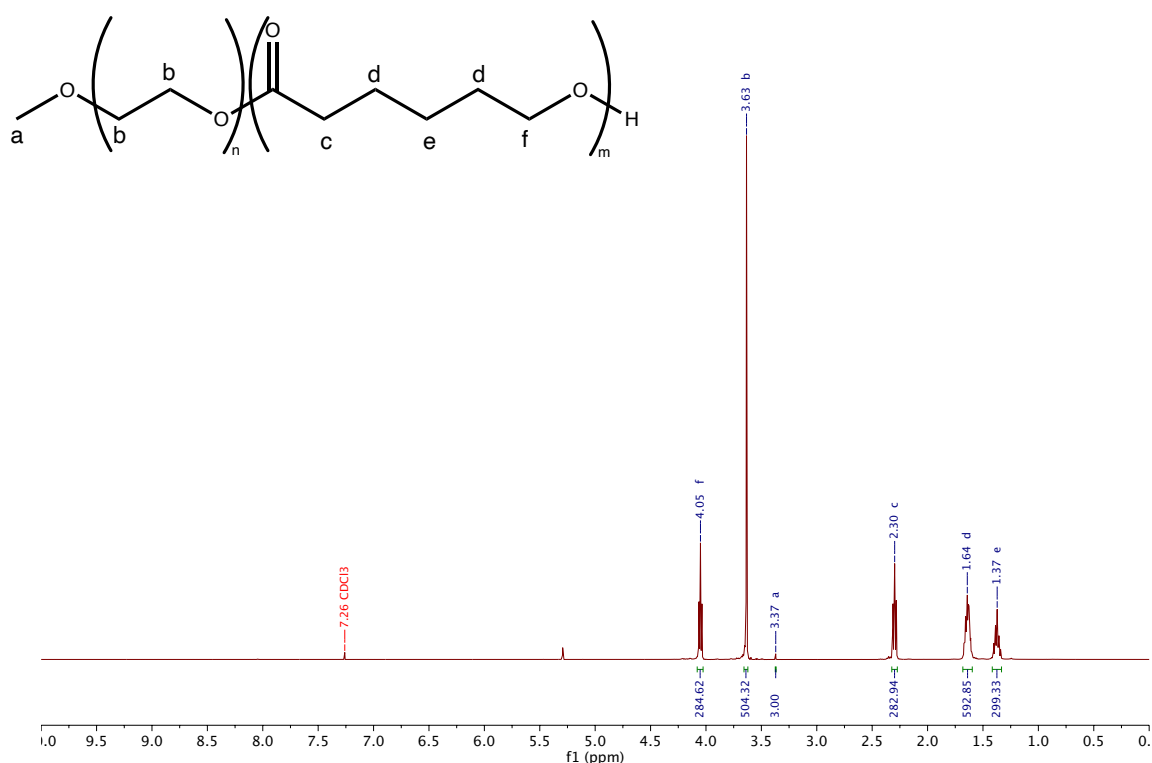


Figure III.2.  $^1\text{H}$  NMR (500MHz;  $\text{CDCl}_3$ ) spectrum of  $PEO_{126}$ - $b$ - $PCL_{142}$ .

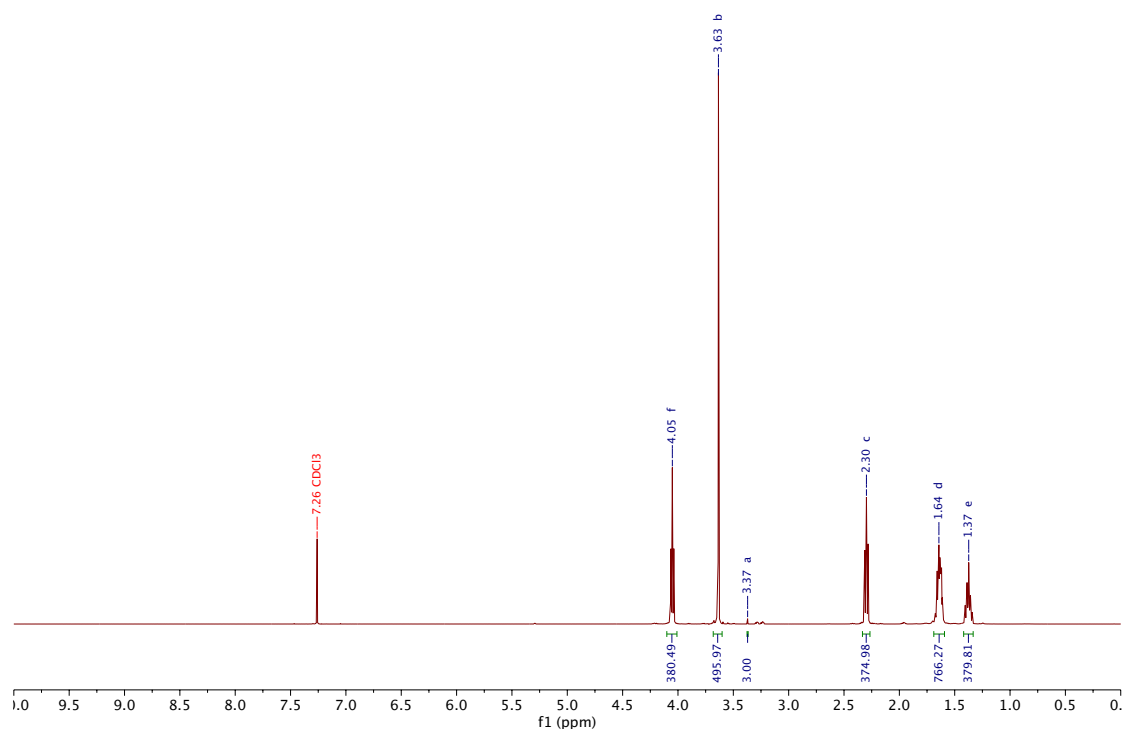


Figure III.3.  $^1\text{H}$  NMR (500MHz;  $\text{CDCl}_3$ ) spectrum of  $\text{PEO}_{124}\text{-}b\text{-PCL}_{190}$ .

### III.2.1.2 Determination of the dispersity of the copolymer by SEC

Another important parameter is the dispersity index of the copolymer that can be determined by Size Exclusion Chromatography (SEC) analyses. Indeed, this parameter represents the polydispersity in size of the chains. The molar mass dispersity is obtained according to the following equation:

$$\mathcal{D} = M_w/M_n \quad (\text{Equation III.3})$$

Where  $M_w$  is the weight-average molar mass and  $M_n$  is the number-average molar mass of the chains.

As expected on Figure III.4,  $\text{PEO}_{124}\text{-}b\text{-PCL}_{190}$  is eluted before  $\text{PEO}_{126}\text{-}b\text{-PCL}_{142}$  due to its higher hydrodynamic size, both samples being characterized by a molar mass dispersity of 1.7 and 1.8 respectively. The dispersity values of both polymers are relatively broad taking into consideration that a controlled polymerization usually corresponds to a dispersity value near 1.2-1.3, but it is nevertheless acceptable.

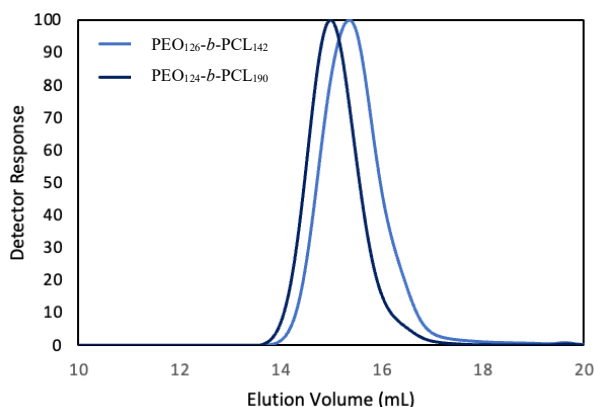


Figure III.4. SEC of the two copolymers  $\text{PEO}_n\text{-}b\text{-PCL}_m$ .

### III.2.2. PEO-*b*-PCL self-assembly

The self-assembly of various diblock copolymers into micelles or vesicles was described in literature for different compositions. D. Discher and A. Eisenberg evidenced a general rule to expect to form polymersomes in the case of polybutadiene-based copolymers (PBut-*b*-PEO). They consider that a range of  $f_{\text{hydrophilic}}$  of approximately  $35 \pm 10 \%$  is needed to form such vesicular structure.<sup>190</sup> Moreover, Adams *et al.* evidenced the possibility to form vesicles made with PEO-*b*-PCL with a hydrophilic fraction of 15%.<sup>78</sup> According to literature, the interval leading to vesicular morphology is thus rather  $20 \pm 5 \%$ .<sup>191</sup> In view of the information found in literature, the two copolymers synthesized can theoretically form polymeric vesicles.

#### III.2.2.1 Nanoprecipitation

Nanoprecipitation, consisting in the addition of an aqueous phase that can contain the drug and/or fluorophore due to their hydrophilicity in the case of this work, miscible with organic medium, to an organic phase containing the polymer, has been performed. This method introduced long time ago by Fessi *et coll.* is very common in pharmaceutical sciences to prepare drug-loaded nanocarriers.<sup>76</sup> This step is followed by either dialysis or the natural evaporation of the organic medium leading to the formation of polymersomes in the case of a favourable hydrophilic-hydrophobic ratio (otherwise, spherical or wormlike micelles are most likely obtained, as they constitute the equilibrium state of the amphiphilic copolymer self-assemblies).<sup>79</sup> It is also important to keep in mind that the sequence of addition and the speed of addition can modify the dispersity in the case of drop addition, as shown by Sanson *et al.* on poly(trimethylene carbonate)-*b*-PEO vesicles.<sup>192</sup> Therefore, the same protocol must be used for all copolymers to get comparable results. First, an optimization of the polymer concentration

was performed to obtain the most concentrated suspension in the end. Indeed, the preparative SEC treatment necessary to eliminate non-encapsulated dye or drug when it is used leads to partial loss of material. Solutions with copolymer concentration of 20 mg/mL in THF were prepared and diluted 10 times with the addition of aqueous medium. This concentration has been chosen since further increase in concentration leads to the formation of precipitate. Since a too quick evaporation of the solvent would also lead to the formation of a precipitate, we set the temperature at  $\sim 21^{\circ}\text{C}$  to get natural evaporation of the THF from the vial overnight.

### *III.2.2.2 Dynamic Light Scattering results*

Nanoprecipitation of PEO<sub>126</sub>-*b*-PCL<sub>142</sub> ( $f = 25\%$ ) leads to a relatively low polydispersity index of 0.17 (PDI of 0.1 in DLS is usually considered as a monodisperse size distribution) with an average hydrodynamic size of 58 nm certainly corresponding to polymer micelles as polymersomes show typically an average diameter around 100 nm instead. The manipulation was performed several times and the results always tend towards a size of about 50 nm. Same results were obtained after encapsulation of a dye followed by purification by preparative SEC on a Sephadex<sup>TM</sup> G-100 superfine column showing a size corresponding to micelles domains. This polymer is therefore no longer used.

For PEO<sub>124</sub>-*b*-PCL<sub>190</sub> ( $f = 20\%$ ), a broad dispersity of the nanoprecipitated suspension PDI of 0.27 was observed with an average size of 105 nm. The size dispersity can be lowered by using the extrusion technique, leading to a PDI of 0.2 with an average size of 90 nm. This size range may correspond to the formation of polymersomes. As a reminder, the extrusion technique consists in forcing the objects to go through different filters from 0.8 to 0.2  $\mu\text{m}$  under pressure in a block heating near the  $T_m$  of the copolymer, in this case  $\sim 40^{\circ}\text{C}$ . Another technique is to pass the resulting suspension through a syringe filter to eliminate directly aggregated structures, 0.2  $\mu\text{m}$  filter pore size allowing the passage of objects with a size below 0.2  $\mu\text{m}$ .

### *III.2.2.3 Cryo-TEM results*

To confirm the formation of the polymersomes, cryo-TEM analyses were performed on the most promising samples (from DLS), to get access to the structure of the nano-assemblies. Figure III.5 shows the presence of solid round structures and long fibers. Nevertheless, solid round structures exhibit too high sizes to be micelles. Based on research conducted by Mai and

Eisenberg<sup>51</sup>, the obtained structures seem to be close to the ones observed for PS-*b*-PAA copolymer, namely flexible rods (worm-like micelles) and large compound micelles (LCMs).

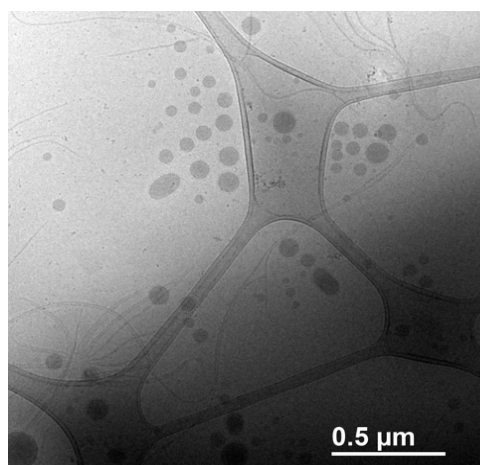


Figure III.5. Cryo-TEM of PEO<sub>136</sub>-*b*-PCL<sub>208</sub> nanostructures resulting from nanoprecipitation technique.

To finish this part, the first tests of encapsulation and *in vitro* release with a dye were performed, by co-assembly with the copolymer PEO<sub>124</sub>-*b*-PCL<sub>190</sub> followed by the adjustment of the purification step. Nevertheless, in view of the cryo-TEM results, it was decided to stop the experiments based on this type of copolymer. Indeed, the obtained results are concordant with the ones of Qi *et al.*<sup>193</sup> which evidenced that using a PEO chain of 5 or 5.8 kg/mol with different hydrophilic fractions always leads to solid nanostructures (filled micelles) instead of vesicles.

It was therefore necessary to change the copolymer composition to obtain the desired polymersome structure. The thought at this step was in the context of the synthesis of a new copolymer needed to form the polymersomes: “Why not use a more original copolymer which is not yet described in the literature in the context of polymersomes?”

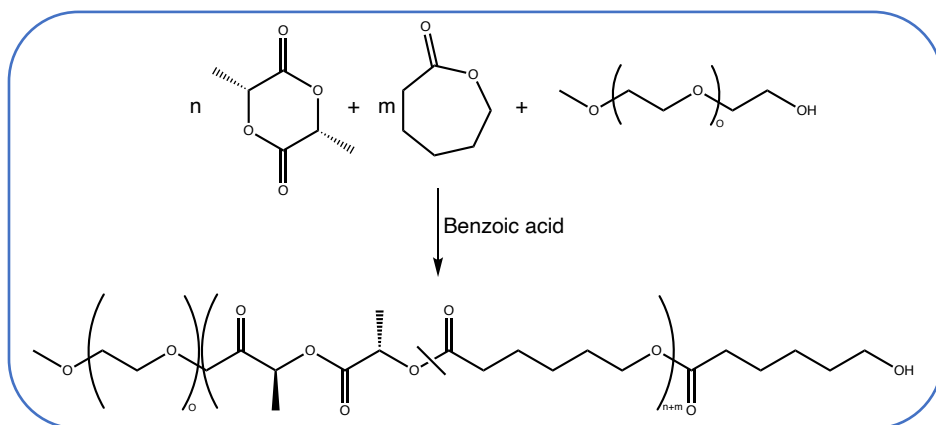
### III.2.3. Synthesis and characterization of diblock copolymers, PEO-*b*-P(CL-*co*-LA)

In view of the introduction, using a system having a statistical hydrophobic chain composed of LA and CL could be a great alternative to improve the pH sensitivity of the system.

Previous students at LCPO tested few years ago the formation of polymersomes with a copolymer composed of a hydrophilic block made of polyethylene oxide and a hydrophobic block made of a statistical block of polycaprolactone and polylactide. The idea was to tune the melting temperature and the crystallinity rate of the polyester block, to obtain thermosensitive vesicles (*i.e.* with membrane permeability increased by heating above  $T_m$ ) while keeping the pH-sensitivity (acidolysis). These tests were performed in the framework of Dr L. Mezzasalma's researches. It was chosen to use methods developed by Mezzasalma *et al.*<sup>194,195</sup> for several reasons: (i) the catalyst used for the synthesis must be removed or has to be safe and benign, for the future *in vitro* and *in vivo* tests. Therefore, the organocatalyzed polymerization was chosen, and they have developed an organocatalyzed ring-opening polymerization (ROP) to produce statistical block copolyesters composed by both lactidyl and caproyl ester repeating units. Interestingly, this statistical copolymer is prepared in the bulk, *i.e.* in absence of solvent, from benzoic acid acting as catalyst and an exogenous alcohol as initiator, also limiting the potential harmful effect of the use of solvent. (ii) They have also studied the toxicity on cells of benzoic acid, and they have found that it is not toxic at a concentration between 1 and 300  $\mu\text{M}$ . These results are thus compatible with the targeting application of the project if PEO (-OH terminated) is used as macroinitiator. (iii) The LA was added in a statistical way due to the hypothesis that the degradation of PLA, faster than PCL moiety, will lead to the formation of free lactic acid. It could herein increase the acidity of the microenvironment and thus promote the degradation of the hydrophobic polyester block.

#### *III.2.3.1 Synthesis and determination of the composition of the PEO-*b*-P(CL-*co*-LA) by <sup>1</sup>H NMR spectroscopy*

Copolymers were synthesized by the same method as previously described, *i.e.* ring opening polymerization (ROP). (Scheme III.1)



Scheme III.1. ROP reaction for PEO-*b*-P(CL-*co*-LA).

The  $^1\text{H}$  NMR is calibrated on the chain end of the PEO moiety, which is a methyl (peak **a** at  $\delta = 3.37$  ppm) and allows to extract the DP of the copolymers. The  $\text{DP}_{\text{EO}}$  is extracted from the Equation III.1 giving a DP of 50.  $\text{DP}_{\text{LA}}$  can be extracted from the peak **b** at  $\delta = 5.12$  ppm, which represents 2H (due to the lactide unit), according to the following equation:

$$\text{DP}_{\text{LA}} = I_{5.12 \text{ ppm}} / 2 \quad (\text{Equation III.4})$$

The  $\text{DP}_{\text{CL}}$  can be extracted from the relative intensity of the protons from the statistical block at  $I_{5.12 \text{ ppm}}$ ,  $I_{4.13 \text{ ppm}}$  and  $I_{4.05 \text{ ppm}}$  compared to the intensity of the methylene protons **e** of end chains at  $I_{3.55 \text{ ppm}}$  after the subtraction of the  $\text{DP}_{\text{LA}}$ :

$$\text{DP}_{\text{CL}} = \left( \frac{\frac{I_{5.12 \text{ ppm}} + I_{4.13 \text{ ppm}} + I_{4.05 \text{ ppm}}}{2}}{\frac{I_{3.55 \text{ ppm}}}{2}} \right) - \text{DP}_{\text{LA}} \quad (\text{Equation III.5})$$

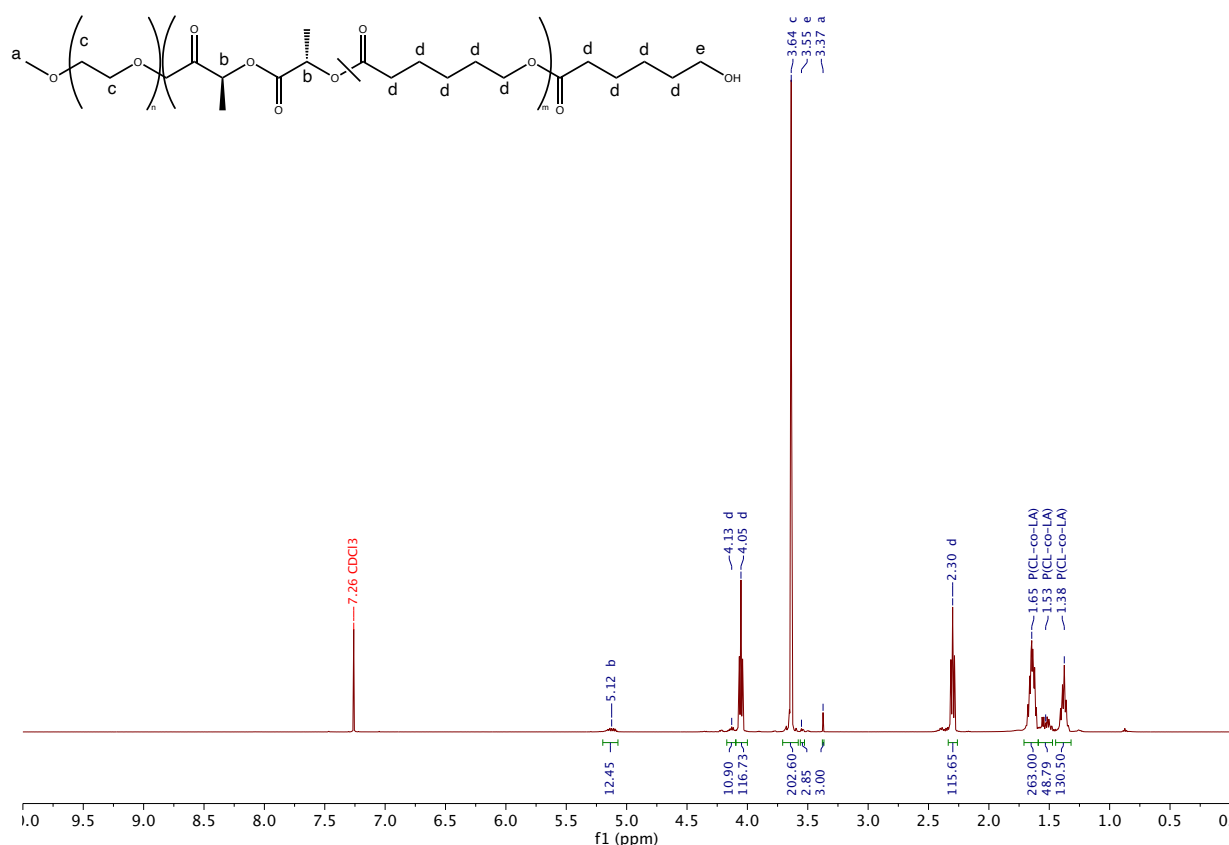


Figure III.6.  $^1\text{H}$  NMR (500 MHz;  $\text{CDCl}_3$ ) of  $\text{PEO}_{50}\text{-}b\text{-P}(\text{CL}\text{-}co\text{-LA})_6$ .

### III.2.3.2 Determination of the molar mass dispersity ( $\mathfrak{D}$ ) of the copolymer by SEC

Size exclusion chromatography brings two main pieces of information: (i) The SEC analyses evidence the presence of free PEO chains (*i.e.* that have not initiated the ROP reaction), which is particularly true for  $\text{PEO}_{45}\text{-}b\text{-P}(\text{CL}\text{-}co\text{-LA})_n$ . A washing step with water was thereby added to eliminate this free PEO. (Figure III.7) (ii) Figure III.8 represents the typical elution profile for the copolymer (RI signal), where a second peak can be observed on the dark blue curve. The question then was raised: “is it possible to already have lactic acid in solution induced by the washing with water?” To answer this question, the SEC chromatogram of lactic acid and THF were analyzed. According to these analyses, we can conclude that the second peak observed for the copolymer corresponds to THF. This specific peak is due to the pulse of RI signal produced by the injection, modifying the baseline of the THF. The obtained dispersity values  $\mathfrak{D}$  are *c.a.* 1.3 for  $\text{PEO}_{45}\text{-}b\text{-P}(\text{CL}\text{-}co\text{-LA})_n$ . Second information extracted from SEC is the weight-average molecular weight obtained on the basis of a calibration with standard polystyrene chains. The obtained  $M_w$  can be far from the right  $M_w$  as all polymers do not present

the same swelling degree in THF and therefore the same hydrodynamic volume, which is the criterion for separation in SEC. To palliate to this issue, it is possible to determine the true value  $M_w$  of the chains by using the signal of a multi-angle light scattering (MALS) detector instead of the RI detector, which necessitating to first determine the refractive index increment of the polymer in the solvent, which will be the next point.

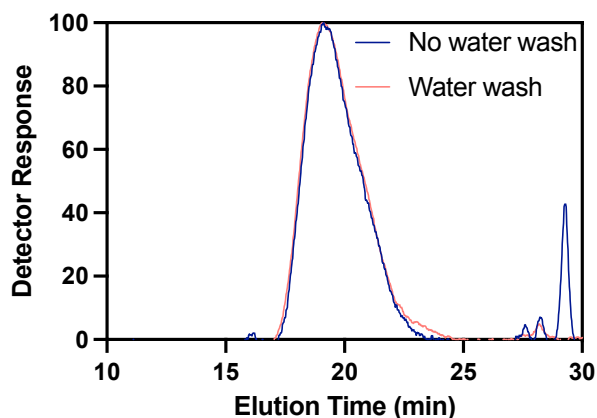


Figure III.7. Comparison of SEC analyses before and after water washing.

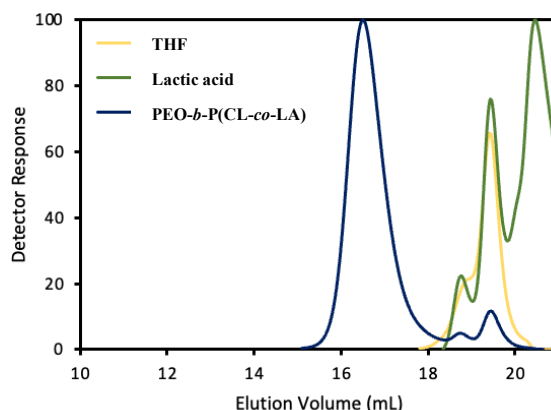


Figure III.8. SEC analyses of THF (yellow), lactic acid (green) and PEO-*b*-P(CL-*co*-LA) (dark blue).

### III.2.3.3. Determination of the refraction index increment ( $dn/dc$ )

When using a MALS detector, the average molecular weight is obtained following:<sup>196</sup>

$$M_w = \frac{1}{\left(\frac{k_c}{R_\theta - 2A_2c}\right)} \text{ where } k_c = \left(\frac{2\pi n_0^2}{\lambda^4 N_A}\right) \left(\frac{dn}{dc}\right)^2 \quad (\text{Equation III.6})$$

$R_\theta$ , excess Rayleigh factor;  $A_2$ , second virial coefficient;  $c$ , weight concentration (g/L);  $n_0$ , refractive index of the solvent;  $\lambda$ , wavelength;  $N_A$  number of Avogadro and  $dn/dc$ , change in refractive index as a function of the concentration (or “RI increment”).

The signal obtained by the refractive index (RI) detector measured for a series of different polymer concentrations injected in a column without separation beads allows to finally obtain the  $dn/dc$  value by linear regression, according to the following equation:<sup>196</sup>

$$S^{RI} = k^{RI} c \left( \frac{dn}{dc} \right) \quad (\text{Equation III.7})$$

$S^{RI}$ , signal of the refractive index detector;  $k^{RI}$ , calibration constant for the refractive index detector and  $c$ , weight concentration in polymer.

The  $dn/dc$  value was determined for PEO<sub>45</sub>-*b*-P(CL<sub>46</sub>-*co*-LA<sub>6</sub>) giving 0.0751 instead of 0.1850 used with the polystyrene calibration. This leads to a slight modification of the  $M_w$  (*i.e.* 10.8 kg.mol<sup>-1</sup> (be careful that these values are based on a weak load sensing signal)) and a dispersity of  $\mathcal{D} = 1.3$  whereas a previous  $M_w$  of 13.3 kg.mol<sup>-1</sup> with a dispersity of  $\mathcal{D} = 1.4$  was obtained.

#### III.2.3.4. Determination of the degree of crystallinity of the copolymer

The self-assembly of copolymers into nanostructures for drug delivery can be critically dependent upon the crystallinity of the copolymers. Indeed, the degree of crystallinity – defined as the weight fraction of the copolymer that can crystallize below a certain temperature – is correlated to the dynamic properties and in particular the drug permeability of the nanostructure. In our case, both PL-LA, PCL and PEO are semi-crystalline, and influenced by the copolymer stereo-regularity also called tacticity.<sup>62,197,198</sup> The melting point of pure PL-LA is usually around 170°C,<sup>199</sup> but it is not visible due to the presence of only 5 repeating units statistically distributed in the P(CL-*co*-L-LA) random copolymer block. Instead, it is expected that the presence of *L*-lactic acid moieties in the chain will increase the degree of crystallinity as reported for bulk samples of statistical P(CL-*co*-L-LA),<sup>5</sup> which would make our copolymer not only pH-sensitive but also thermosensitive. On the thermogram of Figure III.9, we identify the two observed melting points at 41.7 and 47.7 °C to respectively PEO and P(CL-*co*-L-LA), which is also an experimental proof of their phase separation at the nanoscale (otherwise there would be a single peak). Finally, the rates of crystallinity were obtained from the integration of the melting peaks. To define the crystallinity ( $\chi$ ) of PEO and PCL, the enthalpy of fusion ( $\Delta H_m$ ) has to be measured as a function of the weight fraction of each block. Therefore, the measured enthalpy of fusion of 5 J/g (of sample) associated to the PCL must be corrected with the weight

fraction of PCL (62.8 wt %) and becomes 8 J/g (of PCL). Same correction is performed on  $\Delta H_m$  (19 J/g) associated to PEO (34.5 wt %) giving a  $\Delta H_m$  of 60.3 J/g of PEO. This leads to  $\chi$  values of 6% and 31% for P(CL-*co*-LA) and PEO (196 J/g for 100% crystalline PEO) copolymer blocks, respectively. It is important to note that the theoretical melting enthalpy used for the calculation of the crystallinity rate for the hydrophobic block is the one of pure PCL (139 J/g) due to the low number of LA repeating units in comparison to that of CL. (Please note that the melting peaks in the DSC curve are not well separated and overlap, thus there is an uncertainty on the determination of the absolute value of crystallinity rate.)

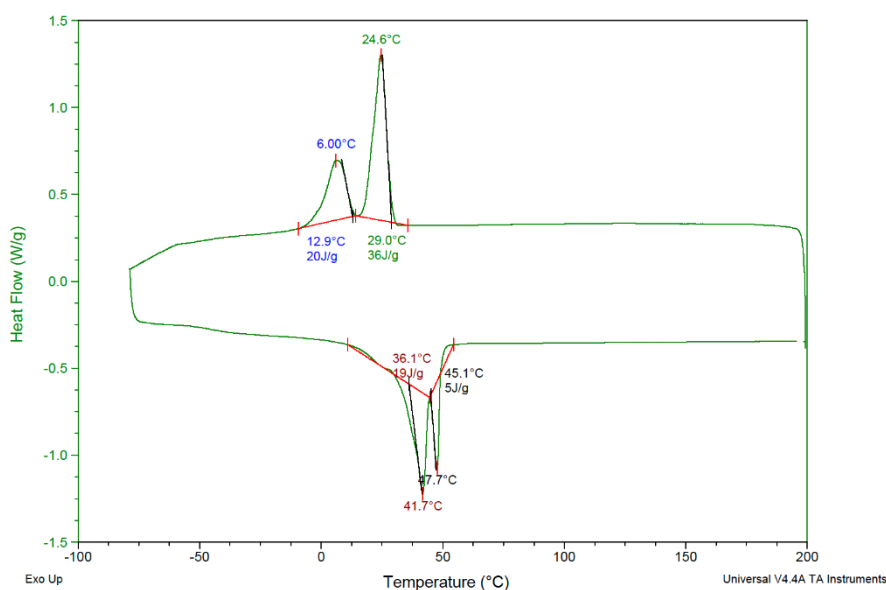


Figure III.9. DSC curve of PEO<sub>45</sub>-*b*-P(CL<sub>35</sub>-*co*-LA<sub>5</sub>), second heat, 10°C/min. The inflection point around -50°C is ascribed to the glass transition ( $T_g$ ) of the polyester.

To conclude on this part, we note that we got some difficulties to obtain reproducible batches with the same size of hydrophobic block. (Table AIII.1) It is thus imperative to find a synthetic way leading to reproducible batches of copolymers. An interesting alternative could be using aluminium alkoxydes like Ti(OiPr)<sub>3</sub> as catalysts and initiators of the ROP of lactides and lactones which are not toxic.<sup>2</sup> Moreover, it has recently been used at very low content (down to 0.1%) by Meimoun *et al.* to prepare statistical P(LA-*co*-CL) copolymers leading to the incorporation of an important fraction of lactidyl units.<sup>3-5</sup> Moreover, the catalytic quantities of aluminium used in the synthesis should not bring toxicity. Indeed, the body is daily exposed to aluminium (approximately 30 mg per day).<sup>6</sup>

III.2.4. PEO-*b*-P(CL-*co*-LA) self-assembly

Copolymers used in the following section are composed of PEO-*b*-P(CL-*co*-LA) with a  $f_{\text{hydrophilic}}$  between 20% and 30%. (Table III.2) Different techniques of characterization were used to probe the structure and morphology of the nanoobjects. At first, an easy and accessible technique in the laboratories such as DLS was used. Nevertheless, it is important to determine the gyration and hydrodynamic radii respectively  $R_g$  and  $R_h$  to get a closer insight of the structure. To do that, more advanced techniques are available like multi-angle light scattering (MALS), asymmetric flow field-flow fractionation (AF4) which shows encouraging preliminary results, small angle X-ray scattering (SAXS) and finally cryo-transmission electron microscopy (Cryo-TEM). It is important to develop other techniques that are easier to access and less expensive than cryo-TEM, which that can be used as a final characterization technique due to its expensive and time-consuming analyses. Therefore, we used all the panel of techniques accessible to us to scan the morphologies of the samples prepared by several self-assembly processes.

Table III.2. Structure of PEO-*b*-P(CL-*co*-LA) copolymers used in this work for the different analyses where the index represents the DP of the different moieties calculated from  $^1\text{H}$  NMR.

Techniques	Methods	Copolymers	$f_{\text{hydrophilic}}$ (%)
DLS	Nanoprecipitation	PEO <sub>45</sub> - <i>b</i> -P(CL <sub>49</sub> - <i>co</i> -LA <sub>8</sub> )	23
	Thin film	PEO <sub>45</sub> - <i>b</i> -P(CL <sub>35</sub> - <i>co</i> -LA <sub>5</sub> )	30
MALS	Nanoprecipitation	/	
	Thin film	PEO <sub>45</sub> - <i>b</i> -P(CL <sub>35</sub> - <i>co</i> -LA <sub>5</sub> )	30
AF4	Nanoprecipitation	PEO <sub>45</sub> - <i>b</i> -P(CL <sub>58</sub> - <i>co</i> -LA <sub>8</sub> )	20
	Thin film	PEO <sub>45</sub> - <i>b</i> -P(CL <sub>35</sub> - <i>co</i> -LA <sub>5</sub> )	30
SAXS	Nanoprecipitation	PEO <sub>45</sub> - <i>b</i> -P(CL <sub>58</sub> - <i>co</i> -LA <sub>8</sub> )	20
	Thin film	PEO <sub>45</sub> - <i>b</i> -P(CL <sub>35</sub> - <i>co</i> -LA <sub>5</sub> )	30
Cryo-TEM	Nanoprecipitation	PEO <sub>45</sub> - <i>b</i> -P(CL <sub>49</sub> - <i>co</i> -LA <sub>8</sub> )	23
	Thin film	PEO <sub>45</sub> - <i>b</i> -P(CL <sub>35</sub> - <i>co</i> -LA <sub>5</sub> )	30

### III.2.4.1 Nanoprecipitation

As defined previously, nanoprecipitation is used for its simplicity, feasibility at higher scale, the narrow size distribution of the polymersomes, .... Same conditions than described previously (section III.2.2.1) after optimisation were used in the case of these new copolymers ( $\sim 20$  mg/mL of copolymer in THF put under stirring, followed by the addition of five volumes of aqueous medium overnight at  $\sim 21^\circ\text{C}$ ). DLS analyses were performed after the nanoprecipitation in PBS of the copolymer giving an average diameter of  $88 \pm 23$  nm (average on 6 samples loaded or not) after filtration through syringe filter of  $0.22 \mu\text{m}$  pore size. Indeed, in this case, nanoprecipitation led to slightly broad size distribution ( $\text{PDI} = 0.18 \pm 0.11$ ). Moreover,  $0.22 \mu\text{m}$  filtration has to be performed prior to biological tests to remove any bacterial contamination from the medium. That is why samples were filtered to be close to the real conditions of the samples to be used for *in vivo* and *in vitro* tests.

The results obtained by DLS were similar to the ones obtained for PEO-*b*-PCL described previously, *i.e.* micellar structures.

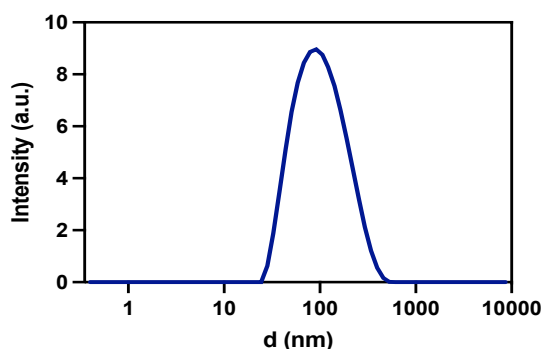


Figure III.10. DLS analyses of PEO<sub>45</sub>-*b*-P(CL<sub>49</sub>-*co*-LA<sub>8</sub>) nanoprecipitation,  $Z_{\text{ave}}$  diameter = 85.7 nm; PDI = 0.23; in PBS; not loaded.

### III.2.4.2 Thin film rehydration

Another technique often used is the thin film rehydration. Also called “reverse-phase hydration”, this technique was introduced for liposomes long time ago but can be extended to polymersomes.<sup>200</sup> This method consists in the solubilisation of the copolymer in an organic solvent followed by its evaporation by a rotavapor with a heating bath above the  $T_m$  of the copolymers to form a thin film on the round bottom flask. Thanks to heating, the block copolymer film is in the fluid state and thus much more dynamic to rearrange and self-assemble

into vesicles when aqueous medium is introduced, a prerequisite for a semi-crystalline copolymer such as PEO-*b*-PCL.<sup>201</sup> This film is then hydrated with five volumes of aqueous buffer with a bath at  $\sim 70^\circ\text{C}$ . A vigorous agitation, helping the multi-lamellar film to swell and form enclosed vesicles, is kept during approximately 2 hours. This manipulation leads to the formation of nanostructures with a mean hydrodynamic size of  $121 \pm 13$  nm (average on 9 samples loaded or not) and a low PDI of  $0.17 \pm 0.05$  by DLS, after filtration through a syringe filter of  $0.22 \mu\text{m}$ . This size distribution gets closer to what is expected for a suspension of mostly polymersomes, without interference with object of other sizes or morphologies.

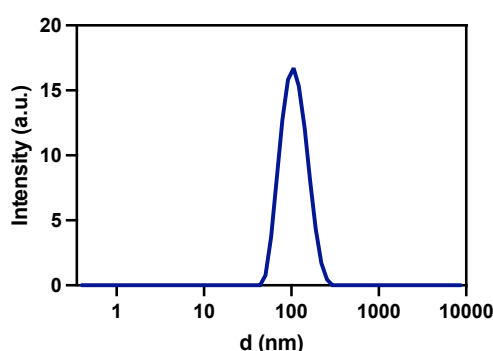


Figure III.11. DLS analyses of objects self-assembled by the thin film rehydration method; PEO<sub>45</sub>-*b*-P(CL<sub>35</sub>-LA<sub>5</sub>),  $Z_{\text{aver}}$  diameter = 103.2 nm; PDI = 0.16; in PBS; not loaded.

#### III.2.4.3. Multi-angle light scattering (MALS)

MALS is a technique that couples dynamic light scattering (DLS), giving access to the hydrodynamic radii ( $R_h$ ), and static light scattering (SLS), allowing determination of radii of gyration ( $R_g$ ) and potentially also the molar mass of the scattering particles ( $M_w$ ). Their measured ratio,  $\rho = R_g/R_h$ , allows to determine the morphology of the nanostructures and therefore it is sometimes called the “shape parameter”.<sup>202</sup> In theory, a  $\rho$  parameter of 0.775 is expected for a suspension of filled micelles, while vesicles should exhibit a value of 1.<sup>192,203</sup> This arises from the theoretical value  $R_g = \sqrt{(3/5)r}$  in the case of a solid sphere of radius  $r$ , instead of  $R_g = r$  in the case of a hollow spherical shell like vesicle.

DLS gives access to  $R_h$  according to the Stoke-Einstein relation relating the translational diffusion coefficient to the radius of the equivalent hydrodynamic sphere. The decay rate values ( $\Gamma$ ) of the autocorrelation function  $G(t)$  determined by analyzing the fluctuations of scattered

light intensity are measured at varying scattering angle  $\theta$  between  $30^\circ$  to  $150^\circ$  in steps of  $10^\circ$ , and plotted as a function of  $q^2$ , which is the squared scattering vectors. The linear regression gives access to the diffusion coefficient ( $D$ ) according to the following equation:

$$\Gamma = D q^2 \quad (\text{Equation III.8})$$

where the scattering vector ( $q$ ) is defined as:<sup>204</sup>  $q = \frac{4 \pi n_0}{\lambda} \sin(\theta/2)$  (Equation III.9)

with  $n_0$ , refractive index of solvent;  $\theta$ , scattering angle between scattered and incident beams;  $\lambda$ , laser beam wavelength (usually 633 nm).

The  $R_h$  value is then calculated from the Stoke-Einstein relation:

$$R_h = \frac{k_B T}{6 \pi \eta_s D} \quad (\text{Equation III.10})$$

with  $k_B$ , Boltzmann constant;  $T$ , absolute temperature;  $\eta_s$  solvent viscosity

Figure III.12 gives access to the fitting method allowing to extract the value of  $D$  coefficient, then leading to  $R_h$ . These results are in the same range than the hydrodynamic diameter ( $d_h = 2 R_h$ ) obtained by DLS measurement at single  $90^\circ$  angle on the Zetasizer setup, even though the diameter values are slightly larger. (Table III.3)

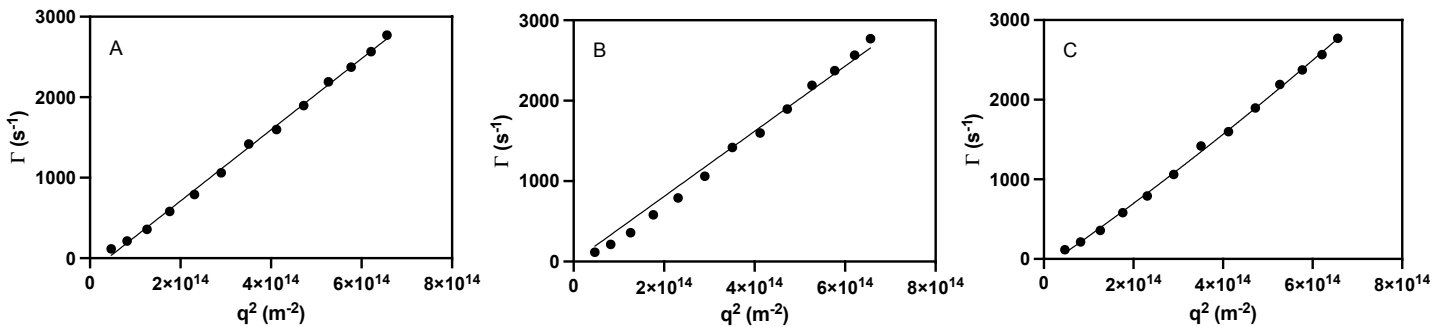


Figure III.12. Plot of the main decay rate of the autocorrelation function of scattered light intensity determined by the 2<sup>nd</sup> order Cumulant method and fitting as a function of the square of the scattering vector: (A) Linear regression (B) linear regression with the constrain of zero intercept with the vertical axis (C) second order polynomial fit, which takes into account the effect of size polydispersity. (Sample PEO<sub>45</sub>-*b*-P(CL<sub>35</sub>-*co*-LA<sub>5</sub>), prepared by the thin film hydration method, not loaded with drug and/or dye)

SLS (measurement of the static scattered light intensity at different angles) gives access to the  $R_g$ .  $R_g$  values are obtained according to different laws governed by Zimm, Guinier and Berry plots. In our case, Guinier plot is used since it allows determining the  $R_g$  for particles in

suspension with the limitation of using particles with a maximum radius of 100 nm. According to Zimm law, both the  $R_g$  and  $M_w$  values can be extracted by the variation of  $Kc/\Delta R_\theta$  as a function of  $q^2$ :

$$\frac{Kc}{\Delta R_\theta} = \frac{1}{M_w} \left( 1 + \frac{1}{3} R_g^2 q^2 \right) + 2 A_2 c \quad (\text{Equation III.11})$$

$$\text{Where } K \text{ is a constant defined as: } K = \frac{4 \pi^2 n_0^2 \left( \frac{dn}{dc} \right)^2}{N_A \lambda^4} \quad (\text{Equation III.12})$$

$$\Delta R_\theta, \text{ the Rayleigh ratio defined by } \Delta R_\theta = \left( \frac{I_{\text{susp}} - I_0}{I_{\text{tol}}} \right) \left( \frac{n_0}{n_{\text{tol}}} \right)^2 R_\theta^{\text{tol}} \quad (\text{Equation III.13})$$

With  $c$ , the concentration ( $\text{g} \cdot \text{cm}^{-3}$ );  $dn/dc$ , refraction index increment of the particles already introduced for the SEC experiments,  $M_w$ , the weight – average molecular weight of the scattering objects;  $R_g$ , their radius of gyration;  $A_2$  the second coefficient of Viriel development;  $I_{\text{susp}}$ , intensity (count rate) measured on suspension;  $I_{\text{tol}}$ , intensity measured on toluene;  $I_0$ , background intensity measured on pure solvent;  $n_0=1.332$ , refraction index of PBS;  $n_{\text{tol}}=1.496$ , refraction index of toluene;  $R_\theta^{\text{tol}} = 1.355 \times 10^{-5} \text{ cm}^{-1}$ , tabulated value of the Rayleigh ratio of toluene (independent of  $\theta$ );  $N_A$ , Avogadro number;  $\lambda$ , laser wavelength.

Finally, instead of performing the whole Zimm plot (*i.e.* measuring the Rayleigh ratios for different scattering angles and concentrations to verify the Equation III.11), one can measure at a single concentration and then  $\ln I(q)$  can simply be plotted as a function of  $q^2$  in the very low  $q$  limit ( $qR_g \ll 1$ ) according to Guinier's equation:

$$\ln I(q) = \ln I_0 - \frac{q^2 R_g^2}{3} \quad (\text{Equation III.14})$$

Sometimes a linearized version of this relationship is used, also called Debye's equation:

$$I(q) \cong I_0 \left( 1 - \frac{q^2 R_g^2}{3} \right) \quad (\text{Equation III.15})$$

Alternatively, another form called Berry's equation is used:

$$1/\sqrt{I(q)} \cong 1/\sqrt{I_0} \left( 1 + \frac{q^2 R_g^2}{6} \right) \quad (\text{Equation III.16})$$

The slope  $R_g^2/3$  obtained by a Guinier plot (Figure III.13) gives access to  $R_g$ , with a value of 62.9 nm for this sample.

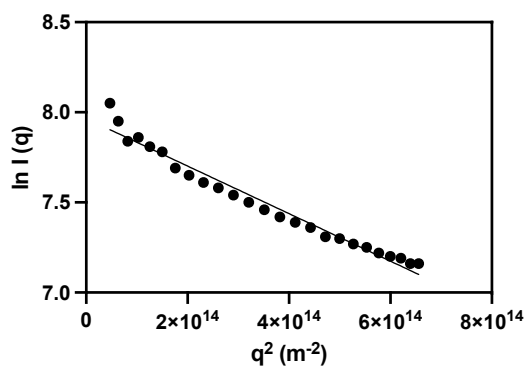


Figure III.13. Guinier plot for sample PEO<sub>45</sub>-*b*-P(CL<sub>35</sub>-*co*-LA<sub>5</sub>), prepared by the thin film hydration method, not loaded with drug and/or dye.

Finally, Table III.3. shows the  $R_g/R_h$  ratio calculated with the different regressions obtained by DLS. Results show a ratio close to 1 which evidences the presence of vesicles in the medium.

Table III.3. Ratio of the  $\rho$  parameter ( $R_g/R_h$ ) according to the different regression methods for  $R_h$  determination.  $R_g$  was obtained by a Guinier plot of the static light scattering data (Figure III.13).

Multi-angle DLS analysis method:	linear regression	linear regression through (0,0)	parabolic regression fit
$\rho = R_g/R_h$	62.9/55.2 = 1.14	62.9/60.3 = 1.04	62.9/63.25 = 1.00

Nevertheless, these MALS analyses were performed only on the rehydrated film samples which most likely lead to polymersomes, because the sample has to be relatively monodisperse to obtain convincing results. Although this technique is quite useful, it still suffers from two main limitations (i) the radius has to be below 100 nm to verify the  $qR_g \ll 1$  limit of Guinier's law, and (ii) the sample has to be monodisperse and thus cannot be constituted of a mix between two types of particles, *e.g.* vesicles and micelles. In the following section, we will show and explain why this analysis has not been carried out on micelle-rich samples. To palliate to these issues, another technique allowing separation of the different populations present in the samples will be used.

#### III.2.4.4. Asymmetric flow field-flow fractionation (AF4)

First tests on asymmetric flow field-flow fractionation were performed as a powerful tool mainly in the case of a mix of structures in the sample. This technique allows to separate different particles – of nanoscale size – according to their hydrodynamic sizes, like SEC can separate between individual polymer chains. The principle of this technique is based on the combination of both a diffusion flow and a convective crossflow of solvent, in perpendicular directions. After being injected in a thin channel, the colloidal particles follow a parabolic (Poiseuille type) laminar flow in the channel. The sample distribution spreads through the channel under the action of the two opposite flow forces. The diffusion profile is governed by the diffusion coefficient giving access to the  $R_h$  value, with following modifications compared to Equation III.10 due to the utilization of a solute and the presence of channel walls:<sup>205,206</sup>

$$R_h = \frac{k_B T V^0}{6 \pi \eta_s D \omega^2 \dot{V}} \frac{t_r}{t^0} \quad (\text{Equation III.17})$$

$k_B$ , Boltzmann constant;  $\eta_s$ , solvent viscosity;  $T$ , absolute temperature;  $V^0$ , volume of the channel;  $\omega$ , channel thickness;  $\dot{V}$ , crossflow rate;  $t_r$ , retention time of the solute and  $t^0$ , time for the solvent molecules to pass through the channel.

Where  $V^0$ ,  $\omega$  and  $t^0$  are defined by the channel used during the experimental measurement, and  $t_r$  is obtained by a calibration with a reference solution containing particles of known sizes.

The AF4 system, in our case, is coupled to a MALS detector giving the possibility to extract the  $R_g$  as previously explained in the case of SLS. For the AF4 MALS signal analysis, different theories can be used with the Astra 8 analysis software to extract the  $R_g$  values according to one of the equations described in the SLS section. Different examples of AF4 fractograms corresponding to different nanostructures are given in Figure III.14 and Figure III.15, (a), (b) and (c), in particular showing the Burchard-Stockmayer plots which are the curves of the shape factor  $\rho$  (point) as a function of the elution volume in the channel (straight line), starting from the smallest particles on the left towards the largest particles on the right (which is the opposite compared to SEC chromatograms for soluble polymer chains). The shape factor was extracted at three different elution times on the resulting curve of detection for each sample to evidence the presence of one or more population.

The first sample analyzed by AF4 was the one prepared by nanoprecipitation and was constituted by other structures than vesicles, according to two types of fit (Figure III.14):

(a) and (b) The Berry equation was used to fit the same MALS signal, and obtain the  $R_g$ , whereas the  $R_h$  was determined by standard Cumulant fit of the DLS correlograms, for a part of the fractions along the fractogram.

(c) Rod-like structure fit with a cylinder form factor which allows to extract the  $R_g$  value, related to the cylinder dimensions by:

$$R_g^2 = r^2/2 + L^2/12 \quad (\text{Equation III.18})$$

where  $R$  is the cylinder radius and  $L$  its length.

Then the measured shape parameter  $\rho = R_g/R_h$  exhibit high values, starting from 0.77 for the smallest size objects to about 2.31 for the largest ones. Theoretically, the  $\rho$  value tends towards  $\frac{8}{3}\sqrt{\pi} \cong 4.7$  for infinitively long cylinders, therefore such values are compatible with cylindrical micelles, in accordance with the rod-like shape factor analysis.<sup>207</sup> Table III.4 evidences the extracting parameter leading to the shape factor of each point. The beginning of the curve (point (a)) exhibits micelle morphology followed by a supposed mixture between micelles and rods due to the increase of the form factor. The end of the curve exhibits the presence of rods in the medium.

The second sample analyzed by AF4 was the one prepared by thin film method and was constituted by polymeric vesicles, according to one fit (Figure III.15):

(a), (b) and (c) The fit of MALS signal for a sample made of polymersomes was made with Debye theory to extract the  $R_g$ . This led to a  $R_g/R_h$  ratio of nearly 1 over the whole distribution, which evidenced the formation of polymer vesicles exclusively.

Table III.5 shows that, regardless of the elution time, the  $R_g/R_h$  ratio is  $\sim 1$  as polymersomes nanostructures.

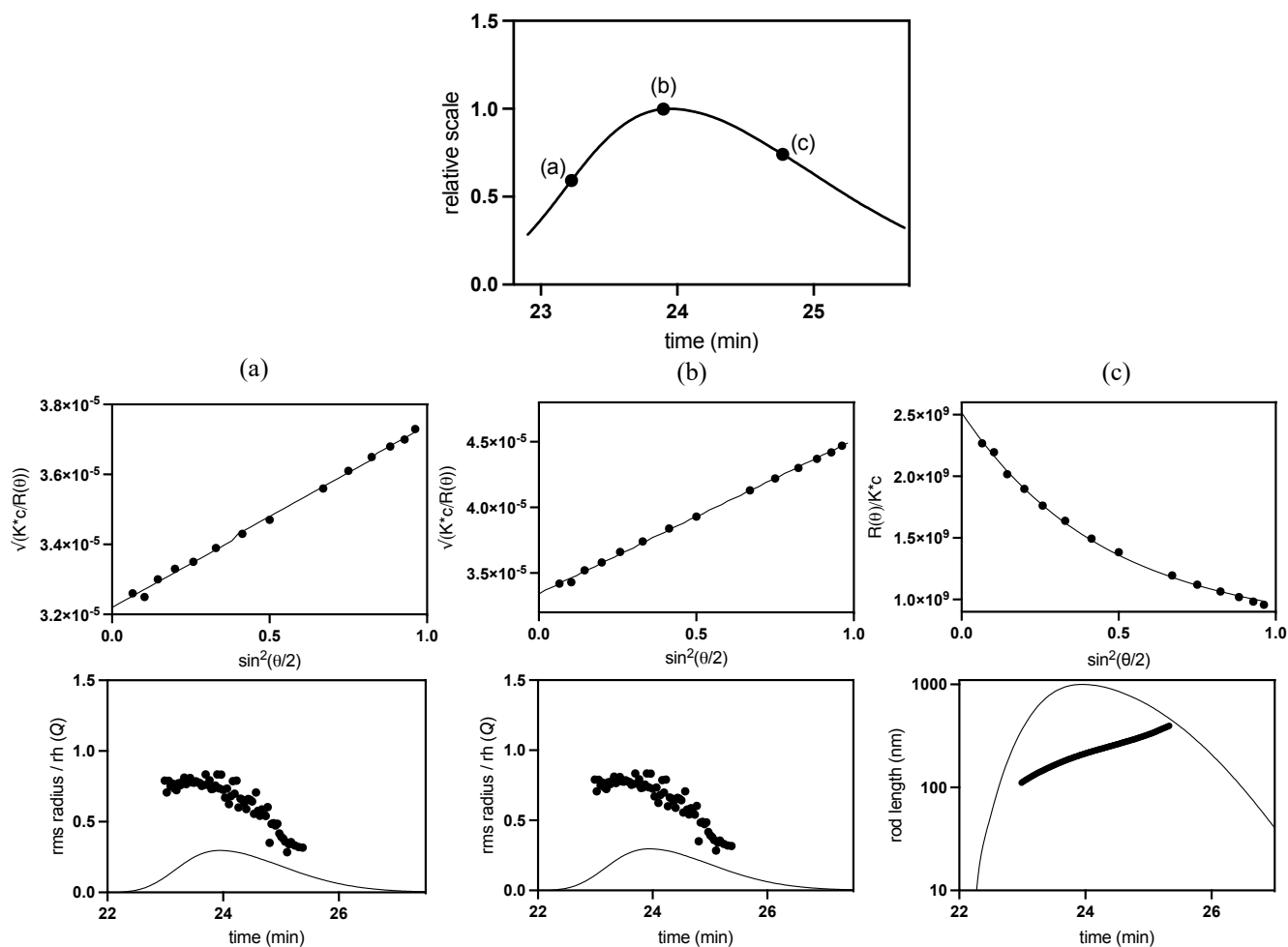


Figure III.14. On the upper Figure, the chromatogram of elution was represented with the corresponding measurement at 3 different times (a) and (b) Fit of MALS signal giving  $R_g$  according to Berry's law Eq. 3.16 and Burchard-Stockmayer plot below (c) Fit of MALS signal according to the rod theoretical shape factor and rods plot below for sample  $\text{PEO}_{45}\text{-}b\text{-P}(\text{CL}_{58}\text{-}co\text{-LA}_8)$ , prepared by nanoprecipitation (where points represent  $\rho$  and straight line represent the elution curve).

Table III.4. Extraction of the  $R_g$  and  $R_h$  values from the different fittings of Figure III.14.

	(a)	(b)	(c)
	(Berry fit)	(Berry fit)	(Rod fit)
$dn/dc$ (mL/g)	0.0751	0.0751	0.0751
Elution time (min)	23.2	23.9	24.8
$R_g$	$39.2 \pm 0.2$ nm	$57.5 \pm 0.3$ nm	$293.5 \pm 2.6$ nm
$R_h$	$50.9 \pm 12.4$ nm	$68.9 \pm 29.2$ nm	$127.2 \pm 87.3$ nm
$\rho = R_g/R_h$	0.77	0.83	2.31
Nanostructures	Micelles	Micelles (+ Rods)	Rods

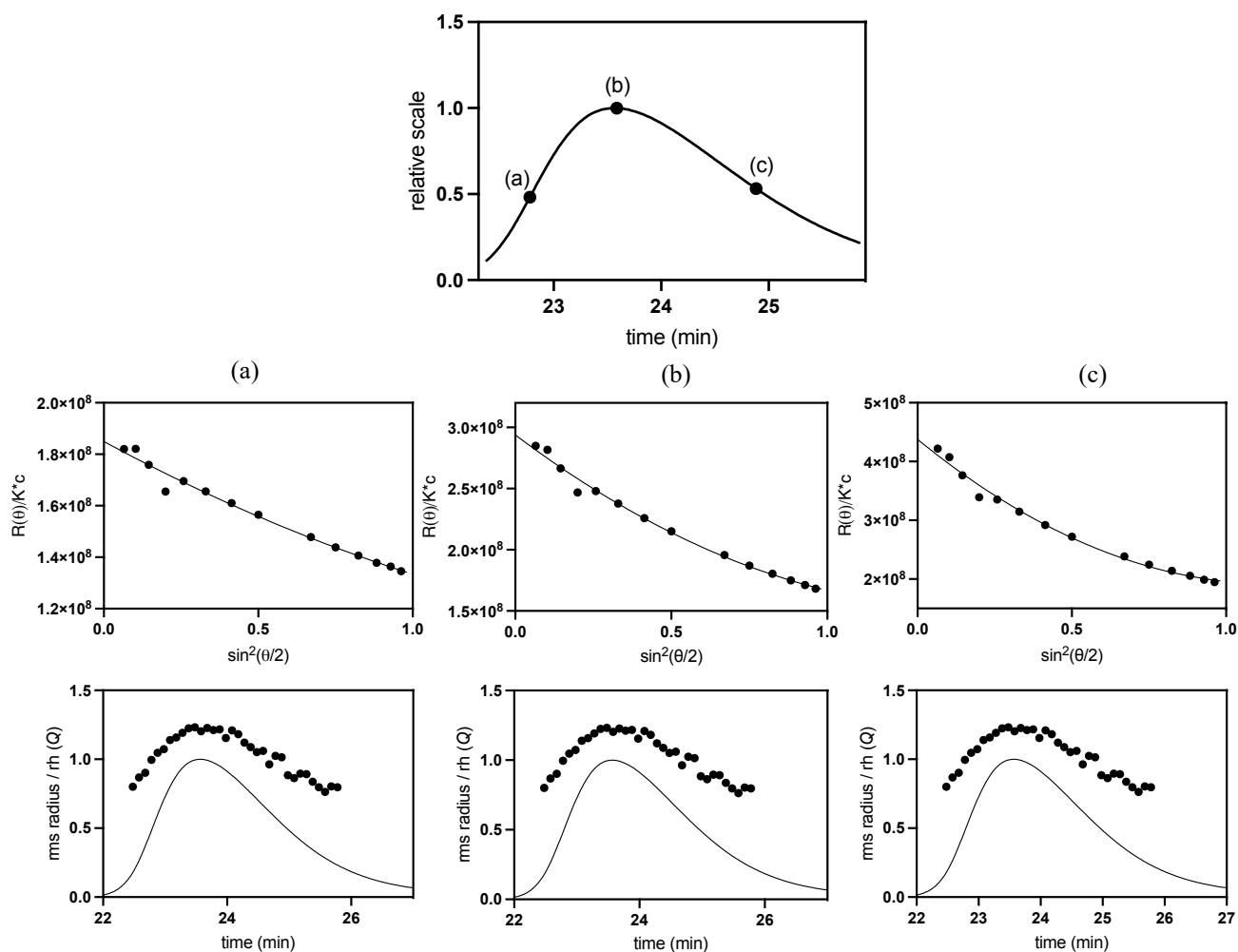


Figure III.15. On the upper Figure, the chromatogram of elution was represented with the corresponding measurement at 3 different times (a), (b) and (c) Fit of MALS signal giving  $R_g$  according to Debye's law Eq. III.15 and Burchard-Stockmayer plot (where points represent  $\rho$  and straight line represent the elution curve) of the shape parameter  $\rho$  along the fractogram below for sample PEO<sub>45</sub>-b-P(CL<sub>35</sub>-co-LA<sub>5</sub>), self-assembled by the thin film rehydration method.

Table III.5. Extraction of the  $R_g$  and  $R_h$  values from the different fitting of Figure III.15.

	(a)	(b)	(c)
	(Debye fit)	(Debye fit)	(Debye fit)
$dn/dc$ (mL/g)	0.0751	0.0751	0.0751
Elution time (min)	22.8	23.9	24.9
$R_g$	$40.8 \pm 2.80$ nm	$55.6 \pm 2.2$ nm	$68.0 \pm 2.5$ nm
$R_h$	$41.0 \pm 9.2$ nm	$46.2 \pm 18.0$ nm	$67.0 \pm 24.8$ nm
$\rho = R_g/R_h$	0.99	1.20	1.01
Nanostructures	Polymersomes	Polymersomes	Polymersomes

### III.2.4.5. Small angle X-ray scattering (SAXS)

When vesicles are evidenced, small angle X-ray scattering gives access to the thickness of their membrane. This method is called “reciprocal” in the sense that it makes the analogue of a Fourier transform of the shape or of repetitive patterns of the matter at the nanoscale, giving access to the global morphology and average size of nanoparticles, under the condition that their radii of gyration respect the Guinier limit  $qR_g \ll 1$ , or at least  $qR_g < 1$ . As shown on the Figure III.16, the size and the dimensionality of the nanostructures can be extract by plotting the intensity as function of  $q$  in a log-log scale, in the so-called Guinier domain (*i.e.* at low  $q$ ).

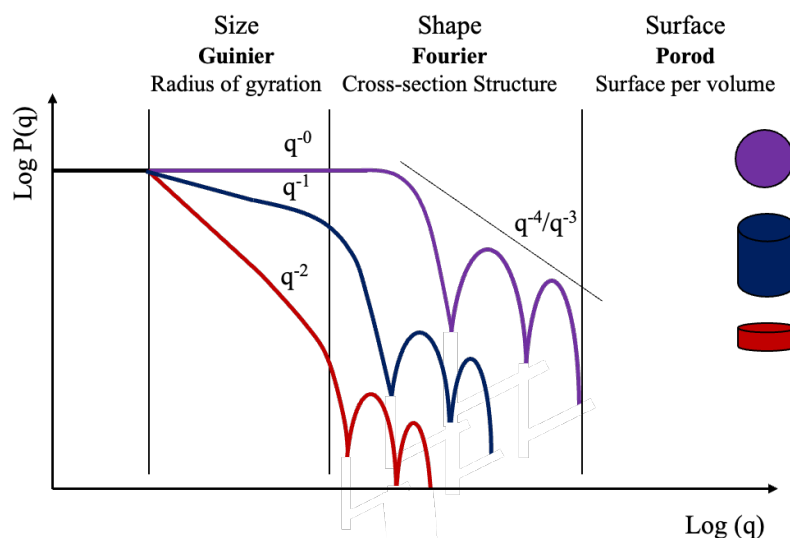


Figure III.16. Information that can be extracted from X-rays scattering for the form factor inspired from Anton-Paar documentation on SAXS.

SAXS measurement is based on the deviation of a collimated beam of X-rays (*i.e.* made parallel, thanks to apertures) at small angles typically  $\theta \leq 1^\circ$  induced by the particles dispersed in the solvent in the case of this study (yet SAXS can also be applied on thin solid films, if their absorption is not too high). This X-rays scattering induced by nanoparticles is defined by the differential scattering cross-section (*i.e.* the fraction of photons scattered by the particles under an illumination beam flux  $I_0$ , at a direction  $\theta$  and in a solid angle  $d\Omega$ ) as:<sup>208</sup>

$$\frac{d\Sigma}{d\Omega}(q) = \frac{\phi_p(1-\phi_p)}{V_p} I_1(q) \quad (\text{Equation III.19})$$

$$I_1(q) = \frac{1}{N_p} \left| \sum_{i=1}^{N_p} F_i(\vec{q}) e^{-j\vec{q} \cdot \vec{r}_i} \right|^2 = \frac{1}{N_p} \sum_{i=1}^{N_p} \sum_{j=1}^{N_p} F_i(q) F_j(q) \frac{\sin(qr_{ij})}{qr_{ij}} \quad (\text{Equation III.20})$$

where  $I_1$  represent the Fourier transform of all the particle form factor  $F_i(q)$  taking into account their phase differences due to their different positions  $\vec{r}_i$  and orientations relatively to the scattering vector  $\vec{q}$ ;  $N_p$ , number of particles in the scattering volume  $V$  (with  $\frac{N_p}{V} = \frac{1}{V_p}$  for a homogeneous suspension);  $\phi_p$ , volume fraction of the particles in suspension.

The right hand of Equation III.20 is an approximation for particles having spherical geometry: in case of anisotropic particles, it is hypothesized that they exhibit random orientations in the suspension. Within this hypothesis, and also under condition that the suspension is diluted enough so that inter-particle interactions can be neglected, the SAXS measurements can be fitted according to theoretical form factors  $P(q)$  which have been derived for all simple or complex geometries (spheres, cylinders, plates, core-shells and hollow shells *i.e.* vesicles...), in particular by Jan S. Pederson. In addition, the scattering invariant ( $Q$ ) which represents the volume of the entire reciprocal space scattering can be used to access to the volume fraction of the particles, when their contrast is known (or the reverse).<sup>209</sup> For a suspension of particles, whatever their shape, the equation is:

$$Q = \int_0^\infty I(q)q^2 dq = 2\pi^2(\Delta\rho)^2 \phi_p (1 - \phi_p) \quad (\text{Equation III.21})$$

$Q$ , scattering invariant;  $\Delta\rho$ , contrast of X-ray scattering length density between particles and solvent;  $\phi_p$ , volume fraction.

In practice, the integration is performed numerically from the experimental  $I(q)$  from  $q_{\min}$  to  $q_{\max}$ . The system is very sensitive to background subtraction (for example, the reference capillary filled with pure PBS must be identical to sample capillary, with same diameter), but nevertheless, the experimental invariant can give good insight on the actual concentration of the scattering particles (if their contrast to X-rays,  $\Delta\rho$ , is well-known). In X-ray scattering, the contrast of the particle can be easily calculated from the chemical formula of the compound by counting the number of electrons of all their constituting atoms, which all exhibit the same scattering length (*i.e.* square root of their scattering cross-section),  $b_e = 2.812 \times 10^{-13}$  cm. The sum is then divided by the molecular volume (known from the molar mass and the mass density) to compute the scattering length density (SLD),  $\rho$ . The contrast  $\Delta\rho$  is then simply the difference with the SLD of the solvent, here  $\rho_{\text{water}} = 9.4 \times 10^{10} \text{ cm}^{-2}$ , the salts having negligible effect unless they contain high  $Z$  number metal cations like lanthanides. Taking into account the

monomer formulas of PLA, PCL and PEO and their mass densities, which vary between 1.1 and 1.2  $\text{g}\cdot\text{cm}^{-3}$  (or even 1.4  $\text{g}\cdot\text{cm}^{-3}$  for the crystalline form of PLA), we can consider an average SLD  $\rho_{\text{PCL}} \cong \rho_{\text{PLA}} \cong \rho_{\text{PEO}} = 11 \times 10^{10} \text{ cm}^{-2}$ . Therefore, we deduce an average contrast to X-rays  $\Delta\rho = 1.6 \times 10^{10} \text{ cm}^{-2}$  for all the copolymers.

As expected, Figure III.17 shows the SAXS curves of samples prepared by nanoprecipitation (with or without drug loading) which do not exhibit the  $q^{-2}$  envelope expected for vesicles. With rather a  $q^{-4}$  behavior, the curves are representative of a polydisperse sphere form factor. In order to compare their sizes by SAXS with the DLS measurement, the  $R_{Z\text{-average}}$  value was calculated from the  $P(R)$  Log-normal distribution function of radii used to fit the data by convolution of  $P(R)$  with the theoretical form factor  $P(q,R)$  of spheres of radius  $R$ .

On the other hand, the SAXS curve  $I(q)$  plotted on Figure III.18 exhibits a  $q^2$  which is typical for a hollow shell. Moreover, the  $R_g$  can be extracted from the following Guinier equation:

$$\ln[I(q)] \cong \ln I_0 - \frac{R_g^2}{3} q^2 \quad (\text{Equation III.22})$$

In theory, the largest  $R_g$  values that can be measured are of the order of  $q_{\text{min}}^{-1} \sim 222 \text{ \AA}$  (22 nm), but in practice we can manage to determine the onset of the ‘‘Guinier plateau’’ of objects for  $R_g$  values up to 40-50 nm (although with more uncertainty). In this case, the extracted  $R_g$  value is 49 nm, within the margin of error of the Guinier’s fit. The membrane thickness is determined with much better precision, giving it a value of 12.6 nm typical for polymersomes.

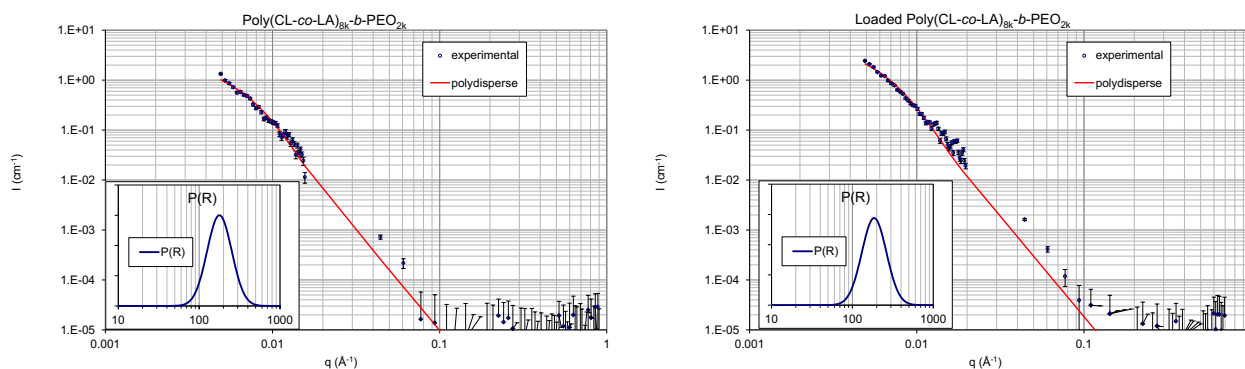


Figure III.17. SAXS curves of (L)P(CL<sub>58</sub>-co-LA<sub>8</sub>)-b-PEO<sub>45</sub> samples, loaded (L) and unloaded obtained by nanoprecipitation technique as micelles structures, after subtraction of the intensity measured on a capillary filled with pure PBS buffer. The curves were fitted with the theoretical  $P(q)$  form factor of polydisperse filled spheres. In order to compare to the DLS results, the Z-average radii defined by  $R_{Z\text{-ave}}^3 = \langle R^6 \rangle / \langle R^3 \rangle$  were calculated using the Log-normal size distributions shown as insets, yielding:  $R_{Z\text{-ave}} = 35$  and 36.5 nm, respectively for unloaded P(CL-co-LA) and loaded P(CL-co-LA) samples. The weight concentrations of the suspensions were measured by thermogravimetric analysis (TGA), respectively 4.8, and 4.7  $\text{g}\cdot\text{L}^{-1}$ .

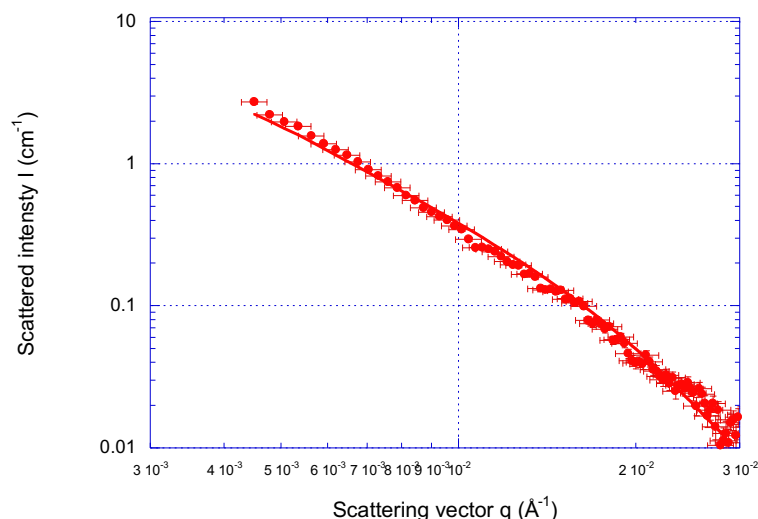


Figure III.18. SAXS curve of PEO<sub>45</sub>-*b*-P(CL<sub>35</sub>-*co*-LA<sub>5</sub>) formulated by thin film rehydration method, after subtraction of the intensity measured on a capillary filled with pure PBS buffer. Dry extract concentration measured by TGA: 4.9 g·L<sup>-1</sup>, after subtraction of the weight of PBS salt. The solid line corresponds to the calculated  $P(q)$  for a hollow shell of core radius 32.3 nm (taking into account a polydispersity index of 0.35) and a membrane thickness of 12.6 nm (PDI=0.15). The  $R_g$  value is 49 nm as calculated by Guinier plot but as explained above, it is the upper limit that can be measured in this configuration (the curve does not exhibit a Guinier plateau towards low- $q$  values).

#### III.2.4.6. Cryo-TEM

For sample prepared by nanoprecipitation, cryo-TEM evidenced small solid nanostructures,  $21.2 \pm 4.4$  nm in size, as shown in Figure III.19. The broad signal previously obtained by DLS can also be explained by the presence of rods in the sample. These results finally evidenced the presence of micelles in the medium as opposed to the structure obtained with thin film rehydration. Figure III.20 clearly shows the presence of nanostructures with a bilayer. The Cryo-TEM allows to determine an average diameter of the vesicle of  $90 \pm 30$  nm with a membrane thickness of  $11 \pm 1$  nm (average on  $n \approx 100$  particles and  $n \approx 59$  bilayer). Comparing cryo-TEM of nanoprecipitated samples with the ones prepared by the thin film method, it is possible to clearly evidence the difference between the structures obtained using both methods. (Figure AIII.1 ; Figure AIII.2) We can interpret this result like in the work of Zhou *et al.* on PCL-*b*-PEO self-assemblies, who demonstrated the positive role of heating above the  $T_m$  during the film rehydration step, which gives more mobility to the chains than the presence of the THF solvent in the nanoprecipitation route.<sup>201</sup>

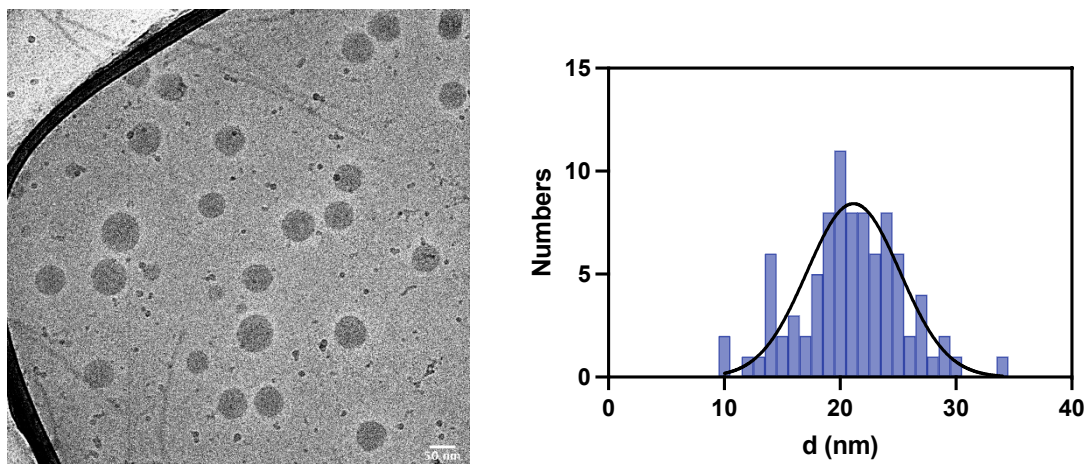


Figure III.19. Cryo-TEM of  $\text{PEO}_{45}\text{-}b\text{-P}(\text{CL}_{49}\text{-}co\text{-LA}_8)$  obtained by nanoprecipitation showing the presence of micelles and rods, and the corresponding histogram based on measurement of 100 micelles fitted by a gaussian function.

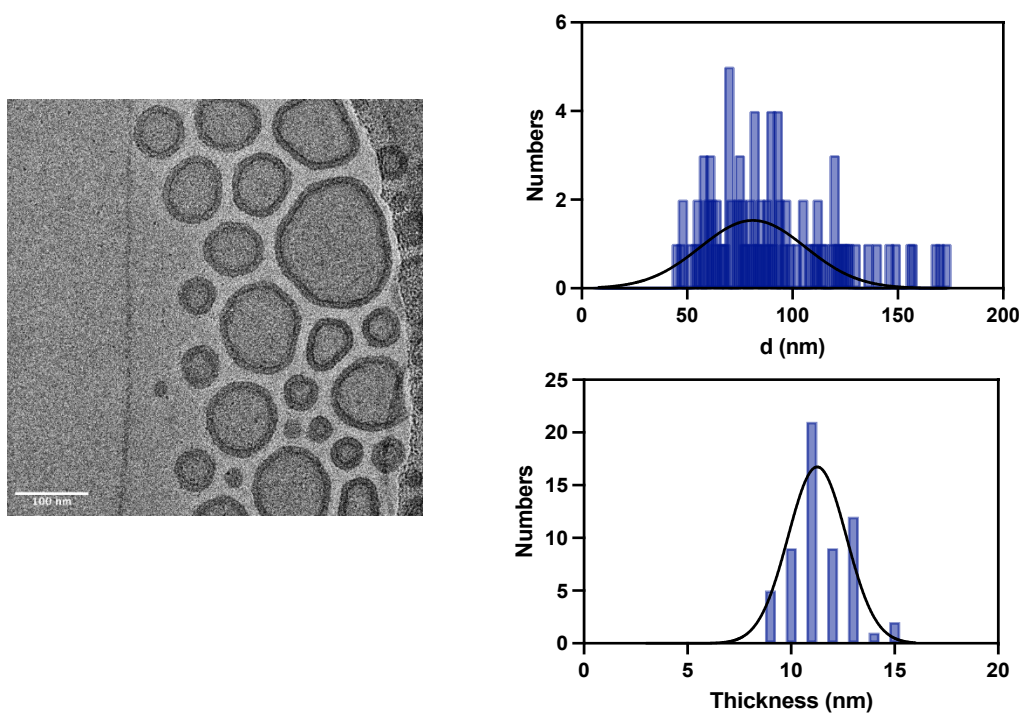


Figure III.20. Cryo-TEM of  $\text{PEO}_{45}\text{-}b\text{-P}(\text{CL}_{35}\text{-}co\text{-LA}_5)$  obtained by thin film rehydration and on the upper right, their histogram corresponding to a measurement of 101 vesicles fitted by a gaussian function. On the bottom right, a histogram obtained on the measurement of the thickness of the membrane measured on 59 membranes fitted by a gaussian function.

### III.2.4.7. Stability over time

To ensure the stability of the resulting polymersomes over time, measurement of the  $Z_{\text{average}}$  diameter and the PDI were performed by DLS on polymersomes made of a PEO-*b*-P(CL-*co*-LA) by thin film method in PBS. Measurements were carried out for approximately two months and Figure III.21 confirms a stable  $Z_{\text{average}}$  with a slight increase of the PDI. Polymersomes structures kept their integrity over two months, but it could be interesting to perform new analyses to evidence their shape or to confirm their integrity at longer term.

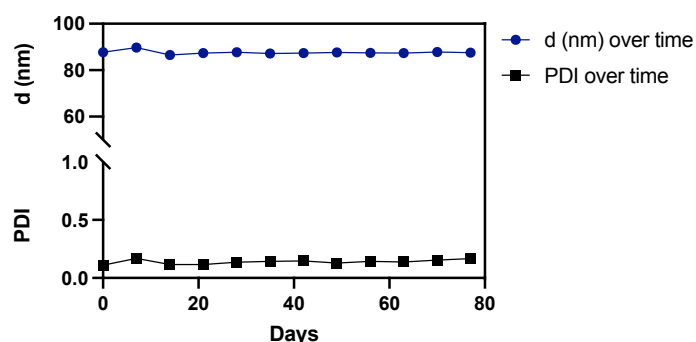


Figure III.21 . Stability of polymersomes obtained by thin film in PBS over time by measuring their size and their PDI for 77 days (one measurement every 7 days). The  $Z_{\text{average}}$  on 3 measurements were plotted as a function of time as the PDI.

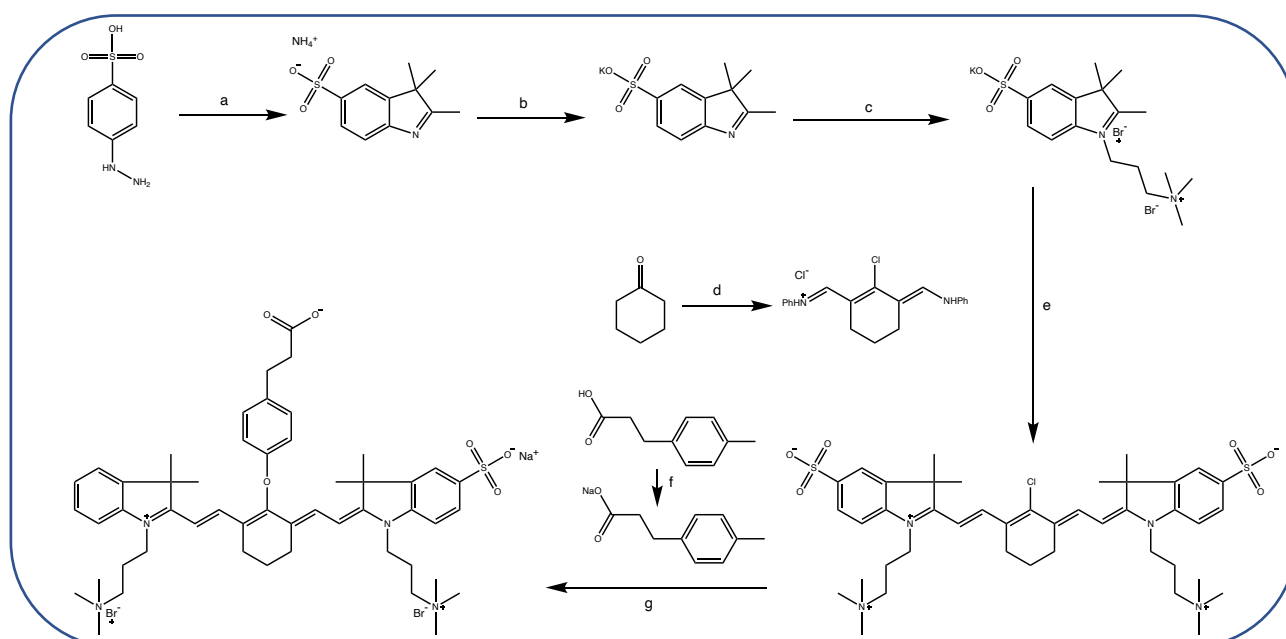
Now that we have solved the issues to obtain vesicles as compared to spherical or cylindrical rods (worm-like micelles) thanks to the self-assembly route, we will describe in the next section the method to encapsulate bioactive substances or fluorescent dyes in their aqueous cores and wash the external phase. But first of all, we need to precise which compounds will be loaded and how to obtain them.

### III.2.5. Encapsulation of active substances and dyes in PEO-*b*-P(CL-*co*-LA) self-assembly

#### III.2.5.1. Synthesis of ZW800-1

Optical imaging (OI) allows the visualization of different kinds of luminescence processes that generate light emission. Among them, fluorescence imaging (FLI), which is based on photoluminescence, requires the use of fluorescent dyes that absorb an excitation light

and then emit back instantaneously photons at an upper wavelength. The visible light (400-650nm) penetration into biological tissues is limited to few mm due to the presence of highly absorbing molecules such as melanin and hemoglobin, and by the multiple scattering caused by tissues, membranes, fibers etc... Fortunately, this biological absorbance of photons decreases drastically in the near-infrared (NIR) region, particularly in NIR-I window *i.e.* 700-900 nm range, allowing of few cm of depth of imaging. Moreover, autofluorescence of biological tissues is far weaker in the NIR as compared to the visible range, leading to far less background. For these reasons, exogen fluorophores are developed to absorb light in the NIR and achieve the best penetration and sensitivity. The only NIR fluorescent dye approved by the FDA for human use is the indocyanine green (ICG), but this compound is instable in aqueous media and has a moderate quantum yield.<sup>210,211</sup> Hence, Choi *et al.*<sup>211,212</sup> developed a zwitterionic near-infrared fluorophore that absorbs at a wavelength of 772 nm and named ZW800. Interestingly, ZW800-1, a ZW800 derivative with a carboxylic function, shows a quantum yield (QY) of 15% and an extinction molar coefficient,  $\epsilon$ , of 249k L·mol<sup>-1</sup>·cm<sup>-1</sup>, making it a good candidate for FLI (the product of QY and  $\epsilon$  determines the “brilliance” of a fluorescent probe). The synthesis of this molecule allows its functionalization by taking advantage of the presence of the arm in the center of the molecule. (Scheme III.2) Still, some steps of the synthesis remain laborious and time consuming, moreover the desired product lacks in purity. Regarding this, the 3<sup>rd</sup> step of the synthesis was optimized in collaboration with J. Razafimahefa based on the protocol developed by Yang *et al.*<sup>213</sup>



Scheme III.2. Synthetic scheme of ZW800-1, adapted from reference 211, with some modifications in our work (a) 3-methyl-2-butanone AcOH, Ar atm, 180°C overnight (b) KOH, 2-propanol, 40°C, few hours (c) (3-bromopropyl)trimethylammonium bromide, toluene, atm Ar 120°C, overnight (d) Vielsmeier-Haack : i) DMF, POCl<sub>3</sub>, 0°C ; ii) cyclohexanone/DCM, reflux (100°C), 2 h iii) Aniline/EtOH, 0°C to r.t. (e) AcONa, EtOH atm Ar, reflux, 6 h (f) NaOH/MeOH, 2 h (g) H<sub>2</sub>O/DMSO, atm Ar, 70°C, 6 h.

The third step was investigated because the reaction developed by Choi *et al.* required 48 h and, when reproduced in our laboratory, led to a yield under 10%. Moreover, the potassium 2,3,3-trimethyl-3H-indole-5-sulfonate should be added as a thin powder due to its poor solubility in toluene. The reaction temperature was also modified to 70°C (Choi's synthesis: 180°C) since the end-product was insoluble in toluene and stucked at the bottom of the flask. Given that the temperature of the reaction determines the kinetics of reaction, it was decided to increase the temperature and stop the reaction once all the product has been dissolved and that no supernatant is still visible. The reaction time is therefore dependent on the amount of material used for the reaction. For example, using 5 g of potassium 2,3,3-trimethyl-3H-indole-5-sulfonate at a temperature of 120°C, approximately 4 hours are needed to fully dissolve the reactant and leads to a final yield between 20-36%. Finally, the first step of filtration after reaction was suppressed and the solvent of reprecipitation, MeOH was added directly into toluene.

The reaction leading to Vilsmeier-Haack moiety was also optimized to improve the purity. Indeed, the by-product induced during this reaction leads to the formation of a blue by-product after the last reaction which is difficult to eliminate by washing steps. The protocol optimized by Yang *et al.* allows to obtain a product with a better purity.<sup>213</sup>

#### III.2.5.2. Encapsulation of ZW800-1, rhodamine B and doxorubicin

In the following, the copolymer self-assemblies described so far were used to encapsulate ZW800-1, rhodamine B and doxorubicin, with the aim to act as driving vehicles to deliver a drug at a tumor site. As reminder, the ZW800-1 is a fluorophore used to perform NIR FLI, doxorubicin is a common anticancer drug very used in chemotherapy, and rhodamine B is a fluorophore used to perform confocal analyses of cells for the preliminary *in vitro* studies, before preclinical assays, *i.e.* in mice. Moreover, rhodamine B has a similar structure than ZW800-1 in term of charge allowing, supposedly, a similar encapsulation behavior. In another way, it was supposed that due to charges presence on rhodamine B, as ZW800-1, it does not cross the hydrophobic membrane (11-12 nm thickness as estimated by SAXS and cryo-TEM). Actually, ZW800-1 could not be used for confocal microscopy analyses because it absorbs at 772 nm while standard confocal equipment does not possess the right lens to probe the NIR region. Therefore, it is necessary to use another fluorescent dye, in the visible range, herein rhodamine B. The rate of encapsulation of each dye was first optimized. An increase in the rate of encapsulation was evidenced while increasing solution concentration to 5 mM during the

copolymer self-assembly. Above this concentration, the loss of compounds during the step of encapsulation became too high compared to the small increase of compound encapsulated in the nanostructure. Thus, it was chosen to limit the consumption of the different compounds by using a loading concentration of 5 mM.

The encapsulation efficiency of drug and dyes by the nanostructures is evaluated by two different parameters: the drug loading content (DLC) and the encapsulation efficiency (EE). (Equation III.23; Equation III.24). The concentration in doxorubicin, ZW800-1 and rhodamine B were determined by fluorescence spectroscopy from a previously performed calibration curve, after addition of Triton™ X-100 in the medium to destabilize the nanostructure, releasing dyes and drug. (Please note that the calibration lines were performed in the presence of 10% of Triton™ X-100) Results on Table III.6 show that spherical and rod-like micelles exhibit a poor capacity to entrap dyes and drug, with a high error that can be due to uncertainty on low fluorescence measurements, or dilution, etc. On the opposite, polymersomes show a high capacity to encapsulate doxorubicin due probably to the amphiphilic behavior of doxorubicin leading to its presence both within the bilayer and in the hydrophilic cavity. Instead, ZW800-1 exhibits a highly hydrophilic behavior (owing to its multivalent charge), leading to its encapsulation only in the hydrophilic cavity.

$$DLC (\%) = \left( \frac{\text{weight of drug in polymers}}{\text{Final weight of (polymers+drug)}} \right) \times 100 \quad (\text{Equation III.23})$$

$$EE (\%) = \left( \frac{\text{weight of drug in polymers}}{\text{weight of initial quantities of drug}} \right) \times 100 \quad (\text{Equation III.24})$$

Table III.6. Comparison of DLC and EE\* between micelles/rods and polymersomes.

		ZW800-1	Doxorubicin
Micelles	DLC (%)	0.17 ± 0.19	1.8 ± 1.14
	EE (%)	0.006 ± 0.0055	0.27 ± 0.07
Polymersomes	DLC (%)	0.47 ± 0.38	49.9 ± 18.29
	EE (%)	0.052 ± 0.047	8.73 ± 1.87

\*Dyes and drug were titrated by fluorescence spectroscopy thanks to prior calibration curves and disruption of the nanostructures by adding 10% of Triton™ X-100.

Preliminary results on the capacity of polymersomes to release the dye and doxorubicin in an acidic medium were recorded on flow-through dissolution systems.<sup>214</sup> The absorbance of drug or dye was recorded at different time intervals in the continuous flow of the medium, at a regulated temperature of 37°C. Release tests were performed at pH 5.5 and 7.4, in parallel. At both pH, we observe a burst release phenomenon of doxorubicin from polymersomes in the first minutes of the test. (Figure III.22) Still, a higher burst release can be observed when the polymersomes were subjected to a pH of 5.5, mimicking the acidic environment of the endosome. After this burst effect, we can note that doxorubicin is still released from the polymersomes at pH 5.5 while at pH 7.4, no more doxorubicin is released. In the case of ZW800-1, no release was observed at both pH. This can probably be explained by the presence of charges on ZW800-1 making it unable to diffuse through the bilayer while doxorubicin, owing to its amphiphilic behavior, is able to diffuse through the hydrophobic membrane. Nevertheless, this analysis should be performed with the optimized conditions to obtain a percentage of release versus time giving access to the diffusion law followed by the nanoparticles in closer conditions to the preclinical assays.

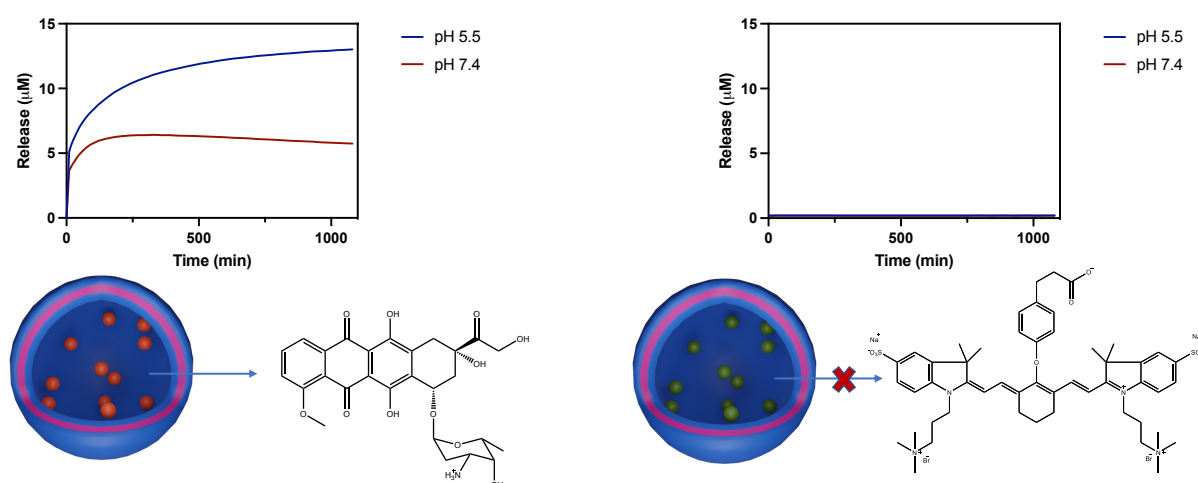


Figure III.22. Drug (left, doxorubicin) or dye (right, ZW800-1) release assay from polymersomes using Sotax™ USP-4 flow-through dissolution system in two different conditions of pH, at 37°C.

To summarize, nanoprecipitation was first used due to its ease and potential to be adapted to scale up production. Unfortunately, it was found by several methods (ALS, AF4,

SAXS, cryo-TEM...) that this technique leads to micellar structures, either spherical or wormlike, *i.e.* which present a hydrophobic core. Moreover, a signal has been detected in fluorescence even after the purification step, which corresponds to partial encapsulation, or at least an adsorption of the dye and of the drug. As a reminder, we use  $2 \text{ kg}\cdot\text{mol}^{-1}$  PEO chains as hydrophilic copolymer block, thus it is possible that some molecules are trapped in the hydrophilic corona of the micelles. Moreover, doxorubicin exhibits an amphiphilic behavior and can partition between the two domains of the structures. It was thus decided to test the micelles *in vitro* and *in vivo*. These samples are also constituted of rods and Ridolfo *et al.* evidenced the utility in drug loading of rods made of PEO-*b*-P(TMC-*co*-CL).<sup>215</sup>

The modification of the structure for the thin film method can be explained by the plasticizing effect of chloroform used in the formation of the film. Although THF is a better solvent for polyester (as can be evidenced from the Hansen solubility parameters, leading to a calculated solubility parameter of PCL  $\chi=0.01$  in THF *versus*  $\chi=0.13$  in chloroform), it is also miscible with water, therefore THF is more rapidly eliminated for the membranes during the nanoprecipitation process than chloroform during the film rehydration method.<sup>216</sup> In previous work by J. Xu *et al.* with another polyester, poly(lactic-*co*-glycolic acid) (PLGA), the authors showed that adding 10% of chloroform during nanoprecipitation (with DMSO as solvent) enabled to improve the encapsulation rate of drugs (doxorubicin and tamoxifen) in PLGA nanoparticles.<sup>217</sup> Moreover, using a bath with a temperature near to the melting point increase molecular chain motions which ease the formation of polymersomes.<sup>201</sup> It would also have been interesting to tune the proportion in *L*-LA moiety to obtain the best release system while still keeping the formation of polymersomes. Moreover, Yin *et al.* evidenced the biocompatibility of a triblock polymer composed of PL-LA-*b*-PCL-*b*-PEO in different proportions, validating the potential of combing two different polyesters in the same copolymer for *in vivo* applications.<sup>218</sup>

### III.2.6 *In vitro* tests on PEO-*b*-P(CL-*co*-LA) self-assembly

#### III.2.6.1. Micelles

At first, the toxicity threshold of micelles was determined. The micelles at different concentrations in polymers containing ZW800-1 and rhodamine B were tested on MKN45-eGFP-FLuc cell line. These cells come from gastric carcinomas and were chosen for several

reasons: (i) they express luciferase allowing bioluminescence imaging (BLI) to evidence the rate of mortality;<sup>219</sup> (ii) cells exhibit the property to aggregate and form a spheroid called “tumosphere”, which will be lost after cell mortality for example; (iii) Nguyen *et al.* evidenced that the use of verapamil, a drug used in the case of heart diseases, could entail a better internalization for this cellular line. More precisely, verapamil inhibits the drug efflux pump systems in the cell plasma membranes, allowing an increase of intracellular internalization.<sup>220</sup>

It is noticeable that the assays were performed on fresh solutions of micelles to avoid the burst release phenomenon that could false results. To ensure that no toxicity was due to the micelles themselves, preliminary cell toxicity tests in the presence of encapsulated ZW800-1 and rhodamine B were performed. Two concentrations (0.1 and 0.4 mg/mL) with survival rate above 80% determined by BLI (based on ISO 109993-5 assay) were used for further conditions. (Figure AIII.4) For reasons mentioned above and to ensure, also in this case, that the toxicity is not ascribed to verapamil, two concentrations of it were tested, and no toxicity was observed. Doxorubicin was incubated in the presence of verapamil and no significant increase in toxicity was observed in comparison with doxorubicin at the same concentration. In a second phase, micelles encapsulating all together doxorubicin, ZW800-1 and rhodamine B, in the presence or not of verapamil, were tested. An increase in concentration of verapamil did not evidence a modification in toxicity induced by a higher internalization, supposedly due to the presence of verapamil. Actually, no toxicity increase was observed in comparison with micelles without verapamil. (Figure III.23) Nevertheless, it is difficult in this case to conclude if the micelles allow a decrease of the doxorubicin toxicity compared to free doxorubicin, because the concentrations tested were not exactly the same (The concentrations in doxorubicin in micelles were approximately contained between 50 and 100  $\mu$ M). To conclude on these assays, Figure III.23 shows that the adjunction of verapamil does not bring a significative effect on the toxicity. Moreover, these assays do not allow to conclude sharply that the presence of micelles lead to a decrease in toxicity of doxorubicin. Despite nearly 80% of survival rate, all micelles loaded with doxorubicin still exhibit a loss in the capacity of cells to form spheroids, which would be related to a tumor growth inhibition *in vivo*. (Figure AIII.3)

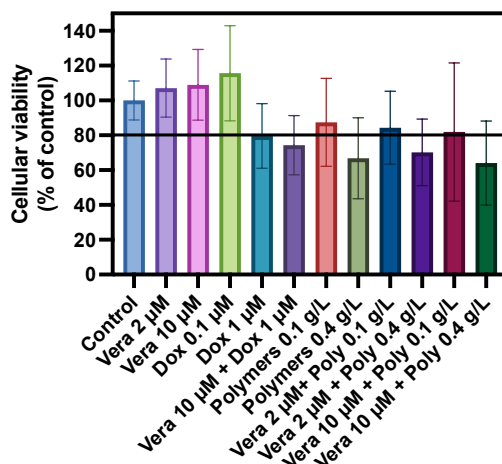


Figure III.23. Cellular viability of MNK45 cell incubated on different conditions (error bar correspond to replicated experiments,  $n = 3$ ).

To evidence the cell internalization of the nanostructures containing ZW800-1, rhodamine B and doxorubicin, they were incubated with MKN45 cells and then were observed using a confocal microscope. To ensure the internalization of the micelles within the lysosomes (having an acidity allowing the degradation of the copolymer), these were marked by incubating the cells with lysotracker™ green DND-26 dye, followed by a co-localization study under the microscope. The modification of pH in lysosome renders the lysotracker positively charged, leading to its accumulation (as it cannot cross the lysosomal membrane anymore). The lysotracker green was incubated with the cells at 0.1 µM (from a stock solution at 1 mM in DMSO) for 1 min before classical cell fixation with glutaraldehyde. The dyes were excited with a green channel at 496 nm. As the excitation wavelength of doxorubicin is also 500 nm, there is an overlap of their emission signals in confocal microscopy. The red channel at 561 nm allows to excite rhodamine B molecules, and the blue channel excites DAPI at 405 nm, staining the cells' nuclei. A second overlapping can occur between rhodamine B and doxorubicin/Lysotracker™ green if the excitation spectra are compared, but in a lesser extent. (Figure AIII.5)

Confocal microscopy results show that our nanostructures were internalized by cells, as shown by red and green channels, as compared to the halogen lamp channel (bright field). The granular aspect of the green channel is a good indication that it corresponds mostly to the lysosomal compartments, which are small organelles in the cells. Colocalization between red and green channels is also strong (as seen from the yellow regions in the overlay image), but the overlap of rhodamine B, lysotracker green and doxorubicin fluorescence signals limits the good

identification of these molecules. It could be interesting to perform again these experiments without doxorubicin or with another lysotracker dye to discriminate the internalization of the lysotracker and the doxorubicin. Moreover, rhodamine B and doxorubicin red emission signals are also superimposed (both are located around a wavelength of 600 nm), which prevents to discriminate between doxorubicin-loaded micelles and free doxorubicin in the cytoplasm. So, the next experiments were performed with another lysotracker, with absorption in the deep red allowing its discrimination. Similarly, rhodamine B and doxorubicin would need to be better separated to be sure of the origin of the recorded signal. This spectral overlap clearly limits the interpretation of confocal microscopy results, although these first experiments already bring qualitative insight on the internalization of the micelles through the classical endocytosis pathway, leading to their final accumulation in lysosomes.<sup>221</sup>

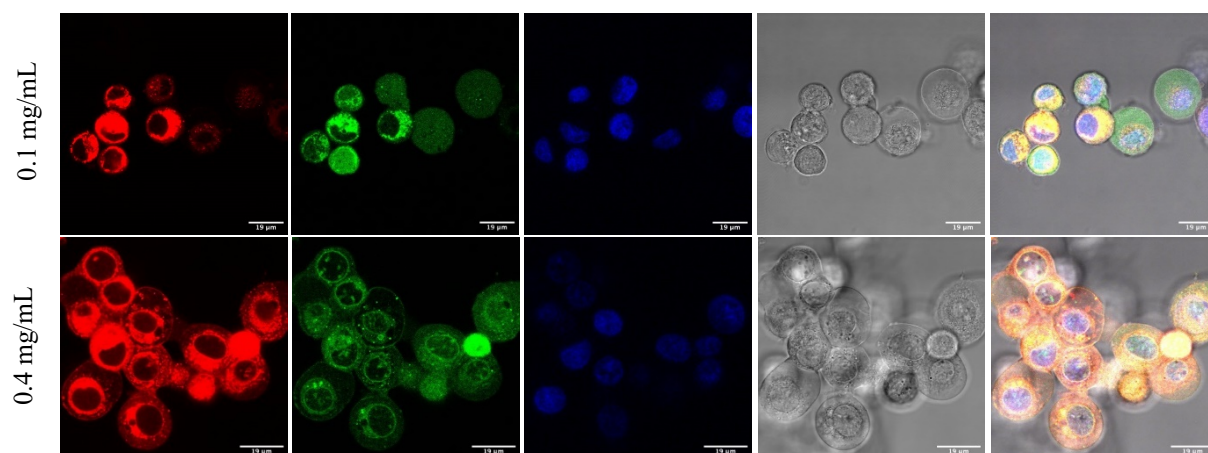


Figure III.24. confocal analyses on MKN45 with two different micelles concentrations encapsulating doxorubicin: 1) rhodamine B with  $\lambda_{ex} = 561$  nm (red channel); 2) Doxorubicin and lysotracker green excitation  $\lambda_{ex} = 496$  nm (green channel); 3) DAPI  $\lambda_{ex} = 405$  nm (blue channel 3); 4) bright field channel; 5) merge of the fourth channels.

### III.2.6.2. Polymersomes

As previously determined for micelles, the toxicity of polymersomes at different concentrations has been determined using classical MTT (3-(4,5-dimethylthiazol-2-yl)-2,5-diphenyltetrazolium bromide) assays measuring the mitochondrial activity. In this case, two other cellular lines were chosen, also expressing the gene of luciferase in order to use them to induce tumors that can be measured by BLI, to see if the toxicity is not dependent on the cell type. MCF7-Luc2 cells are breast adenocarcinoma and HT29-Luc cells are colon adenocarcinoma. In this case the toxicity was expressed based on MTT tests, but BLI signal was also recorded for both cells. (Figure AIII.6 ; Figure AIII.7) MCF7 results are similar to

MKN45 results obtained for micelles, as a survival rate above 80% has been reached with a concentration of 0.8 and 1 mg/mL, while HT29 always exhibit survival rate above 80% no matter the polymersomes concentration. Please note that the cellular viability upper than 100% for HT29 comes from experimental uncertainties that show the limitation of this technique, but this apparent absence of cytotoxicity is compatible with the BLI assay. Anyway, a clear dose dependence is visible for MCF7 cells with both cytotoxicity assays (MTT and BLI), and to a lesser extend for HT29 cells. (Figure III.25)

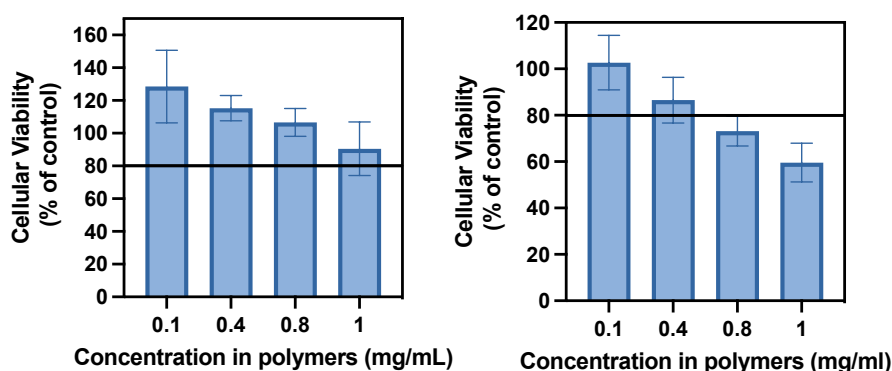


Figure III.25. Impact on the cells viability for a growing concentration in polymersomes revealed by MTT assays without loading of doxorubicin on HT29 cells (left) and on MCF7 cells (right).

Toxicity in the presence of encapsulated doxorubicin was then evaluated. For such tests, triplicate must be performed in the same conditions. However, it was not possible to easily control the concentration of doxorubicin encapsulated in the polymersomes. Therefore, it has been decided to first determine the concentration of encapsulated doxorubicin. Then for each assay, the tests using free doxorubicin have been performed using the same concentration than the ones of the encapsulated doxorubicin instead of always using the same concentration. Doxorubicin-loaded polymersomes induced a slight increase of toxicity in HT29 cells (at same concentration) as compared to blank polymersomes. (Figure III.25) In MCF7 cells, the impact of doxorubicin is higher as a decrease of approximately 33% is observed. (Figure III.26) Nevertheless, Figure III.26 also clearly evidences an increase in cellular viability when the doxorubicin is encapsulated in vesicles. Indeed, the cells viability fell under 10% when exposed to free doxorubicin, proving the efficiency of this drug to kill cancer cells. These results are concordant with the recorded BLI. (Figure AIII.8 ; Figure AIII.9)

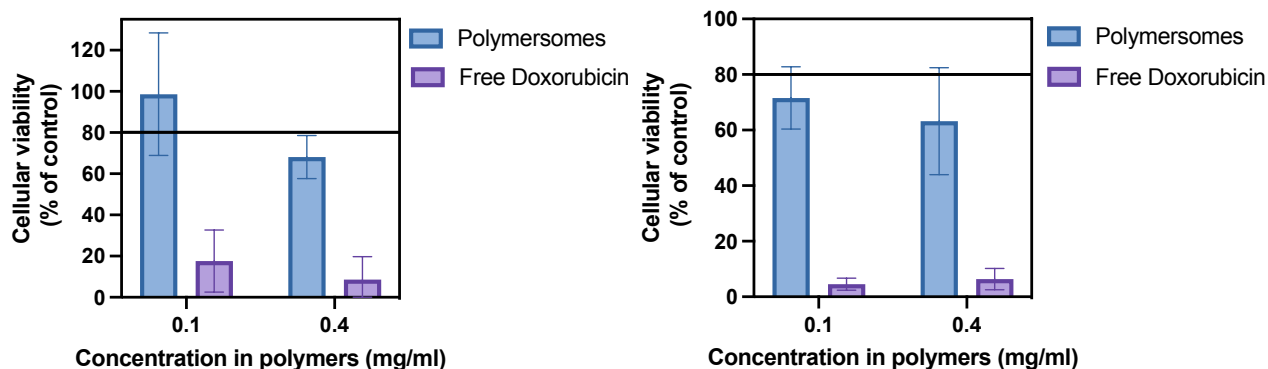


Figure III.26. Impact on the cells viability for a growing concentration in polymersomes revealed by MTT assays using encapsulated doxorubicin compared with free doxorubicin in same amount than it encapsulated on HT29 (left) and on MCF7 (right).

This MTT assay allows to highlight the impact of the encapsulation inside vesicles on the toxicity induced by doxorubicin. Such results are encouraging to decrease the side effects induced by doxorubicin on healthy cells by its encapsulation in polymer nanocarriers.

One possibility to explain the difference in toxicity obtained between MCF7 and HT29 could be their different internalization level of the vesicles. To explain this phenomenon, confocal microscope imaging observations were recorded in different conditions. To mitigate the issues observed with previous confocal analyses, the lysotracker green was replaced by a “deep red” lysotracker to avoid a superposition of signals between the lysotracker probe and doxorubicin. It was also decided to replace DAPI staining with Hoechst staining for nucleus. Indeed, Hoechst staining allows staining nucleic acids without permeabilizing the cells, which could alter polymersomes uptake. Moreover, two types of vesicles were tested: (i) polymersomes encapsulating doxorubicin only and (ii) polymersomes encapsulating ZW800-1 and rhodamine B to avoid a possible superposition of signal between doxorubicin and rhodamine B. (Figure AIII.5) It is important to note that the extracted signal on FITC channel ( $\lambda_{ex} = 488 \text{ nm}$  and  $\lambda_{em} = 500\text{-}550 \text{ nm}$ ) is closer to green than Alexa channel ( $\lambda_{ex} = 640 \text{ nm}$  and  $\lambda_{em} = 663\text{-}738 \text{ nm}$ ) explaining the color chosen. Moreover, it facilitated the interpretation and the visibility in merge imaging. (To have a complete idea of the wavelengths, DAPI probe channel has  $\lambda_{ex} = 405 \text{ nm}$  and  $\lambda_{em} = 425\text{-}475 \text{ nm}$ .)

For HT29 cells, and both types of polymersomes, no significant signal in green is observed (with subtraction of background). Since only slight green signal is observed at this step, for HT29 in presence of 0.1 and 0.4 mg/mL polymersomes, we can deduce that the

particles are weakly internalized in this type of cells, which could explain the very low toxicity observed with MTT assays. Or more simply, HT29 cells are more robust than MCF7 cells.

The results for MCF7 cells are relatively different. Indeed, in the presence of doxorubicin at 0.1 mg/mL, no signal in the green channel is observed, unlike the case of 0.4 mg/mL, where the green signal colocalizes with the red signal around the cell nuclei (blue signal). This confirms the presence of the nanostructures in cells. MCF7 cells in the presence of rhodamine-loaded polymersomes at the same concentration show the same results despite the overlap of staining problem with lysotracker™ deep red. In this case the green signal appears more diffuse around the nucleus. This can be explained by the time of incubation. Indeed, 24 h of incubation can lead to the destruction of polymersomes in lysosomes leading to the release of rhodamine B or doxorubicin into the cytoplasm. It could be interesting to perform confocal microscopy analyses along time to evidence the evolution of the signal and the probable disruption of polymersomes. A slight signal of rhodamine B is also present at 0.1 mg/mL, which is also present around the nucleus.

Nevertheless, the differences between the two types of cells cannot be easily explained. Indeed, currently the mechanisms of internalization are still misunderstood for each type of cells leading to some difficulties to explain the differences between the two cell lines. (Figure III.27 ; Figure III.28). It is important to note that these results were performed on  $n = 1$  and need to be considered as preliminary results, needing some improvement of the staining and confirmation by  $n = 2$  or 3 repeats. To conclude, these analyses allow to confirm the internalization of nanoparticles with a preferred localization of doxorubicin/rhodamine B signal around the nuclei for MCF7 cells instead of HT29 cells. Polymersomes at a concentration of 0.4 mg/mL in MCF7 cells clearly show a colocalization with lysotracker™ deep red, confirming an endocytosis pathway of the uptake.

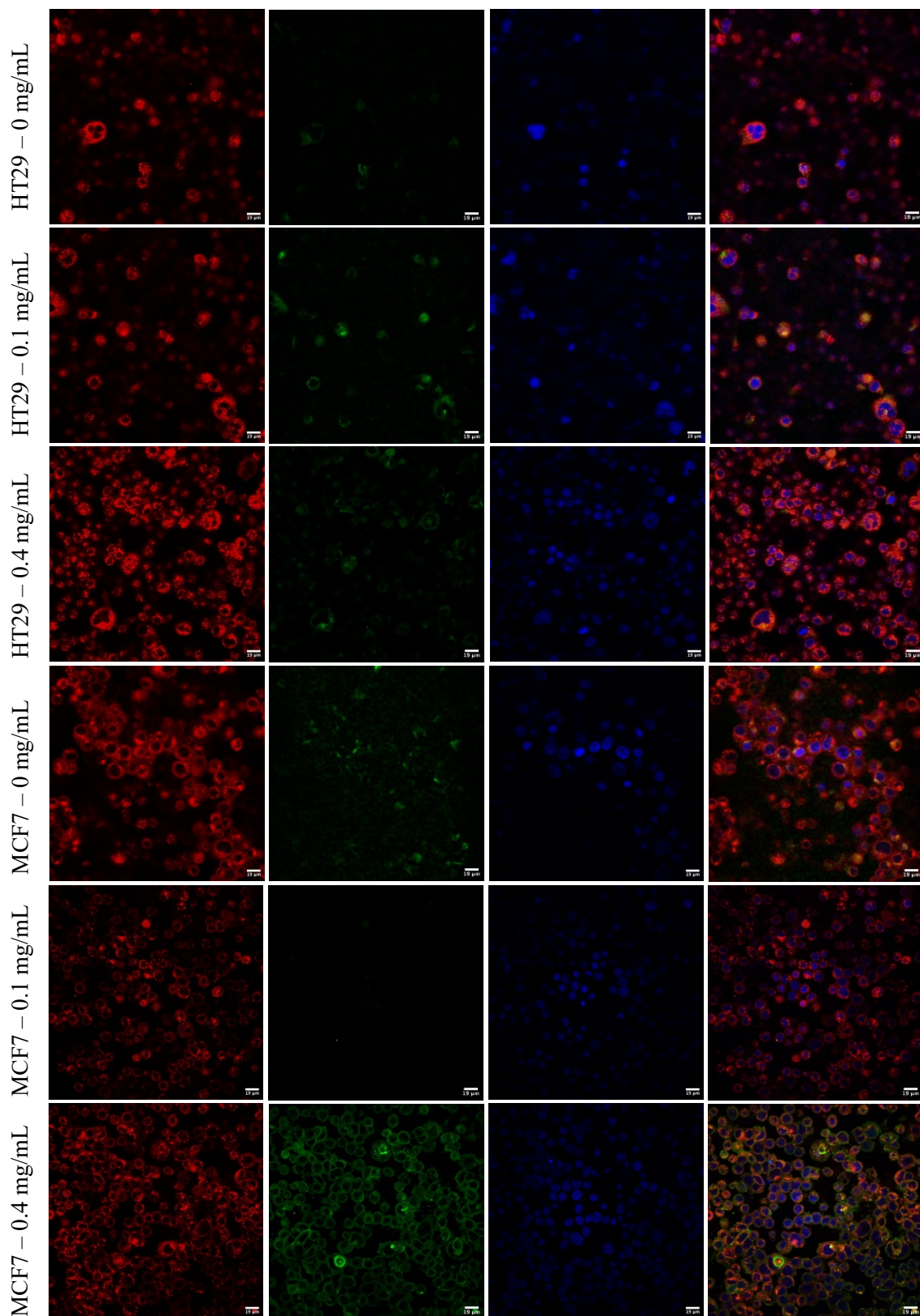


Figure III.27. Confocal analyses on MCF7 and HT29 at different polymersome concentrations which encapsulated doxorubicin: 1) LysoTracker  $\lambda_{ex} = 640$  nm (deep-red channel); 2) doxorubicin  $\lambda_{ex} = 488$  nm (green channel); 3) Hoechst  $\lambda_{ex} = 405$  nm (blue channel); 4) merge of the three channels.

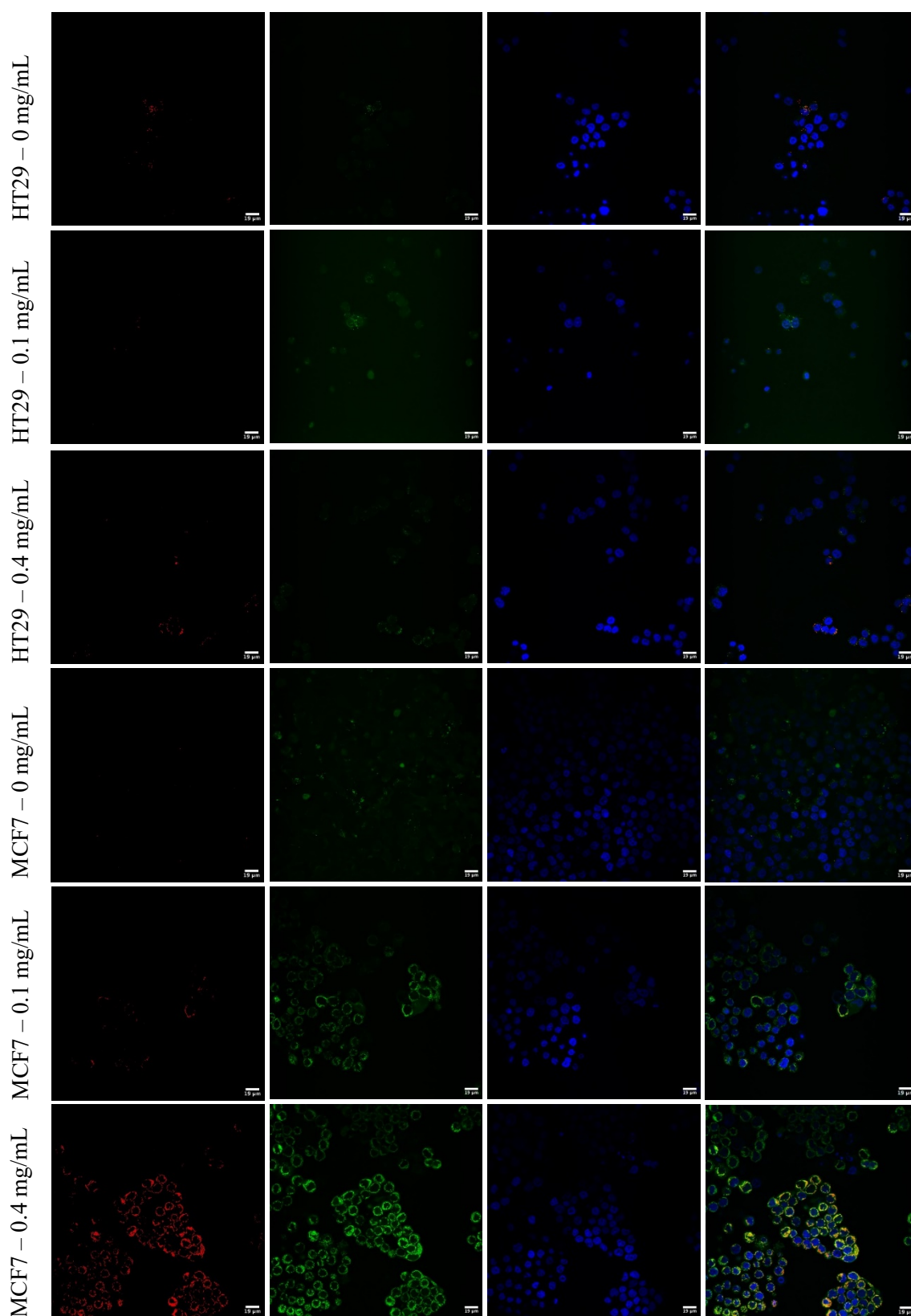


Figure III.28. Confocal microscope analyses on MCF7 and HT29 at different polymersome concentrations which encapsulated rhodamine B and ZW800-1: 1) Lysotracker deep red  $\lambda_{ex} = 670$  nm (red channel); 2) rhodamine B  $\lambda_{ex} = 488$  nm (green channel); 3) Hoechst  $\lambda_{ex} = 405$  nm (blue channel); 4) merge of the three channels.

### III.2.7. *In vivo* tests on PEO-*b*-P(CL-*co*-LA) self-assembly

#### III.2.7.1. *Micelles*

*In vivo* tests were performed on mice with implanted tumor on the leg with MKN45-Luc cells. *In vivo* BLI attests of the presence of induced tumor. (Figure III.29)

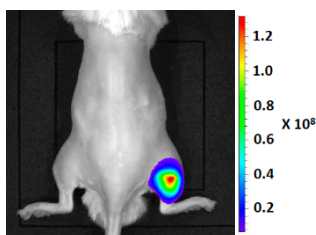


Figure III.29. Bioluminescence image to control the implanted tumor in the right posterior leg.

Concentrated suspensions, constituted of ZW800-1, rhodamine B and doxorubicin loaded micelles, were filtered at  $0.22 \mu\text{m}$  for sterilization and injected by intravenous way into mice ( $100 \mu\text{L}$ , in tail vein), and the micelle signal was tracked by FLI. An increase in the intensity of the signal is observed between 2 and  $7 \text{ mg/mL}$  of micelles due to an increase of dye concentration. After injection, the micelles are distributed in the mouse body, with a rapid clearance by kidneys after 1 hour. A second clearance can be observed, mainly for  $7 \text{ mg/mL}$ , by the liver (hepatobiliary route). After 3 hours in both cases, the signal almost disappeared due to the urination except for the liver for  $7 \text{ mg/mL}$ , which shows a slower clearance. Nevertheless, imaging also evidenced that the tumor (present in the right posterior leg) does not exhibit a fluorescent signal. (Figure III.30, Figure III.31)

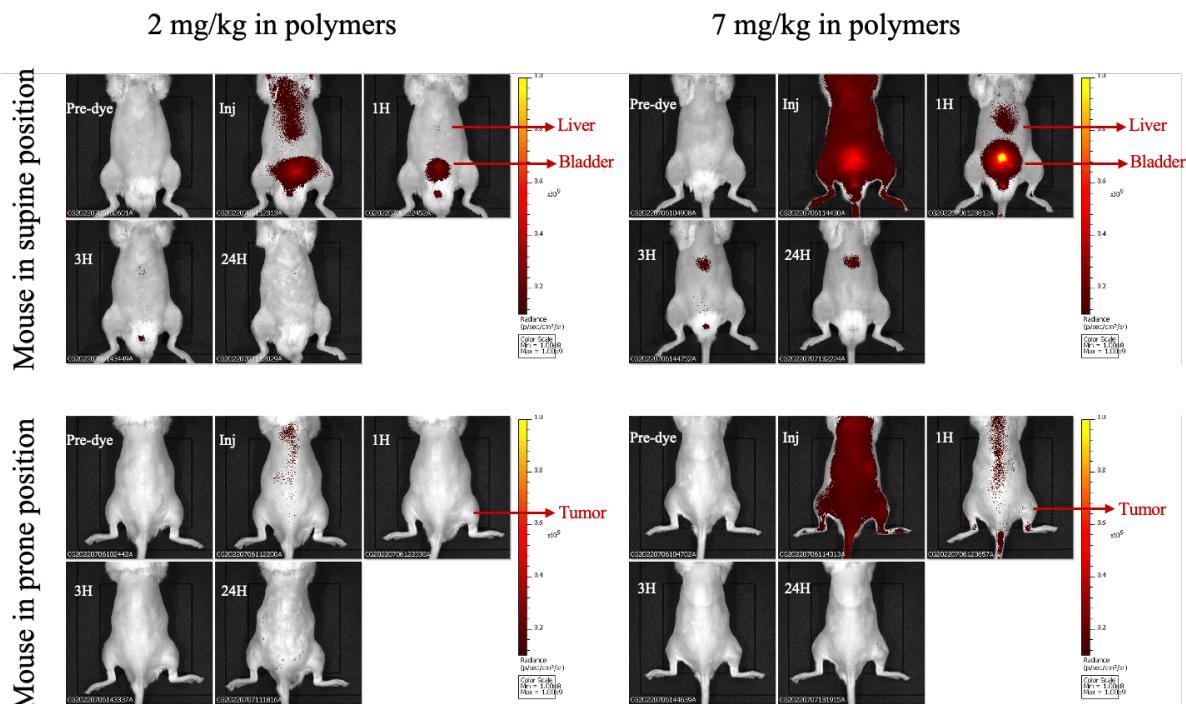


Figure III.30. Distribution of micelles over time at two different polymer concentrations (2 mg/kg and 7 mg/kg in polymers) tracked by FLI.

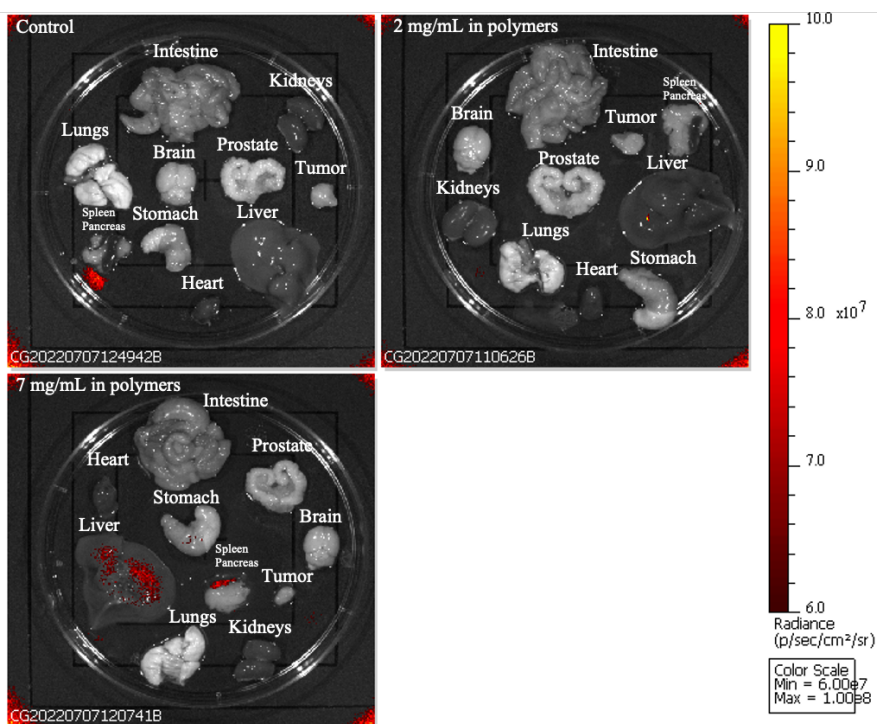


Figure III.31. *Ex vivo* FLI of control and injected mice organs with two different polymer concentrations (2 mg/kg and 7 mg/kg in polymers) performed 1 day post-injection.

*Ex vivo* imaging was performed after 1 day to determine if there was a residual signal of micelles. For the concentration of 7 mg/mL a clear residual signal is present in the liver. Moreover, it also shows a signal in spleen and pancreas. At both concentrations, no signal was recorded in tumor during *in vivo* and *ex vivo* experiments. (Figure III.31)

As a reminder, micelles do not possess a hydrophilic cavity able to encapsulate both these dyes, and the first hypothesis was that dyes were trapped in the PEO moiety of the micelles, in the hydrophilic corona of the nanostructures. After nanoprecipitation, a purification step on Sephadex™ column was performed to eliminate all free dye molecules. Nevertheless, the *in vivo* experiments show a rapid clearance by kidneys, as observed for small dyes and imaging probes. For nanoparticles of sizes above 60 nm, the principal expected way of elimination is by the liver. Based on *in vivo* results, the nanoprecipitation was performed without the presence of dyes. After that, dyes were added in solution to incubate micelles already formed. After purification step, an absorbance signal was measured in UV-Vis spectrometry. (Figure AIII.10) The hypothesis is thus that the dyes are physisorbed on the surface of the micelles, yet not irreversibly trapped in the PEO corona. This explains the *in vivo* results where, after injection, the dyes become off the hook of the surface of micelles leading to fast kidneys elimination due to the ultralow size of the molecules. This led to a loss of signal, with a residual part of micelles still containing some residual traces of the dyes that can explain the signal in the liver.

In view of these results, it was decided to stop micelles analyses and experiments. That explains why the confocal imaging was not performed with an optimization of the used conditions. Biological assays on micelles were performed by C. Genevois (U1312 – BRIC, Inserm, University of Bordeaux) on platform Vivoptic (CNRS UAR 3427, INSERM US 005, Univ. Bordeaux, France). Vivoptic is a France Life Imaging labelled platform.

### III.2.7.2 Polymersomes

First tests were performed to determine the biodistribution of the polymersomes. Indeed, it is important to evidence that the same phenomenon as for the micelles does not occur with the polymersomes, leading to a total elimination of the nanostructures in a few hours. After injection, the product is distributed in the mouse body with a highlight of kidneys, quickly followed by a strong accumulation in the bladder. A very weak highlight of the liver also occurs around one day post-injection. (Figure AIII.11) By decreasing the maximum of the signal

intensity scale of images, mice appeared still fluorescent 1 week to 2 weeks after the injection. (Figure III.32)

Interestingly, images showed an increase of the signal in the spleen area at these later time points. This organ is well perfused with a high blood flow and possesses splenic macrophages which, in the case of nanoparticles, also play a role in the clearance. Indeed, an increase in size of nanoparticles leads to an increasing use of splenic macrophages. This phenomenon is particularly true for PEGylated particles due to the formation of anti-bodies directed against PEG and take place after the uptake by Kupfer cells in the liver.<sup>222</sup>

These observations are confirmed by *ex vivo* experiments showing in a first time a high signal in kidneys followed by an increasing signal in the liver at 24 h, and finally detection of a high signal in spleen after a few days. (Figure AIII.12 ; Figure III.33)

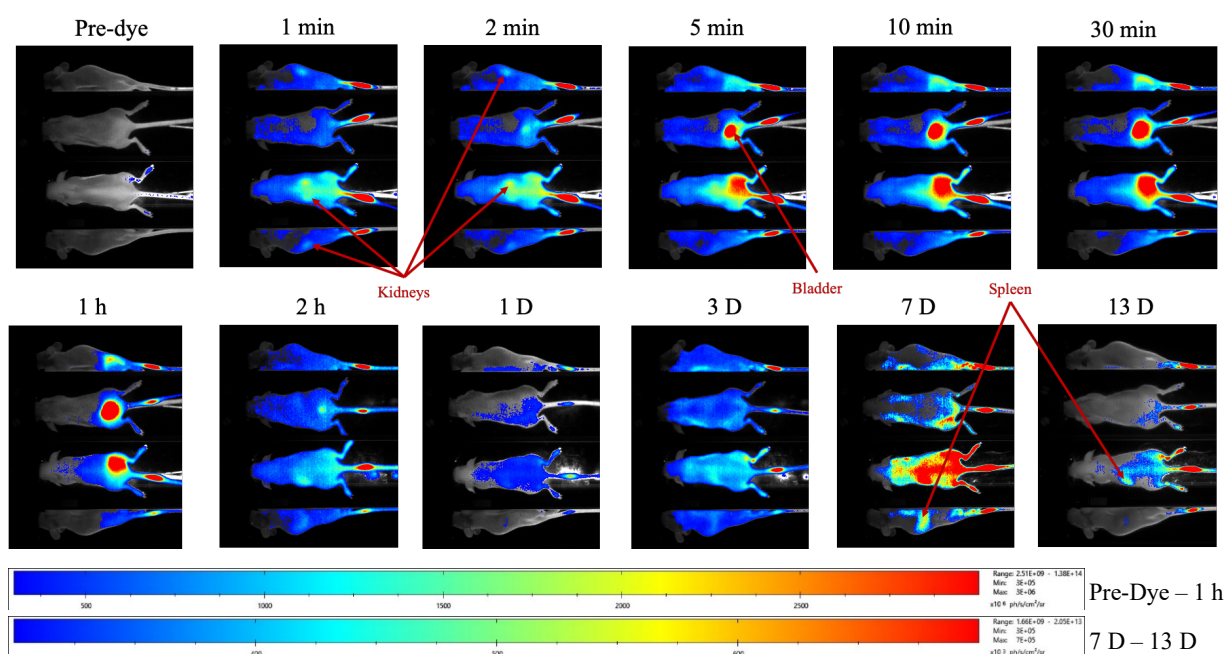


Figure III.32. FLI monitoring of the biodistribution of polymersomes at a concentration of  $10 \mu\text{M}$  in ZW800-1 over time (the scale of artificial colors was readjusted between 7 and 13 days).

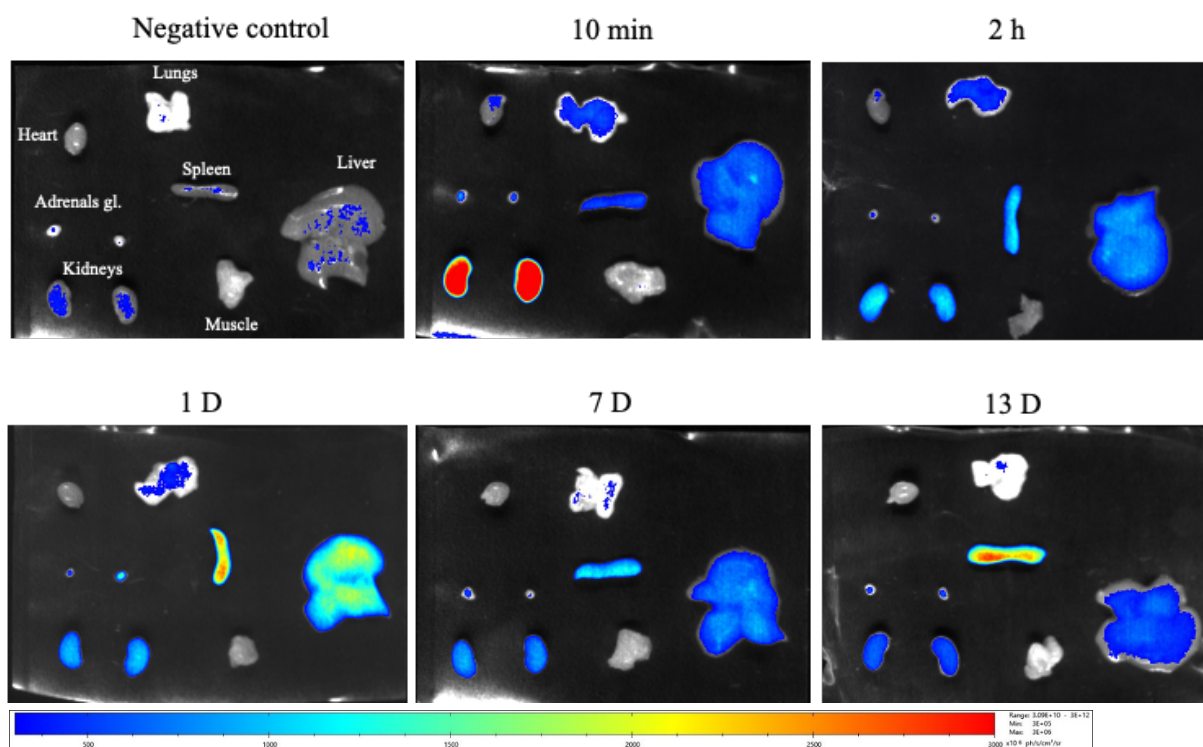


Figure III.33. *Ex vivo* FLI observations of organs after different times of sacrifice.

To evidence the damages or inflammation induced by the injection of polymersomes, blood was collected from each mouse to extract the plasma and evaluate different biomarkers able to highlight these issues. The first two markers are GOT, glutamic oxacetic transaminase or aspartate aminotransferase, and GPT, glutamic pyruvic transaminase or alanine aminotransferase, enzymes which are released in reaction of damages induced to tissues or organ tissues. Thus, these markers are not exclusive to liver failures.<sup>177</sup> GOT levels in bloodstream decreased with a significant impact after 10 min, 7 days and 13 days compared to a  $p < 0.05$ , while GPT levels did not significantly changed. In case of damage, the observation should be an increase. A decrease in levels would demonstrate the effectiveness of a treatment which is not the case in this study, but the results also exhibit wide error bars and experiments probably need a larger panel to obtain indisputable results. The third marker, LDH, lactate deshydrogenase, follows the same type of failures than GOT and GPT which are released after cells death. No significant modification of LDH rate is observed except at 7 days post injection which shows, as for GOT, a more important decrease. The kidney failures were evaluated by BUN, blood urea nitrogen, and cannot be evaluated by ureic acid due to a too weak concentration in plasma. No significant damage from kidneys were detected due to an increase in urea concentration induced by kidney failure. Indeed, the rate of BUN in plasma is linear. (Figure III.34)

To conclude on these analyses, it is important to keep in mind that the measurements were performed on  $n = 3$  which does not allow a real statistic measurement but rather allows to highlight high differences in the markers. It has also to be noted that similar blood analyses were also performed on micelles containing ZW800-1, rhodamine B and doxorubicin on plasma (AST, ALT, creatinine, urea, and lactic acid) and urine (creatinine, total urinary protein, and urea) but analyses did not evidence any inflammatory reaction. Moreover, according to the *in vivo* results, they were not considered as relevant results due to the supposed separation of micelles and dyes.

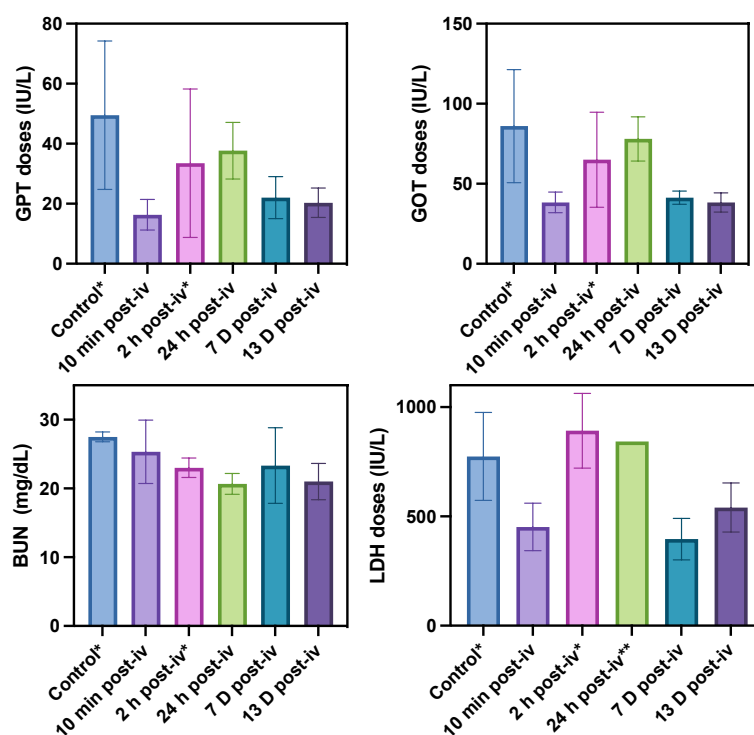


Figure III.34. Analyses of different factors present in plasma (GPT, GOT, BUN and LDH) able to put in evidence inflammatory reactions or failures in organs (\* :  $n = 2$  and \*\* :  $n = 1$  due to insufficient volume in plasma or aberrant values).

Interestingly, an old SKH1 mouse (6 months old) developed a spontaneous tumor in its right flank. It was decided to inject polymersomes containing both dyes, ZW800-1 and rhodamine B. Using spontaneous instead of induced tumors as model tends to be more translatable to human disease.<sup>223</sup> The desired accumulation in tumor is based on the enhanced permeability and retention (EPR) effect. This effect is based on the principle that the tumor exhibits an aberrant vascular system allowing a passive targeting.<sup>224</sup> Recent work by Miller *et al.* shows that despite high heterogeneity in the EPR effect among individuals, there is a high

correlation between the labelling of tumors by contrast agents (either optical or MRI) and the therapeutic efficacy of nanomedecines.<sup>225</sup>

In the few minutes following the injection, as observed in the biodistribution experiments, polymersomes accumulate in the bladder and also in the tumor. The polymersomes were eliminated from the bladder after a few hours, but the signal in tumor was still present 7 days post injection. (Figure III.35) This observation was confirmed by *ex vivo* experiments that showed an intense signal compared to the signal of liver, kidneys or spleen. These results evidenced the good tumor uptake of polymersomes by EPR effect, and their ability to remain in the tumor. (Figure III.36) Indeed, signal in tumor remains constant until next day, and even still increased, probably thanks to the progressive accumulation of the polymersomes coming from the bloodstream. (Figure AIII.13 ; Figure AIII.14)

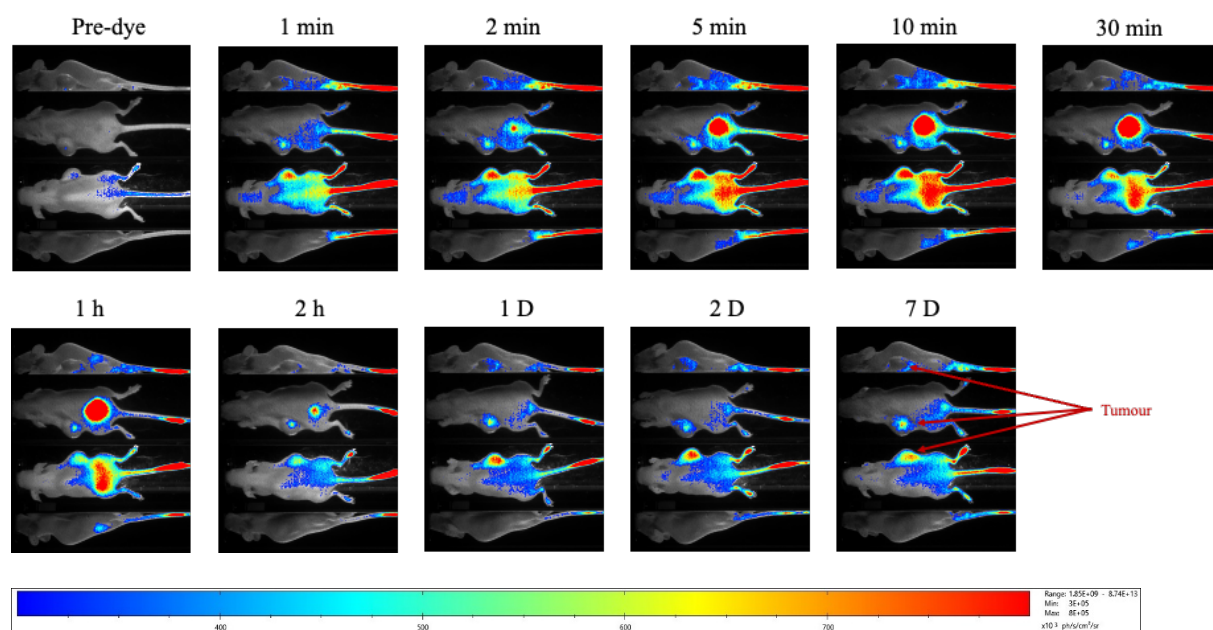


Figure III.35. FLI monitoring of the biodistribution of polymersomes at a concentration of  $10 \mu\text{M}$  in ZW800-1 on a mouse developing a spontaneous tumor over time.

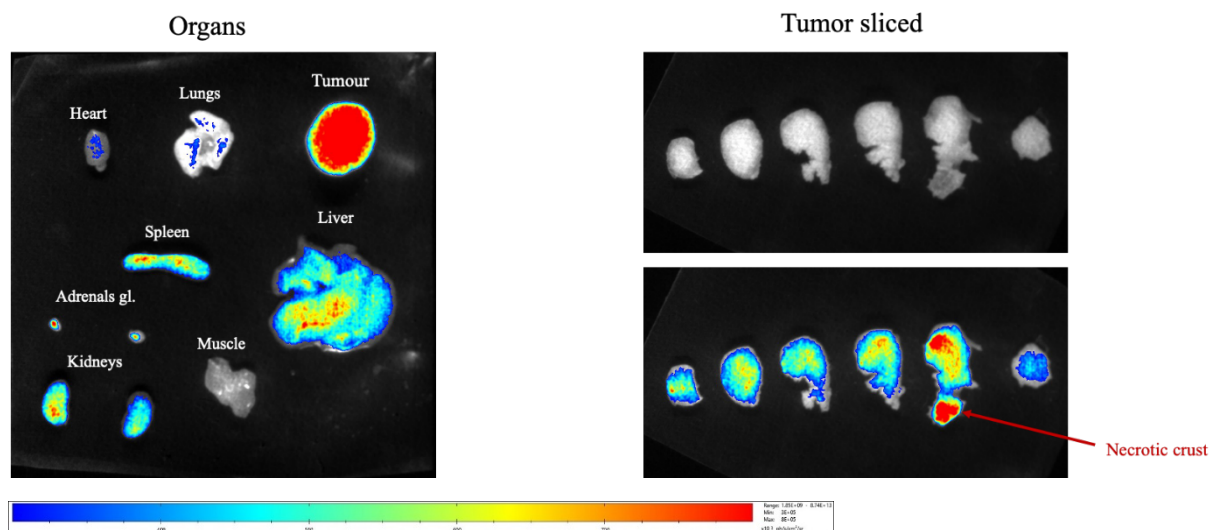


Figure III.36. *Ex vivo* FLI of organs and tumor of the mouse presenting a spontaneous tumor (left) FLI of tumor and organs; (right) tumor slices showing the region of accumulation of the polymersomes.

In view of the confocal analyses based on HT29 cells, it was considered that the biodistribution with an induced tumor with HT29 cells is not pertinent. Nevertheless, as part of the thesis of Gevert T., they tried to implant MCF7 cells to induce tumor, but it currently does not work. That is why, it was not performed on the second type of cells. These *in vivo* assays on polymersomes and BLI/FLI imaging were performed by Dr. L. Larbanoix at the CMMI in Gosselies, Belgium.

### III.3. Conclusion and perspectives

First of all, this chapter dealt with the design of copolymers, then the formation of nanostructures based on PEO<sub>5k</sub>-*b*-PCL diblock copolymers, which were evidenced to be solid spheres with a size of approximately 200 nm and a broad distribution. The results led to the development of a more original copolymer system based on a hydrophobic block composed of a statistical copolymer of PLA and PCL, and a hydrophilic block of PEO<sub>2k</sub>. These copolymers were fully characterized and then used to form nanostructures by two methods of self-assembly. The nanoprecipitation evidenced the formation of micelles (more precisely a mixture of spherical and cylindrical ones), while the thin film method gave polymersomes. These two nanostructures were characterized by different techniques as SAXS, MALS, AF4 and finally Cryo-TEM to obtain images confirming the previous analyses.

The next point was the introduction of dye and/or drug in these micellar or vesicular nanostructures to obtain on one side the capacity to follow them *in vitro* and *in vivo*, and on the other side to treat cancer, in this case by adding a drug. Polymersomes showed greater capacity to encapsulate hydrophilic dyes and doxorubicin drug, although new analyses should be performed with the continuous flow dissolution apparatus. Indeed, this side of experiment should be deepened to clearly evidence the capacity of the polymersomes to respond to a pH stimulus and deliver the drug more efficiently to the tumor. After that, it could be interesting to tune the number of LA moieties in the copolymer chains in order to optimize the rate of encapsulation and the release phenomenon of the resulting nanostructures. This optimization would finally allow to obtain the best proportion leading to an optimal system able to deal with tumor *in vivo*.

After that, the toxicity of polymers was evaluated, and the toxicity, when the cells are able to internalize, respond to ISO 10993-5 with a polymer concentration of 0.1 and 0.4 mg/mL. Finally, the nanostructures were evaluated *in vivo*. Micelles seem to have the dyes and drug only adsorbed on the surface instead of being encapsulated, leading to a direct clearance of it by desorption even at the level of the tumor. On the other hand, polymersomes showed the capacity to remain over time in a tumor, as least for 1 week. These preliminary results are encouraging to ultimately evidence an efficiency to treat tumor using the EPR effect with these systems. It could be interesting to encapsulate doxorubicin into such polymersomes, and check if it can slow down or stop the tumor growth.

These nanostructures could also be used in photoacoustic imaging. As shown on Figure III.37, the nanostructures which encapsulate ZW800-1 emit a photoacoustic signal. This imaging technique is emerging due to its capacity to obtain a signal deeper in the body because in this case this is an acoustic wave that is detected and not photons as for optical imaging, which are strongly absorbed or scattered by tissues at depths above a few mm. Our system can therefore already be considered as a multimodal imaging probe, although it does not contain right now a contrasting effect in magnetic resonance imaging, which will be the topic of the next chapter.

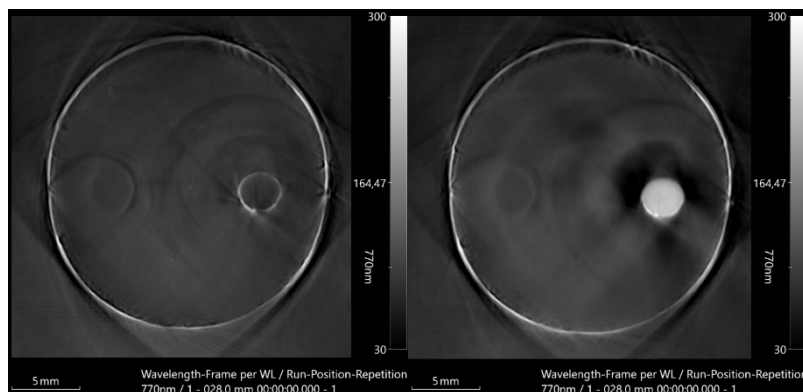


Figure III.37. (left) negative control with saline solution and (right) polymersomes at a concentration of 10  $\mu\text{M}$  in ZW800-1.

### III.4 Annexes

Table AIII.1. Comparison of 4 different polymerizations performed in the same conditions where the DP of each polymer was determined by  $^1\text{H}$  NMR. The quantities engaged for PEO<sub>2k</sub>, L-LA, CL and benzoic acid are approximately the same as 55 mg, 26 mg, 350 mg and 9 mg (except for polymerization 2, 7 mg) respectively. This table evidences the disparities in polymerization of the hydrophobic chain on the hydrophilic block.

	DP <sub>PEO</sub>	DP <sub>LA</sub>	DP <sub>CL</sub>	$f_{\text{hydrophilic}}$ (%)
Polymerization 1	45	7	35	29
Polymerization 2	45	6	34	30
Polymerization 3	45	7	54	22
Polymerization 4	45	6	25	35

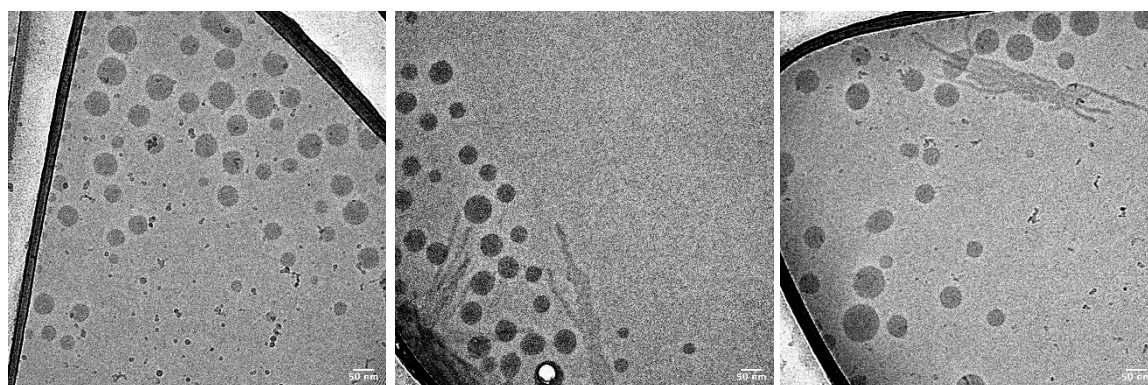


Figure AIII.1. Cryo-TEM of PEO<sub>45</sub>-*b*-P(CL<sub>49</sub>-*co*-LA<sub>8</sub>) obtained by nanoprecipitation showing the presence of micelles and rods.

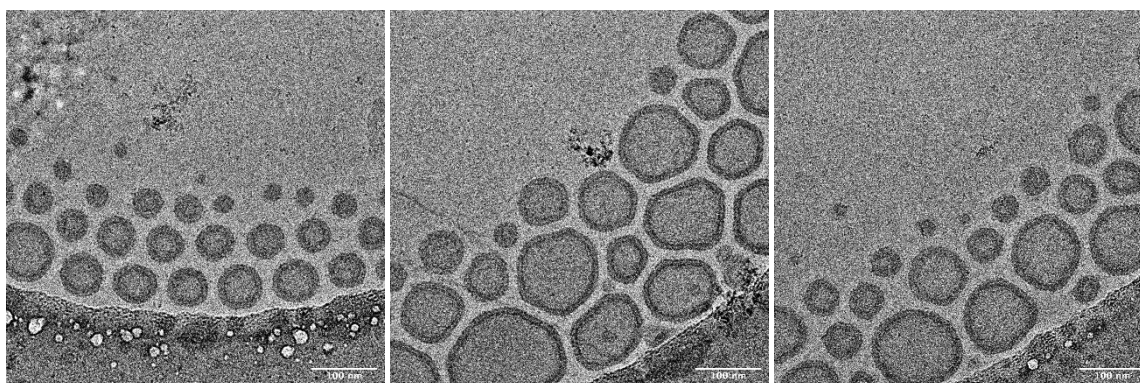


Figure AIII.2. Cryo-TEM of PEO<sub>45</sub>-*b*-P(CL<sub>35</sub>-*co*-LA<sub>5</sub>) obtained by thin film rehydration.

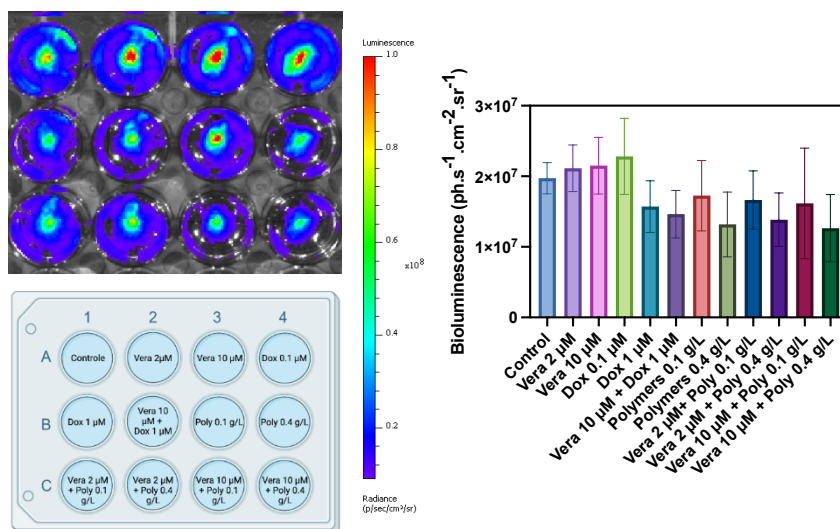


Figure AIII.4. BL imaging (left) of cells incubated in different conditions, and the resulting detected bioluminescence signal analysis (right) (well plate was designed with Biorender).

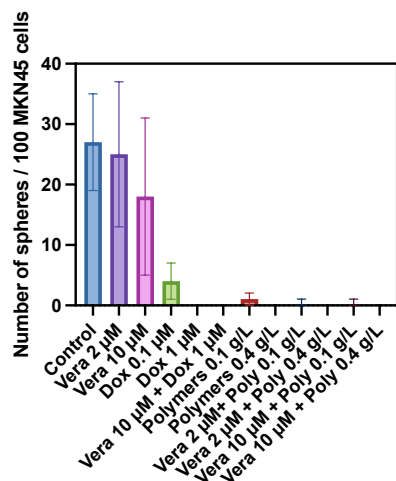


Figure AIII.3. Number of spheroids produced in 5 days by initially 100 cells of MKN45, for the different conditions.

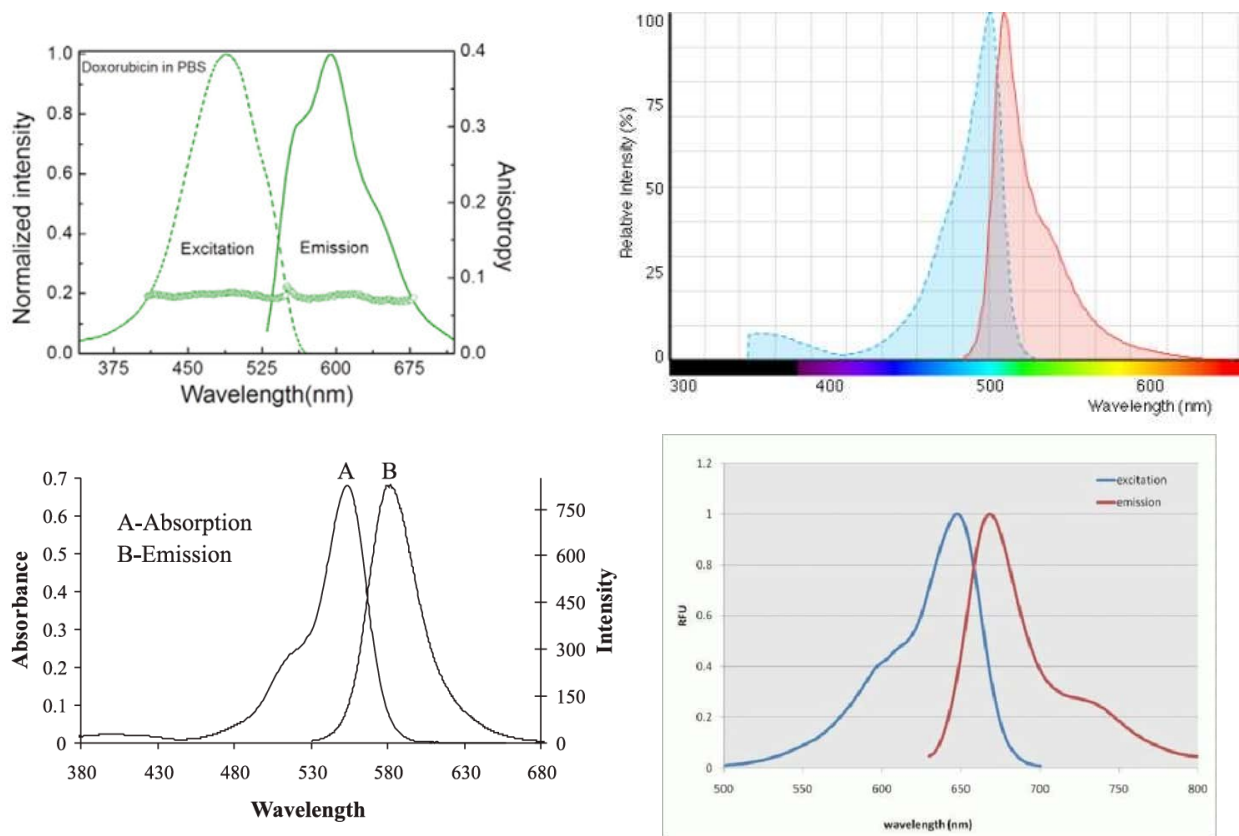


Figure AIII.5. (Upper left) Fluorescence spectrum of doxorubicin in PBS.  $\lambda_{ex} = 500$  nm (observed) and  $\lambda_{em} = 600$  nm (upper right) Fluorescence spectrum of LysoTracker™ green DND-26.  $\lambda_{ex} = 504$  nm and  $\lambda_{em} = 511$  nm (below left) Fluorescence spectrum of rhodamine B (a) absorption and (b) emission in water.  $\lambda_{ex} =$  c.a. 540 nm and  $\lambda_{em} =$  c.a. 590 nm (below right) Fluorescence spectrum of LysoTracker™ deep red.  $\lambda_{ex} = 647$  nm and  $\lambda_{em} = 668$  c.a. nm.<sup>226,227,228,229</sup>

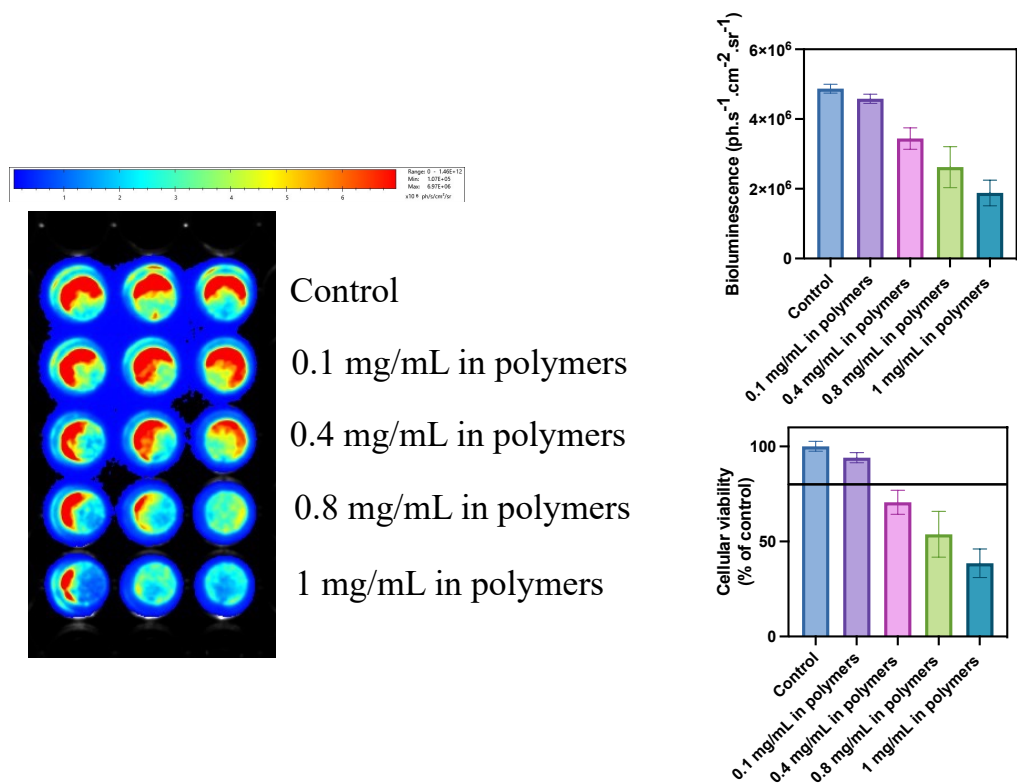


Figure AIII.7. BLI on MCF7 cells in presence of polymersomes without doxorubicin (left) and the signal intensity in the different concentrations giving the viability of cells compared to control ( $n = 1$ ) (right).

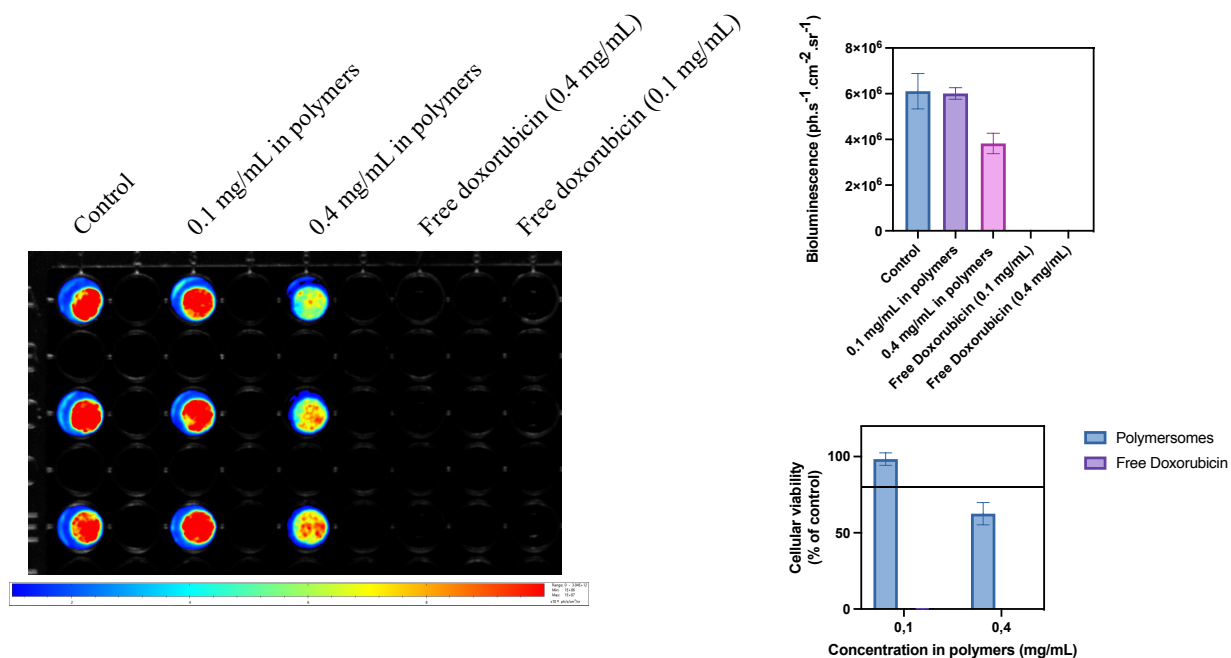


Figure AIII.6. BLI on MCF7 cells in presence of polymersomes with doxorubicin (left) and the signal intensity in the different concentrations giving the viability of cells compared to control and to cells in presence of free doxorubicin at the same concentration than in the polymersomes ( $n = 1$ ) (right).

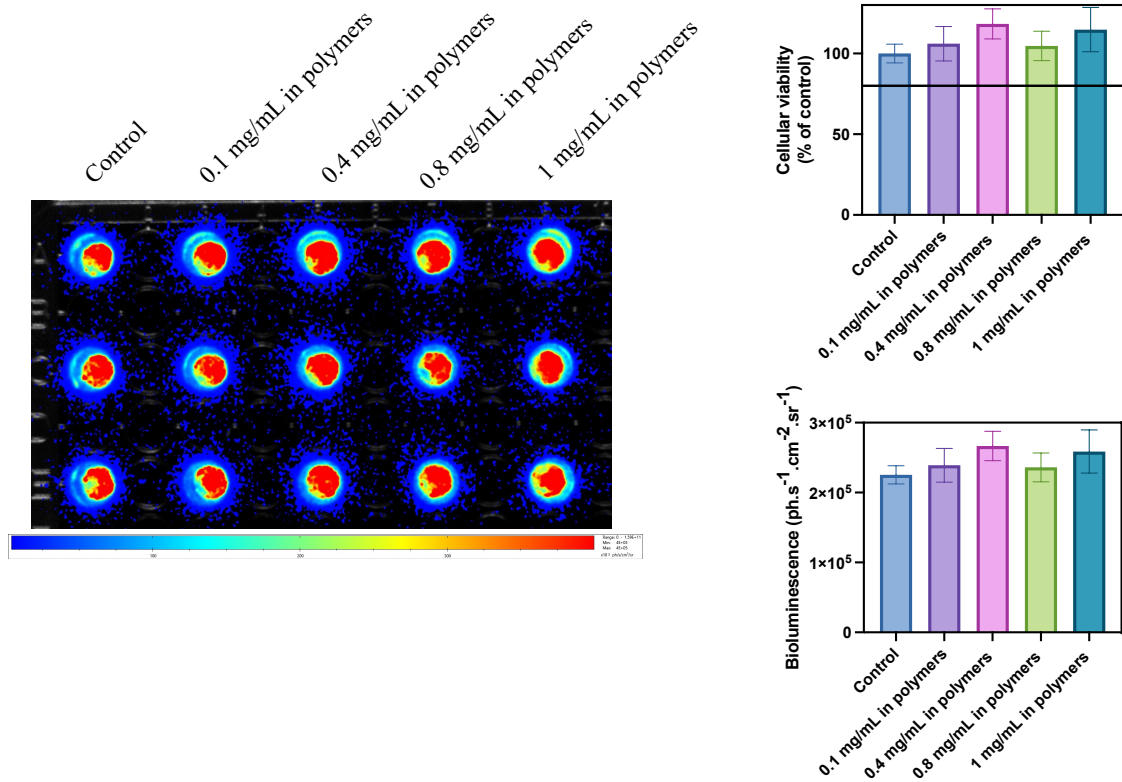


Figure AIII.8. BLI on HT29 cells in presence of polymersomes without doxorubicin (left) and the signal intensity in the different concentrations giving the viability of cells compared to control ( $n = 1$ ) (right).

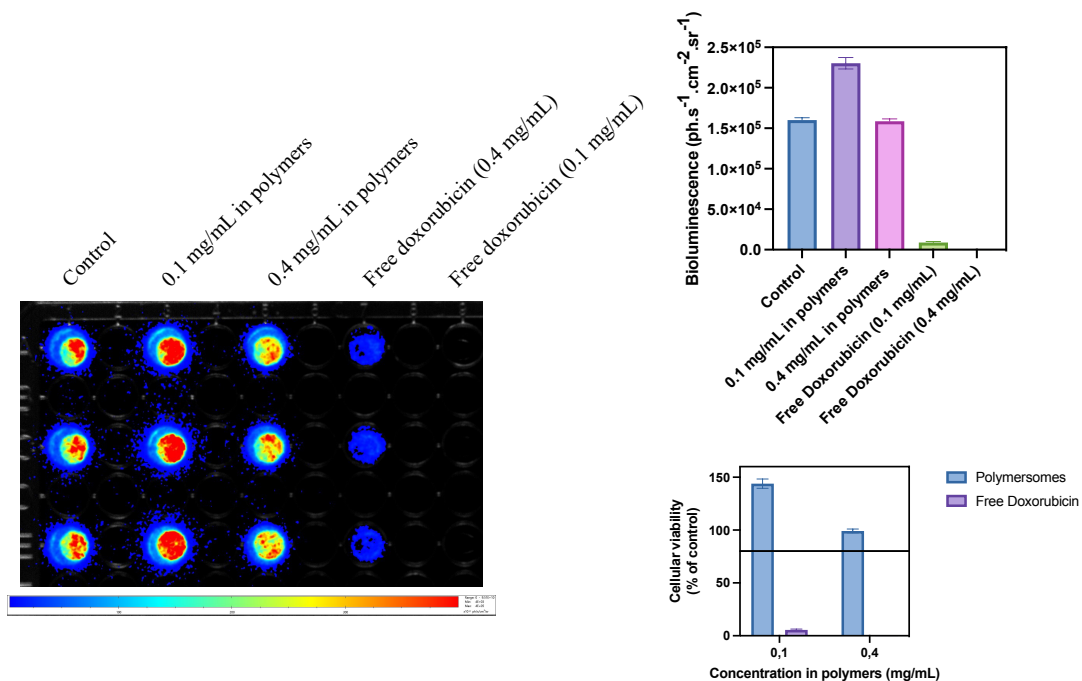


Figure AIII.9. BLI on HT29 cells in presence of polymersomes with doxorubicin (left) and the signal intensity in the different concentrations giving the viability of cells compared to control and to cells in presence of free doxorubicin at the same concentration than in the polymersomes ( $n = 1$ ) (right).

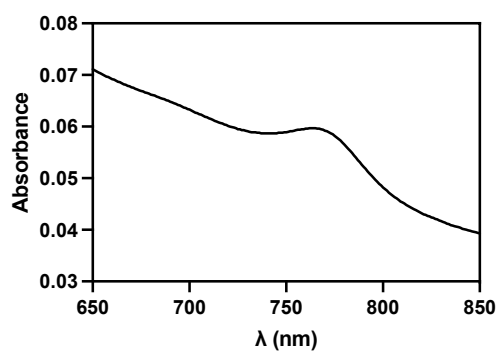


Figure AIII.10. UV-Vis spectrum of micelles incubated overnight made in PEO-*b*-P(CL-*co*-LA) obtained by nanoprecipitation technique in presence of ZW800-1 after purification by Sephadex™ column.

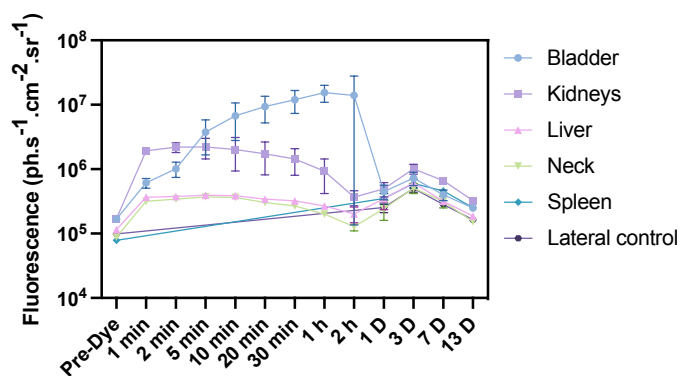


Figure AIII.11. *In vivo* fluorescence as a function of time for different organs.

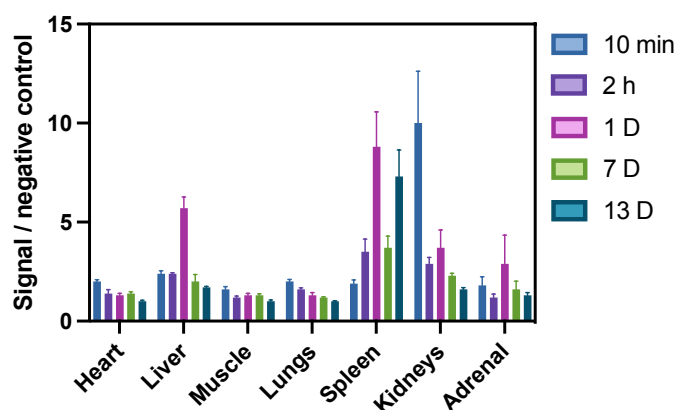


Figure AIII.12. Fluorescence normalized with the control signal as a function of time for the controlled organs in *ex vivo* experimentations.

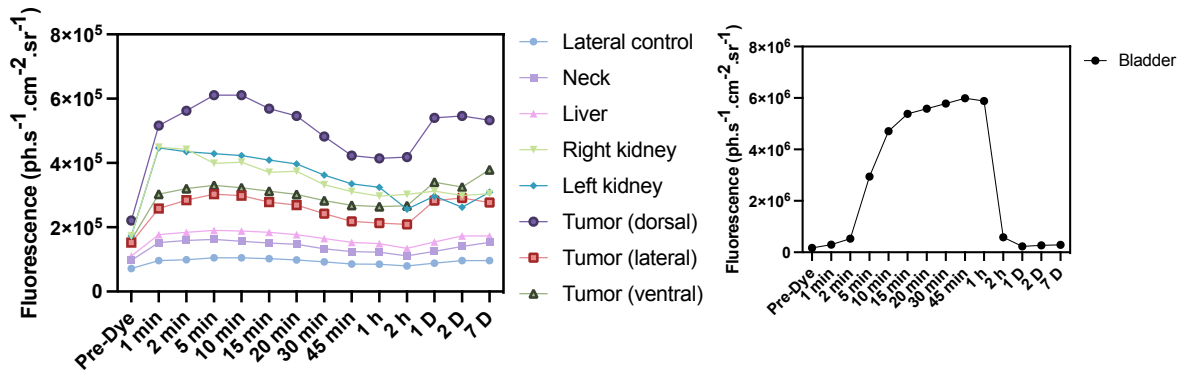


Figure AIII.14. FLI fluorescence as a function of time for different organs and tumors on different sides of the mouse.

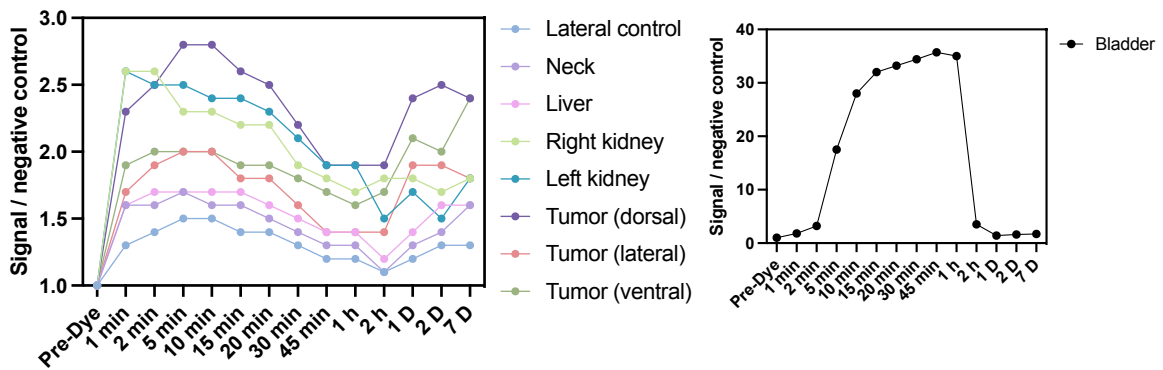


Figure AIII.13. Fluorescence normalized with the control signal as a function of time for the controlled organs in *in vivo* experimentations.

### III.4. Materials and methods

#### III.4.1. Synthesis and characterizations of copolymers

##### III.4.1.1. Materials

PEO,  $\epsilon$ -CL monomer, LLA monomer and benzoic acid were bought at Sigma-Aldrich. All chemical reagents were previously dried and placed in a glovebox. The NMR spectra ( $^1\text{H}$ ) were recorded at 298K and reported in ppm. (Bruker<sup>®</sup> AVANCEII-500 at 500 MHz, USA). The multiplicity of the peaks is defined as s (singlet), d (doublet), t (triplet), q (quintuplet) and m (multiplet).  $^1\text{H}$  NMR recording were performed on Bruker<sup>®</sup> Avance II-500 at 500 MHz (11.75 T) or Bruker<sup>®</sup> NEO 600 MHz (14 T) spectrometers at 25°C (USA). SEC was performed in Belgium on Agilent 1200 devices (Agilent Technologies, USA) in THF (containing 2 wt% of Et<sub>3</sub>N) sample in solution (~ 5 mg/mL) are injected with a flow rate of 1 mL/min at 35°C. The pre-column PL gel 10 mm is followed by two PL gel 10 mm mixed-B. The molecular weight was obtained based on a calibration with polystyrene standards. The data were treated by the provider's software (Agilent GPC-Addon). SEC was performed in France on Ultimate 3000 system from Thermo Fischer Scientific (USA) with a diode array detector (UV-Vis). The system is also equipped with a multiangle light scattering (MALS) and a differential refractive index detector (dRI) from Wyatt (Wyatt Technology, USA). Solutions (~ 5 mg/mL) are injected with a flow rate of 1 mL/min at 40°C with trichlorobenzene as flow marker. The system is composed of three columns of TOSOH TSK HXL gel. The molecular weight is obtained based on a calibration with polystyrene standards. The data were treated with Astra. DSC were performed on DSC Q200 from TA instruments (TA Instruments, Inc, France). The analyses were performed according to a sequence heat-cool-heat from -80°C to 200°C at a heating and cooling rate of 10°C per minute.

##### III.4.1.2. Synthesis of PEO-*b*-PCL

CH<sub>3</sub>-PEO<sub>114</sub>-OH (288 mg) as macroinitiator, PCL (1,8 g), TBD (18 mg) and toluene (6,45 g) were placed in a round bottom flask under inert atmosphere in a glovebox. The medium was placed under stirring at room temperature. After 1 h, a second volume of toluene (12g) was added to the solution. After 16 h of stirring, heptane was added to the medium to induce the precipitation of the copolymer. The product obtained is PEO<sub>124</sub>-*b*-PCL<sub>190</sub>.  $^1\text{H}$  NMR (CDCl<sub>3</sub>,

500 MHz)  $\delta$  (ppm) : 1.37 (m, 380 H, -CO-CH<sub>2</sub>-CH<sub>2</sub>-CH<sub>2</sub>-CH<sub>2</sub>-CH<sub>2</sub>-); 1.64 (m, 766 H, -CO-CH<sub>2</sub>-CH<sub>2</sub>-CH<sub>2</sub>-CH<sub>2</sub>-CH<sub>2</sub>-); 2.30 (t, *J* 7.53 Hz, 375 H, -CO-CH<sub>2</sub>-CH<sub>2</sub>-CH<sub>2</sub>-CH<sub>2</sub>-CH<sub>2</sub>-); 3.37 (s, 3 H, CH<sub>3</sub>-PEO); 3.63 (s, 496 H, -PEO-); 4.05 (t, *J* 6.73 Hz, 380 H, -CO-CH<sub>2</sub>-CH<sub>2</sub>-CH<sub>2</sub>-CH<sub>2</sub>-CH<sub>2</sub>-).

CH<sub>3</sub>-PEO<sub>114</sub>-OH (1 g) as macroinitiator, PCL (3.13 g), TBD (31.3 mg) and toluene (11.3 g) were placed in a round bottom flask under inert atmosphere in a glovebox. The medium was placed under stirring at room temperature. After 1 h, a second volume of toluene (21 g) was added to the solution. After 16 h of stirring, heptane was added to the medium to induce the precipitation of the copolymer. The product is PEO<sub>126</sub>-*b*-PCL<sub>142</sub>. <sup>1</sup>H NMR (CDCl<sub>3</sub>, 500 MHz)  $\delta$  (ppm) : 1.37 (m, 299 H, -CO-CH<sub>2</sub>-CH<sub>2</sub>-CH<sub>2</sub>-CH<sub>2</sub>-CH<sub>2</sub>-); 1.64 (m, 592 H, -CO-CH<sub>2</sub>-CH<sub>2</sub>-CH<sub>2</sub>-CH<sub>2</sub>-CH<sub>2</sub>-); 2.30 (t, *J* 7.52 Hz, 283 H, -CO-CH<sub>2</sub>-CH<sub>2</sub>-CH<sub>2</sub>-CH<sub>2</sub>-CH<sub>2</sub>-); 3.37 (s, 3 H, CH<sub>3</sub>-PEO); 3.63 (s, 504 H, -PEO-); 4.05 (t, *J* 6.72 Hz, 285 H, -CO-CH<sub>2</sub>-CH<sub>2</sub>-CH<sub>2</sub>-CH<sub>2</sub>-CH<sub>2</sub>-).

#### III.4.1.3. Synthesis of PEO-*b*-P(CL-*co*-LA):

CH<sub>3</sub>-PEO<sub>45</sub>-OH (55mg, 0.027 mmol) as macroinitiator, LLA (26 mg, 0.18 mmol),  $\epsilon$ -CL (350 mg, 3 mmol) and benzoic acid (9 mg, 0.07 mmol) were placed in a vial and closed with a cap in a glovebox. The cap of the vial was sealed with Teflon and covered with aluminum paper. The vial was placed in a graphite bath at 155°C for 24 hours under stirring. The vial came back to room temperature, the product was dissolved in THF and added drop by drop to glacial heptane. The precipitate was centrifuged at ~ 15 °C. The solvent was eliminated. This step was repeated 2 times. The copolymer was dried under vacuum. Cold water was added, and the suspension was vortexed. The resulting solution was centrifuged at ~ 10 °C. This step was repeated 2 times. The copolymer was finally lyophilized, and a white powder was obtained. <sup>1</sup>H NMR (CDCl<sub>3</sub>, 500 MHz)  $\delta$  (ppm) : 5.12 (m, -CH- PLA moiety); 4.13 and 4.05 (m and t, -CH<sub>2</sub>- PCL moiety); 3.64 (s, -CH<sub>2</sub>- PEO moiety); 3.55 (m, OH-CH<sub>2</sub>-P(CL-*co*-LA)); 3.37 (s, CH<sub>3</sub>-PEO), 2.30 (t, -CH<sub>2</sub>- PCL moiety); 1.65, 1.53 and 1.38 (m, P(CL-*co*-LA) statistical arrangement between PLA and PCL)

### III.4.2. Self-assembly of micelles and polymersomes

#### *III.4.2.1. Nanoprecipitation*

The copolymer (~ 20 mg) was dissolved in THF to obtain a solution at 20 mg/mL. The solution (1 mL) was placed under stirring in a vial at 21°C and PBS was added (10 mL). The vial was let opened and stirred overnight.

#### *III.4.2.2. Thin film*

The copolymer (~ 20 mg) was dissolved in chloroform (3-4 mL) in a round bottom flask. The flask was placed on the rotavapor under vacuum with a bath at ~ 70°C. All the chloroform was eliminated followed by the addition of PBS (at the same temperature). The solution was stirred vigorously in the hot bath for approximately 2 hours. The bath and round bottom flask were covered with aluminum.

#### *III.4.2.3. Encapsulation of drug/dyes*

In presence of drug/dye, dyes and/or drug were dissolved in PBS at a concentration of 5 mM and added to the copolymer solution. The resulting solution after nanoprecipitation or thin film method was concentrated by ultrafiltration (30 kDa membrane in regenerated cellulose, Ø 25 mm, Ultracel®, Merck, Germany) until the obtention of 1-2 mL of solution. The solution was purified on Sephadex™ G-100 columns (Cytiva, Germany) and fractions of ~ 1-1.5 mL were collected.

Sephadex™ G-100 columns (Cytiva, Germany) were prepared by inflating the beads in Milli-Q water (approximately 3g / 200 mL of water) during 3 days at room temperature with much care (*i.e.* not at too fast stirring speed that can break them). The medium was degassed under vacuum during 15-30 min. The extra water was removed and the gel was flowed in column (~ 25 cm, Ø 1 cm). The gel was finally washed with PBS. The concentration of encapsulated drug and/or dyes was determined after addition of 10% of Triton™ X-100 in the medium followed by the extraction of the concentration based on the calibration curve of each species in the presence of 10% of Triton™ X-100 recorded on spectrofluorimeters FP-8500 (Jasco, France) in France or LS-55 equipped with a R928 photomultiplier (Perkin Elmer, USA) in Belgium. Parameters on fluorimeter used in France are: doxorubicin (excitation and

emission slits: 5 nm;  $\lambda_{\text{ex}} = 480$  nm), rhodamine B (excitation and emission slits: 2.5 nm;  $\lambda_{\text{ex}} = 555$  nm) and ZW800-1 (excitation and emission slits: 5 nm;  $\lambda_{\text{ex}} = 769$  nm) with a scan speed set to 100 nm/min for all fluorophores. Parameters on fluorimeter used in Belgium are: doxorubicin (excitation and emission slits: 10 nm;  $\lambda_{\text{ex}} = 550$  nm), rhodamine B (excitation and emission slits: 2.5 nm;  $\lambda_{\text{ex}} = 553$  nm) and ZW800-1 (excitation and emission slits: 7.5 nm;  $\lambda_{\text{ex}} = 766$  nm) with a scan speed set to 100 nm/min for all fluorophores.

#### *III.4.2.3. Physico-chemical characterization*

##### *Dynamic light scattering (DLS)*

DLS 90° measurements were performed on a Zetasizer nanoZS (Malvern, United Kingdom) instrument with a laser He-Ne at 633 nm. Typically, 50  $\mu\text{L}$  of the nanoparticles suspension is diluted in 950  $\mu\text{L}$  of PBS in a quartz cell of 1 cm on 1 cm (PCS1115). The refractive index of the copolymer is based on the PEO refractive index with a value of 1.46. The medium used to perform the measurement is water with a refractive index of 1.3314 and a viscosity of 0.8872 cp. Measurements are performed at 25°C with three averaged repetitions.

##### *Cryo-transmission electronic microscopy (Cryo-TEM)*

Cryo-TEM in France was performed at the Institut de Minéralogie, Physique des Matériaux et de Cosmochimie in Paris on a LaB6 JEOL 2100 (JEOL Ltd, Japan) working at 200 kV with the acknowledged help of Jean-Michel Guinier. The grids were prepared by placing a drop of sample on holey carbon grids (Quantifoil Micro Tools GmbH, Germany). The grids were then dried by capillarity with a filter paper. They were placed rapidly into liquid ethane and placed on a Gatan 626 cryo-holder. They were then placed in the microscope. The grids were observed at -180°C under low dose conditions (JEOL minimum dose system). Images were taken with an Ultrascan 2k CDD camera (Gatan Inc, USA). Images were treated with Fiji (ImageJ).

In Belgium, images were recorded at the CMMI (ULB) on Talos F200C 200 keV (FEI, Thermo Fisher, USA) with the acknowledged help of Dr Gaëtan Dias Mirandela. Preparation of negative staining was performed on Cu° 200 mesh grids treated under plasma during 25 seconds in a vacuum chamber of  $2.0 \cdot 10^{-1}$  with a current of 1.5 mA. 3  $\mu\text{L}$  of sample were applied

on carbon faces and incubated during 1 min. The grids were then dried by capillarity with a Whatmann n°1 paper. A succession of two washing/ drying cycles were done. Preparation of Cryo-TEM grids was performed on Lacey Carbon or Quantifoil Cu° 300 mesh 2/2 treated under plasma during 35 seconds in a vacuum chamber of  $2.0 \cdot 10^{-1}$  with a current of 1.5 mA. 3  $\mu$ L of sample was applied on carbon dived in liquid ethane before cooling by liquid nitrogen with Vitrobot IV (FEI, Thermo Fisher, USA). Diving parameters were: blot force = 2, blot time = 3s, waiting time = 0s, temperature = 10°C and humidity 100%. The acquisition was performed on Talos F200C 200 kEV (FEI, Thermo Fisher, USA) with Cryo-holder Gatan 626 Single Tilt (Gatan Inc., USA) to insert the grid. Images were recorded with magnification of 73000 $\times$  and Céta (FEI, Thermo Fisher, USA) camera for negative staining grids or Falcon II (FEI, Thermo Fisher, USA) for Cryo-EM grids. A Beam of 55 electrons/pixels/second was applied during 1 second with an acquisition of 20 frames/second. Images were taken with a defocus between 2 to 20  $\mu$ m for Cryo-EM. The resolution of imaging is 1.4 Å/pixel. The images were treated on Fiji (ImageJ).

#### *Multi angle light scattering (MALS)*

MALS were performed on ALV-5000 (ALV, Germany) goniometer with He-Ne laser at 633 nm and ALV-5000/EPP multiple tau digital correlator with initial sampling time of 125 ns with the acknowledged help of Paul Marque. The suspension of nanoparticles is diluted between 2 to 5 times and placed in a cylindrical quartz tube of 10 mm. The tube is placed in a bath of toluene at 25°C. Measurements were performed at different angles between 30° and 15° by step of 5° for SLS and step of 10° for DLS. Results were normalized with the signal of toluene and PBS to obtain the  $R_h$  in DLS (Stokes-Einstein) and the  $R_g$  in SLS (Guinier's law). The data were treated with ALV software.

#### *Asymmetric flow field-flow fractionation (AF4)*

The system used with the acknowledged help of Amélie Vax-Weber is composed of a Wyatt Eclipse AF4 channel (Wyatt technology, USA), an isocratic pump (Agilent 1100) (Agilent Technologies, USA), an auto-sampler (Agilent 1200), a Wyatt Dawn Helios-II 18 scattering angle MALS detector, a DLS detector and an Optilab differential RI detector (Optilab, USA). The data were treated and fitted on the Astra 8 software.

### *Small angle X-rays scattering (SAXS)*

The SAXS measurements of our samples were made on the Xeuss 2.0 SAXS spectrometer (Xenocs, France) coupled with FOX3D (Xenocs, France), single reflection optical mirror, available at the Transform platform (<https://transform.cnrs.fr/>) on the campus of Univ Bordeaux, with the acknowledged help of Ahmed Bentaleb. The X-ray source is a standard copper cathode, therefore  $\lambda=1.54189 \text{ \AA}$ , the detector is a highly sensitive CCD camera (Pilatus, Swiss Light Source) centered on  $K_{\alpha}$  ray ( $\lambda= 1.54 \text{ \AA}$ ) of copper. The samples were put in Lindeman glass capillaries (transparent to X-rays) with diameter  $< 0.5 \text{ mm}$  at the tip (WJM Glas, Glastechnik und Konstruktion, <http://www.wjm-glas.de/>), which are sealed with a flame. The system delivered a collimated beam of 8KeV under vacuum defined by two motorized anti-diffusing slots. Samples were exposed two times for 3 hours and the data are collected in absolute intensity. Using a sample-detector distance of 2.5 m, the scattering vector  $q$ -range spans from  $q_{\min}=4.5\times 10^{-3} \text{ \AA}^{-1}$  to  $q_{\max}=0.4 \text{ \AA}^{-1}$  (WAXS domain). The largest  $R_g$  values that can be theoretically measured are thus of  $q_{\min}^{-1}=222 \text{ \AA}$  (22 nm), but in practice we can manage to determine the onset of the Guinier “plateau” of objects for  $R_g$  values up to 40-50 nm (although with more uncertainty). The curves of scattered intensity as a function of  $q$  were obtained by treating data with Foxtrot software (Collaboration between Xenocs and Soleil synchrotron).

### *Flow-through dissolution systems*

Flow-through dissolution systems were recording on USP-4 Sotax™ CE7 USP apparatus 4 equipped with 22.6 mm diameter cells (Sotax Corporation, Germany) online with CE 7smart and UV-Vis measurement (the USP-4 having 7 measuring cells). Sample was placed in float-a-lyzer™ dialysis tubing of 100 kDa molar mass cut-off and in two different cells containing medium at pH 5.5 or 7.4. The whole device was thermostated at 37°C. The flow rate through the cells took place at 25 mL/min with an UV-Vis absorbance (wavelength depending on dye or drug at their maximum absorbance) every 5 min during 30 min following by measurement every 10 min during 1 hour and finally every 30 min for 16 more hours.

## III.4.4. Synthesis and characterization of ZW800-1

## III.4.4.1. Materials

The chemicals and solvents were purchased from different companies: ChemLab, Sigma Aldrich, Roth, TCI, VWR, Merck and Fluka. The chemicals and solvents (excepted DCM) were used without further purification. The DCM was distilled under vacuum. The NMR spectra ( $^1\text{H}$ ) were recorded at 298K and reported in ppm. (Bruker® AVANCEII-500 at 500 MHz, USA). The multiplicity of the peaks is defined as s (singlet), d (doublet), t (triplet), q (quintuplet), m (multiplet) and -Phe (phenyl). The molecular extinction coefficient ( $\epsilon$ ) was determined by UV-Vis (Lamba 35, Perkin Elmer, USA) as the origin of equation of the straight section. The straight section was obtained by slope of the curve absorbance versus concentration, with dilution between 10 and 0.6  $\mu\text{M}$  with a  $R^2$  that tends to 0.99.

## III.4.4.1 Synthesis of ZW800-1

Compounds **1**, **2**, **4**, **6** and **7** were synthesized according to the protocol of Hyun *et al.*<sup>212</sup>

Compounds **3** and **5** were synthesized according to a modified protocol of Yang *et al.*<sup>213</sup>

2,3,3-Trimethyl-1-[3-(trimethylammonio)propyl]-3H-indolium-5-sulfonic acid dibromide compound **3**: Potassium 2,3,3-trimethyl-3H-indole-5-sulfonate (5.50 g, 19.8 mmol, 1 eq) and 3-bromopropyl)trimethylammonium bromide (5.95 g, 22.8 mmol, 1.15 eq) were suspended in toluene. The medium was placed at  $110 \pm 5^\circ\text{C}$  under Ar atmosphere for one night. Once the medium is at room temperature, MeOH (26.4 mL) was added directly and stirred for 30 min. The precipitate was filtered on Büchner. The resulting solid was dissolved in a solution of water: methanol (2:1) (26 mL: 13 mL /v:v). The solution was added gently drop by drop to acetonitrile (390 mL). The resulting precipitate was filtered on Büchner and dried under vacuum. Compound **3** (6.08 g, 11.3 mmol) was obtained with a yield of 57 % as dark pink powder.  $^1\text{H}$  NMR (DMSO, 600 MHz)  $\delta$  (ppm) : 1,56 (s, 6H, -C-(CH<sub>3</sub>)<sub>2</sub>) ; 2,33 (Broad m, 2H, -CH<sub>2</sub>-CH<sub>2</sub>-CH<sub>2</sub>-N<sup>+</sup>Br<sup>-</sup>-(Me)<sub>3</sub>) ; 2.90 (s, 2H, -CH<sub>2</sub>-CH<sub>2</sub>-CH<sub>2</sub>-N<sup>+</sup>Br<sup>-</sup>-(Me)<sub>3</sub>) ; 3,11 (broad s, 9H, -N<sup>+</sup>-(CH<sub>3</sub>)<sub>3</sub>) ; 3,58 (broad t, 3H, -N<sup>+</sup>=C-CH<sub>3</sub>) ; 4.49 (broad t, 2H, -CH<sub>2</sub>-CH<sub>2</sub>-CH<sub>2</sub>-N<sup>+</sup>Br<sup>-</sup>-(Me)<sub>3</sub>) ; 7.76 (d,  $J$  8.17 Hz, -Phe-CH) ; 7.99 (d,  $J$  8.39Hz, 1H, -Phe-CH) ; 8.04 (s, 2H, -Phe-CH).

N-(((3E)-3-(anilinomethylene)-2-chlorocyclohex-1-en-1-yl)methylene)benzen-aminium chloride compound **5**: Phosphorous oxychloride (21 mL, 230 mmol, eq) was added drop by drop to DMF (25 mL) under stirring at 0°C. A solution of cyclohexanone (5.2 mL, 50 mmol) and DCM (10mL) was added also drop by drop to the previous medium under Ar atmosphere. The medium was stirred for 1 hour. After that, the solution was placed at 100 ± 5°C during 2 hours. The medium came back to room temperature and was placed in an ice bath. When the temperature decreases to 0°C, it was added drop to drop to glacial water (500 mL). The resulting solution was stirred for 4 hours. The precipitate was filtered on Büchner and dried under vacuum. The precipitate was dissolved in DMF (15 mL) and HCl 6M (10.5 mL) and placed in an ice bath. A solution of aniline (8 mL, 87.76 mmol) and ethanol (16 mL) was added drop by drop to the previous solution. After removing the ice bath, the medium was let under stirring for 1 hour. The product was precipitated in glacial water (500 mL) and stirred for 30 min. The precipitate was filtered on Büchner. Compound **5** (15 g, 44.5 mmol) was obtained as dark brown powder with a yield of 89%. <sup>1</sup>H NMR (DMSO, 500 MHz) δ (ppm) : 1.86 (broad q, 2H, -C-CH<sub>2</sub>-CH<sub>2</sub>-); 2.75 (broad t, 4H, -C-CH<sub>2</sub>-CH<sub>2</sub>-); 7.28 (t, *J* 7.38 Hz, 2H, -C-CH-CH-CH- (-Phe)); 7.47 (t, *J* 7.94 Hz, 4H, -C-CH-CH- (-Phe)); 7.60 (d, *J* 7.92 Hz, 4H, -C-CH- (-Phe)); 8.55 (s, 2H, -C-CH-N<sup>+</sup>-).

### III.4.5. Biological Methods and materials

#### *III.4.5.1. Materials*

All consumables for cell culture were bought from Thermofisher Scientific, Ibidi, VWR, Sigma and Novolab.

#### *III.4.5.2. In vitro experiments on micelles*

##### *Cellular cultures*

The MKN45 cells were harvested in RPMI medium supplemented by 10% fetal bovine serum (FBS) and 0.1% vancomycin (antibiotics) on a 24-well plate (50k cells in 500 μM medium).

*Cellular viability*

Cellular viability assays were performed on 24-well plates with 50 000 cells per well with 500  $\mu\text{L}$  of medium in triplicate. After 24 h, medium in wells are replaced with fresh medium containing polymersomes or doxorubicin and incubated during 24 h. In the well containing verapamil drug, the verapamil was added 10 minutes before the treatment. Medium is removed and wells were washed with PBS. PBS was added and cells were incubated with  $6.10^{-4}$  M of luciferin for 5 minutes. BLI were recorded on Lumina III (Perkin Elmer, USA) (acquisition 20 s, binning 4x4, pictures black and white 100 ms).

*Tumor sphere*

For the tumorsphere formation test, cells were detached just after the BLI measurement and 100 cells were spiked into 100  $\mu\text{L}$  of M11 medium (DMEM-F12-Glutamax enriched with 20 ng/mL of human epithelial growth factor, 20 ng/mL basic fibroblast growth factor, 5  $\mu\text{g}/\text{mL}$  insulin, 0.3% glucose, 1:100 N2-supplement) in 96-well plates coated with polyHEMA repulsive polymer brush to avoid cell adhesion on the substrate. The tumorspheres were then counted after 5 days.

*Confocal images*

Confocal images were recorded on TCS SP5 Leica apparatus with an objective HCX PL APO 63X NA 1.4 immersed with oil. The images were recorded: LysoTracker green,  $\lambda_{\text{ex}} = 504$  nm and  $\lambda_{\text{em}} = 511$  nm (Thermo Fisher, scientific USA), doxorubicin,  $\lambda_{\text{ex}} = 496$  nm and  $\lambda_{\text{em}} =$  around 600 nm (green channel); rhodamine B,  $\lambda_{\text{ex}} = 561$  nm and  $\lambda_{\text{em}} =$  around 600 nm (channel red); DAPI,  $\lambda_{\text{ex}} = 405$  nm and  $\lambda_{\text{em}} = 425\text{-}475$  nm (channel blue).

*III.4.5.3. In vitro experiments on polymersomes**Cellular culture*

MCF7-luc2 were cultivated with RPMI 1640 modified medium (RPMI 1640 modified: RPMI supplemented with 10% of bovine fetal serum, 0.01 mg/mL insulin and 4  $\mu\text{g}/\text{mL}$  filtered blasticidine). HT29-Luc were cultivated with DMEM (DMEM supplemented with 10% bovine fetal serum and 1% penicillin-streptomycin). For both cell lines, the cells were maintained at

37°C with 5% of CO<sub>2</sub> and passages have been performed at 80% of confluence. During passages, cells were washed with PBS after removing medium and trypsin-EDTA 0.25% was added to cleave membrane adhesion proteins. The trypsin was neutralized by adding medium (9 mL for 3 mL of trypsin-EDTA) and the suspension was centrifuged for 5 min at 300g. The cell pellet was dispersed in medium and replaced in flask.

#### *MTT viability assays*

MTT viability assays were performed on 96-well plates with 5000 cells per well. The plate was placed during 24 h at 37°C with 5% in CO<sub>2</sub>. After 24 h, medium in wells was replaced by medium containing polymersomes or free doxorubicin in triplicate and plates were placed to incubate for 24 h at 37°C with 5% in CO<sub>2</sub>. Then, wells were emptied and rinsed two times with PBS. 100 µL of MTT (solution of 5 mg/mL in PBS in 3-(4,5-dimethylthiazol-2-yl)-2,5-diphenyl tetrazolium) was placed in each well. After 3 h of incubation, MTT solution was replaced by 100 µL of DMSO. The plate was agitated for 30 min protected from light. Finally, absorbance at 570 nm was recorded for each well on SpectraMax ABS Plus or SpectraMax M2 microplate reader (Molecular Device, USA).

#### *BL imaging*

BLI was performed on 96-well plates with 5000 cells per well. The plate was placed during 24 h at 37°C with 5% in CO<sub>2</sub>. After 24 h, medium in well was replaced by medium containing polymersomes or free doxorubicin (at the same concentration that doxorubicin encapsulated in vesicles) in triplicate and the plates were placed to incubate for 24 h at 37°C with 5% in CO<sub>2</sub>. Then, wells were emptied and rinsed two times with PBS. PBS was added in wells. Finally, the PBS was removed from each well and luciferin (100 µL at 0.2 g/L in PBS) was added. Images were acquired with a PhotonIMAGER Optima (Biospace Lab, France). The bioluminescence signal intensity was measured after drawing ROIs in the area surrounding the analyzed wells using M3Vision software (Biospace Lab, France). It was exported and expressed as photons per second per square centimeter per steradian (ph/s/cm<sup>2</sup>/ sr).

*Confocal microscopy images*

Confocal microscopy images were recorded on Nikon Eclips A1R/Ti2E (Nikon, Japan). Cells were placed during 24h in Ibidi  $\mu$ -Slide 8 well (Ibidi, Germany) and were incubated 24 h with polymersomes. Medium was removed and wells were incubated with 5  $\mu$ L of LysoTracker deep red (Thermo Fisher scientific, USA) and 1  $\mu$ L of Hoechst (Thermo Fisher scientific, USA) for 2 mL of PBS during 30 min. Wells were then rinsed two times with PBS and PBS was placed in each well. The images were recorded: LysoTracker  $\lambda_{\text{ex}} = 640$  nm (deep red channel); doxorubicin,  $\lambda_{\text{ex}} = 488$  nm and  $\lambda_{\text{em}} =$  around 600 nm (green channel); Hoechst,  $\lambda_{\text{ex}} = 405$  nm and  $\lambda_{\text{em}} = 461$  nm (channel blue) and rhodamine B,  $\lambda_{\text{ex}} = 488$  nm and  $\lambda_{\text{em}} =$  around 600 nm (channel green). Images were treated on Fiji (ImageJ) with a subtraction of background on green channel homogeneously on all pictures on Figure III.27 and an increase of red signal homogeneously on all pictures on Figure III.28.

Performed work with the acknowledged help of Thomas Gevert and Valentin Lecomte.

*III.4.5.4. In vivo experiments on micelles**Mouse strains and housing conditions*

The experiments were performed on males immunodeficient NSG (NOD/SCID/IL-2R $\gamma$ null). All experiments were performed according to the ethical protocol number 11443. At the end of experiments, mice were sacrificed by cervical dislocation.

*In vivo tumor and bioluminescence imaging*

The tumors were induced by implantation of 100 000 cells of MKN45 per 100  $\mu$ L of Matrigel<sup>TM</sup>. The cells were grafted on the right leg of mice. The growing of the tumor was followed by bioluminescent imaging on Lumina III (Perkin Elmer, USA). Before BLI, mice were shaved, and 3 mg of luciferin were injected in intraperitoneally. The mice were anesthetized with isoflurane 5 min before the injection and images were recorded 10 min after injection. 13 days after injection, tumor raised 4.5 to 6.5 mm in diameter which is the size used for *in vivo* fluorescence imaging of micelle solutions.

### *In vivo fluorescence imaging*

Mice were anaesthetized using isoflurane. Mice were then placed on a preparation pad. A volume of 100  $\mu$ l of the micellar solution (at 2 mg/kg or 7 mg/kg in polymers) was injected intravenously. Images were acquired with a Lumina III (Perkin Elmer, USA) (acquisition 1s, binning 4 $\times$ 4 and pictures black and white 100 ms). The bandpass filters were set, centered on 780 and 845 nm for excitation and emission respectively. Images were acquired before and 1, 60 min 3 h and 24 h, after injection of micelles. At day 1, mice were sacrificed. The fluorescent signal intensity was measured after drawing ROIs, with Living Image, on the mouse in the area surrounding the analyzed organs and tumor. It was exported and expressed as photons per second per square centimeter per steradian ( $\text{ph/s/cm}^2/\text{sr}$ ).

Performed with the acknowledged help of Coralie Genevois

### *III.4.5.5. In vivo experiments on polymersomes*

#### *Mouse strains and housing conditions*

Female 6-week-old hairless SKH1 mice (for FLI) were purchased from Charles River (Ecully, France) and kept under individually ventilated cage (IVC) housing conditions (12 h / 12 h night and day cycles,  $22 \pm 2^\circ\text{C}$ ,  $55 \pm 10\%$  relative humidity) and were given dry food and water ad libitum. All experiments were performed in accordance with EU Directive 2010/63/EU for animal experiments and were approved by the CEBEA (Comité d'Ethique et du Bien-Etre Animal) of the CMMI under approval number CMMI-2021-01. At the end of experiments, mice were sacrificed by cervical dislocation.

#### *In vivo fluorescence imaging*

Hairless female SKH1 mice were anaesthetized using isoflurane (4% for induction and then 2% for mouse imaging) vaporized in 100% oxygen at  $0.3 \text{ L min}^{-1}$ ;  $N = 3$  for each group. Mice were then placed on a preparation pad, and a catheter (home-made with 30 G needle) was placed in the tail vein and fixed using tissue glue. A volume of 100  $\mu$ l of the polymersomes solution (prepared at 10  $\mu\text{M}$  of ZW800) was injected intravenously. Images were acquired with a PhotonIMAGER Optima (Biospace Lab, France) equipped with a 4-views module, which allows the simultaneous acquisition of the back, the belly and both flanks, and a homogenous

excitation from 3 angles around the mouse body. 25 nm bandpass filters were set, centered on 737 and 797 nm for excitation and emission respectively. Images were acquired before and 1, 2, 5, 10, 15, 20, 30, 45, 60 min and 2 h, 24 h, and 7 and 14 days after injection of polymersomes. At day 14, blood samples were harvested, and mice were sacrificed. The fluorescent signal intensity was measured after drawing ROIs on the mouse in the area surrounding the analyzed organs (liver, right kidney, bladder and neck) using M3Vision software (Biospace Lab). It was exported and expressed as photons per second per square centimeter per steradian ( $\text{ph/s/cm}^2/\text{sr}$ ).

#### *Ex vivo fluorescence imaging*

Main organs (heart, lungs, spleen, liver, kidneys, adrenal glands and leg's muscle) of mice were studied by *in vivo* FLI and were harvested just after mice sacrifice at day 14. Four other groups of mice ( $N = 3$ ) were injected, as for *in vivo* FLI, but mice were sacrificed at different timepoints (10 min, 2h, 24h and 7 days), and organs were collected. Finally, organs from non-injected mice ( $N = 3$ ) were also collected as background reference. Organs were rinsed in PBS, and they were directly scanned in the PhotonImager Optima in 2D mode (Biospace Lab, France) (all organs of a mouse together in 1 acquisition). The fluorescent signal intensity of organs was measured after drawing ROIs around each of them using M3Vision software (Biospace Lab, France). It was exported and expressed as photons per second per square centimeter per steradian ( $\text{ph/s/cm}^2/\text{sr}$ ).

#### *Mice sacrifice and plasma collection*

Retro-orbital blood collection was performed under deep isoflurane anesthesia. Mice were then sacrificed immediately by cervical dislocation. Blood samples were centrifuged for 10 min at 10.000 rpm to separate the plasma from the cellular fraction. At least 250  $\mu\text{l}$  of plasma had to be obtained for dosage of several toxicity markers using Spotchem EZ Sp-4430 (Arkay, Japan) colorimeter. "Panel-1" and "Panel-2" strip sets (Arkay, Japan) were used and one relevant marker of each was considered to identify possible liver (with glutamate oxaloacetate transaminase (GOT), glutamate pyruvate transaminase (GPT) and lactate dehydrogenase (LDH)) and kidney (with blood urea nitrogen (BUN)) damage, as a preliminary ( $n = 3$ ) assessment.

Performed with the acknowledged help of Dr Lionel Larbanoix.

# Chapter IV

## Chapter IV

---

### Chapter IV: Grafting of manganese complexes onto polymeric nanocarriers

#### IV.1 Introduction

As discussed in chapter II, MRI is a powerful imaging technique due to its high spatial resolution, but it suffers from a poor sensitivity. This can be palliated by using contrast agents as Dotarem<sup>®</sup>, a FDA approved gadolinium complex commonly used in the clinic. Even though their capacity to enlighten areas of accumulation is appealing, paramagnetic molecules still suffer from major hurdles, particularly their low relaxivity, requiring high amounts of complexes to obtain a significant signal. For instance, Dotarem<sup>®</sup> is injected at 0.1 mmol/kg dose, and exhibits fast elimination, leading to a narrow imaging window.<sup>117,230</sup> Alternatives based on nanoparticles and in our specific case, polymersome-based systems, have therefore emerged to modify the relaxivity and increase the blood circulation time.

One possibility consists in encapsulating complexes inside the hydrophilic core of the polymersomes or in the bilayered membrane. Grüll *et al.*<sup>231</sup> showed that non-amphiphilic Gd-complexes exhibit a low relaxivity (below  $1.5 \text{ mM}^{-1}\cdot\text{s}^{-1}$  at 20 MHz and 25°C) when they are encapsulated in the aqueous core of polymersomes composed of 1,4-polybutadiene-*b*-poly(ethylene oxide), 1,4-PB-*b*-PEO, copolymer. This low relaxivity can be explained by the limitation of the water diffusion across the membrane. On the other hand, using complexes with an amphiphilic moiety, encapsulated in the membrane of polymersomes composed of 1,2-PB-*b*-PEO copolymer, led to a higher relaxivity of  $22 \text{ mM}^{-1}\cdot\text{s}^{-1}$  at 20 MHz and 25°C, indicating a restricted tumbling motion of the  $\text{Gd}^{3+}$ -complex.<sup>231</sup> Another strategy developed by Cheng *et al.*<sup>232</sup> lays on a system composed of different ratios in PCL-*b*-PEO and PB-*b*-PEO encapsulating Gd-DTPA-PAMAM, a macromolecular Gd-complex. Mixing PB blocks with PCL in different proportions allows to obtain a porous system due to the acidic hydrolysis of the ester function present in the PCL moiety. As a proof of concept, carboxyfluorescein was encapsulated and they evidenced that a ratio of PCL-*b*-PEO/PB-*b*-PEO 25/75 allowed a release upper than 90% within 4 days, whereas a 0/100 ratio only exhibited a release smaller than 5%. This porous system containing Gd-DTPA-PAMAM then allowed to obtain a relaxivity of  $7.5 \text{ mM}^{-1}\cdot\text{s}^{-1}$  at

40°C and 60 MHz compared to a relaxivity of 3.4 mM<sup>-1</sup>·s<sup>-1</sup> and 1.7 mM<sup>-1</sup>·s<sup>-1</sup> for Gd-DTPA-PAMAM and Gd-DTPA complexes respectively, encapsulated in non-porous vesicles. Herein, the modification of the relaxivity comes from the higher capacity of water molecules to diffuse through the bilayer of the polymersomes, thanks to the pore formation in their bilayer.<sup>232</sup> Nevertheless, this type of technique still requires high amount of complexes. For instance, Gröll *et al.*<sup>231</sup> encapsulated 200 mM of Gd-complexes in the aqueous core of the polymersomes, or 10 mol% of the amphiphilic complexes inside the membrane.

While encapsulating the complexes both in the hydrophilic core and in the membrane or using porous vesicles to enhance the relaxivity of the system, it is still necessary to improve it to limit the required amount of complexes. Therefore, the strategy followed in this work consists in modifying one of the principal parameters influencing the efficacy of paramagnetic complexes: the rotational correlation time,  $\tau_R$ , as described before, by grafting Mn-complexes on bigger entities around 100 nm in size such as the polymersomes described in Chapter III. Moreover, using nanosized systems allows to increase the half time blood circulation compared to small macromolecules that show a very fast kidneys clearance (*ca.* 30 min), allowing a larger window to perform imaging.<sup>232</sup>

To covalently graft Mn-complexes on the surface of polymersomes, different strategies can be envisaged. The most used is the peptidic coupling reaction between carboxylic acid and amine functions in the presence of a coupling agent. In aqueous media, the coupling agent is 1-ethyl-3-carbodiimide hydrochloride (EDC·HCl) in Sorensen buffer (pH 5.8; 25°C). The Sorensen buffer allows to keep the medium at a constant pH after adding the coupling agent to ensure deprotonated functions that will have a better reactivity. Garifo *et al.* grafted NIR-dye (ZW800-2) on the surface of silica nanoparticles using this technique. The rate of grafting was determined by UV-Vis and was of 15%.<sup>233</sup> Nevertheless, in the presence of a targeting nanosystem, where a vector such as a peptide has to be grafted onto the polymersomes, some amino acids bearing amine or carboxylate groups will lead to undesired side reactions. To avoid it, it is possible to use a protected peptide, but this will add some synthetic steps. Moreover, the polymers used in this framework are based on polyesters able to undergo acidic hydrolysis. Thus, the Sorensen buffer cannot be used to perform the coupling reaction, and a large decrease of pH could even lead to a destruction of the polymersomes. Additionally, the use of a buffer or ions to regulate the pH could lead to an osmolarity imbalance between the interior and outside medium of the polymersomes, causing modification of their shape, like studied by Salvat *et al.* on PB-*b*-PEO polymersomes.<sup>234</sup> Another strategy needs to be found, among the more recent

and more specific techniques belonging to the toolbox of “click chemistry”. This chemistry awarded with the 2022 Nobel prize is highly selective, fast, regiospecific and uses mild conditions. It can also be used in a lot of different fields and topics and has moreover a tolerance to different functional groups, and lead to stable products. The first click chemistry reaction was based on a copper catalyzed system between azide and alkyne functions (CuAAC), giving a 5-membered ring.<sup>235,236</sup> Nazemi *et al.*<sup>237</sup> designed polymersomes made with PEO-*b*-PCL and bearing azide or methoxy functions as end-groups in order to click Gd<sup>3+</sup> complexes on the surface. They synthesized and compared the <sup>1</sup>H NMRD profiles of dendron-Gd-DTPA, Gd-DTPA-polymersomes, and dendron-Gd-DTPA-polymersomes using Gd-DTPA complex as a reference, which exhibits a relaxivity of 4.6 mM<sup>-1</sup>·s<sup>-1</sup> at 20 MHz and 298 K. In this study, click chemistry was used in order to graft on the surface the Gd-DTPA and dendron-Gd-DTPA complexes which were functionalized with an alkyne group able to react with the azide groups present on the surface of the polymersomes. Interestingly, dendron-Gd-DTPA, Gd-DTPA-polymersomes and dendron-Gd-DTPA-polymersomes respectively exhibit relaxivity values of 12.1 ± 0.3, 10.6 ± 0.4 and 26.1 ± 1.2 mM<sup>-1</sup>·s<sup>-1</sup> at 20 MHz and 25°C, highlighting the interest of bigger structures than small complexes. Indeed, the drastic increase in relaxivity for dendrons grafted on polymersomes is probably due to the inhibition of the free rotation of Gd-complexes compared to Gd-DTPA grafted on polymersomes, which keep some rotation flexibility.<sup>237,238</sup> If results are compared with Cheng *et al.*, who obtained a relaxivity of 7.5 mM<sup>-1</sup>·s<sup>-1</sup> at 40°C and 60 MHz for their Gd-DTPA-PAMAM encapsulated in polymersomes made with a mix of PB-*b*-PEO and PCL-*b*-PEO, the relaxivity of the dendron-Gd-DTPA-polymersomes is higher.<sup>232</sup> Nevertheless, click chemistry using azide-alkyne system needs the presence of Cu<sup>+</sup> as catalyst (usually obtained by *in situ* reduction of Cu<sup>2+</sup>), which can lead to two different problems in the case of our particular study:<sup>235</sup> (i) free copper ions lead to certain toxicity in different organisms<sup>239</sup> and (ii) Garda *et al.*<sup>1</sup> calculated the stability constant at 25°C by pH-potentiometric titrations for their 3,9-PC2A, which is the same molecule as the ligand 1 presented in chapter II, and obtained a log  $K_{MnL}$  of 17.1 in a 0.15 M NaCl solution and a log  $K_{CuL}$  of 23.6 in a 1 M NaCl solution. These results show that transmetallation would occur between Mn<sup>2+</sup> and Cu<sup>2+</sup> and that the Cu-complexes will be more favored than the Mn-complexes due to their higher stability.<sup>1</sup> Moreover, copper click-chemistry brings some limitations for *in vivo* applications due to the presence of metal ions giving bio-orthogonal reaction toxicity and issues. Indeed, this type of reaction can also take place in living systems where copper can be toxic. As alternatives, strain-promoted azide-alkyne cycloaddition (SPAAC) or inverse electron-demand Diels-Alder (IEDDA) were developed.<sup>240</sup> SPAAC reaction used, most of the time, cyclooctyne

moieties as strained cycles. Among cyclooctynes, dibenzocyclooctyne (DBCO) and bicyclo(6.1.0)nonyne (BCN) are extensively used. Nevertheless, compared to CuAAC, the reaction rate is slower and cyclooctynes are less stable than alkynes. Firstly described by C. Bertozzi *et al.*, the macrocyclic DBCO derivative allows highly specific reactions and does not need copper, owing to the destabilization of the alkyne induced by the cycle stress, and the presence of the electron withdrawing group.<sup>236,241</sup>

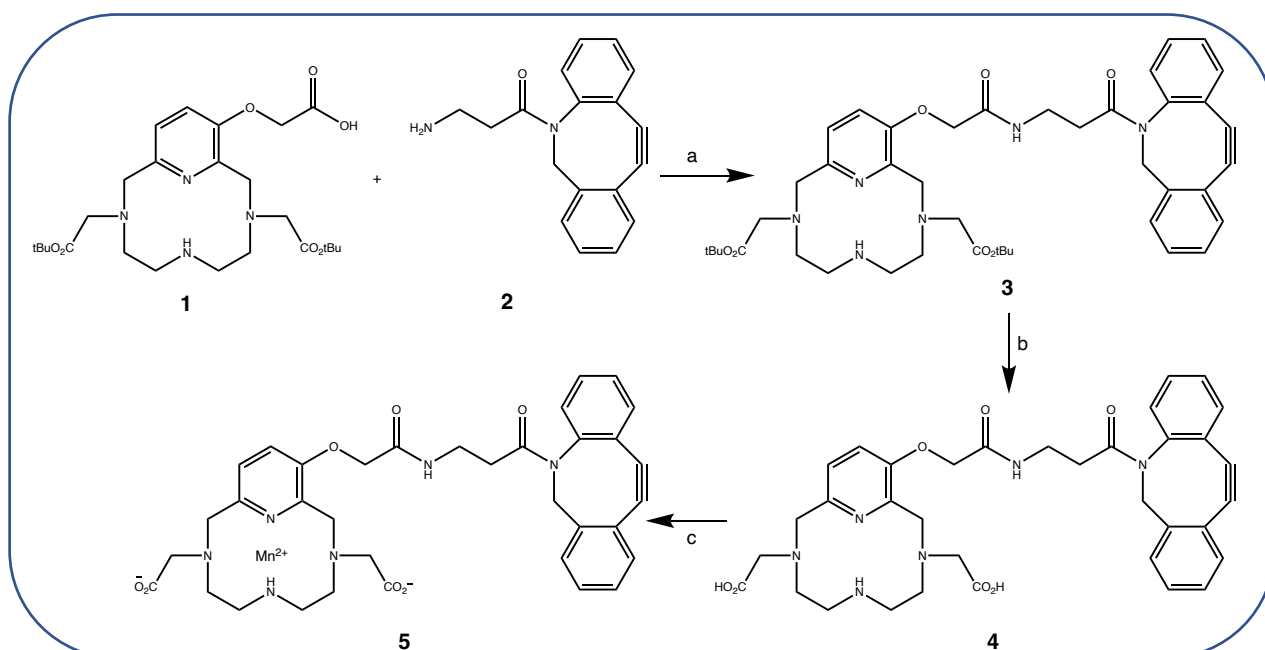
## IV.2 Results and discussion

### IV.2.1 Click chemistry on N<sub>3</sub>-PEO-*b*-P(CL-*co*-LA)

To develop click chemistry on the surface of polymersomes, it is necessary to functionalize manganese complexes with either one of both functions and the polymers with the other one. Due to the costly price of the DBCO moiety, it was decided to couple the DBCO on the pycnen derivatives and to functionalize the copolymers with azide function (N<sub>3</sub>-PEO-*b*-P(CL-*co*-LA)). For the reverse case indeed, during the formation of polymersomes, DBCO would be partially incorporated inside the nanostructure, pointing to the aqueous vesicle core, which would represent a significant loss for the surface functionalization.

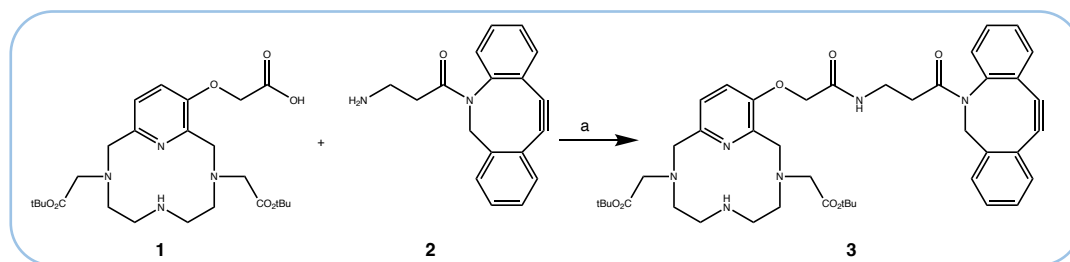
#### IV.2.1.1 Synthesis of DBCO-Mn-complexes

The first developed strategy consists in a coupling reaction between the pycnen derivative L<sub>2</sub>COO<sup>-</sup> (see chapter II) and the amino-DBCO, followed by the deprotection of -tBu groups in order to finally complex the macrocycle with manganese ions. (Scheme IV.1)



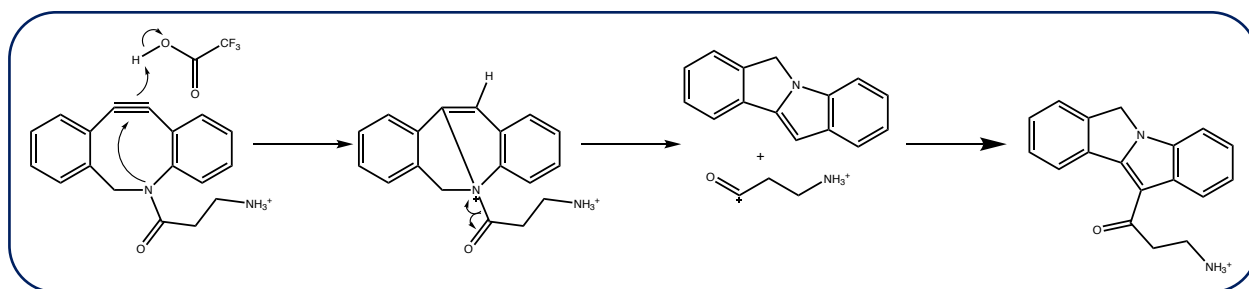
Scheme IV.1. First strategy for the synthesis of DBCO-Mn-complexes. Expected reactions: (a) HBTU, DIPEA, CH<sub>2</sub>Cl<sub>2</sub> at r.t. (b) TFA/CH<sub>2</sub>Cl<sub>2</sub> at r.t. (c) MnCl<sub>2</sub>·4H<sub>2</sub>O, H<sub>2</sub>O, pH = 5-6, 40°C, Ar atm, overnight.

Herein, a 3-step synthesis method is performed to develop a clickable amino-DBCO attached on a pyclyen moiety. Firstly, the pyclyen derivative is coupled with the amino-DBCO giving the compound **3**. The coupling reaction is performed in the presence of HBTU and DIPEA in CH<sub>2</sub>Cl<sub>2</sub> and is followed by a purification on a silica column with a gradient of CH<sub>2</sub>Cl<sub>2</sub>/MeOH in order to eliminate the by-products induced by the coupling agent. (Scheme IV.2) <sup>1</sup>H NMR analyses and mass spectrometry confirmed the formation of compound **3** with a mass of  $m/z$  767 [M+H]<sup>+</sup>.



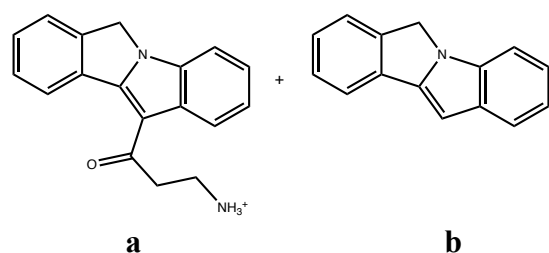
Scheme IV.2. Synthesis of compound **3**, (a) HBTU, DIPEA, CH<sub>2</sub>Cl<sub>2</sub>, few h at r.t..

As a second step, -tBu groups are removed to obtain free carboxylic acid functions able to complex manganese ions. To obtain compound **4**, the usual method of deprotection is to use an acidic medium, such as an equimolar mixture of TFA and CH<sub>2</sub>Cl<sub>2</sub>, that was already used in chapter III. Nevertheless, mass spectrometry and <sup>1</sup>H NMR do not exhibit the characteristic signals of compound **4**, meaning that the desired product has not been formed. Following these results, the proportion in TFA has been decreased but still without success. According to the protocol of Beck *et al.*<sup>242</sup>, the reaction has then been performed in the presence of triisopropylsilane (TIS) under argon atmosphere. Indeed, TIS is used as a cation scavenger to avoid side reactions. Using this protocol (without using Ar atmosphere), <sup>1</sup>H NMR and mass spectrometry analyses seemed to show the presence of the desired molecule with the presence of by-products. Nevertheless, the compound could not be isolated. Chigrinova *et al.*<sup>243</sup> tried to evidence the mechanisms that could occur on derivatives of the octyne moiety in the presence of TFA, that could explain our results. Indeed, they showed the possibility for the cyclooctyne to rearrange in two 5-membered cycles induced by the attack of the nitrogen atom on the alkyne link. Moreover, Shi *et al.* evidenced the possible side reaction that could occur on DBCO having a carbamate function in the presence of 10-20% in TFA. The system will undergo a rearrangement to 4 rings system. Based on the Brønsted acid conditions, they proposed the following mechanism that could occur: (Scheme IV.3)<sup>244</sup>



Scheme IV.3. Proposed mechanism by Shi *et al.* for the amino-DBCO rearrangement in the presence of TFA.<sup>244</sup>

Moreover, they evidenced the presence of a mixture between molecules **a** and **b**. (Figure IV.1) By modifying the quantity of TFA, the proportion of the two molecules is varied.<sup>244</sup> This observation could explain the presence of side products and the difficulty to separate them by flash chromatography.



Solvent	Acids	Conversion (%)	
		<b>a</b>	<b>b</b>
CH <sub>2</sub> Cl <sub>2</sub>	TFA 10%	58.8	31.5
CH <sub>2</sub> Cl <sub>2</sub>	TFA 20%	73	27

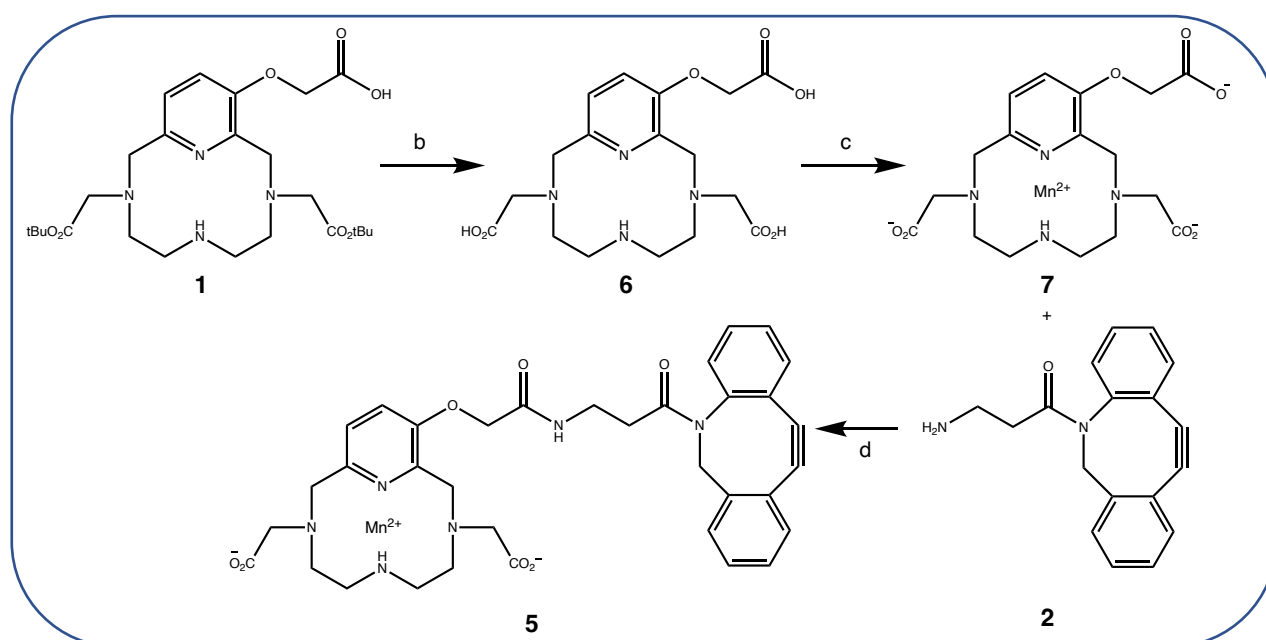
Figure IV.1. Resulting compounds evidenced by Shi *et al.* and their proportion according to the acidic conditions used.<sup>244</sup>

Thereby, in the light of these results, we decided to perform the deprotection in a basic medium instead. The reaction was then performed in MeOH in the presence of LiOH. However, mass spectrometry analyses only exhibited the signal of compound **3**. The medium was further placed under reflux and the desired product, mixed with compound **3**, was observed by mass spectrometry. To complete the reaction, 2 additional equivalents of LiOH were added to the solution. Nevertheless, despite the increase in the number of LiOH equivalents, the modification of the heating temperature and a regular following by mass spectrometry, the deprotection was never complete. In order to isolate compound **4**, different conditions by thin layer chromatography were used and the optimal one seemed to be MeOH/CH<sub>2</sub>Cl<sub>2</sub>+1% triethylamine. The product was purified by flash chromatography with a gradient

MeOH/CH<sub>2</sub>Cl<sub>2</sub>+1% triethylamine (5/95 to 20/80 v/v) but the desired product could not be isolated as a pure compound.

#### IV.2.1.2 Other strategy to prepare DBCO-Mn-complexes

A second strategy could be to couple the Mn-complex with the amino-DBCO. (Scheme IV.4) This scheme is in general not chosen preferentially due to the impossibility to confirm the reaction by <sup>1</sup>H NMR. Indeed, the paramagnetic manganese ions present in the macrocycle induce broadening of the peaks in the <sup>1</sup>H NMR spectra. The reaction can nevertheless be followed by mass spectrometry, so that it was tried. Unfortunately, amino-DBCO is not soluble in water. This reaction was thus performed in a mixture of water and THF. THF was chosen due to its ability to solubilize the amino-DBCO and its miscibility with water. The reaction was performed in the presence of EDC·HCl with a controlled pH at 6, but the desired product has unluckily never been observed by mass spectrometry.



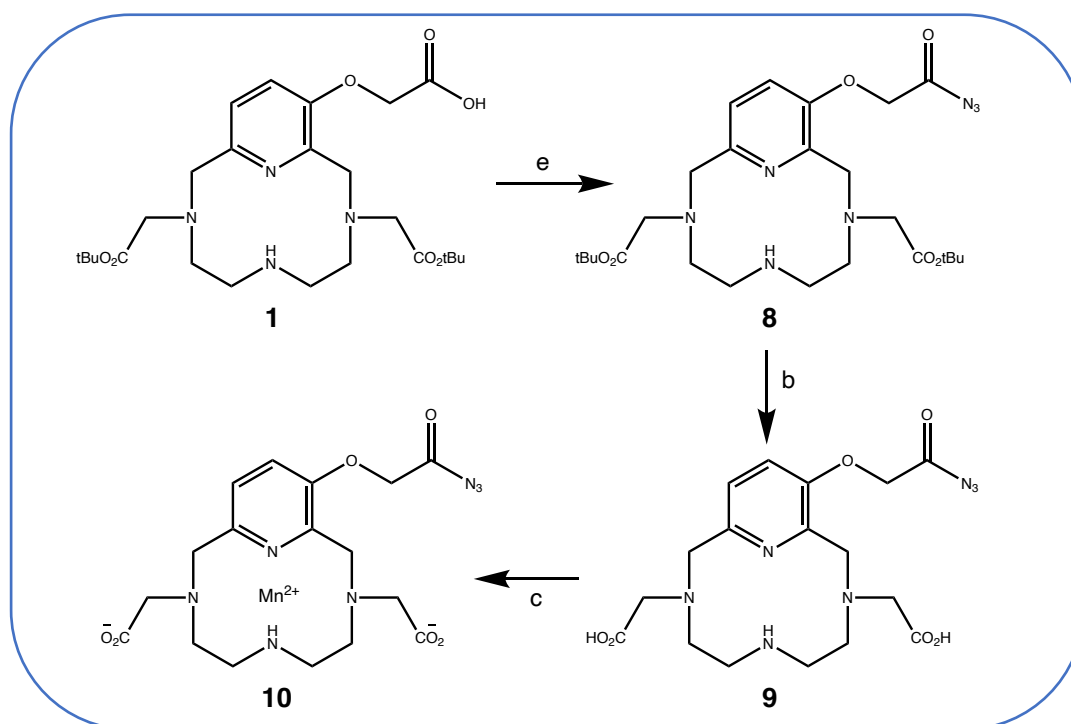
Scheme IV.4. Second strategy for the synthesis of DBCO-Mn-complexes. Expected reactions: (b) TFA/CH<sub>2</sub>Cl<sub>2</sub> at r.t. (c) MnCl<sub>2</sub>·4H<sub>2</sub>O, H<sub>2</sub>O, pH = 5-6, 40°C, Ar atm, overnight (d) EDC·HCl, pH = 6, THF/H<sub>2</sub>O, r.t..

#### IV.2.2 Click chemistry on DBCO-PEO-*b*-P(CL-*co*-LA)

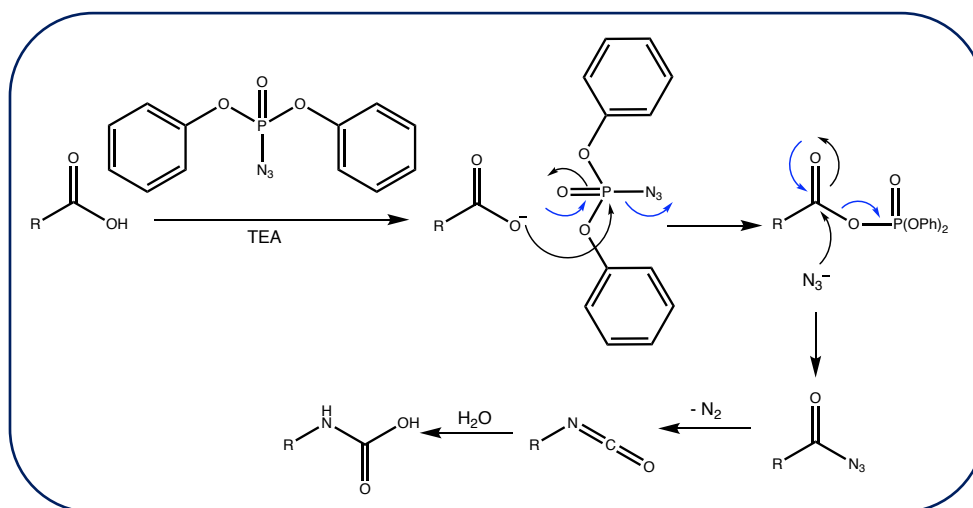
Based on the results, the strategy was modified by grafting the DBCO rather onto the copolymer (DBCO-PEO-*b*-P(CL-*co*-LA)) and the azide function on the Mn-complexes, so that the same click chemistry reaction can be envisaged to couple Mn-complexes on polymersomes.

IV.2.2.1 Synthesis of  $N_3$ -Mn-complexes

The first used strategy was the modification of the carboxylic acid function of the ligand  $L_2COO^-$  into an azide function. (Scheme IV.5) Compound **8** can theoretically be obtained using triethylamine (TEA) and diphenylphosphoryl azide (DPPA) in  $CH_2Cl_2$ . However, mass spectrometry analysis showed a mass of  $m/z$  523 which is smaller than expected (*i.e.*,  $m/z$  534  $[M+H]^+$ ). This smaller mass can be attributed to the azide function that suffered from a Curtius rearrangement followed by a hydrolysis.<sup>245,246</sup> (Scheme IV.6) Thereby, we attempted to isolate the  $-N_3$  derivative using acyl chloride as an intermediate. The azide derivative synthesis was herein performed during 4 h in  $CH_2Cl_2$  at  $0^\circ C$  by adding DMF and  $SOCl_2$  to the macrocycle solution under argon atmosphere until reaching room temperature. Then, the medium was evaporated and redissolved in  $CH_2Cl_2$  followed by the addition of  $NaN_3$ . The medium was finally heated at  $50^\circ C$ . Still, we did not succeed in isolating compound **8**.



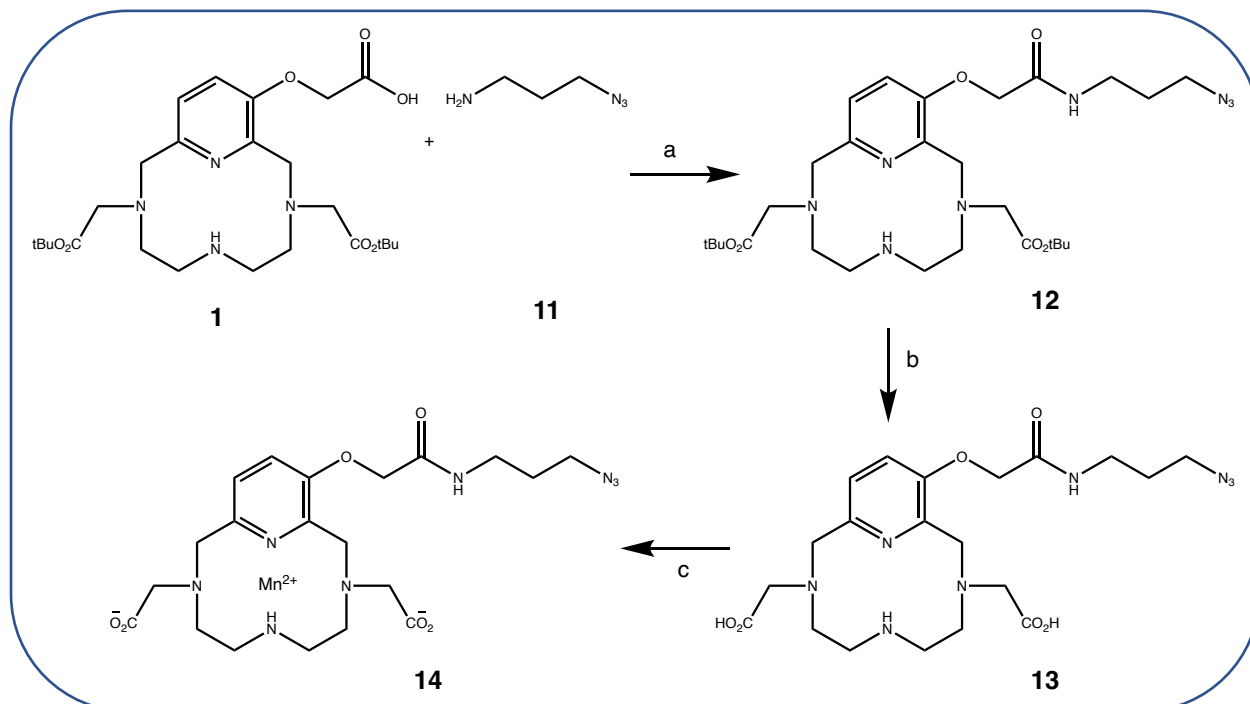
Scheme IV.5. First strategy for the synthesis of  $N_3$ -Mn-complexes. Expected reactions: (e) TEA, DPPA,  $CH_2Cl_2$  at r.t. (b) TFA/ $CH_2Cl_2$  at r.t. (c)  $MnCl_2 \cdot 4H_2O$ ,  $H_2O$ , pH = 5-6,  $40^\circ C$ , Ar atm, overnight.



Scheme IV.6. Curtius rearrangement and hydrolysis of isocyanate function that can be observed on azide functions.

In the light of the previous results, a second strategy has been elaborated. This second strategy is based on a peptidic coupling of a  $N_3$ -amino derivative similarly to the strategy used previously with DBCO moiety. (Scheme IV.7) Herein, a coupling reaction between the macrocycle and 3-azido-1-propanamine was envisaged. This reaction was performed with HBTU and DIPEA in  $CH_2Cl_2$  followed by a purification step on a silica column with a  $CH_2Cl_2/MeOH$  gradient.  $^1H$  NMR and mass spectrometry evidenced the formation of the product with still the presence of urea (which is inert for the next step). FT-IR analyses also evidenced the stretching band of  $-N_3$  function ( $2100\text{ cm}^{-1}$ , Figure IV.2) Then, deprotection of  $-tBu$  groups was performed in an equimolar mixture of TFA and  $CH_2Cl_2$ . The  $^1H$  NMR and mass spectrometry confirmed the formation of compound **13**. The last step was the complexation of the macrocycle with manganese ions as described in chapter II. Finally, to perform mass spectrometry, the medium was desalted by steric exclusion chromatography on a Sephadex<sup>TM</sup> column. The osmolarity of the different fractions was determined with an osmometer to obtain the ions concentration in solution. The formation of compound **14** was confirmed by mass spectrometry at  $m/z$  554  $[M+Na]^+$ . However, infrared spectroscopy evidenced the supposed loss of the  $-N_3$  function with the disappearance of the characteristic band at  $2100\text{ cm}^{-1}$ . It is possible that a hydrolysis reaction of the azide group occurred in the medium but this was not confirmed by mass spectrometry.<sup>247</sup> This phenomenon has thus to be investigated to confirm the presence of the  $-N_3$  function. This function being difficult to evidence by NMR, it could be interesting to perform a click chemistry reaction, with a little molecule possessing the DBCO moiety, to check if the expected product is obtained. Another

solution could be to use UV-Vis, but it will be complicated in our case since the complexes absorb in the same range of wavelengths than the azide function.



Scheme IV.7. Second strategy for the synthesis of  $N_3$ -Mn-complexes. Expected reactions: (a) HBTU, DIPEA,  $CH_2Cl_2$  at r.t. (b) TFA/ $CH_2Cl_2$  at r.t. (c)  $MnCl_2 \cdot 4H_2O$ ,  $H_2O$ , pH = 5-6,  $40^\circ C$ , Ar atm, overnight which was validated.

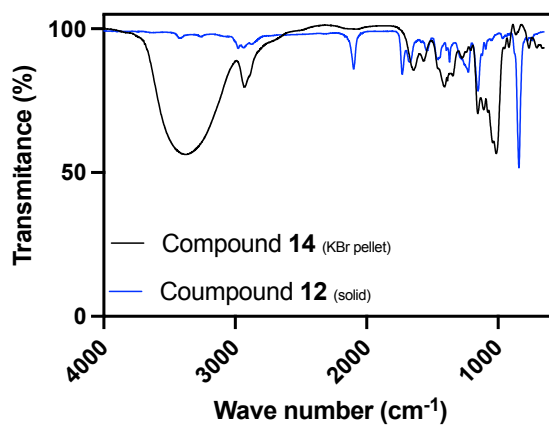


Figure IV.2. FT-IR spectra of compound **12** (in blue) and compound **14** (in black) showing the disappearance of the  $N_3$  characteristic vibration peak at  $2100\text{ cm}^{-1}$  wave number.

### IV.2.3 Synthesis of the copolymer with DBCO end-group

Since the  $N_3$ -Mn-complex was obtained, a new diblock copolymer with the DBCO moiety at the end had to be synthesized to allow the formation of polymersomes composed of PEO-*b*-P(CL-*co*-LA) and DBCO-PEO-*b*-P(CL-*co*-LA). At the end, the presence of the DBCO moieties at the surface of the polymersomes will allow the grafting of the  $N_3$ -Mn-complexes by SPAAC click chemistry reaction. To synthesize this second diblock copolymer, a commercially available DBCO-PEO<sub>1k</sub> from Biochempeg® was used. However, the received batch clearly exhibits two polymer distributions with a dispersity  $D=1.25$  and a  $M_n \sim 1600 \text{ g}\cdot\text{mol}^{-1}$  as evidenced by SEC analyses. (Figure IV.3) Moreover, some impurities are visible on the  $^1\text{H}$  NMR spectrum. (Figure IV.4) Some problems during the formation of polymersomes can thus be anticipated, but the synthesis of the copolymer was nevertheless tried by Prof. O. Coulembier.

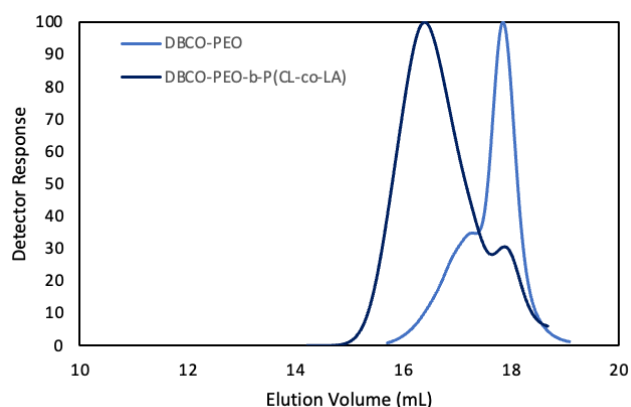


Figure IV.3. SEC traces in THF of DBCO-PEO and DBCO-PEO-*b*-P(CL-*co*-LA).

As expected, after the synthesis of the DBCO-PEO-*b*-P(CL-*co*-LA) by ROP, SEC analysis shows the increase in molar mass of the polymer, but with the presence of the second distribution. (Figure IV.3) The dispersity is slightly broader (*i.e.*  $D=1.4$ ) with an associated  $M_n \sim 7400 \text{ g}\cdot\text{mol}^{-1}$ . On the  $^1\text{H}$  NMR spectrum (Figure IV.5), the presence of the statistical hydrophobic block with PLA and PCL is evidenced between 1 and 2 ppm as well as the appearance of peaks at 2.3 and  $\sim 4$  ppm induced by the presence of PCL.

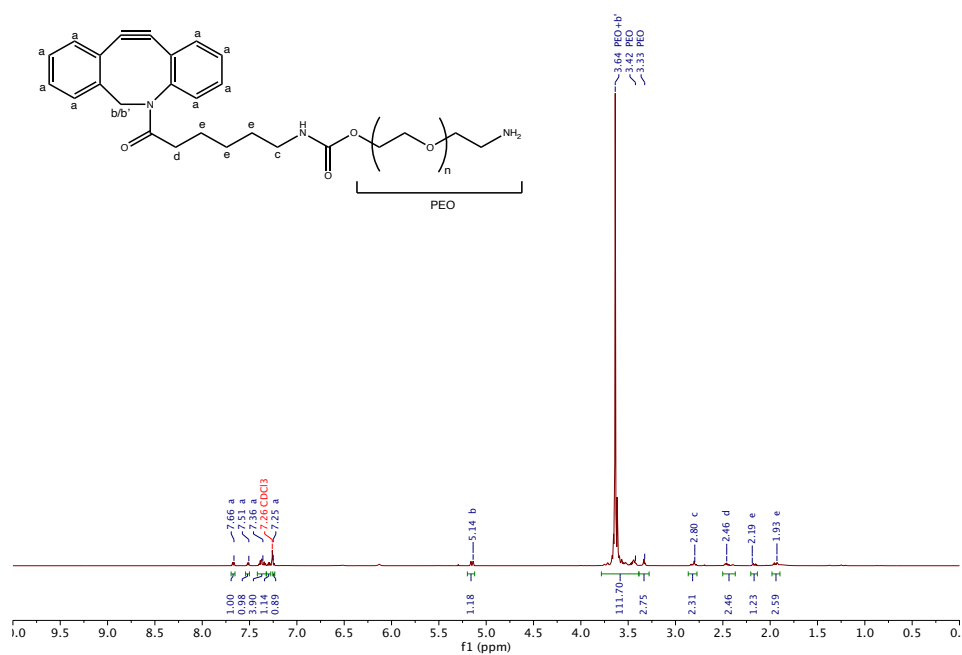


Figure IV.4.  $^1\text{H}$  NMR (500 MHz;  $\text{CDCl}_3$ ) spectrum of DBCO-PEO bought to Biochempeg (USA).

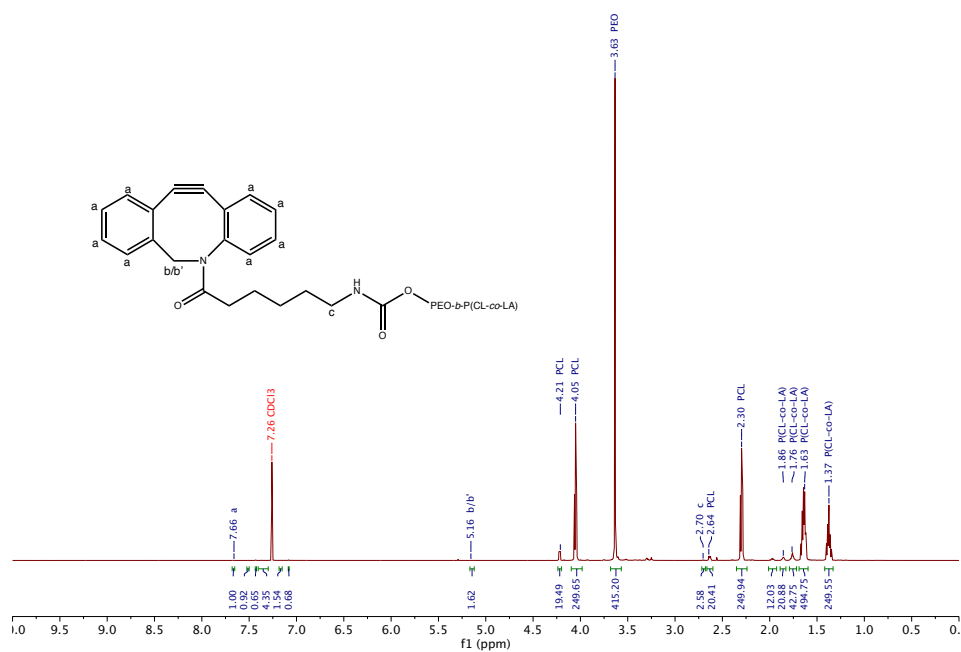


Figure IV.5.  $^1\text{H}$  NMR (500 MHz;  $\text{CDCl}_3$ ) spectrum of DBCO-PEO-*b*-P(CL-*co*-LA).

## IV.2 Conclusion and perspectives

To conclude on this chapter, several difficulties have been met to obtain the Mn-complexes bearing a functional group needed for SPAAC click chemistry, either the DBCO or the azide functions. The main encountered difficulty came from the -tBu deprotection in an acidic medium and different strategies have been developed to palliate this issue. The optimal solution seems to be the grafting of 3-azido-1-propanamine on  $L_2COO^-$  leading to the obtention of the complex after -tBu deprotection and complexation with manganese ions. Nevertheless, some improvements or other characterization techniques have to be performed to evidence the presence of azide function on the complexes. On the other hand, the functionalized copolymer DBCO-PEO-*b*-P(CL-*co*-LA) was synthesized using a commercial DBCO-PEO with an unsatisfying purity leading to a bimodal dispersity in SEC analyses. This synthesis should thus also require some improvements and optimizations. Two solutions could be attempted: either to buy the polymer to another provider like JenKem™ (USA) or try to purify the current one.

The next step will be the formation of the polymersomes constituted of different proportions of DBCO-PEO-*b*-P(CL-*co*-LA) and PEO-*b*-P(CL-*co*-LA). It could be interesting to determine the number of DBCO on the surface to add exactly the right number of  $N_3$ -Mn-complexes in the medium. This amount will probably depend on the proportion between functionalized and unfunctionalized polymers used to form the polymersomes. Indeed Nazemi *et al.* have shown the formation of aggregates with  $N_3$ -PEO-PBD polymer and certain ratios of the - $N_3$  function.<sup>238</sup> Different proportions between functionalized and unfunctionalized polymer will thus have to be tried to check if the same phenomenon is observed. The quantity of DBCO in the polymersomes could then be quantified by NMR, by assuming that the half of it is expressed at their surface. The subsequent grafting of the  $N_3$ -Mn-complexes will then allow to refine the results since the Mn concentration can easily be determined by relaxometry measurement or by ICP after digestion of the complexes. Finally, a complete relaxometric study of the grafted polymersomes should allow to evaluate the impact of the grafting on the rotational correlation time  $\tau_R$  and on the efficacy of the nanoobjects as MRI contrast agents.

Moreover, in future works, this type of DBCO-functionalized polymersomes could also allow to graft peptides or other specific targeting molecules, leading to the formation of a versatile targeted theranostic nano-platform.

### IV.3 Materials and methods

#### IV.3.1 Materials

The  $^1\text{H}$  NMR spectra were recorded at 298K and reported in ppm. (Bruker<sup>®</sup> AVANCEII-500 at 500 MHz, USA) The multiplicity of the peaks is defined as s (singlet), d (doublet), t (triplet), q (quintuplet), m (multiplet) and -Phe (phenyl). The reactions were monitored by mass spectrometry (Waters<sup>®</sup>, ZQ-2000, USA) and all the compounds were characterized by mass spectrometry (Waters<sup>®</sup>, ZQ-2000, USA). The chemicals and solvent were purchased from different companies: ChemLab, Sigma Aldrich, Roth, TCI, VWR, Merck and Fluka. The chemicals and solvents (excepted  $\text{CH}_2\text{Cl}_2$ ) were used without further purification.  $\text{CH}_2\text{Cl}_2$  was distilled under vacuum. PEO,  $\epsilon$ -CL monomer, *L*-LA monomer and benzoic acid were bought from Sigma-Aldrich. All chemical reagents were beforehand dried and placed in glovebox (MBraun Labmaster 130, Germany). Infrared spectra were recorded on Spectrum 100 FT-IR Spectrometer (Perkin Elmer, USA), either with the Universal ATR Sampling accessory (Perkin Elmer, USA), or using a KBr pellet formed from a mixture between 1% of compound and 99% of KBr, pressed with a Specac press (United Kingdom). SEC were performed on Agilent 1200 devices in THF (containing 2 wt% of  $\text{Et}_3\text{N}$ ). Samples in solution (~ 5 mg/mL) were injected at a flow rate of 1 mL/min at 35°C. The pre-column PL gel 10 mm was followed by two PLgel 10 mm mixed-B. The molecular weight was obtained based on a calibration with polystyrene standards. The data were treated by the provider's software (Agilent GPC-Addon). The flash chromatography was performed on Teledyne<sup>®</sup> Vasco Flash EZprep (USA) using pre-packed cartridges. The collection is based on absorption at 254 and 270 nm by UV detection. The used osmometer is an Advanced Micro Osmometer Model 3300 (Advanced Instruments, USA)

#### IV.3.2 Synthetic methods

di-*tert*-butyl 2,2'-(2-((3-amidoDBCOpopyl)amino)-2-oxoethoxy)-3,6,9-triaza-1(2,6)-pyridinacyclodecaphane-3,9-diyl)diacetate compound **3**: Compound **1** (57.2 mg, 0.11 mmol) and HBTU (87.35 mg, 0.22 mmol, 2 eq) are solubilized in  $\text{CH}_2\text{Cl}_2$  (4-5 mL), followed by the addition of compound **2** (37.2 mg, 0.13 mmol, 1.2 eq) and DIPEA (76.5  $\mu\text{L}$ , 0.45 mmol, 4 eq).

The solution is stirred during few hours at room temperature, then the medium is washed two times with water (5 mL). The resulting material is purified by chromatography on silica gel (CH<sub>2</sub>Cl<sub>2</sub>/MeOH 100/20 to 90/10 v/v) and led to the desired product **3**. Yield 48% (presence of urea in the medium). <sup>1</sup>H NMR (CDCl<sub>3</sub>, 500 MHz) δ (ppm): 1.47 (s, 9H, *-tBu*); 1.48 (s, 9H, *-tBu*); 2.01-2.05 (m, 1H, NH-CH<sub>2</sub>-CH<sub>2</sub>-CO-); 2.47-2.54 (m, 1H, NH-CH<sub>2</sub>-CH<sub>2</sub>-CO-); 3.11 (broad s, 4H, NH-CH<sub>2</sub>-CH<sub>2</sub>-N-); 3.24 - 3.30 (m, 4H, NH-CH<sub>2</sub>-CH<sub>2</sub>-N-); 3.57 (broad s, -N-CH<sub>2</sub>-C- ); 3.70 (d, *J* 13.91Hz, 1H -N-CH<sub>2</sub>-phe); 3.98 ( broad s, 2H, -N-CH<sub>2</sub>-CO<sub>2</sub>-); 4.09-4.17 (m, 2H, -NH-CH<sub>2</sub>-CH<sub>2</sub>-CO-); 4.40 (s, 2H, -O-CH<sub>2</sub>-CO-); 5.15 (d, *J* 14.03 Hz, 1H -N-CH<sub>2</sub>-phe); 7.18 (d, *J* 7.56 Hz, 1H, -O-C=CH-CH=C-); 7.24-7.44 (m, 10 H, -Phe); 7.66 (d, *J* 7.74 Hz, 1H, -O-C=CH-CH=C-).

di-*tert*-butyl 2,2'-(2-((3-azidopropyl)amino)-2-oxoethoxy)-3,6,9-triaza-1(2,6)-pyridinacyclodecaphane-3,9-diyl)diacetate compound **12**: Compound **1** (45.8 mg, 0.09 mmol) and HBTU (76.8 mg, 0.2 mmol, 2.2 eq) are solubilized in CH<sub>2</sub>Cl<sub>2</sub> (4-5 mL) followed by the addition of compound **11** (9.6 μL, 0.1 mmol, 1.1 eq) and DIPEA (43.6 μL, 0.25 mmol, 2.8 eq). The solution is stirred during few hours at room temperature, then the medium is washed two times with water (5 mL). The resulting material is purified by chromatography on silica gel (CH<sub>2</sub>Cl<sub>2</sub>/MeOH 100/20 to 90/10 v/v) and led to the desired product **12**. Yield 79% (presence of urea in the medium and residual solvent). <sup>1</sup>H NMR (CDCl<sub>3</sub>, 500 MHz) δ (ppm): 1.43 (s, 9H, *-tBu*); 1.44 (s, 9H, *-tBu*); 1.81 (q, *J* 6.66 Hz, 2H, -N<sub>3</sub>-CH<sub>2</sub>-CH<sub>2</sub>-); 3.06 (broad s, 4H, NH-CH<sub>2</sub>-CH<sub>2</sub>-N-); 3.16-3.23 (m, 4H, NH-CH<sub>2</sub>-CH<sub>2</sub>-N-); 3.34 (t, *J* 6.58 Hz, -N<sub>3</sub>-CH<sub>2</sub>-CH<sub>2</sub>- ); 3.39 - 3.44 (m, 4H, -N<sub>3</sub>-CH<sub>2</sub>-CH<sub>2</sub>-CH<sub>2</sub>- and -N-CH<sub>2</sub>-CO<sub>2</sub>-); 3.46 (s, 2H, -N-CH<sub>2</sub>-CO<sub>2</sub>-); 3.92 (s, -N-CH<sub>2</sub>-C- ); 4.13 (s, 2H, -N-CH<sub>2</sub>-C- ); 4.50 (s, 2H, -O-CH<sub>2</sub>-CO-); 7.01 (d, *J* 8.45 Hz, 1H, -O-C=CH-CH=C-); 7.07 (d, *J* 8.48 Hz, 1H, -O-C=CH-CH=C-). ESI-MS (C<sub>20</sub>H<sub>46</sub>N<sub>8</sub>O<sub>6</sub>) *m/z*: 591 [M+H]<sup>+</sup>, 613 [M+Na]<sup>+</sup>

2,2'-(2-((3-azidopropyl)amino)-2-oxoethoxy)-3,6,9-triaza-1(2,6)-pyridinacyclodecaphane-3,9-diyl)diacetic acid compound **13**: Compound **12** (8 mg, 0.01 mmol) is solubilized in CH<sub>2</sub>Cl<sub>2</sub> (0.8 mL), followed by the addition of trifluoroacetic acid (0.2 mL). The mixture is stirred overnight, and the solution is concentrated and washed two times with diethyl ether to give the desired compound **13** as TFA salt. <sup>1</sup>H NMR (CD<sub>3</sub>OD, 500 MHz) δ (ppm) : 1.78 (q, *J* 6.68 Hz, 2H, -N<sub>3</sub>-CH<sub>2</sub>-CH<sub>2</sub>-); 3.11 (broad s, 4H, NH-CH<sub>2</sub>-CH<sub>2</sub>-N-); 3.16-3.25 (m, 4H, NH-CH<sub>2</sub>-CH<sub>2</sub>-N-); 3.33 - 3.33 (m, 4 H, -N<sub>3</sub>-CH<sub>2</sub>-CH<sub>2</sub>-CH<sub>2</sub>- ); 3.57 - 3.60 (m, 4H,

-N-CH<sub>2</sub>-CO<sub>2</sub>-); 3.67 (s, 2H, -N-CH<sub>2</sub>-CO<sub>2</sub>-); 4.03 (s, 2H, -N-CH<sub>2</sub>-C- ); 4.26 (s, 2H, -N-CH<sub>2</sub>-C- ); 4.63 (s, 2H, -O-CH<sub>2</sub>-CO-); 7.17 (broad d, *J* 8.45 Hz, 1H, -O-C=CH-CH=C-); 7.28-7.32 (m, 1H, -O-C=CH-CH=C-). ESI-MS (C<sub>20</sub>H<sub>30</sub>N<sub>8</sub>O<sub>6</sub>): *m/z* 479 [M+H]<sup>+</sup>

2,2'-(2-((3-azidopropyl)amino)-2-oxoethoxy)-3,6,9-triaza-1(2,6)-pyridinacyclodecaphane-3,9-diyl)diacetate manganese compound **14**: A solution of MnCl<sub>2</sub>·4H<sub>2</sub>O (18 mg, 0.14 mmol) in water (~ 0.5 mL) is added dropwise to a solution of compound **13** ( some mg ) in water (~ 1 mL). The pH is adjusted and maintained to 5 < pH < 6 with aqueous solution of NaOH. The mixture is warmed at 40°C overnight. The presence of free Mn<sup>2+</sup> ions is revealed by the colorimetric test with orange xylenol. The aqueous mixture is treated with Chelex<sup>®</sup> resin, then freeze-dried to give the desired compound **14**. ESI-MS (C<sub>20</sub>H<sub>28</sub>MnN<sub>8</sub>O<sub>6</sub>): *m/z* 554 [M+Na]<sup>+</sup>

Compound **14** was desalted using Sephadex<sup>™</sup> G-100 columns (Cytiva, Germany) that were prepared by inflating the beads in Milli-Q water (approximately 3g / 200 mL of water) during 3 days at room temperature. The medium was degassed under vacuum during 15-30 min. The extra water was eliminated, and the gel was flowed in column (~ 25 cm, Ø 1 cm). The Mn-complexes powder was dissolved in demineralized water (1 mL) and added in front of the column. Fractions of approximately 1 mL were collected and characterized (Table IV.1).

Table IV.1. Measurements of osmolarity, ESI-MS and colorimetric tests with orange xylenol on all fractions

Fraction	(mOsm·kg <sup>-1</sup> )	Tests orange xylenol	<i>m/z</i> [M+Na] <sup>+</sup>
1	6	Neg	554
2	6	Neg	554
3	5	Neg	554
4	5	Neg	554
5	6	Neg	554
6	5	Neg	554
7	10	Neg	554
8	6	Neg	554
9	6	Neg	554
10	5	Pos / Neg ?	554
11	6	Neg	554
12	43	Pos	/
14	237	Pos	/

Synthesis of DBCO-PEO-*b*-P(CL-*co*-LA): this ROP reaction was performed by Prof. O. Coulembier (SMPC Laboratory, UMONS)

Before use, DBCO-PEO<sub>1k</sub> (Biochempeg, USA) was dried under vacuum in a steam room at 60°C for 12 hours and placed in a glovebox. DBCO-PEO (100 mg) was placed in a glass vial followed by the addition of benzoic acid (23 mg), *L*-LA (72 mg) and  $\epsilon$ -CL (660 mg) leading to a molar ratio of 1/8/94 (w/w/w) for [DBCO]/[*L*-LA]/[CL] respectively. The vial was sealed and got out of the glovebox. The vial was placed under stirring at 155°C during 24 h. Once at room temperature, THF (2 mL) was then added to solubilize the copolymer, followed by the addition of eight volumes of cold heptane (12 mL). The resulting precipitate was filtered and dried under vacuum until constant weight. Yield: 61%.  $M_n$  SEC = 7400 g·mol<sup>-1</sup> with a dispersity  $D = 1.49$ . <sup>1</sup>H NMR (CCl<sub>3</sub>, 500 MHz)  $\delta$  (ppm) : 1.34 – 1.41 (m, 249H, P(CL-*co*-LA)); 1.60 – 2.01 (m, 569H, P(CL-*co*-LA)); 2.30 (t, *J* 7.52 Hz, 240H, PCL); 2.60 -2.66 (m, 20H, PCL); 2.68- 2.71 (m, 2H, -CH<sub>2</sub>-NH-CO-); 3.63 (s, 415H, PEO); 4.05 (t, *J* 6.74 Hz, 240H, PCL); 4.20 – 4.24 (m, 19H, PCL); 5.12 – 5.17 (broad d, 2H, -N-CH<sub>2</sub>-phe); 7.08 – 7.68 (m, 8H, -phe).



# **Chapter V**

## Conclusions and outlooks

## Chapter V

---

### Chapter V: Conclusions and outlooks

As a reminder of the context of this study, cancer remains a major cause of death in the world. A lot of efforts are thus made to diagnose it at an earlier stage and to treat it more efficiently. Indeed, the currently used treatments are invasive or lead to multi drug resistance by using several times chemotherapy techniques. Therefore, for several reasons there is a growing interest in nanomedicine, and more particularly in polymeric nanoobjects, to improve current treatments. To develop a theranostic platform, we first synthesized, in chapter II, manganese complexes based on several pyclen derivatives. This macrocyclic structure was chosen to allow the presence of one water molecule in the inner sphere of the magnetic center. After the synthesis of the complexes, different Mn-pyclen derivatives, functionalized or not, were fully characterized by different relaxometry techniques to evidence that one water molecule is present in the inner sphere and is characterized by a very short residence time (in the nanosecond range), which is benefic for the MRI contrast enhancement. The relaxivity at clinical field is closed to that of commercial gadolinium complexes giving a proof of concept of the interest of this type of molecules, confirmed by phantom imaging. Finally, preliminary experiments on *in vivo* biodistribution were performed on a short cohort of mice, which evidenced kidneys elimination within few hours and enlightenment of the liver and, on some mice, hepatobiliary excretion pathway. This phenomenon allows to conclude on a possible decomplexation of  $Mn^{2+}$  ions, which has to be further investigated. Still, such results are encouraging and are one of the pillars of the development of the theranostic platform which, at the end, will combine MRI and fluorescence imaging (FLI).

Then, Chapter III treated the formation by self-assembly of nanostructures composed of PEO-*b*-P(CL-*co*-LA) amphiphilic copolymers where the hydrophobic block is constituted of a statistical polymer of biocompatible and biodegradable polyesters (PCL and PLA) obtained by ring opening polymerization (ROP) with an organic catalyzer. Such nanostructures are essential in the development of the theranostic platform as they will be used as carriers and drug delivery systems. The method used for self-assembly was shown to be essential to their morphology as the nanoprecipitation route led to the formation of spherical and cylindrical micelles, while vesicles (polymersomes) were obtained with the thin film rehydration method.

These nanostructures were evidenced with different types of methods as AF4, MALS, SAXS and Cryo-TEM. The obtained nanostructures are thus depending strongly on the self-assembly method, which we attributed to the semi-crystalline property of the copolyester. The next step was the encapsulation of drug, doxorubicin, and fluorescent dyes, ZW800-1 and rhodamine B. Results evidence best drug loading content (DLC) for the polymersome structures, as compared to micelles. The subsequent *in vitro* and *in vivo* studies showed a survival rate below 80% of the cells for higher concentration than 0.8 mg/mL in copolymer. This phenomenon was observed for cells able to internalize the nanocarriers, which was confirmed by confocal microscopy analyses. Moreover, the nanocarriers have demonstrated their capacity to decrease the toxicity of doxorubicin due to its entrapment, demonstrating their interest for such applications. Concerning *in vivo* assays, results evidence different behaviors. First, micelles show an almost instantaneous release, probably due to the physisorption on their surface of the drug and of the dyes. This phenomenon translates into a fluorescent signal in the kidneys and bladder within 1 hour and no accumulation at the tumor site. However, this way of elimination is well-known for small organic molecules, and not favored for objects in the size range of micelles. On the contrary, polymersomes exhibit a signal during the first hour in the kidneys, followed during the next hours and days by a fluorescent signal in the liver and the spleen. Moreover, one mouse having a spontaneous tumor evidenced tumoral accumulation of the nanostructures. This final result evidences the proof of concept of polymersome capacity to accumulate in tumor by the EPR effect, which is promising for targeted release of drug allowing also to reduce the side effect of free anti-cancer drugs.

While Chapter II and Chapter III discussed the development of important parts of the theranostic platform, the last chapter IV opens ways of synthesis to incorporate Mn-complexes onto polymersomes, allowing to bring the bimodality to the theranostic platform on one side and, on the other side, to increase the relaxivity of the complexes by modifying the  $\tau_R$  parameter. The chosen synthetic route was based on copper-free click chemistry (SPAAC) reaction and consists in grafting an azide function on the Mn-complex arm, and a cyclooctyne (DBCO) group on the copolymer chain-end. Nevertheless, those syntheses still need to be improved and a proof of concept of the grafting onto the surface of the polymersomes has still to be brought.

This work opens the route to a lot of different perspectives. First of all, polymersomes made of PEO-*b*-P(CL-*co*-LA) copolymer have shown their interest in drug delivery and their possible accumulation in tumor area. Nevertheless, they still need some improvements. Foremost, the synthesis has to be better controlled. A solution is to use aluminium alkoxydes like  $\text{Ti}(\text{OiPr})_3$  which represents an interesting alternative as catalyst and initiator of the ROP of lactides and lactones.<sup>2</sup> Those last have recently been used at very low content (down to 0.1%) to prepare statistical P(LA-*co*-CL) copolymers with an important fraction of lactidyl units.<sup>3-5</sup> Moreover, the body is daily exposed to aluminium with quantities of approximately 30 mg per day.<sup>6</sup> Thus, the catalytic quantities of aluminium used in the synthesis should not bring any toxicity to the organism. Still, extensive washing steps of the copolymers will be necessary, but this route remains an interesting option for further work. After that, it could be interesting to increase the number of lactidyl units to ensure a high drug release capacity, whereas allowing the obtention of polymersomes, the drug release capacity and a low toxicity of the resulting nanostructure. Indeed, as a reminder, LA moieties have the capacity to be degraded faster than PCL moieties and to increase the degradation rate in the tumor microenvironment as the pH decreases with the production of lactic acid, but it could also generate issues in polymersomes formation. It could thus be interesting to determine the right proportions of LA moieties that allows the formation of polymersomes, increases the drug release kinetics, and finally does not exhibit toxicity *in vitro* and *in vivo*. Verifying all those requirements will allow to obtain an optimal nanosystem having the right properties for controlled drug delivery. These systems have also to be fitted with drug delivery laws to evidence if the adding of LA moieties impact the rate of delivery as expected. After that, *in vivo* experiments on mice bearing tumors have to be performed to evidence the capacity of polymersomes to accumulate in tumors by EPR effect, as well as the drug release and its capacity to decrease the tumor size. Finally, the bimodality advantage of the nanostructure has to be evaluated by, first, performing photoacoustic imaging (PAI) which could also be combined with MRI, and secondly, by grafting Mn-complexes onto the surface. Indeed ZW800-1 can also be used as contrast agent in PAI, which could be more interesting than optical imaging thanks to the higher penetration depth of the acoustic waves.

Concerning the Mn-complexes needed to visualize the nanoobjects by MRI, they could require further investigation and improvements. Indeed, *in vivo* experiments showed a probable decomplexation phenomenon. This decomplexation could occur by competition with zinc and copper ions also present in the body if the stability constants are compared (for  $\text{MnL}_1\text{H}$ ) and in view of our transmetalation tests in the presence of zinc ions.<sup>1</sup> To evidence this issue, it could

be interesting to use radiolabeled manganese ions which should allow to follow only the exogenous manganese ions and to track it in mice. Though, it could also be interesting to evaluate if the presence of an arm on the pyridine ring has an impact on the kinetic and on the thermodynamic stability constants of the system. To improve the kinetic inertness of  $Mn^{2+}$ -complexes, it could be interesting to replace the two acetate complexing groups by non-ionizable groups such as amides. In this case, the positive charge on the results cationic  $Mn^{2+}$ -complexes could be protective against acid-assisted dissociation, although grafting of neutral macromolecules might be necessary in that case to insure stealthness against adsorption of blood plasma proteins. Those modifications of the structure will have to be characterized by relaxometry to ensure that they do not impact the efficiency of the complexes as MRI contrast agents. On the other hand, another way of investigation could be to evidence the viscosity of kidney fluids to check if the contrast is brought only by the contrast agents or by a modification of the viscosity induced by the presence of the contrast agents. All of this will also have to be evaluated once the Mn-complexes will be grafted on the polymersome surface since the grafting could modify the stability of the complexes. Moreover, their efficacy as MRI contrast agents and the associated parameters  $\tau_M$ ,  $\tau_R$  and  $q$  should also be reevaluated to evidence the impact of the nanostructure. Another interesting way to fully evaluate the improvement, as demonstrated by Nazemi *et al.*, is the presence of dendritic structure which totally blocks the free rotation of the complexes, which allows to increase significantly their relaxivity.<sup>237</sup> The two systems (dendrimers *vs.* polymersomes) may be compared to evidence correctly the impact of these different types of structure on the (thumbling rate)  $\tau_R$  factor.

Finally, I would also like to give a critical aspect on this thesis that could bring issues in the future population, due to a continual increase of using PEG in a lot of different applications thanks to its biocompatible properties. Indeed, PEG is daily found in different formulations as (i) in cosmetics products : PEO plays a role of emulsifying and surfactant agent in a large panel of products<sup>248</sup>. (ii) drug formulations: it is often used as a coating to stabilize nanostructures, and to increase their half time circulation in blood thanks to a decrease of the opsonization.<sup>249,250</sup> (iii) daily used objects: due to its plasticizer properties, it is blended with other polymers to modify the plastic properties of different objects. Therefore, approximately 72% of people which never took pegylated drugs exhibit the presence of anti-PEG antibodies in their blood.<sup>43</sup>

At the end of the 20<sup>th</sup> century, Richter *et al.* evidenced the detection of anti-PEG antibodies in rabbits followed by their detection in man.<sup>251–253</sup> Therefore, some researchers tried to understand the development of these antibodies, their mechanism and the formation of allergic problems in human leading to an hypersensitivity to pegylated nanoparticles. Moreover, efforts are made to develop different assays allowing to obtain the rate of antibodies because no predetermined procedure already exist.<sup>254,255</sup> As example, a study using liposomes decorated with PEO moiety to decrease the immune response, has shown an accelerated blood clearance after the second injection due to the formation of anti-PEG antibodies. This phenomenon is however governed by the structure of the PEG and the used concentration.<sup>43</sup> Indeed, Liu *et al.* demonstrated, with a pegylated nano-emulsion, a decrease of the hepatic accumulation with an increase in the molecular weight of PEO, and a modification of the clearance speed after repeated injections.<sup>256</sup> A recent study of Senti *et al.* based on pegylated lipid tried to evidence the mechanism of complement activation triggered by anti-PEG antibody and its impact on the liposomes structure. They show that this way of activation can compromise the bilayer structure and induce a premature drug release.<sup>257</sup> All those results could thus compromise the treatments based on nanomedicine, while in 2019, already 19 treatments using PEG were approved by the FDA.<sup>255</sup>

A relevant example, which concerns all the society due to the covid-19 pandemic and could become a societal problem, is based on the small amount of PEG used in the mRNA vaccines to stabilize lipid nanoparticles. Two different research teams have studied the impact of the multiple dose injections on the proportion of Anti-PEG in human plasma. Ju *et al.* evidenced a non-negligible boosting effect on IgM and IgG (antibodies) in their cohort for the Moderna vaccine, whereas Guirriini *et al.* only found a boosting effect on IgM and no change for IgG (please note that their cohort can contain people who receive Pfizer or Moderna for their two first doses, with the same or the other one for their third dose). Moreover, some rare cases of allergic reactions were also reported due to the already present anti-PEG antibody. Due to the recent massive use of mRNA in the population, Ju *et al.* concluded that it will be important to study on the long term the impact of the vaccine on the rate of IgG and IgM.<sup>250,258</sup>

Different strategies can take place to avoid the formation of anti-PEG antibodies or to overcome it. One strategy consists in using a pre-treatment based on the injection of free high molecular weight PEG. McSweeney *et al.* evidenced a decrease in the immune response based on the hypothesis that free PEG is saturating the B cell receptors and increases the blood half time of the pegylated treatment.<sup>259</sup> To conclude, one can ask the following question which

seems very important for the future of nanomedicine (though not studied at all in the current thesis...):

Will the impressive stealth properties of PEG surpass the immune response of Humans?



## References

---

- (1) Garda, Z.; Molnár, E.; Hamon, N.; Barriada, J. L.; Esteban-Gómez, D.; Váradi, B.; Nagy, V.; Pota, K.; Kálmán, F. K.; Tóth, I.; Lihi, N.; Platas-Iglesias, C.; Tóth, É.; Tripier, R.; Tircsó, G. Complexation of Mn(II) by Rigid Pyclen Diacetates: Equilibrium, Kinetic, Relaxometric, Density Functional Theory, and Superoxide Dismutase Activity Studies. *Inorg. Chem.* **2021**, *60* (2), 1133–1148. <https://doi.org/10.1021/acs.inorgchem.0c03276>.
- (2) Ropson, N.; Dubois, Ph.; Jerome, R.; Teyssie, Ph. Macromolecular Engineering of Polylactones and Polylactides. 20. Effect of Monomer, Solvent, and Initiator on the Ring-Opening Polymerization As Initiated with Aluminum Alkoxides. *Macromolecules* **1995**, *28* (23), 7589–7598. <https://doi.org/10.1021/ma00127a002>.
- (3) Nomura, N.; Akita, A.; Ishii, R.; Mizuno, M. Random Copolymerization of  $\epsilon$ -Caprolactone with Lactide Using a Homosalen–Al Complex. *J. Am. Chem. Soc.* **2010**, *132* (6), 1750–1751. <https://doi.org/10.1021/ja9089395>.
- (4) Shi, T.; Luo, W.; Liu, S.; Li, Z. Controlled Random Copolymerization of *Rac*-Lactide and  $\epsilon$ -Caprolactone by Well-Designed Phenoxyimine Al Complexes. *J. Polym. Sci. Part Polym. Chem.* **2018**, *56* (6), 611–617. <https://doi.org/10.1002/pola.28932>.
- (5) Meimoun, J.; Sutapin, C.; Stoclet, G.; Favrelle, A.; Roussel, P.; Bria, M.; Chirachanchai, S.; Bonnet, F.; Zinck, P. Lactide Lactone Chain Shuttling Copolymerization Mediated by an Aminobisphenolate Supported Aluminum Complex and  $\text{Al}(\text{O}i\text{Pr})_3$ : Access to New Poly lactide Based Block Copolymers. *J. Am. Chem. Soc.* **2021**, *143* (50), 21206–21210. <https://doi.org/10.1021/jacs.1c09744>.
- (6) Exley, C. Human Exposure to Aluminium. *Env. Sci Process. Impacts* **2013**, *15* (10), 1807–1816. <https://doi.org/10.1039/C3EM00374D>.
- (7) Ferlay, J.; Colombet, M.; Soerjomataram, I.; Parkin, D. M.; Piñeros, M.; Znaor, A.; Bray, F. Cancer Statistics for the Year 2020: An Overview. *Int. J. Cancer* **2021**, *149* (4), 778–789. <https://doi.org/10.1002/ijc.33588>.
- (8) Pérez-Herrero, E.; Fernández-Medarde, A. Advanced Targeted Therapies in Cancer: Drug Nanocarriers, the Future of Chemotherapy. *Eur. J. Pharm. Biopharm.* **2015**, *93*, 52–79. <https://doi.org/10.1016/j.ejpb.2015.03.018>.

- (9) Lammers, T.; Subr, V.; Ulbrich, K.; Hennink, W. E.; Storm, G.; Kiessling, F. Polymeric Nanomedicines for Image-Guided Drug Delivery and Tumor-Targeted Combination Therapy. *Nano Today* **2010**, *5* (3), 197–212. <https://doi.org/10.1016/j.nantod.2010.05.001>.
- (10) Cryer, A. M.; Thorley, A. J. Nanotechnology in the Diagnosis and Treatment of Lung Cancer. *Pharmacol. Ther.* **2019**, *198*, 189–205. <https://doi.org/10.1016/j.pharmthera.2019.02.010>.
- (11) Woodman, C.; Vundu, G.; George, A.; Wilson, C. M. Applications and Strategies in Nanodiagnosis and Nanotherapy in Lung Cancer. *Semin. Cancer Biol.* **2021**, *69*, 349–364. <https://doi.org/10.1016/j.semcancer.2020.02.009>.
- (12) Hossen, S.; Hossain, M. K.; Basher, M. K.; Mia, M. N. H.; Rahman, M. T.; Uddin, M. J. Smart Nanocarrier-Based Drug Delivery Systems for Cancer Therapy and Toxicity Studies: A Review. *J. Adv. Res.* **2019**, *15*, 1–18. <https://doi.org/10.1016/j.jare.2018.06.005>.
- (13) Grodzinski, P.; Kircher, M.; Goldberg, M.; Gabizon, A. Integrating Nanotechnology into Cancer Care. *ACS Nano* **2019**, *13* (7), 7370–7376. <https://doi.org/10.1021/acsnano.9b04266>.
- (14) Stocke, N. A.; Meenach, S. A.; Arnold, S. M.; Mansour, H. M.; Hilt, J. Z. Formulation and Characterization of Inhalable Magnetic Nanocomposite Microparticles (MnMs) for Targeted Pulmonary Delivery via Spray Drying. *Int. J. Pharm.* **2015**, *479* (2), 320–328. <https://doi.org/10.1016/j.ijpharm.2014.12.050>.
- (15) Nishimoto, K.; Mimura, A.; Aoki, M.; Banura, N.; Murase, K. Application of Magnetic Particle Imaging to Pulmonary Imaging Using Nebulized Magnetic Nanoparticles. *Open J. Med. Imaging* **2015**, *5* (2), 49–55. <https://doi.org/10.4236/ojmi.2015.52008>.
- (16) Sadhukha, T.; Wiedmann, T. S.; Panyam, J. Inhalable Magnetic Nanoparticles for Targeted Hyperthermia in Lung Cancer Therapy. *Biomaterials* **2013**, *34* (21), 5163–5171. <https://doi.org/10.1016/j.biomaterials.2013.03.061>.
- (17) Sperling, R. A.; Gil, P. R.; Zhang, F.; Zanella, M.; Parak, W. J. Biological Applications of Gold Nanoparticles. *Chem. Soc. Rev.* **2008**, *37* (9), 1896–1908. <https://doi.org/10.1039/B712170A>.
- (18) Tiwari, P. M.; Vig, K.; Dennis, V. A.; Singh, S. R. Functionalized Gold Nanoparticles and Their Biomedical Applications. *Nanomaterials* **2011**, *1* (1), 31–63.

<https://doi.org/10.3390/nano1010031>.

(19) Qian, X.; Peng, X.-H.; Ansari, D. O.; Yin-Goen, Q.; Chen, G. Z.; Shin, D. M.; Yang, L.; Young, A. N.; Wang, M. D.; Nie, S. In Vivo Tumor Targeting and Spectroscopic Detection with Surface-Enhanced Raman Nanoparticle Tags. *Nat. Biotechnol.* **2008**, *26* (1), 83–90. <https://doi.org/10.1038/nbt1377>.

(20) Guo, J.; Rahme, K.; He, Y.; Li, L.-L.; Holmes, J. D.; O’Driscoll, C. M. Gold Nanoparticles Enlighten the Future of Cancer Theranostics. *Int. J. Nanomedicine* **2017**, *12*, 6131–6152. <https://doi.org/10.2147/IJN.S140772>.

(21) Badrzadeh, F.; Rahmati-Yamchi, M.; Badrzadeh, K.; Valizadeh, A.; Zarghami, N.; Farkhani, S. M.; Akbarzadeh, A. Drug Delivery and Nanodetection in Lung Cancer. *Artif. Cells Nanomedicine Biotechnol.* **2016**, *44* (2), 618–634. <https://doi.org/10.3109/21691401.2014.975237>.

(22) Hardman, R. A Toxicologic Review of Quantum Dots: Toxicity Depends on Physicochemical and Environmental Factors. *Environ. Health Perspect.* **2006**, *114* (2), 165–172. <https://doi.org/10.1289/ehp.8284>.

(23) He, X.; Ma, N. An Overview of Recent Advances in Quantum Dots for Biomedical Applications. *Colloids Surf. B Biointerfaces* **2014**, *124*, 118–131. <https://doi.org/10.1016/j.colsurfb.2014.06.002>.

(24) Jin, S.; Hu, Y.; Gu, Z.; Liu, L.; Wu, H.-C. Application of Quantum Dots in Biological Imaging. *J. Nanomater.* **2011**, *2011*, e834139. <https://doi.org/10.1155/2011/834139>.

(25) She, W.; Pan, D.; Luo, K.; He, B.; Cheng, G.; Zhang, C.; Gu, Z. PEGylated Dendrimer-Doxorubicin Conjugates as pH-Sensitive Drug Delivery Systems: Synthesis and In Vitro Characterization. *J. Biomed. Nanotechnol.* **2015**, *11* (6), 964–978. <https://doi.org/10.1166/jbn.2015.1865>.

(26) Kaminskas, L. M.; McLeod, V. M.; Porter, C. J. H.; Boyd, B. J. *Association of Chemotherapeutic Drugs with Dendrimer Nanocarriers: An Assessment of the Merits of Covalent Conjugation Compared to Noncovalent Encapsulation*. ACS Publications. <https://doi.org/10.1021/mp2005966>.

(27) Lin, C.; Wong, B. C. K.; Chen, H.; Bian, Z.; Zhang, G.; Zhang, X.; Kashif Riaz, M.; Tyagi, D.; Lin, G.; Zhang, Y.; Wang, J.; Lu, A.; Yang, Z. Pulmonary Delivery of Triptolide-

Loaded Liposomes Decorated with Anti-Carbonic Anhydrase IX Antibody for Lung Cancer Therapy. *Sci. Rep.* **2017**, 7 (1), 1097. <https://doi.org/10.1038/s41598-017-00957-4>.

(28) Ahmed, K. S.; Hussein, S. A.; Ali, A. H.; Korma, S. A.; Lipeng, Q.; Jinghua, C. Liposome: Composition, Characterisation, Preparation, and Recent Innovation in Clinical Applications. *J. Drug Target.* **2019**, 27 (7), 742–761. <https://doi.org/10.1080/1061186X.2018.1527337>.

(29) Jabłczyńska, K.; Janczewska, M.; Kulikowska, A.; Sosnowski, T. R. Preparation and Characterization of Biocompatible Polymer Particles as Potential Nanocarriers for Inhalation Therapy. *Int. J. Polym. Sci.* **2015**, 2015, e763020. <https://doi.org/10.1155/2015/763020>.

(30) Liang, Z.; Ni, R.; Zhou, J.; Mao, S. Recent Advances in Controlled Pulmonary Drug Delivery. *Drug Discov. Today* **2015**, 20 (3), 380–389. <https://doi.org/10.1016/j.drudis.2014.09.020>.

(31) Anderson, C. F.; Grimmitt, M. E.; Domalewski, C. J.; Cui, H. Inhalable Nanotherapeutics to Improve Treatment Efficacy for Common Lung Diseases. *WIREs Nanomedicine Nanobiotechnology* **2020**, 12 (1). <https://doi.org/10.1002/wnan.1586>.

(32) Mottaghitalab, F.; Farokhi, M.; Fatahi, Y.; Atyabi, F.; Dinarvand, R. New Insights into Designing Hybrid Nanoparticles for Lung Cancer: Diagnosis and Treatment. *J. Controlled Release* **2019**, 295, 250–267. <https://doi.org/10.1016/j.jconrel.2019.01.009>.

(33) Madni, A.; Batool, A.; Noreen, S.; Maqbool, I.; Rehman, F.; Kashif, P. M.; Tahir, N.; Raza, A. Novel Nanoparticulate Systems for Lung Cancer Therapy: An Updated Review. *J. Drug Target.* **2017**, 25 (6), 499–512. <https://doi.org/10.1080/1061186X.2017.1289540>.

(34) Kita-Tokarczyk, K.; Grumelard, J.; Haeefe, T.; Meier, W. Block Copolymer Vesicles—Using Concepts from Polymer Chemistry to Mimic Biomembranes. *Polymer* **2005**, 46 (11), 3540–3563. <https://doi.org/10.1016/j.polymer.2005.02.083>.

(35) Lee, J. C.; Bermudez, H.; Discher, B. M.; Sheehan, M. A.; Won, Y. Y.; Bates, F. S.; Discher, D. E. Preparation, Stability, and in Vitro Performance of Vesicles Made with Diblock Copolymers. *Biotechnol. Bioeng.* **2001**, 73 (2), 135–145. <https://doi.org/10.1002/bit.1045>.

(36) Rideau, E.; Dimova, R.; Schwille, P.; Wurm, F. R.; Landfester, K. Liposomes and Polymersomes: A Comparative Review towards Cell Mimicking. *Chem. Soc. Rev.* **2018**, 47 (23), 8572–8610. <https://doi.org/10.1039/c8cs00162f>.

- (37) Mansour, H. M.; Rhee, Y.-S.; Wu, X. Nanomedicine in Pulmonary Delivery. *Int. J. Nanomedicine* **2009**, *4*, 299–319. <https://doi.org/10.2147/ijn.s4937>.
- (38) Pappalardo, D.; Mathisen, T.; Finne-Wistrand, A. Biocompatibility of Resorbable Polymers: A Historical Perspective and Framework for the Future. *Biomacromolecules* **2019**, *20* (4), 1465–1477. <https://doi.org/10.1021/acs.biomac.9b00159>.
- (39) Mangal, S.; Gao, W.; Li, T.; Zhou, Q. (Tony). Pulmonary Delivery of Nanoparticle Chemotherapy for the Treatment of Lung Cancers: Challenges and Opportunities. *Acta Pharmacol. Sin.* **2017**, *38* (6), 782–797. <https://doi.org/10.1038/aps.2017.34>.
- (40) Tran, S.; DeGiovanni, P.; Piel, B.; Rai, P. Cancer Nanomedicine: A Review of Recent Success in Drug Delivery. *Clin. Transl. Med.* **2017**, *6* (1). <https://doi.org/10.1186/s40169-017-0175-0>.
- (41) Martinez, J. O.; Brown, B. S.; Quattrocchi, N.; Evangelopoulos, M.; Ferrari, M.; Tasciotti, E. Multifunctional to Multistage Delivery Systems: The Evolution of Nanoparticles for Biomedical Applications. *Chin. Sci. Bull.* **2012**, *57* (31), 3961–3971. <https://doi.org/10.1007/s11434-012-5387-5>.
- (42) Rehman, N.; Pandey, A. *Engineered Nanoparticles as Drug Delivery Systems*, 1st ed.; CRC Press: Boca Raton, 2022. <https://doi.org/10.1201/9781003252122>.
- (43) Cao, Y.; Dong, X.; Chen, X. Polymer-Modified Liposomes for Drug Delivery: From Fundamentals to Applications. *Pharmaceutics* **2022**, *14* (4), 778. <https://doi.org/10.3390/pharmaceutics14040778>.
- (44) From “Banghasomes” to Liposomes: A Memoir of Alec Bangham, 1921–2010. <https://doi.org/10.1096/fj.10-0503>.
- (45) Lefley, J.; Waldron, C.; Remzi Becer, C. Macromolecular Design and Preparation of Polymersomes. *Polym. Chem.* **2020**, *11* (45), 7124–7136. <https://doi.org/10.1039/D0PY01247E>.
- (46) Hasannia, M.; Aliabadi, A.; Abnous, K.; Taghdisi, S. M.; Ramezani, M.; Alibolandi, M. Synthesis of Block Copolymers Used in Polymersome Fabrication: Application in Drug Delivery. *J. Controlled Release* **2022**, *341*, 95–117. <https://doi.org/10.1016/j.jconrel.2021.11.010>.
- (47) Nuyken, O.; Pask, S. D. Ring-Opening Polymerization—An Introductory Review.

*Polymers* **2013**, 5 (2), 361–403. <https://doi.org/10.3390/polym5020361>.

(48) Lee, J. S.; Feijen, J. Polymersomes for Drug Delivery: Design, Formation and Characterization. *J. Controlled Release* **2012**, 161 (2), 473–483. <https://doi.org/10.1016/j.jconrel.2011.10.005>.

(49) Raval, N.; Maheshwari, R.; Shukla, H.; Kalia, K.; Torchilin, V. P.; Tekade, R. K. Multifunctional Polymeric Micellar Nanomedicine in the Diagnosis and Treatment of Cancer. *Mater. Sci. Eng. C* **2021**, 126, 112186. <https://doi.org/10.1016/j.msec.2021.112186>.

(50) Bleul, R.; Thiermann, R.; Maskos, M. Techniques To Control Polymersome Size. *Macromolecules* **2015**, 48 (20), 7396–7409. <https://doi.org/10.1021/acs.macromol.5b01500>.

(51) Mai, Y.; Eisenberg, A. Self-Assembly of Block Copolymers. *Chem. Soc. Rev.* **2012**, 41 (18), 5969. <https://doi.org/10.1039/c2cs35115c>.

(52) Choucair, A.; Eisenberg, A. Control of Amphiphilic Block Copolymer Morphologies Using Solution Conditions. *Eur. Phys. J. E* **2003**, 10 (1), 37–44. <https://doi.org/10.1140/epje/e2003-00002-5>.

(53) Zhou, Q.; Zhang, L.; Yang, T.; Wu, H. Stimuli-Responsive Polymeric Micelles for Drug Delivery and Cancer Therapy. *Int. J. Nanomedicine* **2018**, 13, 2921–2942. <https://doi.org/10.2147/IJN.S158696>.

(54) García, M. C. Stimuli-Responsive Polymersomes for Drug Delivery Applications. In *Stimuli Responsive Polymeric Nanocarriers for Drug Delivery Applications*; Elsevier, 2019; pp 345–392. <https://doi.org/10.1016/B978-0-08-101995-5.00019-2>.

(55) Ahmed, F.; Pakunlu, R. I.; Brannan, A.; Bates, F.; Minko, T.; Discher, D. E. Biodegradable Polymersomes Loaded with Both Paclitaxel and Doxorubicin Permeate and Shrink Tumors, Inducing Apoptosis in Proportion to Accumulated Drug. *J. Controlled Release* **2006**, 116 (2), 150–158. <https://doi.org/10.1016/j.jconrel.2006.07.012>.

(56) Zou, Y.; Meng, F.; Deng, C.; Zhong, Z. Robust, Tumor-Homing and Redox-Sensitive Polymersomal Doxorubicin: A Superior Alternative to Doxil and Caelyx? *J. Controlled Release* **2016**, 239, 149–158. <https://doi.org/10.1016/j.jconrel.2016.08.022>.

(57) Barve, A.; Jain, A.; Liu, H.; Zhao, Z.; Cheng, K. Enzyme-Responsive Polymeric Micelles of Cabazitaxel for Prostate Cancer Targeted Therapy. *Acta Biomater.* **2020**, 113, 501–511. <https://doi.org/10.1016/j.actbio.2020.06.019>.

- (58) Khaledian, M.; Nourbakhsh, M. S.; Saber, R.; Hashemzadeh, H.; Darvishi, M. H. Preparation and Evaluation of Doxorubicin-Loaded PLA–PEG–FA Copolymer Containing Superparamagnetic Iron Oxide Nanoparticles (SPIONs) for Cancer Treatment: Combination Therapy with Hyperthermia and Chemotherapy. *Int. J. Nanomedicine* **2020**, *15*, 6167–6182. <https://doi.org/10.2147/IJN.S261638>.
- (59) Hernández Becerra, E.; Quinchia, J.; Castro, C.; Orozco, J. Light-Triggered Polymersome-Based Anticancer Therapeutics Delivery. *Nanomaterials* **2022**, *12* (5), 836. <https://doi.org/10.3390/nano12050836>.
- (60) Saravanakumar, G.; Park, H.; Kim, J.; Park, D.; Lim, J.; Lee, J.; Kim, W. J. Polymersomes with Singlet Oxygen-Labile Poly( $\beta$ -Aminoacrylate) Membrane for NIR Light-Controlled Combined Chemo-Phototherapy. *J. Controlled Release* **2020**, *327*, 627–640. <https://doi.org/10.1016/j.jconrel.2020.09.010>.
- (61) Leong, J.; Teo, J. Y.; Aakalu, V. K.; Yang, Y. Y.; Kong, H. Engineering Polymersomes for Diagnostics and Therapy. *Adv. Healthc. Mater.* **2018**, *7* (8), 1–27. <https://doi.org/10.1002/adhm.201701276>.
- (62) Rijpkema, S. J.; Toebes, B. J.; Maas, M. N.; Kler, N. R. M.; Wilson, D. A. Designing Molecular Building Blocks for Functional Polymersomes. *Isr. J. Chem.* **2019**, *59* (10), 928–944. <https://doi.org/10.1002/ijch.201900039>.
- (63) Miller, A. J.; Pearce, A. K.; Foster, J. C.; O'Reilly, R. K. Probing and Tuning the Permeability of Polymersomes. *ACS Cent. Sci.* **2021**, *7* (1), 30–38. <https://doi.org/10.1021/acscentsci.0c01196>.
- (64) Trucillo, P. Drug Carriers: A Review on the Most Used Mathematical Models for Drug Release. *Processes* **2022**, *10* (6), 1094. <https://doi.org/10.3390/pr10061094>.
- (65) Xu, J.; Gattacceca, F.; Amiji, M. Biodistribution and Pharmacokinetics of EGFR-Targeted Thiolated Gelatin Nanoparticles Following Systemic Administration in Pancreatic Tumor-Bearing Mice. *Mol. Pharm.* **2013**, *10* (5), 2031–2044. <https://doi.org/10.1021/mp400054e>.
- (66) Behl, A.; Parmar, V. S.; Malhotra, S.; Chhillar, A. K. Biodegradable Diblock Copolymeric PEG-PCL Nanoparticles: Synthesis, Characterization and Applications as Anticancer Drug Delivery Agents. *Polymer* **2020**, *207*, 122901. <https://doi.org/10.1016/j.polymer.2020.122901>.

- (67) Siepmann, J.; Siepmann, F. Modeling of Diffusion Controlled Drug Delivery. *J. Controlled Release* **2012**, *161* (2), 351–362. <https://doi.org/10.1016/j.jconrel.2011.10.006>.
- (68) Brandt, J. V.; Piazza, R. D.; dos Santos, C. C.; Vega-Chacón, J.; Amantéa, B. E.; Pinto, G. C.; Magnani, M.; Piva, H. L.; Tedesco, A. C.; Primo, F. L.; Jafelicci, M.; Marques, R. F. C. Synthesis and Colloidal Characterization of Folic Acid-Modified PEG-b-PCL Micelles for Methotrexate Delivery. *Colloids Surf. B Biointerfaces* **2019**, *177*, 228–234. <https://doi.org/10.1016/j.colsurfb.2019.02.008>.
- (69) “polymeric nanostructures cancer” Reference Search | CAS SciFinder<sup>®</sup>. <https://scifinder-n.cas.org/search/reference/64243ecee06a8c1bbef02777/1> (accessed 2023-03-29).
- (70) da Silva, D.; Kaduri, M.; Poley, M.; Adir, O.; Krinsky, N.; Shainsky-Roitman, J.; Schroeder, A. Biocompatibility, Biodegradation and Excretion of Polylactic Acid (PLA) in Medical Implants and Theranostic Systems. *Chem. Eng. J.* **2018**, *340*, 9–14. <https://doi.org/10.1016/j.cej.2018.01.010>.
- (71) Shen, A. M.; Minko, T. Pharmacokinetics of Inhaled Nanotherapeutics for Pulmonary Delivery. *J. Controlled Release* **2020**, *326*, 222–244. <https://doi.org/10.1016/j.jconrel.2020.07.011>.
- (72) Blanco, E.; Kessinger, C. W.; Sumer, B. D.; Gao, J. Multifunctional Micellar Nanomedicine for Cancer Therapy. *Exp. Biol. Med.* **2009**, *234* (2), 123–131. <https://doi.org/10.3181/0808-MR-250>.
- (73) Deshmukh, A. S.; Chauhan, P. N.; Noolvi, M. N.; Chaturvedi, K.; Ganguly, K.; Shukla, S. S.; Nadagouda, M. N.; Aminabhavi, T. M. Polymeric Micelles: Basic Research to Clinical Practice. *Int. J. Pharm.* **2017**, *532* (1), 249–268. <https://doi.org/10.1016/j.ijpharm.2017.09.005>.
- (74) Dariva, C. G.; Figueiredo, J. P. H.; Ferreira, C.; Laranjo, M.; Botelho, M. F.; Fonseca, A. C.; Coelho, J. F. J.; Serra, A. C. Development of Red-Light Cleavable PEG-PLA Nanoparticles as Delivery Systems for Cancer Therapy. *Colloids Surf. B Biointerfaces* **2020**, *196*, 111354. <https://doi.org/10.1016/j.colsurfb.2020.111354>.
- (75) Hu, Y.; He, Y.; Ji, J.; Zheng, S.; Cheng, Y. Tumor Targeted Curcumin Delivery by Folate-Modified MPEG-PCL Self-Assembly Micelles for Colorectal Cancer Therapy. *Int. J. Nanomedicine* **2020**, *15*, 1239–1252. <https://doi.org/10.2147/IJN.S232777>.

- (76) Thioune, O.; Fessi, H.; Devissaguet, J. P.; Puisieux, F. Preparation of Pseudolatex by Nanoprecipitation: Influence of the Solvent Nature on Intrinsic Viscosity and Interaction Constant. *Int. J. Pharm.* **1997**, *146* (2), 233–238. [https://doi.org/10.1016/S0378-5173\(96\)04830-2](https://doi.org/10.1016/S0378-5173(96)04830-2).
- (77) Mohammadi, M.; Ramezani, M.; Abnous, K.; Alibolandi, M. Biocompatible Polymersomes-Based Cancer Theranostics: Towards Multifunctional Nanomedicine. *Int. J. Pharm.* **2017**, *519* (1–2), 287–303. <https://doi.org/10.1016/j.ijpharm.2017.01.037>.
- (78) Adams, D. J.; Kitchen, C.; Adams, S.; Furzeland, S.; Atkins, D.; Schuetz, P.; Fernyhough, C. M.; Tzokova, N.; Ryan, A. J.; Butler, M. F. On the Mechanism of Formation of Vesicles from Poly(Ethylene Oxide)-Block-Poly(Caprolactone) Copolymers. *Soft Matter* **2009**, *5* (16), 3086–3096. <https://doi.org/10.1039/b907628j>.
- (79) Martínez Rivas, C. J.; Tarhini, M.; Badri, W.; Miladi, K.; Greige-Gerges, H.; Nazari, Q. A.; Galindo Rodríguez, S. A.; Román, R. Á.; Fessi, H.; Elaissari, A. Nanoprecipitation Process: From Encapsulation to Drug Delivery. *Int. J. Pharm.* **2017**, *532* (1), 66–81. <https://doi.org/10.1016/j.ijpharm.2017.08.064>.
- (80) Ianiro, A.; Wu, H.; van Rijt, M. M. J.; Vena, M. P.; Keizer, A. D. A.; Esteves, A. C. C.; Tuinier, R.; Friedrich, H.; Sommerdijk, N. A. J. M.; Patterson, J. P. Liquid–Liquid Phase Separation during Amphiphilic Self-Assembly. *Nat. Chem.* **2019**, *11* (4), 320–328. <https://doi.org/10.1038/s41557-019-0210-4>.
- (81) Sui, X.; Kujala, P.; Janssen, G.-J.; Jong, E. de; Zuhorn, I. S.; Hest, J. C. M. van. Robust Formation of Biodegradable Polymersomes by Direct Hydration. *Polym. Chem.* **2015**, *6* (5), 691–696. <https://doi.org/10.1039/C4PY01288G>.
- (82) Blanazs, A.; Ryan, A. J.; Armes, S. P. Predictive Phase Diagrams for RAFT Aqueous Dispersion Polymerization: Effect of Block Copolymer Composition, Molecular Weight, and Copolymer Concentration. *Macromolecules* **2012**, *45* (12), 5099–5107. <https://doi.org/10.1021/ma301059r>.
- (83) Cornel, E. J.; Jiang, J.; Chen, S.; Du, J. Principles and Characteristics of Polymerization-Induced Self-Assembly with Various Polymerization Techniques. *CCS Chem.* **2020**, *3* (4), 2104–2125. <https://doi.org/10.31635/ccschem.020.202000470>.
- (84) Seo, H.; Lee, H. Recent Developments in Microfluidic Synthesis of Artificial Cell-like Polymersomes and Liposomes for Functional Bioreactors. *Biomicrofluidics* **2021**, *15* (2),

021301. <https://doi.org/10.1063/5.0048441>.

(85) Lebleu, C.; Rodrigues, L.; Guigner, J.-M.; Brûlet, A.; Garanger, E.; Lecommandoux, S. Self-Assembly of PEG-b-PTMC Copolymers: Micelles and Polymersomes Size Control. *Langmuir* **2019**, *35* (41), 13364–13374. <https://doi.org/10.1021/acs.langmuir.9b02264>.

(86) Capretto, L.; Carugo, D.; Mazzitelli, S.; Nastruzzi, C.; Zhang, X. Microfluidic and Lab-on-a-Chip Preparation Routes for Organic Nanoparticles and Vesicular Systems for Nanomedicine Applications. *Adv. Drug Deliv. Rev.* **2013**, *65* (11), 1496–1532. <https://doi.org/10.1016/j.addr.2013.08.002>.

(87) Indoria, S.; Singh, V.; Hsieh, M.-F. Recent Advances in Theranostic Polymeric Nanoparticles for Cancer Treatment: A Review. *Int. J. Pharm.* **2020**, *582*, 119314. <https://doi.org/10.1016/j.ijpharm.2020.119314>.

(88) Hosseini, S. M.; Mohammadnejad, J.; Salamat, S.; Beiram Zadeh, Z.; Tanhaei, M.; Ramakrishna, S. Theranostic Polymeric Nanoparticles as a New Approach in Cancer Therapy and Diagnosis: A Review. *Mater. Today Chem.* **2023**, *29*, 101400. <https://doi.org/10.1016/j.mtchem.2023.101400>.

(89) Roth, C. G.; Deshmukh, S. *Fundamentals of Body MRI E-Book*, 2nd Edition.; Elsevier Health Sciences, 2016.

(90) Hazelton, J. M.; Chiu, M. K.; Abujudeh, H. H. Nephrogenic Systemic Fibrosis: A Review of History, Pathophysiology, and Current Guidelines. *Curr. Radiol. Rep.* **2019**, *7* (2), 5. <https://doi.org/10.1007/s40134-019-0312-1>.

(91) Malikova, H. Nephrogenic Systemic Fibrosis: The End of the Story? *Quant. Imaging Med. Surg.* **2019**, *9* (8), 1470–1474. <https://doi.org/10.21037/qims.2019.07.11>.

(92) Minton, L. E.; Pandit, R.; Porter, K. K. Contrast-Enhanced MRI: History and Current Recommendations. *Appl. Radiol.* **2021**, 15–19. <https://doi.org/10.37549/AR2776>.

(93) Vangijzegem, T.; Stanicki, D.; Panepinto, A.; Socoliuc, V.; Vekas, L.; Muller, R. N.; Laurent, S. Influence of Experimental Parameters of a Continuous Flow Process on the Properties of Very Small Iron Oxide Nanoparticles (VSION) Designed for T1-Weighted Magnetic Resonance Imaging (MRI). *Nanomaterials* **2020**, *10* (4), 757. <https://doi.org/10.3390/nano10040757>.

(94) Robic, C.; Port, M.; Rousseaux, O.; Louguet, S.; Fretellier, N.; Catoen, S.; Factor, C.;

Le Greneur, S.; Medina, C.; Bourrinet, P.; Raynal, I.; Idée, J. M.; Corot, C. Physicochemical and Pharmacokinetic Profiles of Gadopiclesol: A New Macrocyclic Gadolinium Chelate With High T1 Relaxivity. *Invest. Radiol.* **2019**, *54* (8), 475–484. <https://doi.org/10.1097/RLI.0000000000000563>.

(95) Overman, D. FDA Approves Elucirem (Gadopiclesol) Injection for Use in Contrast-Enhanced MRI. *AXIS Imaging News Overl. Park Anthem Media Group* **2022**.

(96) Murray, K. Guerbet Releases First Production Batch of Elucirem Injection. *AXIS Imaging News Overl. Park Anthem Media Group* **2023**.

(97) Le Fur, M.; Caravan, P. The Biological Fate of Gadolinium-Based MRI Contrast Agents: A Call to Action for Bioinorganic Chemists. *Met. Integr. Biometal Sci.* **2019**, *11* (2), 240–254. <https://doi.org/10.1039/c8mt00302e>.

(98) Strzeminska, I.; Factor, C.; Robert, P.; Grindel, A.-L.; Comby, P.-O.; Szpunar, J.; Corot, C.; Lobinski, R. Long-Term Evaluation of Gadolinium Retention in Rat Brain After Single Injection of a Clinically Relevant Dose of Gadolinium-Based Contrast Agents: *Invest. Radiol.* **2020**, *55* (3), 138–143. <https://doi.org/10.1097/RLI.0000000000000623>.

(99) Babaei, M.; Abnous, K.; Nekooei, S.; Mohammad Taghdisi, S.; Amel Farzad, S.; Ramezani, M.; Alibolandi, M. Synthesis of Manganese-Incorporated Polycapactone-Poly (Glyceryl Methacrylate) Theranostic Smart Hybrid Polymersomes for Efficient Colon Adenocarcinoma Treatment. *Int. J. Pharm.* **2022**, *623*, 121963. <https://doi.org/10.1016/j.ijpharm.2022.121963>.

(100) Xie, X.; Chen, Y.; Chen, Z.; Feng, Y.; Wang, J.; Li, T.; Li, S.; Qin, X.; Wu, C.; Zheng, C.; Zhu, J.; You, F.; Liu, Y.; Yang, H. Polymeric Hybrid Nanomicelles for Cancer Theranostics: An Efficient and Precise Anticancer Strategy for the Codelivery of Doxorubicin/MiR-34a and Magnetic Resonance Imaging. *ACS Appl. Mater. Interfaces* **2019**, *11* (47), 43865–43878. <https://doi.org/10.1021/acsami.9b14908>.

(101) Liu, D.; Zhou, Z.; Wang, X.; Deng, H.; Sun, L.; Lin, H.; Kang, F.; Zhang, Y.; Wang, Z.; Yang, W.; Rao, L.; Yang, K.; Yu, G.; Du, J.; Shen, Z.; Chen, X. Yolk-Shell Nanovesicles Endow Glutathione-Responsive Concurrent Drug Release and T1 MRI Activation for Cancer Theranostics. *Biomaterials* **2020**, *244*, 119979. <https://doi.org/10.1016/j.biomaterials.2020.119979>.

(102) Liu, Q.; Song, L.; Chen, S.; Gao, J.; Zhao, P.; Du, J. A Superparamagnetic Polymersome

with Extremely High T<sub>2</sub> Relaxivity for MRI and Cancer-Targeted Drug Delivery. *Biomaterials* **2017**, *114*, 23–33. <https://doi.org/10.1016/j.biomaterials.2016.10.027>.

(103) Zavvar, T. S.; Babaei, M.; Abnous, K.; Taghdisi, S. M.; Nekooei, S.; Ramezani, M.; Alibolandi, M. Synthesis of Multimodal Polymersomes for Targeted Drug Delivery and MR/Fluorescence Imaging in Metastatic Breast Cancer Model. *Int. J. Pharm.* **2020**, *578* (January), 119091. <https://doi.org/10.1016/j.ijpharm.2020.119091>.

(104) Weber, J.; Beard, P. C.; Bohndiek, S. E. Contrast Agents for Molecular Photoacoustic Imaging. *Nat. Methods* **2016**, *13* (8), 639–650. <https://doi.org/10.1038/nmeth.3929>.

(105) Li, S.; Lui, K.-H.; Li, X.; Fang, X.; Lo, W.-S.; Gu, Y.-J.; Wong, W.-T. PH-Triggered Poly(Ethylene Glycol)–Poly(Lactic Acid/Glycolic Acid)/Croconaine Nanoparticles-Assisted Multiplexed Photoacoustic Imaging and Enhanced Photothermal Cancer Therapy. *ACS Appl. Bio Mater.* **2021**, *4* (5), 4152–4164. <https://doi.org/10.1021/acsabm.0c01578>.

(106) Yang, Z.; Cheng, R.; Zhao, C.; Sun, N.; Luo, H.; Chen, Y.; Liu, Z.; Li, X.; Liu, J.; Tian, Z. Thermo- and PH-Dual Responsive Polymeric Micelles with Upper Critical Solution Temperature Behavior for Photoacoustic Imaging-Guided Synergistic Chemo-Photothermal Therapy against Subcutaneous and Metastatic Breast Tumors. *Theranostics* **2018**, *8* (15), 4097–4115. <https://doi.org/10.7150/thno.26195>.

(107) Webb, A. *Introduction to Biomedical Imaging*; John Wiley & Sons, 2022.

(108) Zou, Y.; Wei, Y.; Sun, Y.; Bao, J.; Yao, F.; Li, Z.; Meng, F.; Hu, C.; Storm, G.; Zhong, Z. Cyclic RGD-Functionalized and Disulfide-Crosslinked Iodine-Rich Polymersomes as a Robust and Smart Theranostic Agent for Targeted CT Imaging and Chemotherapy of Tumor. *Theranostics* **2019**, *9* (26), 8061–8072. <https://doi.org/10.7150/thno.37184>.

(109) Cao, J.; Wei, Y.; Zhang, Y.; Wang, G.; Ji, X.; Zhong, Z. Iodine-Rich Polymersomes Enable Versatile SPECT/CT Imaging and Potent Radioisotope Therapy for Tumor in Vivo. *ACS Appl. Mater. Interfaces* **2019**. <https://doi.org/10.1021/acsami.9b04294>.

(110) Yang, X.; An, J.; Luo, Z.; Yang, R.; Yan, S.; Liu, D.-E.; Fu, H.; Gao, H. A Cyanine-Based Polymeric Nanoplatfrom with Microenvironment-Driven Cascaded Responsiveness for Imaging-Guided Chemo-Photothermal Combination Anticancer Therapy. *J. Mater. Chem. B* **2020**, *8* (10), 2115–2122. <https://doi.org/10.1039/C9TB02890K>.

(111) Yang, Y.; Kozlovskaya, V.; Zhang, Z.; Xing, C.; Zaharias, S.; Dolmat, M.; Qian, S.;

- Zhang, J.; Warram, J. M.; Yang, E. S.; Kharlampieva, E. Poly(N-Vinylpyrrolidone)-Block-Poly(Dimethylsiloxane)-Block-Poly(N-Vinylpyrrolidone) Triblock Copolymer Polymersomes for Delivery of PARP1 siRNA to Breast Cancers. *ACS Appl. Bio Mater.* **2022**, *5* (4), 1670–1682. <https://doi.org/10.1021/acsabm.2c00063>.
- (112) Yang, W.; Noh, J.; Park, H.; Gwon, S.; Singh, B.; Song, C.; Lee, D. Near Infrared Dye-Conjugated Oxidative Stress Amplifying Polymer Micelles for Dual Imaging and Synergistic Anticancer Phototherapy. *Biomaterials* **2018**, *154*, 48–59. <https://doi.org/10.1016/j.biomaterials.2017.10.043>.
- (113) Moulahoum, Hichem; Ghorbanizamani, Faezeh; Bayir, Ece; Timur, Suna; Zihnioglu, Figen. A Polyplex Human Saliva Peptide Histatin 5-Grafted Methoxy PEG-b-Polycaprolactone Polymersome for Intelligent Stimuli-Oriented Doxorubicin Delivery. *J. Drug Deliv. Sci. Technol.* **2022**, *67*, 102958. <https://doi.org/10.1016/j.jddst.2021.102958>.
- (114) Han, S. H. Review of Photoacoustic Imaging for Imaging-Guided Spinal Surgery. *Neurospine* **2018**, *15* (4), 306–322. <https://doi.org/10.14245/ns.1836206.103>.
- (115) *Molecular Imaging*; Semmler, W., Schwaiger, M., Eds.; Handbook of experimental pharmacology; Springer: Berlin, 2008.
- (116) Huda, W.; Abrahams, R. B. X-Ray-Based Medical Imaging and Resolution. *Am. J. Roentgenol.* **2015**, *204* (4), W393–W397. <https://doi.org/10.2214/AJR.14.13126>.
- (117) Washner, J.; Gale, E. M.; Rodrigez-Rodriguez, A.; Caravan, P. Chemistry of MRI Contrast Agents: Current Challenges and New Frontiers. *Chem. Rev.* **2019**, *119* (2), 957–1057. <https://doi.org/10.1021/acs.chemrev.8b00363>.
- (118) Grobner, T.; Prischl, F. C. Gadolinium and Nephrogenic Systemic Fibrosis. *Kidney Int.* **2007**, *72* (3), 260–264. <https://doi.org/10.1038/sj.ki.5002338>.
- (119) Beam, A. S.; Moore, K. G.; Gillis, S. N.; Ford, K. F.; Gray, T.; Steinwinder, A. H.; Graham, A. GBCAs and Risk for Nephrogenic Systemic Fibrosis: A Literature Review. *Radiol. Technol.* **2017**, *88* (6), 583–589.
- (120) Pan, D.; Schmieder, A. H.; Wickline, S. A.; Lanza, G. M. Manganese-Based MRI Contrast Agents: Past, Present and Future. *Tetrahedron* **2011**, *67* (44), 8431–8444. <https://doi.org/10.1016/j.tet.2011.07.076.Manganese-based>.
- (121) Botta, M.; Carniato, F.; Esteban-Gómez, D.; Platas-Iglesias, C.; Tei, L. Mn(II)

Compounds as an Alternative to Gd-Based MRI Probes. *Future Med. Chem.* **2019**, *11* (12), 1461–1483. <https://doi.org/10.4155/fmc-2018-0608>.

(122) Ramalho, J.; Semelka, R. C.; Ramalho, M.; Nunes, R. H.; AlObaidy, M.; Castillo, M. Gadolinium-Based Contrast Agent Accumulation and Toxicity: An Update. *Am. J. Neuroradiol.* **2016**, *37* (7), 1192–1198. <https://doi.org/10.3174/ajnr.A4615>.

(123) Kanda, T.; Fukusato, T.; Matsuda, M.; Toyoda, K.; Oba, H.; Kotoku, J.; Haruyama, T.; Kitajima, K.; Furui, S. Gadolinium-Based Contrast Agent Accumulates in the Brain Even in Subjects without Severe Renal Dysfunction: Evaluation of Autopsy Brain Specimens with Inductively Coupled Plasma Mass Spectroscopy. *Radiology* **2015**, *276* (1), 228–232. <https://doi.org/10.1148/radiol.2015142690>.

(124) Gianolio, E.; Gregorio, E. Di; Aime, S. Chemical Insights into the Issues of Gd Retention in the Brain and Other Tissues Upon the Administration of Gd-Containing MRI Contrast Agents. *Eur. J. Inorg. Chem.* **2019**, *2019* (2), 137–151. <https://doi.org/10.1002/ejic.201801220>.

(125) Robert, P.; Lehericy, S.; Grand, S.; Violas, X.; Fretellier, N.; Ideé, J. M.; Ballet, S.; Corot, C. T1-Weighted Hypersignal in the Deep Cerebellar Nuclei after Repeated Administrations of Gadolinium-Based Contrast Agents in Healthy Rats: Difference between Linear and Macrocyclic Agents. *Invest. Radiol.* **2015**, *50* (8), 473–480. <https://doi.org/10.1097/RLI.0000000000000181>.

(126) Gianolio, E.; Bardini, P.; Arena, F.; Stefania, R.; Di Gregorio, E.; Iani, R.; Aime, S. Gadolinium Retention in the Rat Brain: Assessment of the Amounts of Insoluble Gadolinium-Containing Species and Intact Gadolinium Complexes after Repeated Administration of Gadolinium-Based Contrast Agents. *Radiology* **2017**, *285* (3), 839–849. <https://doi.org/10.1148/radiol.2017162857>.

(127) Drahoš, B.; Lukeš, I.; Tóth, É. Manganese (II) Complexes as Potential Contrast Agents for MRI. *Eur. J. Inorg. Chem.* **2012**, No. 12, 1975–1986. <https://doi.org/10.1002/ejic.201101336>.

(128) Pan, D.; Caruthers, S. D.; Senpan, A.; Schmieder, A. H.; Wickline, S. A.; Lanza, G. M. Revisiting an Old Friend: Mn-Based MRI Contrast Agents. *Wiley Interdiscip Rev Nanomed Nanobiotechnol* **2011**, *3* (2), 162–173. <https://doi.org/10.1016/j.molcel.2007.05.041.A>.

(129) Terreno, E.; Castelli, D. D.; Viale, A.; Aime, S. Challenges for Molecular Magnetic

- Resonance Imaging. *Chem. Rev.* **2010**, *110* (5), 3019–3042. <https://doi.org/10.1021/cr100025t>.
- (130) Crossgrove, J.; Zheng, W. Manganese Toxicity upon Overexposure. *NMR Biomed.* **2004**, *17* (8), 544–553. <https://doi.org/10.1002/nbm.931>.
- (131) O’Neal, S. L.; Zheng, W. Manganese Toxicity Upon Overexposure: A Decade in Review. *Curr Env. Health Rep* **2015**, *2* (3), 315–328. <https://doi.org/10.1007/s40572-015-0056-x>.
- (132) Castets, C. R.; Koonjoo, N.; Hertanu, A.; Voisin, P.; Franconi, J. M.; Miraux, S.; Ribot, E. J. In Vivo MEMRI Characterization of Brain Metastases Using a 3D Look-Locker T1-Mapping Sequence. *Sci. Rep.* **2016**, *6*, 1–9. <https://doi.org/10.1038/srep39449>.
- (133) Bianchi, A.; Gobbo, O. L.; Dufort, S.; Sancey, L.; Lux, F.; Tillement, O.; Coll, J. L.; Crémillieux, Y. Orotracheal Manganese-Enhanced MRI (MEMRI): An Effective Approach for Lung Tumor Detection. *NMR Biomed.* **2017**, *30* (11), 1–10. <https://doi.org/10.1002/nbm.3790>.
- (134) Pierre, V. C.; Allen, M. J.; Caravan, P. Contrast Agents for MRI: 30+ Years and Where Are We Going? *J. Biol. Inorg. Chem.* **2014**, *19* (2), 127–131. <https://doi.org/10.1007/s00775-013-1074-5>.
- (135) Elizondo, G.; Fretz, C. J.; Stark, D. D.; Rocklage, S. M.; Quay, S. C.; Worah, D.; Tsang, D. D.; Chia-Mei Chen, M.; Ferrucci, J. T. Preclinical Evaluation of MnDPDP: New Paramagnetic Hepatobiliary Contrast Agent for MR Imaging. *Radiology* **1991**, *178* (1), 73–78.
- (136) Laurent, S.; Vander Elst, L.; Muller, R. N. Comparative Study of the Physicochemical Properties of Six Clinical Low Molecular Weight Gadolinium Contrast Agents. *Contrast Media Mol. Imaging* **2006**, *1* (3), 128–137. <https://doi.org/10.1002/cmml.100>.
- (137) Venter, A.; Szulc, D. A.; Loai, S.; Ganesh, T.; Haedicke, I. E.; Cheng, H. L. M. A Manganese Porphyrin-Based T1 Contrast Agent for Cellular MR Imaging of Human Embryonic Stem Cells. *Sci. Rep.* **2018**, *8*, 1–11. <https://doi.org/10.1038/s41598-018-30661-w>.
- (138) Alhamami, M.; Cheng, W.; Lyu, Y.; Allen, C.; Zhang, X.-A.; Cheng, H.-L. M. Manganese-Porphyrin-Enhanced MRI for the Detection of Cancer Cells: A Quantitative in Vitro Investigation with Multiple Clinical Subtypes of Breast Cancer. *PLoS ONE* **2018**, *13* (5), 1–17. <https://doi.org/10.1371/journal.pone.0196998>.
- (139) Ren, Y.; Sedgwick, A. C.; Chen, J.; Thiabaud, G.; Chau, C. V.; An, J.; Arambula, J. F.; He, X. P.; Kim, J. S.; Sessler, J. L.; Liu, C. Manganese(II) Texaphyrin: A Paramagnetic

Photoacoustic Contrast Agent Activated by Near-IR Light. *J. Am. Chem. Soc.* **2020**, *142* (38), 16156–16160. <https://doi.org/10.1021/jacs.0c04387>.

(140) Csupász, T.; Szücs, D.; Kálmán, F. K.; Hollóczki, O.; Fekete, A.; Szikra, D.; Tóth, É.; Tóth, I.; Tircsó, G. A New Oxygen Containing Pyclen-Type Ligand as a Manganese(II) Binder for MRI and <sup>52</sup>Mn PET Applications: Equilibrium, Kinetic, Relaxometric, Structural and Radiochemical Studies. *Molecules* **2022**, *27* (2), 371. <https://doi.org/10.3390/molecules27020371>.

(141) Paul, G.; Prado, Y.; Dia, N.; Rivière, E.; Laurent, S.; Roch, M.; Vander Elst, L.; Muller, R. N.; Sancey, L.; Perriat, P.; Tillement, O.; Mallah, T.; Catala, L. MnII-Containing Coordination Nanoparticles as Highly Efficient T1 Contrast Agents for Magnetic Resonance Imaging. *Chem. Commun.* **2014**, *50* (51), 6740–6743. <https://doi.org/10.1039/c4cc01251h>.

(142) Ma, H.; Zhang, X.; Pang, L.; Yu, B.; Cong, H.; Shen, Y. Mn-Dox Metal-Organic Nanoparticles for Cancer Therapy and Magnetic Resonance Imaging. *Dyes Pigments* **2022**, *199*, 110080. <https://doi.org/10.1016/j.dyepig.2022.110080>.

(143) Ndiaye, D.; Sy, M.; Pallier, A.; Mème, S.; de Silva, I.; Lacerda, S.; Nonat, A. M.; Charbonnière, L. J.; Toth, E. Unprecedented Kinetic Inertness for a Mn<sup>2+</sup>-bispidine Chelate: A Novel Structural Entry for Mn<sup>2+</sup>-based Imaging Agents. *Angew. Chem. Int. Ed.* **2020**. <https://doi.org/10.1002/anie.202003685>.

(144) Hamon, N.; Roux, A.; Beyler, M.; Mulatier, J.; Andraud, C.; Nguyen, C.; Maynadier, M.; Bettache, N.; Duperray, A.; Grichine, A.; Bresselet, S.; Gary-bobo, M.; Maury, O.; Tripier, R. Pyclen Based Ln(III) Complexes as Highly Luminescent Bioprobes for in Vitro and in Vivo One- and Two-Photon Bioimaging Applications. *J Am Chem Soc* **2020**. <https://doi.org/10.1021/jacs.0c03496>.

(145) Dioury, F.; Sambou, S.; Guéné, E.; Sabatou, M.; Ferroud, C.; Guy, A.; Port, M. Synthesis of a Tricyclic Tetraazatriacetic Ligand for Gadolinium(III) as Potential Contrast Agent for MRI. *Tetrahedron* **2007**, *63* (1), 204–214. <https://doi.org/10.1016/j.tet.2006.10.024>.

(146) Dioury, F.; Ferroud, C.; Guy, A.; Port, M. Synthesis of an Hexadentate Tricyclic Tetraazadiacetic Ligand as Precursor for MRI Contrast Enhancement Agents. *Tetrahedron* **2009**, *65* (36), 7573–7579. <https://doi.org/10.1016/j.tet.2009.06.117>.

(147) Drahoš, B.; Kotek, J.; Cíсарová, I.; Hermann, P.; Helm, L.; Lukeš, I.; Tóth, É. Mn<sup>2+</sup>Complexes with 12-Membered Pyridine Based Macrocycles Bearing Carboxylate or

Phosphonate Pendant Arm: Crystallographic, Thermodynamic, Kinetic, Redox, and  $1\text{H}/17\text{O}$  Relaxation Studies. *Inorg. Chem.* **2011**, *50* (24), 12785–12801. <https://doi.org/10.1021/ic201935r>.

(148) Enel, M.; Leygue, N.; Saffon, N.; Galaup, C.; Picard, C. Facile Access to the 12-Membered Macrocyclic Ligand PCTA and Its Derivatives with Carboxylate, Amide, and Phosphinate. *Eur. J. Org. Chem.* **2018**, No. 15, 1765–1773. <https://doi.org/10.1002/ejoc.201800066>.

(149) Devreux, M.; Henoumont, C.; Dioury, F.; Stanicki, D.; Boutry, S.; Larbanoix, L.; Ferroud, C.; Muller, R. N.; Laurent, S. Bimodal Probe for Magnetic Resonance Imaging and Photoacoustic Imaging Based on a PCTA-Derived Gadolinium(III) Complex and ZW800–1. *Eur. J. Inorg. Chem.* **2019**, No. 29, 3354–3365. <https://doi.org/10.1002/ejic.201900387>.

(150) Garda, Z.; Molnár, E.; Kálmán, F. K.; Botár, R.; Nagy, V.; Baranyai, Z.; Brücher, E.; Kovács, Z.; Tóth, I.; Tircsó, G. Effect of the Nature of Donor Atoms on the Thermodynamic, Kinetic and Relaxation Properties of Mn(II) Complexes Formed with Some Trisubstituted 12-Membered Macrocyclic Ligands. *Front. Chem.* **2018**, *6*, 1–14. <https://doi.org/10.3389/fchem.2018.00232>.

(151) Botár, R.; Molnár, E.; Trencsényi, G.; Kiss, J.; Kalman, F. K.; Tircso, G. Stable and Inert Mn(II)-Based and PH Responsive Contrast Agents. *J Am Chem Soc* **2020**, *142* (4), 1662–1666. <https://doi.org/10.1021/jacs.9b09407>.

(152) Botár, R.; Molnár, E.; Garda, Z.; Madarasi, E.; Trencsényi, G.; Kiss, J.; Kálmán, F. K.; Tircsó, G. Synthesis and Characterization of a Stable and Inert Mn(II)-Based Zn(II) Responsive MRI Probe for Molecular Imaging of Glucose Stimulated Zinc Secretion (GSZS). *Inorg. Chem. Front.* **2022**, *9* (3), 577–583. <https://doi.org/10.1039/D1QI00501D>.

(153) Aime, S.; Botta, M.; Gianolio, E.; Terreno, E. A p(O<sub>2</sub>)-Responsive MRI Contrast Agent Based on the Redox Switch of Manganese(II/III)-Porphyrin Complexes. *Angew. Chem. - Int. Ed.* **2000**, *39* (4), 747–750. [https://doi.org/10.1002/\(SICI\)1521-3773\(20000218\)39:4<747::AID-ANIE747>3.0.CO;2-2](https://doi.org/10.1002/(SICI)1521-3773(20000218)39:4<747::AID-ANIE747>3.0.CO;2-2).

(154) Bianchi, A.; Gobbo, O. L.; Dufort, S.; Sancey, L.; Lux, F.; Tillement, O.; Coll, J. L.; Crémillieux, Y. Orotracheal Manganese-Enhanced MRI (MEMRI): An Effective Approach for Lung Tumor Detection. *NMR Biomed.* **2017**, *30* (11), 1–10. <https://doi.org/10.1002/nbm.3790>.

(155) Hannecart, A.; Stanicki, D.; Elst, L. V.; Muller, R. N.; Lecommandoux, S.; Thévenot,

J.; Bonduelle, C.; Trotier, A.; Massot, P.; Miraux, S.; Sandre, O.; Laurent, S. Nano-Thermometers with Thermo-Sensitive Polymer Grafted USPIOs Behaving as Positive Contrast Agents in Low-Field MRI. *Nanoscale* **2015**, *7* (8), 3754–3767. <https://doi.org/10.1039/C4NR07064J>.

(156) Solomon, I. Relaxation Processes in a System of Two Spins. *Phys Rev* **1955**, *99* (2), 559–565. <https://doi.org/10.1103/PhysRev.99.559>.

(157) Bloembergen, N. Proton Relaxation Times in Paramagnetic Solutions. *J Chem Phys* **1957**, *27* (2), 572–573. <https://doi.org/10.1063/1.1743771>.

(158) Bloembergen, N.; Morgan, L. O. Proton Relaxation Times in Paramagnetic Solutions. Effects of Electron Spin Relaxation. *J Chem Phys* **1961**, *34*, 842. <https://doi.org/10.1063/1.1731684>.

(159) *The Chemistry of Contrast Agents in Medical Magnetic Resonance Imaging*; Merbach, A., Helm, L., Tóth, É., Eds.; John Wiley & Sons, Ltd: Chichester, UK, 2013. <https://doi.org/10.1002/9781118503652>.

(160) Gale, E. M.; Zhu, J.; Caravan, P. Direct Measurement of the Mn(II) Hydration State in Metal Complexes and Metalloproteins through <sup>17</sup>O NMR Line Widths. *J. Am. Chem. Soc.* **2013**, *135* (49), 18600–18608. <https://doi.org/10.1021/ja4094132>.

(161) Peters, J. A.; Geraldes, C. F. G. C. A Semi-Empirical Method for the Estimation of the Hydration Number of Mn(II)-Complexes. *Inorganics* **2018**, *6* (4), 116. <https://doi.org/10.3390/inorganics6040116>.

(162) Swift, T. J.; Connick, R. E. NMR Relaxation Mechanisms of O<sup>17</sup> in Aqueous Solutions of Paramagnetic Cations and the Lifetime of Water Molecules in the First Coordination Sphere. *J. Chem. Phys.* **1962**, *37* (2), 307. <https://doi.org/10.1063/1.1701321>.

(163) Merbach, A. S.; Helm, L.; Toth, E. 4.3.5 Mn<sup>2+</sup>-Based Contrast Agents. In *The Chemistry of Contrast Agents in Medical Magnetic Resonance Imaging, 2nd Edition*; Merbach, A. S., Helm, L., Toth, E., Eds.; Wiley, 2013; pp 179–183. <https://doi.org/10.1002/9781118503652>.

(164) Laurent, S.; Vander Elst, L.; Henoumont, C.; Muller, R. N. How to Measure the Transmetallation of a Gadolinium Complex. *Contrast Media Mol. Imaging* **2010**, *5* (6), 305–308. <https://doi.org/10.1002/cmml.388>.

- (165) Hare, D. J.; New, E. J.; De Jonge, M. D.; McColl, G. Imaging Metals in Biology: Balancing Sensitivity, Selectivity and Spatial Resolution. *Chem. Soc. Rev.* **2015**, *44* (17), 5941–5958. <https://doi.org/10.1039/c5cs00055f>.
- (166) Laurent, S.; Vander Elst, L.; Copoix, F.; Muller, R. N. Stability of MRI Paramagnetic Contrast Media: A Proton Relaxometric Protocol for Transmetallation Assessment. *Invest. Radiol.* **2001**, *36* (2), 115–122. <https://doi.org/10.1097/00004424-200102000-00008>.
- (167) Kim, K.; Jeong, B.; Lee, Y.-M.; Son, H.-E.; Ryu, J.-Y.; Park, S.; Jeong, J. C.; Chin, H. J.; Kim, S. Three-Dimensional Kidney-on-a-Chip Assessment of Contrast-Induced Kidney Injury: Osmolality and Viscosity. *Micromachines* **2022**, *13* (5), 688. <https://doi.org/10.3390/mi13050688>.
- (168) Lancelot, E.; Idée, J. M.; Couturier, V.; Vazin, V.; Corot, C. Influence of the Viscosity of Iodixanol on Medullary and Cortical Blood Flow in the Rat Kidney: A Potential Cause of Nephrotoxicity. *J. Appl. Toxicol.* **1999**, *19* (5), 341–346. [https://doi.org/10.1002/\(SICI\)1099-1263\(199909/10\)19:5<341::AID-JAT584>3.0.CO;2-U](https://doi.org/10.1002/(SICI)1099-1263(199909/10)19:5<341::AID-JAT584>3.0.CO;2-U).
- (169) Seeliger, E.; Flemming, B.; Wronski, T.; Ladwig, M.; Arakelyan, K.; Godes, M.; Möckel, M.; Persson, P. B. Viscosity of Contrast Media Perturbs Renal Hemodynamics. *J. Am. Soc. Nephrol.* **2007**, *18* (11), 2912–2920. <https://doi.org/10.1681/ASN.2006111216>.
- (170) Rozenberg, J. M.; Kamynina, M.; Sorokin, M.; Zolotovskaia, M.; Koroleva, E.; Kremenchutckaya, K.; Gudkov, A.; Buzdin, A.; Borisov, N. The Role of the Metabolism of Zinc and Manganese Ions in Human Cancerogenesis. *Biomedicines* **2022**, *10* (5), 1072. <https://doi.org/10.3390/biomedicines10051072>.
- (171) Karabulut, N.; Elmas, N. Contrast Agents Used in MR Imaging of the Liver. **2006**, *12* (1), 22–30.
- (172) Seale, M. K.; Catalano, O. A.; Saini, S.; Hahn, P. F.; Sahani, D. V. Hepatobiliary-Specific MR Contrast Agents: Role in Imaging the Liver and Biliary Tree. *RadioGraphics* **2009**, *29* (6), 1725–1748. <https://doi.org/10.1148/rg.296095515>.
- (173) Sahani, D. V.; O'Malley, M. E.; Bhat, S.; Hahn, P. F.; Saini, S. Contrast-Enhanced MRI of the Liver With Mangafodipir Trisodium: Imaging Technique and Results. *J. Comput. Assist. Tomogr.* **2002**, *26* (2), 216–222. <https://doi.org/10.1097/00004728-200203000-00010>.
- (174) Gallez, B.; Bacic, G.; Swartz, H. M. Evidence for the Dissociation of the Hepatobiliary

MRI Contrast Agent Mn-DPDP. *Magn. Reson. Med.* **1996**, *35* (1), 14–19. <https://doi.org/10.1002/mrm.1910350104>.

(175) Liu, Q.; Barker, S.; Knutson, M. D. Iron and Manganese Transport in Mammalian Systems. *Biochim. Biophys. Acta BBA - Mol. Cell Res.* **2021**, *1868* (1), 118890. <https://doi.org/10.1016/j.bbamcr.2020.118890>.

(176) Lee, N. K.; Kim, S.; Lee, J. W.; Lee, S. H.; Kang, D. H.; Kim, G. H.; Seo, H. I. Biliary MR Imaging with Gd-EOB-DTPA and Its Clinical Applications. *RadioGraphics* **2009**, *29* (6), 1707–1724. <https://doi.org/10.1148/rg.296095501>.

(177) Huang, X.-J.; Choi, Y.-K.; Im, H.-S.; Yarimaga, O.; Yoon, E.; Kim, H.-S. Aspartate Aminotransferase (AST/GOT) and Alanine Aminotransferase (ALT/GPT) Detection Techniques. *Sensors* **2006**, *6* (7), 756–782. <https://doi.org/10.3390/s6070756>.

(178) Kim, M. G.; Yoo, S. H.; Chei, W. S.; Lee, T. Y.; Kim, H. M.; Suh, J. Soluble Artificial Metalloproteases with Broad Substrate Selectivity, High Reactivity, and High Thermal and Chemical Stabilities. *J. Biol. Inorg. Chem.* **2010**, *15* (7), 1023–1031. <https://doi.org/10.1007/s00775-010-0662-x>.

(179) Laurent, S.; Vander Elst, L.; Houzé, S.; Guérit, N.; Muller, R. N. Synthesis and Characterization of Various Benzyl Diethylenetriaminepentaacetic Acids (Dtpa) and Their Paramagnetic Complexes, Potential Contrast Agents for Magnetic Resonance Imaging. *Helv. Chim. Acta* **2000**, *83* (2), 394–406. [https://doi.org/10.1002/\(SICI\)1522-2675\(20000216\)83:2<394::AID-HLCA394>3.0.CO;2-B](https://doi.org/10.1002/(SICI)1522-2675(20000216)83:2<394::AID-HLCA394>3.0.CO;2-B).

(180) Ahmed, F.; Discher, D. E. Self-Porting Polymersomes of PEG–PLA and PEG–PCL: Hydrolysis-Triggered Controlled Release Vesicles. *J. Controlled Release* **2004**, *96* (1), 37–53. <https://doi.org/10.1016/j.jconrel.2003.12.021>.

(181) Goyal, K.; Konar, A.; Kumar, B. S. H.; Koul, V. Lactoferrin-Conjugated PH and Redox-Sensitive Polymersomes Based on PEG-S-S-PLA-PCL-OH Boost Delivery of Bacosides to the Brain. *Nanoscale* **2018**, *10* (37), 17781–17798. <https://doi.org/10.1039/C8NR03828G>.

(182) Khodaverdi, E.; Tayarani-Najaran, Z.; Minbashi, E.; Alibolandi, M.; Hosseini, J.; Sepahi, S.; Kamali, H.; Hadizadeh, F. Docetaxel-Loaded Mixed Micelles and Polymersomes Composed of Poly (Caprolactone)-Poly (Ethylene Glycol) (PEG-PCL) and Poly (Lactic Acid)-Poly (Ethylene Glycol) (PEG-PLA): Preparation and In-Vitro Characterization. *Iran. J. Pharm. Res. IJPR* **2019**, *18* (1), 142–155.

- (183) Goyal, K.; Konar, A.; Kumar, A.; Koul, V. Bacosides Encapsulated in Lactoferrin Conjugated PEG-PLA-PCL-OH Based Polymersomes Act as Epigenetic Modulator in Chemically Induced Amnesia. *Neurochem. Res.* **2020**, *45* (4), 796–808. <https://doi.org/10.1007/s11064-020-02953-z>.
- (184) Chu, B.; Zhang, L.; Qu, Y.; Chen, X.; Peng, J.; Huang, Y.; Qian, Z. Synthesis, Characterization and Drug Loading Property of Monomethoxy-Poly(Ethylene Glycol)-Poly( $\epsilon$ -Caprolactone)-Poly(D,L-Lactide) (MPEG-PCLA) Copolymers. *Sci. Rep.* **2016**, *6* (1), 34069. <https://doi.org/10.1038/srep34069>.
- (185) Yang, Q.; Yu, X.; Li, T.; Li, W.; Jiang, Q.; Ming, X.; Zhang, J.; Qian, Z. Hemoglobin-Loaded Triblock PCLA-PEG-PCLA Copolymer Vesicles: A Potential Oxygen Carrier. *J. Nanosci. Nanotechnol.* **2016**, *16* (7), 6734–6740. <https://doi.org/10.1166/jnn.2016.11342>.
- (186) Piasentin, N.; Milotti, E.; Chignola, R. The Control of Acidity in Tumor Cells: A Biophysical Model. *Sci. Rep.* **2020**, *10* (1), 13613. <https://doi.org/10.1038/s41598-020-70396-1>.
- (187) Hocine, S.; Cui, D.; Rager, M.-N.; Di Cicco, A.; Liu, J.-M.; Wdzieczak-Bakala, J.; Brûlet, A.; Li, M.-H. Polymersomes with PEG Corona: Structural Changes and Controlled Release Induced by Temperature Variation. *Langmuir* **2013**, *29* (5), 1356–1369. <https://doi.org/10.1021/la304199z>.
- (188) Konishcheva, E.; Häussinger, D.; Lörcher, S.; Meier, W. Key Aspects to Yield Low Dispersity of PEO-b-PCL Diblock Copolymers and Their Mesoscale Self-Assembly. *Eur. Polym. J.* **2016**, *83*, 300–310. <https://doi.org/10.1016/j.eurpolymj.2016.08.011>.
- (189) Šachl, R.; Uchman, M.; Matějčíček, P.; Procházka, K.; Štěpánek, M.; Špírková, M. Preparation and Characterization of Self-Assembled Nanoparticles Formed by Poly(Ethylene Oxide)-Block-Poly( $\epsilon$ -Caprolactone) Copolymers with Long Poly( $\epsilon$ -Caprolactone) Blocks in Aqueous Solutions. *Langmuir* **2007**, *23* (6), 3395–3400. <https://doi.org/10.1021/la063014c>.
- (190) Discher, D. E.; Eisenberg, A. Polymer Vesicles. *Science* **2002**, *297* (5583), 967–973. <https://doi.org/10.1126/science.1074972>.
- (191) Kähkönen, V.; Seitsonen, J.; Tuovinen, H.; Ruokolainen, J.; Hirvonen, J.; Balasubramanian, V.; Santos, H. A. Evaluation of the Effects of Nanoprecipitation Process Parameters on the Size and Morphology of Poly(Ethylene Oxide)-Block-Polycaprolactone Nanostructures. *Int. J. Pharm.* **2020**, *590*, 119900.

<https://doi.org/10.1016/j.ijpharm.2020.119900>.

(192) Sanson, C.; Schatz, C.; Le Meins, J.-F.; Brûlet, A.; Soum, A.; Lecommandoux, S. Biocompatible and Biodegradable Poly(Trimethylene Carbonate)-*b*-Poly(L-Glutamic Acid) Polymersomes: Size Control and Stability. *Langmuir* **2010**, *26* (4), 2751–2760. <https://doi.org/10.1021/la902786t>.

(193) Qi, W.; Ghoroghchian, P. P.; Li, G.; Hammer, D. A.; Therien, M. J. Aqueous Self-Assembly of Poly(Ethylene Oxide)-Block-Poly( $\epsilon$ -Caprolactone) (PEO-*b*-PCL) Copolymers: Disparate Diblock Copolymer Compositions Give Rise to Nano- and Meso-Scale Bilayered Vesicles. *Nanoscale* **2013**, *5* (22), 10908. <https://doi.org/10.1039/c3nr03250g>.

(194) Mezzasalma, L.; Winter, J. D.; Taton, D.; Coulembier, O. Benzoic Acid-Organocatalyzed Ring-Opening (Co)Polymerization (ORO(c)P) of L-Lactide and  $\epsilon$ -Caprolactone under Solvent-Free Conditions: From Simplicity to Recyclability. *Green Chem.* **2018**, *20* (23), 5385–5396. <https://doi.org/10.1039/C8GC03096K>.

(195) Mezzasalma, L.; Harrisson, S.; Saba, S.; Loyer, P.; Coulembier, O.; Taton, D. Bulk Organocatalytic Synthetic Access to Statistical Copolyesters from L-Lactide and  $\epsilon$ -Caprolactone Using Benzoic Acid. *Biomacromolecules* **2019**, *20* (5), 1965–1974. <https://doi.org/10.1021/acs.biomac.9b00190>.

(196) Coto, B.; Escola, J. M.; Suárez, I.; Caballero, M. J. Determination of Dn/Dc Values for Ethylene–Propylene Copolymers. *Polym. Test.* **2007**, *26* (5), 568–575. <https://doi.org/10.1016/j.polymertesting.2007.02.001>.

(197) Lu, C.; Guo, S.; Zhang, Y.; Yin, M. Synthesis and Aggregation Behavior of Four Types of Different Shaped PCL-PEG Block Copolymers. *Polym. Int.* **2006**, *55* (6), 694–700. <https://doi.org/10.1002/pi.2034>.

(198) Lee, S.-Y.; Chin, I.-J.; Jung, J.-S. Crystallization Behavior of Poly(L-Lactide)-Poly(Ethylene Glycol) Multiblock Copolymers. *Eur. Polym. J.* **1999**, *35* (12), 2147–2153. [https://doi.org/10.1016/S0014-3057\(99\)00024-5](https://doi.org/10.1016/S0014-3057(99)00024-5).

(199) Brosset, M.; Herrmann, L.; Kiefer, C.; Falher, T.; Brinkmann, M. Controlling Orientation, Polymorphism, and Crystallinity in Thin Films of Poly(Lactic-Acid) Homopolymer and Stereocomplex Aligned by High Temperature Rubbing. *J. Appl. Polym. Sci.* **2023**, *140* (8), e53532. <https://doi.org/10.1002/app.53532>.

- (200) Szoka, F.; Papahadjopoulos, D. Procedure for Preparation of Liposomes with Large Internal Aqueous Space and High Capture by Reverse-Phase Evaporation. *Proc. Natl. Acad. Sci.* **1978**, *75* (9), 4194–4198. <https://doi.org/10.1073/pnas.75.9.4194>.
- (201) Zhou, J.; Ni, R.; Chau, Y. Polymeric Vesicle Formation via Temperature-Assisted Nanoprecipitation. *RSC Adv.* **2017**, *7* (29), 17997–18000. <https://doi.org/10.1039/C7RA01959A>.
- (202) Kunz, D.; Thurn, A.; Burchard, W. Dynamic Light Scattering from Spherical Particles. *Colloid Amp Polym. Sci.* **1983**, *261* (8), 635.
- (203) Chécot, F.; Brûlet, A.; Oberdisse, J.; Gnanou, Y.; Mondain-Monval, O.; Lecommandoux, S. Structure of Polypeptide-Based Diblock Copolymers in Solution: Stimuli-Responsive Vesicles and Micelles. *Langmuir* **2005**, *21* (10), 4308–4315. <https://doi.org/10.1021/la0468500>.
- (204) Till, U.; Gaucher-Delmas, M.; Saint-Aguet, P.; Hamon, G.; Marty, J.-D.; Chassenieux, C.; Payré, B.; Goudounèche, D.; Mingotaud, A.-F.; Violleau, F. Asymmetrical Flow Field-Flow Fractionation with Multi-Angle Light Scattering and Quasi-Elastic Light Scattering for Characterization of Polymersomes: Comparison with Classical Techniques. *Anal. Bioanal. Chem.* **2014**, *406* (30), 7841–7853. <https://doi.org/10.1007/s00216-014-7891-8>.
- (205) Caputo, F.; Mehn, D.; Clogston, J. D.; Rösslein, M.; Prina-Mello, A.; Borgos, S. E.; Gioria, S.; Calzolari, L. Asymmetric-Flow Field-Flow Fractionation for Measuring Particle Size, Drug Loading and (in)Stability of Nanopharmaceuticals. The Joint View of European Union Nanomedicine Characterization Laboratory and National Cancer Institute - Nanotechnology Characterization Laboratory. *J. Chromatogr. A* **2021**, *1635*, 461767. <https://doi.org/10.1016/j.chroma.2020.461767>.
- (206) Quattrini, F.; Berrecoso, G.; Crecente-Campo, J.; Alonso, M. J. Asymmetric Flow Field-Flow Fractionation as a Multifunctional Technique for the Characterization of Polymeric Nanocarriers. *Drug Deliv. Transl. Res.* **2021**, *11* (2), 373–395. <https://doi.org/10.1007/s13346-021-00918-5>.
- (207) Stockmayer, W. H.; Burchard, W. Quasielastic Light Scattering by Rigid Macromolecules. *J. Chem. Phys.* **1979**, *70* (6), 3138–3139. <https://doi.org/10.1063/1.437807>.
- (208) Li, T.; Senesi, A. J.; Lee, B. Small Angle X-Ray Scattering for Nanoparticle Research. *Chem. Rev.* **2016**, *116* (18), 11128–11180. <https://doi.org/10.1021/acs.chemrev.5b00690>.

- (209) Pedersen, J. S. Analysis of Small-Angle Scattering Data from Colloids and Polymer Solutions: Modeling and Least-Squares Fitting. *Adv. Colloid Interface Sci.* **1997**, *70*, 171–210. [https://doi.org/10.1016/S0001-8686\(97\)00312-6](https://doi.org/10.1016/S0001-8686(97)00312-6).
- (210) Hickson, J. In Vivo Optical Imaging: Preclinical Applications and Considerations. *Urol. Oncol. Semin. Orig. Investig.* **2009**, *27* (3), 295–297. <https://doi.org/10.1016/j.urolonc.2008.10.030>.
- (211) Choi, H. S.; Nasr, K.; Alyabyev, S.; Feith, D.; Lee, J. H.; Kim, S. H.; Ashitate, Y.; Hyun, H.; Patonay, G.; Streckowski, L.; Henary, M.; Frangioni, J. V. Synthesis and In Vivo Fate of Zwitterionic Near-Infrared Fluorophores. *Angew. Chem. Int. Ed.* **2011**, *50* (28), 6258–6263. <https://doi.org/10.1002/anie.201102459>.
- (212) Hyun, H.; Bordo, M. W.; Nasr, K.; Feith, D.; Lee, J. H.; Kim, S. H.; Ashitate, Y.; Moffitt, L. A.; Rosenberg, M.; Henary, M.; Choi, H. S.; Frangioni, J. V. CGMP-Compatible Preparative Scale Synthesis of near-Infrared Fluorophores. *Contrast Media Mol. Imaging* **2012**, *7* (6), 516–524. <https://doi.org/10.1002/cmml.1484>.
- (213) Yang, C.; Wang, H.; Yokomizo, S.; Hickey, M.; Chang, H.; Kang, H.; Fukuda, T.; Song, M. Y.; Lee, S. Y.; Park, J. W.; Bao, K.; Choi, H. S. ZW800-PEG: A Renal Clearable Zwitterionic Near-Infrared Fluorophore for Potential Clinical Translation. *Angew. Chem. Int. Ed.* **2021**, *60* (25), 13847–13852. <https://doi.org/10.1002/anie.202102640>.
- (214) Bhardwaj, U.; Burgess, D. J. A Novel USP Apparatus 4 Based Release Testing Method for Dispersed Systems. *Int. J. Pharm.* **2010**, *388* (1–2), 287–294. <https://doi.org/10.1016/j.ijpharm.2010.01.009>.
- (215) Ridolfo, R.; Arends, J. J.; van Hest, J. C. M.; Williams, D. S. Wormlike Nanovector with Enhanced Drug Loading Using Blends of Biodegradable Block Copolymers. *Biomacromolecules* **2020**, *21* (6), 2199–2207. <https://doi.org/10.1021/acs.biomac.0c00169>.
- (216) Bordes, C.; Fréville, V.; Ruffin, E.; Marote, P.; Gauvrit, J. Y.; Briançon, S.; Lantéri, P. Determination of Poly( $\epsilon$ -Caprolactone) Solubility Parameters: Application to Solvent Substitution in a Microencapsulation Process. *Int. J. Pharm.* **2010**, *383* (1), 236–243. <https://doi.org/10.1016/j.ijpharm.2009.09.023>.
- (217) Xu, J.; Zhang, S.; Machado, A.; Lecommandoux, S.; Sandre, O.; Gu, F.; Colin, A. Controllable Microfluidic Production of Drug-Loaded PLGA Nanoparticles Using Partially Water-Miscible Mixed Solvent Microdroplets as a Precursor. *Sci. Rep.* **2017**, *7* (1), 4794.

<https://doi.org/10.1038/s41598-017-05184-5>.

(218) Yin, G.; Zhao, D.; Wang, X.; Ren, Y.; Zhang, L.; Wu, X.; Nie, S.; Li, Q. Bio-Compatible Poly(Ester-Urethane)s Based on PEG–PCL–PLLA Copolymer with Tunable Crystallization and Bio-Degradation Properties. *RSC Adv.* **2015**, *5* (96), 79070–79080. <https://doi.org/10.1039/C5RA15531B>.

(219) Liu, S.; Su, Y.; Lin, M. Z.; Ronald, J. A. Brightening up Biology: Advances in Luciferase Systems for *in Vivo* Imaging. *ACS Chem. Biol.* **2021**, *16* (12), 2707–2718. <https://doi.org/10.1021/acscchembio.1c00549>.

(220) Nguyen, P. H.; Giraud, J.; Chambonnier, L.; Dubus, P.; Wittkop, L.; Belleannée, G.; Collet, D.; Soubeyran, I.; Evrard, S.; Rousseau, B.; Senant-Dugot, N.; Mégraud, F.; Mazurier, F.; Varon, C. Characterization of Biomarkers of Tumorigenic and Chemoresistant Cancer Stem Cells in Human Gastric Carcinoma. *Clin. Cancer Res.* **2017**, *23* (6), 1586–1597. <https://doi.org/10.1158/1078-0432.CCR-15-2157>.

(221) Hillaireau, H.; Couvreur, P. Nanocarriers' Entry into the Cell: Relevance to Drug Delivery. *Cell. Mol. Life Sci. CMLS* **2009**, *66* (17), 2873–2896. <https://doi.org/10.1007/s00018-009-0053-z>.

(222) Cataldi, M.; Vigliotti, C.; Mosca, T.; Cammarota, M.; Capone, D. Emerging Role of the Spleen in the Pharmacokinetics of Monoclonal Antibodies, Nanoparticles and Exosomes. *Int. J. Mol. Sci.* **2017**, *18* (6), 1249. <https://doi.org/10.3390/ijms18061249>.

(223) Onaciu, A.; Munteanu, R.; Munteanu, V. C.; Gulei, D.; Raduly, L.; Feder, R.-I.; Pirlog, R.; Atanasov, A. G.; Korban, S. S.; Irimie, A.; Berindan-Neagoe, I. Spontaneous and Induced Animal Models for Cancer Research. *Diagnostics* **2020**, *10* (9), 660. <https://doi.org/10.3390/diagnostics10090660>.

(224) Kalyane, D.; Raval, N.; Maheshwari, R.; Tambe, V.; Kalia, K.; Tekade, R. K. Employment of Enhanced Permeability and Retention Effect (EPR): Nanoparticle-Based Precision Tools for Targeting of Therapeutic and Diagnostic Agent in Cancer. *Mater. Sci. Eng. C* **2019**, *98*, 1252–1276. <https://doi.org/10.1016/j.msec.2019.01.066>.

(225) Miller, M. A.; Gadde, S.; Pfirschke, C.; Engblom, C.; Sprachman, M. M.; Kohler, R. H.; Yang, K. S.; Laughney, A. M.; Wojtkiewicz, G.; Kamaly, N.; Bhonagiri, S.; Pittet, M. J.; Farokhzad, O. C.; Weissleder, R. Predicting Therapeutic Nanomedicine Efficacy Using a Companion Magnetic Resonance Imaging Nanoparticle. *Sci. Transl. Med.* **2015**, *7* (314),

314ra183-314ra183. <https://doi.org/10.1126/scitranslmed.aac6522>.

(226) Shah, S.; Chandra, A.; Kaur, A.; Sabnis, N.; Lacko, A.; Gryczynski, Z.; Fudala, R.; Gryczynski, I. Fluorescence Properties of Doxorubicin in PBS Buffer and PVA Films. *J. Photochem. Photobiol. B* **2017**, *170*, 65–69. <https://doi.org/10.1016/j.jphotobiol.2017.03.024>.

(227) *LysoTracker<sup>TM</sup> Green DND-26, special packaging*. <https://www.thermofisher.com/order/catalog/product/L7526> (accessed 2023-03-26).

(228) Kathiravan, A.; Anbazhagan, V.; Jhonsi, M. A.; Renganathan, R. Fluorescence Quenching of Xanthene Dyes by TiO<sub>2</sub>. *Z. Für Phys. Chem.* **2007**, *221* (7), 941–948. <https://doi.org/10.1524/zpch.2007.221.7.941>.

(229) *LysoTracker<sup>TM</sup> Deep Red*. <https://www.thermofisher.com/order/catalog/product/L12492> (accessed 2023-03-26).

(230) FDA Advisory Committee Briefing Document Medical Imaging Drugs Advisory Committee Meeting to Be Held on February 14, 2013 New Drug Application 204-781 Gadoterate Meglumine Injection (Dotarem®), Sponsored by Guerbet LLC, 2013. <https://citeseerx.ist.psu.edu/document?repid=rep1&type=pdf&doi=80e1ed2955de2c946c0f86ffc959ff7c8ce0a29c> (accessed 2023-03-07).

(231) Grüll, H.; Langereis, S.; Messenger, L.; Castelli, D. D.; Sanino, A.; Torres, E.; Terreno, E.; Aime, S. Block Copolymer Vesicles Containing Paramagnetic Lanthanide Complexes: A Novel Class of T1- and CEST MRI Contrast Agents. *Soft Matter* **2010**, *6* (19), 4847–4850. <https://doi.org/10.1039/c0sm00345j>.

(232) Cheng, Z.; Thorek, D. L. J.; Tsourkas, A. Porous Polymersomes with Encapsulated Gd-Labeled Dendrimers as Highly Efficient MRI Contrast Agents. *Adv. Funct. Mater.* **2009**, *19* (23), 3753–3759. <https://doi.org/10.1002/adfm.200901253>.

(233) Garifo, S.; Stanicki, D.; Boutry, S.; Larbanoix, L.; Ternad, I.; Muller, R. N.; Laurent, S. Functionalized Silica Nanoplatform as a Bimodal Contrast Agent for MRI and Optical Imaging. *Nanoscale* **2021**, *13* (39), 16509–16524. <https://doi.org/10.1039/D1NR04972K>.

(234) Salva, R.; Le Meins, J. F.; Sandre, O.; Brûlet, A.; Schmutz, M.; Guenoun, P.; Lecommandoux, S. Polymersome Shape Transformation at the Nanoscale. *ACS Nano* **2013**, *7* (10), 9298–9311. <https://doi.org/10.1021/nn4039589>.

(235) Badria, A. Click Chemistry: A Promising Tool for Building Hierarchical Structures.

- Polymers* **2022**, *14* (19), 4077. <https://doi.org/10.3390/polym14194077>.
- (236) Zou, Y.; Zhang, L.; Yang, L.; Zhu, F.; Ding, M.; Lin, F.; Wang, Z.; Li, Y. “Click” Chemistry in Polymeric Scaffolds: Bioactive Materials for Tissue Engineering. *J. Controlled Release* **2018**, *273*, 160–179. <https://doi.org/10.1016/j.jconrel.2018.01.023>.
- (237) Nazemi, A.; Martínez, F.; Scholl, T. J.; Gillies, E. R. Biodegradable Dendritic Polymersomes as Modular, High-Relaxivity MRI Contrast Agents. *RSC Adv.* **2012**, *2* (21), 7971–7973. <https://doi.org/10.1039/c2ra20886e>.
- (238) Nazemi, A.; Gillies, E. R. Dendritic Surface Functionalization of Nanomaterials: Controlling Properties and Functions for Biomedical Applications. *Braz. J. Pharm. Sci.* **2013**, *49* (SPL.ISS.), 15–32. <https://doi.org/10.1590/S1984-82502013000700003>.
- (239) Boyce, M.; Bertozzi, C. R. Bringing Chemistry to Life. *Nat. Methods* **2011**, *8* (8), 638–642. <https://doi.org/10.1038/nmeth.1657>.
- (240) Macias-Contreras, M.; He, H.; Little, K. N.; Lee, J. P.; Campbell, R. P.; Royzen, M.; Zhu, L. SNAP/CLIP-Tags and Strain-Promoted Azide–Alkyne Cycloaddition (SPAAC)/Inverse Electron Demand Diels–Alder (IEDDA) for Intracellular Orthogonal/Bioorthogonal Labeling. *Bioconjug. Chem.* **2020**, *31* (5), 1370–1381. <https://doi.org/10.1021/acs.bioconjchem.0c00107>.
- (241) Yoon, H. Y.; Lee, D.; Lim, D.; Koo, H.; Kim, K. Copper-Free Click Chemistry: Applications in Drug Delivery, Cell Tracking, and Tissue Engineering. *Adv. Mater.* **2022**, *34* (10), 2107192. <https://doi.org/10.1002/adma.202107192>.
- (242) Beck, S.; Schultze, J.; Räder, H.-J.; Holm, R.; Schinnerer, M.; Barz, M.; Koynov, K.; Zentel, R. Site-Specific DBCO Modification of DEC205 Antibody for Polymer Conjugation. *Polymers* **2018**, *10* (2). <https://doi.org/10.3390/polym10020141>.
- (243) Chigrinova, M.; McKay, C.; Beaulieu, L.-P. B.; Udachin, K. A.; Beauchemin, A. M.; Pezacki, John Paul. Rearrangements and Addition Reactions of Biarylazacyclooctynones and the Implications to Copper-Free Click Chemistry. *Org. Biomol. Chem.* **2013**, *11* (21). <https://doi.org/10.1039/c3ob40683k>.
- (244) Shi, W.; Tang, F.; Ao, J.; Yu, Q.; Liu, J.; Tang, Y.; Jiang, B.; Ren, X.; Huang, H.; Yang, W.; Huang, W. Manipulating the Click Reactivity of Dibenzoazacyclooctynes: From Azide Click Component to Caged Acylation Reagent by Silver Catalysis. *Angew. Chem.* **2020**, *132*

- (45), 20112–20116. <https://doi.org/10.1002/ange.202009408>.
- (245) Ghosh, A. K.; Brindisi, M.; Sarkar, A. The Curtius Rearrangement: Applications in Modern Drug Discovery and Medicinal Chemistry. *ChemMedChem* **2018**, *13* (22), 2351–2373. <https://doi.org/10.1002/cmdc.201800518>.
- (246) Tanimoto, H.; Kakiuchi, K. Recent Applications and Developments of Organic Azides in Total Synthesis of Natural Products. *Nat. Prod. Commun.* **2013**, *8* (7), 1934578X1300800730. <https://doi.org/10.1177/1934578X1300800730>.
- (247) Carvalho, M. de; Sorriha, A. E. P. M.; Rodrigues, J. A. R. Reaction of Aromatic Azides with Strong Acids: Formation of Fused Nitrogen Heterocycles and Arylamines. *J. Braz. Chem. Soc.* **1999**, *10* (5), 415–420. <https://doi.org/10.1590/S0103-50531999000500012>.
- (248) Fiume, M. M.; Bergfeld, W. F.; Belsito, D. V.; Hill, R. A.; Klaassen, C. D.; Liebler, D. C.; Marks, J. G.; Shank, R. C.; Slaga, T. J.; Snyder, P. W.; Gill, L. J.; Heldreth, B. Safety Assessment of PEGylated Alkyl Glycerides as Used in Cosmetics. *Int. J. Toxicol.* **2020**, *39* (2\_suppl), 26S–58S. <https://doi.org/10.1177/1091581820951557>.
- (249) Chen, S.; Yang, K.; Tuguntaev, R. G.; Mozhi, A.; Zhang, J.; Wang, P. C.; Liang, X.-J. Targeting Tumor Microenvironment with PEG-Based Amphiphilic Nanoparticles to Overcome Chemoresistance. *Nanomedicine Nanotechnol. Biol. Med.* **2016**, *12* (2), 269–286. <https://doi.org/10.1016/j.nano.2015.10.020>.
- (250) Guerrini, G.; Gioria, S.; Sauer, A. V.; Lucchesi, S.; Montagnani, F.; Pastore, G.; Ciabattini, A.; Medagliani, D.; Calzolari, L. Monitoring Anti-PEG Antibodies Level upon Repeated Lipid Nanoparticle-Based COVID-19 Vaccine Administration. *Int. J. Mol. Sci.* **2022**, *23* (16), 8838. <https://doi.org/10.3390/ijms23168838>.
- (251) Richter, A. W.; Åkerblom, E. Polyethylene Glycol Reactive Antibodies in Man: Titer Distribution in Allergic Patients Treated with Monomethoxy Polyethylene Glycol Modified Allergens or Placebo, and in Healthy Blood Donors. *Int. Arch. Allergy Immunol.* **1984**, *74* (1), 36–39. <https://doi.org/10.1159/000233512>.
- (252) Richter, A. W.; Åkerblom, E. Antibodies against Polyethylene Glycol Produced in Animals by Immunization with Monomethoxy Polyethylene Glycol Modified Proteins. *Int. Arch. Allergy Immunol.* **1983**, *70* (2), 124–131. <https://doi.org/10.1159/000233309>.
- (253) Freire Haddad, H.; Burke, J. A.; Scott, E. A.; Ameer, G. A. Clinical Relevance of Pre-

Existing and Treatment-Induced Anti-Poly(Ethylene Glycol) Antibodies. *Regen. Eng. Transl. Med.* **2022**, *8* (1), 32–42. <https://doi.org/10.1007/s40883-021-00198-y>.

(254) Neun, B. W.; Barenholz, Y.; Szebeni, J.; Dobrovolskaia, M. A. Understanding the Role of Anti-PEG Antibodies in the Complement Activation by Doxil in Vitro. *Molecules* **2018**, *23* (7), 1700. <https://doi.org/10.3390/molecules23071700>.

(255) Hong, L.; Wang, Z.; Wei, X.; Shi, J.; Li, C. Antibodies against Polyethylene Glycol in Human Blood: A Literature Review. *J. Pharmacol. Toxicol. Methods* **2020**, *102*, 106678. <https://doi.org/10.1016/j.vascn.2020.106678>.

(256) Liu, M.; Chu, Y.; Liu, H.; Su, Y.; Zhang, Q.; Jiao, J.; Liu, M.; Ding, J.; Liu, M.; Hu, Y.; Dai, Y.; Zhang, R.; Liu, X.; Deng, Y.; Song, Y. Accelerated Blood Clearance of Nanoemulsions Modified with PEG-Cholesterol and PEG-Phospholipid Derivatives in Rats: The Effect of PEG-Lipid Linkages and PEG Molecular Weights. *Mol. Pharm.* **2020**, *17* (4), 1059–1070. <https://doi.org/10.1021/acs.molpharmaceut.9b00770>.

(257) Estapé Senti, M.; de Jongh, C. A.; Dijkxhoorn, K.; Verhoef, J. J. F.; Szebeni, J.; Storm, G.; Hack, C. E.; Schiffelers, R. M.; Fens, M. H.; Boross, P. Anti-PEG Antibodies Compromise the Integrity of PEGylated Lipid-Based Nanoparticles via Complement. *J. Controlled Release* **2022**, *341*, 475–486. <https://doi.org/10.1016/j.jconrel.2021.11.042>.

(258) Ju, Y.; Lee, W. S.; Pilkington, E. H.; Kelly, H. G.; Li, S.; Selva, K. J.; Wragg, K. M.; Subbarao, K.; Nguyen, T. H. O.; Rowntree, L. C.; Allen, L. F.; Bond, K.; Williamson, D. A.; Truong, N. P.; Plebanski, M.; Kedzierska, K.; Mahanty, S.; Chung, A. W.; Caruso, F.; Wheatley, A. K.; Juno, J. A.; Kent, S. J. Anti-PEG Antibodies Boosted in Humans by SARS-CoV-2 Lipid Nanoparticle mRNA Vaccine. *ACS Nano* **2022**, *16* (8), 11769–11780. <https://doi.org/10.1021/acsnano.2c04543>.

(259) McSweeney, M. D.; Shen, L.; DeWalle, A. C.; Joiner, J. B.; Ciociola, E. C.; Raghuvanshi, D.; Macauley, M. S.; Lai, S. K. Pre-Treatment with High Molecular Weight Free PEG Effectively Suppresses Anti-PEG Antibody Induction by PEG-Liposomes in Mice. *J. Controlled Release* **2021**, *329*, 774–781. <https://doi.org/10.1016/j.jconrel.2020.10.011>.



## **List of publications and communications**

---

### **Publications**

- Devreux, M., Henoumont, C., Dioury, F., Boutry, S., Vacher, O., Vander Elst, L., Port, M., Muller, R., Sandre, O., & Laurent, S. (2021). Mn<sup>2+</sup> Complexes with Pyclen-Based Derivatives as Contrast Agents for Magnetic Resonance Imaging: Synthesis and Relaxometry Characterization. "Inorganic Chemistry", (60), 3604-3619. doi:10.1021/acs.inorgchem.0c03120
- Devreux, M., Henoumont, C., Dioury, F., Stanicki, D., Boutry, S., Larbanoix, L., Ferroud, C., Muller, R., & Laurent, S. (22 June 2019). Bimodal Probe for Magnetic Resonance Imaging and Photoacoustic Imaging Based on a PCTA-Derived Gadolinium(III) Complex and ZW800-1. "European Journal of Inorganic Chemistry, 29", 3354-3365.
- Devreux, M., Dioury, F., Henoumont, C., Ferroud, C., & Laurent, S. (2018). Dual-modality probe for MRI and photoacoustic imaging: synthesis, and relaxometric characterization. "Mol2Net Biochemphys", 1-5.

### **Oral communication**

- Devreux, M., Gevert, T., Dioury, F., Coulembier, O., Henoumont, C., Boutry, S., Larbanoix, L., Port, M., Couillaud, F., Sandre, O., & Laurent, S. (05 December 2022). "MRI and optical image-guided drug delivery by pH-sensitive polymer nanocarriers". Oral communication at SF Nano, Strasbourg, France.
- Devreux, M., Henoumont, C., Dioury, F., Boutry, S., Vacher, O., Vander Elst, L., Port, M., Muller, R., Sandre, O., & Laurent, S. (16 March 2021). "Relaxometric study of manganese complexes based on a pyclen structure as MRI contrast agents". Oral communication at COST: Conference on achievements and perspectives of NMR relaxometry, Online.
- Devreux, M., Henoumont, C., Dioury, F., Port, M., & Laurent, S. (05 June 2019). "Synthesis and relaxometric characterization of MRI contrast agents based on pyclen structure and complexed with manganese". Paper presented at 11th conference on fast field cycling NMR relaxometry, Pise, Italy.

- Devreux, M., Henoumont, C., Dioury, F., Ferroud, C., Port, M., & Laurent, S. (02 May 2019). "Synthetic way to obtain manganese complexes derivated from pycLEN and their relaxometric measurements". Paper presented at EDT-CHIM, Namur, Belgium.

### Posters

- Devreux, M., Genevois, C., Moins, S., Baleine, N., Coulembier, O., Henoumont, C., Couillaud, F., Laurent, S., & Sandre, O. (07 November 2022). "pH-sensitive Polymer Vesicles for Image-Guided Drug Delivery Monitoring by Magnetic Resonance and Optical Imaging". Poster session presented at 1st Indo-French symposium on Molecules and Nanosciences for Health (SiTH Fall School), France.
- Devreux, M., Genevois, C., Moins, S., Baleine, N., Coulembier, O., Henoumont, C., Couillaud, F., Sandre, O., & Laurent, S. (18 October 2022). "Image-guided drug delivery by pH-sensitive polymeric vesicles, polymersomes, by magnetic resonance and optical imaging". Poster session presented at Journée scientifique de la Société Royale de Chimie, Liege, Belgium.
- Devreux, M., Genevois, C., Moins, S., Baleine, N., Coulembier, O., Henoumont, C., Couillaud, F., Sandre, O., & Laurent, S. (06 September 2022). "Image-guided drug delivery by pH-sensitive polymeric vesicles, polymersomes, by magnetic resonance and optical imaging". Poster session presented at Mardi des chercheurs, 11ème édition, Mons, Belgium
- Devreux, M., Genevois, C., Moins, S., Baleine, N., Coulembier, O., Henoumont, C., Couillaud, F., Laurent, S., & Sandre, O. (13 June 2022). "Image-guided Drug delivery by pH-sensitive Polymeric vesicles by magnetic resonance and optical imaging". Poster session presented at the Bordeaux Polymer Conference (BPC) 2022, Bordeaux, France.
- Devreux, M., Henoumont, C., Dioury, F., Boutry, S., Mutschler, A., Lassalle, C., Vacher, O., Moins, S., Coulembier, O., Vander Elst, L., & Port, M. (25 Augustus 2021). "Improvement of pycLEN-based manganese complexes relaxivity by using polymersome vesicles". Poster session presented at 16th European Molecular Imaging Meeting, EMIM, Lokhalle Göttingen, Germany.
- Devreux, M., Henoumont, C., Dioury, F., Boutry, S., Mutschler, A., Lassalle, C., Vacher, O., Moins, S., Coulembier, O., Vander Elst, L., Port, M., Muller, R., Sandre, O., & Laurent, S. (08 December 2021). "Bimodal nanoparticles for MRI and optical imaging based on polymer vesicles (polymersomes) for image-guided drug delivery". Poster session presented at Congres SFNano, Angers, France.

- Devreux, M., Henoumont, C., Dioury, F., Boutry, S., Vacher, O., Moins, S., Coulembier, O., Vander Elst, L., Port, M., Muller, R., Sandre, O., & Laurent, S. (30 March 2021). "Pyclen derivatives complexed with manganese ions and polymersomes: synthesis and characterization". Poster session presented at Mardi des Chercheurs, Virtual Meeting, Online.
- Devreux, M., Henoumont, C., Dioury, F., Moins, S., Coulembier, O., Port, M., Sandre, O., & Laurent, S. (24 August 2020). "Novel contrast agents based on pyclen derivative manganese complexes to be incorporated inside polymersomes". Poster session presented at 15th EMIM, Virtual Meeting, Online.
- Devreux, M., Henoumont, C., Dioury, F., Port, M., Muller, R., & Laurent, S. (10 October 2019). "Synthetic and relaxometric characterization of manganese complexes based on pyclen structure for magnetic resonance imaging". Paper presented at SRC Scientific Day, Namur, Belgium.
- Devreux, M., Henoumont, C., Dioury, F., Port, M., Sandre, O., Muller, R., & Laurent, S. (12 December 2019). "Novel manganese complexes based on a pyclen derivative: synthesis and relaxometric characterization". Poster session presented at SFNano-C'Nano, Dijon, France.
- Devreux, M., Henoumont, C., Dioury, F., Port, M., Laurent, S., Sandre, O., & Muller, R. (29 May 2019). "Synthesis of a manganese magnetic resonance imaging contrast agent based on pyclen structure". Poster session presented at TRTF, Mons, Belgium.
- Devreux, M., Henoumont, C., Dioury, F., & Laurent, S. (23 April 2019). "Synthesis of a bimodal contrast agent for MRI and photoacoustic". Poster session presented at BMIC, Bruxelles, Belgium.
- Devreux, M., Henoumont, C., Dioury, F., & Laurent, S. (22 March 2019). "Synthesis of a bimodal contrast agent for magnetic resonance imaging and photoacoustic imaging". Poster session presented at 14<sup>th</sup> EMIM, Glasgow, United Kingdom.
- Devreux, M., Henoumont, C., Dioury, F., & Laurent, S. (05 March 2019). "Synthesis of a bimodal contrast agent for magnetic resonance imaging and photoacoustic imaging". Poster session presented at Mardi des Chercheurs, Mons, Belgium.
- Devreux, M., Henoumont, C., Dioury, F., & Laurent, S. (29 May 2018). "Synthèse d'un agent de contraste bimodal pour l'imagerie par résonance magnétique et la photoacoustique". Poster session presented at SRC 2018, Mons, Belgium.

- Devreux, M., Henoumont, C., Dioury, F., & Laurent, S. (23 April 2018). "Synthesis of a bimodal contrast agent based on pyclyen structure for magnetic resonance and photoacoustic imaging". Poster session presented at BMIC @ UCB, Braine-l'Alleud, Belgium.
- Devreux, M., Henoumont, C., Dioury, F., & Laurent, S. (29 March 2018). "Bimodal contrast agent for MRI and photoacoustic: synthesis and relaxometric characterization". Poster session presented at YBMRS, Spa, Belgium.

### **Award**

- Best poster in the category ESMI poster prize at SFNano-C'Nano, Dijon, France.

### **Participation**

- National final of MT180s at Namur, Belgium.
- MT180s of the university of Mons at Mons, Belgium.